The Dissertation Committee for Yaroslav A. Urzhumov
certifies that this is the approved version of the following dissertation:

Sub-wavelength Electromagnetic Phenomena in Plasmonic and Polaritonic Nanostructures: from Optical Magnetism to Super-resolution

Committee:

_____

Gennady Shvets, Supervisor

_____

Herbert Berk

_____

Michael Downer

_____

John Keto

_____

Wolfgang Frey

Sub-wavelength Electromagnetic Phenomena in Plasmonic and Polaritonic Nanostructures: from Optical Magnetism to Super-resolution

by

Yaroslav A. Urzhumov, B. S.; M. S.

Dissertation

Presented to the Faculty of the Graduate School of

The University of Texas at Austin

in Partial Fulfillment

of the Requirements

for the Degree of

Doctor of Philosophy

The University of Texas at Austin

December 2007

Acknowledgments

I am deeply indebted to my supervisor, Prof. Gennady Shvets, whose provident guidance for my research has made this dissertation possible. I am thankful to Dmitriy Korobkin and Burton Neuner III for fabricating optical nanostructures and conducting experiments that validate our theoretic pioneering. Special thanks go to Thomas Taubner and Rainer Hillenbrand for promoting our SiC superlens initiative with their state-of-the-art nanoimaging technique. I acknowledge important contributions from Vitaliy Lomakin, Isaak Mayergoyz and Zhenyu Zhang, whose ideas inspired a substantial portion of this dissertation. I am grateful to Federico Capasso and Jonathan Fan for bringing the idea of plasmonic metafluids to my attention. I am thankful to Peter Nordlander, Daniel Brandl and Nikolai Mirin for interesting discussions concerning highly-symmetric plasmonic metamolecules. It was my pleasure to collaborate with Marcelo Davanço, who shared with us his experience in numerical modeling and practical nanofabrication of negative-index metamaterials. I thank all members of our group, in particular, Chris Fietz, Simeon Trendafilov, James McIlhargey and Yoav Avitzour, for discussions on electromagnetic theory of nanostructures.

The University of Texas at Austin
December 2007

Yaroslav A. Urzhumov

Sub-wavelength Electromagnetic Phenomena in Plasmonic and Polaritonic Nanostructures: from Optical Magnetism to Super-resolution

Publication No. _____

Yaroslav A. Urzhumov, Ph.D.

The University of Texas at Austin, 2007

Supervisor: Gennady Shvets

Effective medium theory of sub-wavelength metallic, semiconducting and dielectric nanostructures that encompasses their electric, magnetic and magneto-electric response at optical frequencies is introduced. Theory development is motivated by the recent surge of interest in electromagnetic metamaterials: nanostructured composites with unusual or naturally unavailable electromagnetic properties. Unlike numerous other studies, this work focuses on strongly sub-wavelength (unit cell size $a \ll \lambda/n$) structures inasmuch as non-subwavelength composites, in general, cannot be described with effective medium parameters. The theory starts

from purely electrostatic description of non-magnetic composites and uses plasmon eigenfunctions as the basis. Magnetism and other retardation phenomena are taken into account as perturbations of electrostatic equations. Theoretic description is validated by experimental data on extraordinary optical transmission through sub-wavelength hole arrays in crystalline silicon carbide films. It is shown that one of the most amazing applications of optical metamaterials, known as the "superlens", enables deeply sub-wavelength spatial resolution not limited by Abbe's resolution of a microscope. Theoretical grounds and designs of proof-of-principle verification experiments for near-field sub-wavelength imaging are presented. Theoretical principles and formulas are applied to the problem of engineering an optical negative-index metamaterial (NIM) that may be used to improve the near-field superlens. NIM engineering begins with simple two-dimensional examples (cylinder arrays, wire pairs) and advances to more complicated metamaterials (strip-film and strip-wire arrays, tetrahedral clusters). Finally, the concept of liquid negative-index metafluids (NIMF) based on plasmonic nanoclusters is introduced and exemplified using tetrahedral cluster colloids. Clusters of plasmonic nanospheres, known as Artificial Plasmonic Molecules (APM), can be easily fabricated in macroscopic amounts and, depending on their symmetry, may exhibit three-dimensionally isotropic electromagnetic response.

Contents

List of Abbreviations

APM	Artificial plasmonic molecule
BP	Bulk plasmon
BZ	Brillouin zone
CPH	Collective photon
CPL	Collective plasmon
DNM	Double-negative (meta)material
GEDE	Generalized eigenvalue differential equation
ED	Electric dipole
EE	Electrostatic eigenvalue
EM	Electromagnetic
EMPR	Effective medium parameter retrieval (from scattering matrix)
EOA	Extraordinary optical absorption
EOT	Extraordinary optical transmission
EQ	Electric quadrupole
ES	Electrostatic
FEFD	Finite element frequency domain (modeling)
FEM	Finite element method
FoM	Figure of merit, Re n_{eff}/Im n_{eff}
FTIR	Fourier Transform Infrared (microspectroscopy)
FWHM	Full width at half maximum
HMM	Higher-order multipole mode
HMR	Higher-order multipole resonance
IR	Infrared
irrep	Irreducible representation
LMA	Leaky mode analysis

LOEM	Lowest-order electric multipole
LSP(R)	Localized surface plasmon (resonance)
MD	Magnetic dipole
MPR	Magnetic plasmon resonance
MSP	Metallic strip pair(s)
NIM	Negative-index (meta)material
NMM	Negative magnetic (permeability) (meta)material
PEC	Perfect electric conductor, perfectly electrically conducting
PH	Plasmon hybridization
PhC	Photonic crystal
PP	(Propagating) plasmon-polariton
QS	Quasistatic
QSED	Quasistatic electric dipole (theory)
SCIE	Surface charge integral equation
SERS	Surface-enhanced Raman scattering/spectroscopy
SP	Surface plasmon
SPC	Subwavelength plasmonic/polaritonic crystal
SPOF	Strip pair one film (structure)
SPP	Surface plasmon-polariton
SR	Split ring
SRR	Split ring resonator
SSP	Slow surface plasmon(-polariton)

List of Tables

List of Figures

xix

xxiii

Chapter 1

Introduction: Electromagnetic Metamaterials and their Applications

1.1 The concept of electromagnetic metamaterial: engineering mesoscopic magnetism

A new area of electromagnetics has recently emerged: electromagnetic metamaterials. The emergence of this new field happened in response to the demand in materials with the electromagnetic properties that are not available in naturally occurring media.

One of the best known properties unattainable without significant metamaterial engineering is a negative refractive index. The main challenge in making a negative index material (NIM) is that both the effective dielectric permittivity ϵ_{eff} and magnetic permeability μ_{eff} must be negative [Ves62]. Numerous applications exist for NIMs in every spectral range, from microwave to optical. Those include "perfect" lenses, transmission lines, antennas, electromagnetic cloaking, and many others [Pen00, YCI05, AE04, ZE06]. Recent theoretical [PSS06, Leo06] and experimental [SMJ$^+$06] work demonstrated that for some applications such as electromagnetic cloaking it may not even be necessary to have a negative index: just controlling the effective magnetic permeability suffices. In cloaking applications [SMJ$^+$06], val-

ues of magnetic permeability between zero and ~ 2 are required; in other words, the difference $|\mu - 1|$ has to reach values of order unity. In NIMs, this difference has to exceed unity significantly.

Control over the magnetic permeability μ is therefore a key to implementing some of the most exciting electromagnetic devices, ranging from superlenses [Pen00] to invisibility cloaks [PSS06, Leo06], electromagnetic wormholes [GKLU07] and quantum levitation [LP07]; we will discuss some of them in more detail below. First realizations of negative-μ materials (NMM) and negative-index materials (NIM) were made in the microwave part of the spectrum [SPV$^+$00]. The unit cell of the proposed composite materials consisted of a metallic split-ring resonator (SRRs) [PHRS99] (responsible for the negative permeability $\mu_{\text{eff}} < 0$) and a continuous thin metal wire [PHSY96] (responsible for the negative permittivity $\epsilon_{\text{eff}} < 0$). Remarkably, even in the first microwave realizations of the NIM its unit cell was strongly sub-wavelength: $a/\lambda \approx 1/7$, where a is the lattice constant and λ is the vacuum wavelength. In fact, the condition of $a \ll \lambda$ must be satisfied in order for the effective description using ϵ_{eff} and μ_{eff} to be sensible. If the electromagnetic structure consists of larger unit cells with $a \geq \lambda/2n_d$, where n_d is the refractive index of a substrate onto which metallic elements are deposited (e.g. Duroid in some of the recent microwave experiments [SMJ$^+$06]), they cannot be described by the averaged quantities such as permittivity and permeability. It is the high λ/a ratio that distinguishes a true electromagnetic metamaterial from its more common cousin, photonic crystal [Yab87, Joh87].

Above-mentioned applications of NMMs and NIMs would be even more fascinating if they worked for the optical frequencies. There are several obvious reasons for the optical band to be very important to mankind. First, our eyes can only see electromagnetic radiation in the visible band; applications that use light as a messenger delivering information directly to our vision must therefore rely on this narrow band. For example, concealing spy airplanes from potential enemy might be useful in the RF spectrum, but making warriors transparent would be useful only in the visible band (Fig. 1.1). Second, wavelength of visible light $\lambda = 400 - 700$ nm is a lot closer to the nanoscale (defined as the range of sizes from 1 to 100 nm) than wavelength of microwaves and RF radiation. Thus, even a factor of 10 enhancement of imaging resolution relative to λ would allow us to handle nano-sized objects. Third, photons of optical radiation are a lot more energetic and
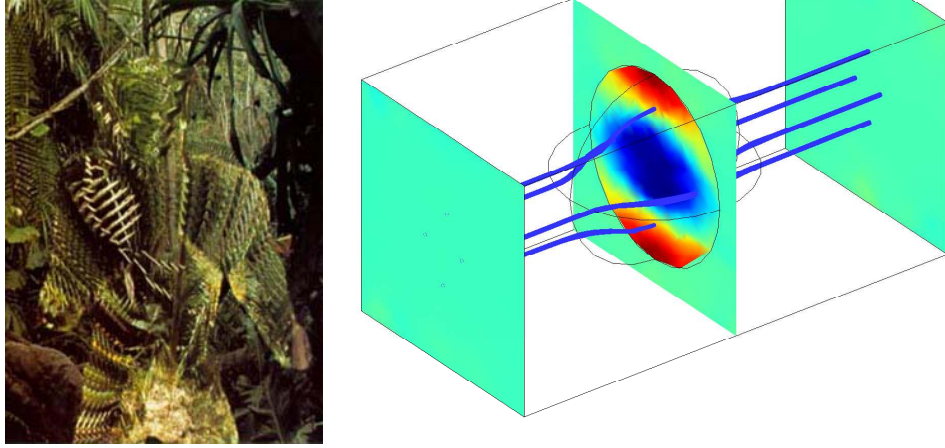
Figure 1.1: Left: A frame from a popular cinematographic film "Predator" (1987): electromagnetic camouflage of the extra-terrestrial Predator. A thin optical layer around the hunter presumably bends light (or transfers it by other means) to conceal the contents of the cavity. Right: a spherical shell bends the flow lines of electromagnetic flux (thick curves) around its core, ensuring that its scattering cross-section and thus disturbance of external field vanishes. Simulation made with COMSOL RF package [Com06].

thus interact with matter more efficiently: they can do various jobs ranging from photolithography [Shv03a] to surface-enhanced Raman scattering [IHH$^+$04, US05a].

Controlling, or enhancing the magnetic response function $\chi_M(\omega)$, however, is a lot more difficult than controlling electric response. In vacuum, there is a precise symmetry (duality) between electric and magnetic fields; as a result, intensities of E and H fields of a plane wave in vacuum are identical. This symmetry is broken in matter because it consists of electric charges only; magnetic charges have never been found in nature. Some interaction between magnetic field and ordinary matter still exists, though: that is because electrons, nuclei and atoms possess magnetic dipole moments. These magnetic dipole moments come from two sources: (1) intrinsic spins of electrons (and nuclei), and (2) angular moments associated with orbital motion of electrons (and nuclei) in atom or molecule around its center of mass. While the former is an essentially quantum phenomenon requiring relativistic field theory [BLP82], the latter moment can be crudely explained using the classical Bohr model of electron orbiting in electrostatic Coulomb field of a nucleus. Such orbital motion is similar to a current loop and naturally produces a magnetic dipole moment

$$\vec{M} = \frac{1}{2c}\vec{r} \times \vec{j}, \tag{1.1}$$

where $\vec{j} = e\vec{v}$. Substituting the radius of the orbit $r \sim a_B$, where a_B is the Bohr radius, and electron velocity $v/c \sim \alpha$, where $\alpha \approx 1/137$ is the fine structure constant, it is found that a typical value of orbital magnetic moment should be of order Bohr magneton

$$\mu_B = \alpha e a_B/2 = \frac{e\hbar}{2m_e c}. \tag{1.2}$$

On the other hand, typical values of electric dipole moment, either induced or permanent, for a single atom, should be of order $e a_B$. Magnetic moments of nuclei related to their intrinsic and orbital spin are suppressed by large factors M_n/m_e, where M_n is a nucleon mass, and can be ignored in comparison with electron contributions. Ultimately, it is the small velocity of electrons $v/c \sim \alpha$ that makes interaction between electric charges in matter and magnetic field so small.

Interaction between electric and magnetic fields of light with atomic systems can be quantified by introducing tensors of linear electric and magnetic response. Electric polarizability tensor of a single atom (or molecule) α_E^{ij} in the frequency

domain is given by a general expression [BLP82]

$$\alpha_E^{ij}(\omega) = \frac{1}{\hbar} \sum_{n \neq 0} \left[\frac{\langle n|p_i|0\rangle\langle 0|p_j|n\rangle}{\omega_{n0} - \omega} + \frac{\langle n|p_j|0\rangle\langle 0|p_i|n\rangle}{\omega_{n0}^* + \omega} \right], \qquad (1.3)$$

where $|0\rangle$ is the ground state of the system, $\omega_{n0} = (E_n - E_0)/\hbar$ are the complex resonance frequencies (including the natural linewidth $\Gamma_{n0}/2 = -\text{Im } \omega_{n0}$) and $\vec{p}$ is the operator of dipole moment (compare this with our Eq. 2.28 from Sec. 2.2 and with Eq. 24 of Ref. [AG06]). Note that electric polarizability tensor is different from the tensor of coherent scattering only by complex conjugation of ω_{n0} in the second term of (1.3), as shown in Ref. [BLP82]. Hence the results of coherent scattering theory can be used to calculate effective medium parameters.

By analogy with Eq. 1.3, magnetic polarizability α_M^{ij} of an atomic particle is given by

$$\alpha_M^{ij}(\omega) = \frac{1}{\hbar} \sum_{n \neq 0} \left[\frac{\langle n|\mu_i|0\rangle\langle 0|\mu_j|n\rangle}{\omega_{n0} - \omega} + \frac{\langle n|\mu_j|0\rangle\langle 0|\mu_i|n\rangle}{\omega_{n0}^* + \omega} \right], \qquad (1.4)$$

in which the magnetic dipole operator $\vec{\mu}$ is defined as [BLP82]

$$\vec{\mu} \equiv \frac{1}{2c} \int [\vec{r} \times \vec{j}] \, d^3x = \mu_B \left(\vec{L} + \frac{\vec{s}}{s} \right), \qquad (1.5)$$

where $\vec{L} = -i\vec{r} \times \vec{\nabla}$ is the dimensionless orbital moment and $\vec{s}$ is the spin moment operators; for electrons $s = 1/2$. Evidently, since angular momentum operators $\vec{L}$, $\vec{s}$ have matrix elements of order unity, the matrix elements of MD operator are of order $\mu_B = \frac{1}{2}\alpha(ea_B)$ in atomic systems.

In accordance with the Drude-Lorentz theory of linear resonances, the absolute value of a linear polarizability α_M is largest at the resonance frequency, i.e. at $\omega = \text{Re } \omega_{n0}$ with some n, where we have $|\alpha_M| \sim \mu_B^2/(\hbar\Gamma_{n0}/2)$; the real part of α_M has a maximum and a minimum at frequencies $\omega_{n0\pm} = \text{Re } \omega_{n0} \pm \Gamma_{n0}/2$, where

$$\max|\text{Re } \alpha_M| = 1/2 \max|\alpha_M| \sim \mu_B^2/\hbar\Gamma_{n0}. \qquad (1.6)$$

Hence, α_M could be strongly enhanced, if for some reason Γ_{n0} is very small.

One good reason why it could be small is that for magnetically-active (M1) transitions, electric-dipole transitions are prohibited by parity selection rule. Therefore, if there are no other radiative channels determining rate of decay of the state

$|n\rangle$, natural linewidth Γ_{n0} is determined by magnetic dipole radiation and is suppressed by factor $(\omega_{n0}a_B/c)^2 \sim \alpha^2$ in comparison with the natural width of E1 transitions. The rate of electric dipole radiation is

$$\Gamma_{ED} = \frac{4\omega^3}{3\hbar c^3}|\langle n|\vec{p}|0\rangle|^2 \sim (ea_B)^2\omega^3/(\hbar c^3), \tag{1.7}$$

omitting all numerical factors of order 1, and for optical transitions with frequency $\omega_{n0} \sim \omega_B \equiv me^4/2\hbar^3$ it becomes $\Gamma_{ED} \sim \alpha^4 c/a_B$. The rate of magnetic dipole radiation is then $\Gamma_{MD} \sim \alpha^2\Gamma_{ED} \sim \alpha^6 c/a_B$. Thus, the ratio $\mu_B^2/\hbar\Gamma_{MD}$, proportional to the quality factor of magnetic resonances, becomes of order $(ea_B)^2/(\hbar\Gamma_{ED}) \sim (a_B/\alpha)^3$. Let us see if that might be enough to obtain optical magnetism on the macroscopic level.

Magnetic susceptibility $\chi = (\mu - 1)/(4\pi)$ of a medium consisting of non-interacting identical particles dispersed in a dielectric medium is approximately [WAM05, Asp82] $\chi = \alpha_M/V_0$, where V_0 is the volume per particle (specific volume). In the densest possible environment, a solid crystal, atoms of size $\sim a_B$ are closely packed, so that $V_0 \sim a_B^3$ and $\chi \sim \alpha^{-3}$. Thus, it may seem possible to have atomic substances with magnetic susceptibility comparable with or exceeding 1 in absolute value. Unfortunately, this estimate is deceptive, as it does not account for widening of the natural linewidth of single-atom MD-transitions. Line broadening is completely unavoidable at solid (or liquid) state densities, when distances between particles contributing to μ-resonance approach $a_B \sim 0.1$ nm or not even $a_B/\alpha \sim 10$ nm. At such densities, optical spectral lines with width as small as $\Gamma_{MD} \sim \alpha^2\Gamma_{ED} \sim 10^6$ s$^{-1} \sim 10^{-8}$ eV are very hard to find. As a result, in all known homogeneous atomic or molecular substances, ranging from crystalline and amorphous solids to liquids and gases, magnetic permeability is practically indistinguishable from unity at wavelengths $\lambda = 100 - 1000$ nm. In addition, even if such small widths could be achieved, large magnetic susceptibilities would only exist in extremely narrow frequency bands $\Delta\omega \sim 10^{-8}$ eV; usefulness of such a magnetic material would be rather questionable.

This simple scaling analysis of electric and magnetic light-matter interactions shows that achieving values of magnetic susceptibility close to or exceeding unity, as required for exciting applications cited above, is unrealistic at optical frequencies using conventional (atom-based) materials. We can, however, go beyond

($\mu\epsilon\tau\alpha$) conventional materials and explore possibilities that emerge in composite metamaterials consisting of mesoscopic "meta-atoms". Note that optical wavelength $\lambda \geq \lambda_B = 2\pi c/\omega_B \sim 100$ nm is at least $4\pi/\alpha = 4\pi \cdot 137 \approx 1.7 \cdot 10^3$ times larger than the size of an atom ($\sim 2a_B \approx 0.1$ nm) or a typical unit cell in atomic crystals; that is because energies of optical transitions are of order Rydberg energy ($Ry = me^4/2\hbar^2 \approx 13.6$ eV) or less. In Richard Feynman's terms, there is "plenty of room at the bottom" for mesoscale optical metamaterials: one can use meta-atoms much larger than $2a_B \approx 0.1$ nm yet much smaller than optical wavelength $\lambda \sim 100 - 1000$ nm. Hence, the size of a meta-atom does not have to be restricted to scales $\sim a_B$, if its elementary components are bound together by forces other than static Coulomb $1/r^2$ force. Also, a meta-atom may contain multiple charges responding collectively to the external field — a phenomenon known as plasmon polariton. In a sense, we are engineering the Bohr magneton by increasing effective charge e and effective "Bohr radius" a_B; however, not much can be done to accelerate electron velocity $v \ll c$ so the magnetic response is still going to be much weaker than electric.

In addition, we may also engineer the frequencies of magnetic-dipole active transitions: those need not be related to atomic or molecular spectral lines, but could be transitions between energy levels of an almost **macro**scopic many-body system. In solid state physics, elementary excitations are often seen as quasi-particles; two examples of quasi-particles that can be used for mesoscale electromagnetic metamaterials are *surface plasmon-polaritons* and *surface phonon-polaritons*. Resonances of these two types, though very different in physical nature, can be used interchangeably for sub-wavelength metamaterial engineering, as we shall see in Chapters 2, 3 and 4. This is because mesoscopic structures are essentially macroscopic in comparison with atomic sizes (grain size $\gg 1$ Å); as a result, they can be described by local dielectric permittivity $\epsilon(\vec{r})$. Surface polaritons exist as long as $\epsilon(\vec{r})$ is negative in some sub-domains of the structure; the physical nature of phenomena causing negative sign of local permittivity is irrelevant on the mesoscopic level of description. Consequently, metamaterials designed with plasmonic components can be modified to work with phonon-polaritonic components and vice versa; the required modification is essentially a dimension scaling that accommodates for the difference between plasmon and phonon-polariton frequencies.

In such a way, we have naturally come to the idea of mesoscopic metama-

terials: composite media consisting of wisely arranged particles of appropriately tailored size, shape, composition and morphology. Electric currents in these particles mimic the orbital motion of electrons in atomic systems and provide artificial orbital magnetism that resembles conventional diamagnetism, in the following sense.

Magnetization of the proposed meta-magnetic systems exists only while it is being induced by external high-frequency fields, and during a short relaxation period. This relaxation time is determined by (a) rate of spontaneous radiation and (b) rate of dissipation. While the former can be strongly quenched by arranging radiators into omnidirectionally periodic arrays (i.e. photonic crystals), not much can be done to suppress resistive damping (except, perhaps, superconductivity [WP07]). On the contrary, electronic, atomic and molecular magnetic moments are permanent (if they aren't zero because of vanishing total spin): quantum mechanics allows charged particles to oscillate even in the ground state, which by definition has no decay rate. Thus, in paramagnetic substances (including gases, liquids and solids) the average magnetic moment may vanish in the absence of external field due to chaotic orientations of individual building blocks, but each block has a permanent, constant magnetic moment proportional to its spin. In diamagnetic substances, the building blocks (atoms, molecules) do not have a permanent magnetic moment, because of zero total spin of an atom; this resembles mesoscopic magnetism studied in this work. However, diamagnetic materials become magnetized (thanks to Larmour theorem) even in static *magnetic* field alone; no electric field is necessary for that.

Such fundamental difference (the need for external high-frequency electric field) between "true" magnetics and "meta" magnetics makes it somewhat difficult to study or even define the magnetic permeability at optical frequencies. One cannot study the high-frequency response of such structures to magnetic field alone, and high-frequency magnetic field cannot exist without the accompanying electric field. Some scientists, including L. D. Landau [LL84] and A. M. Agranovich [AG06], have used this argument to denounce the very notion of magnetic permeability at optical frequencies. For example, Lev Landau made a famous claim [LL84] that "magnetic permeability $\mu(\omega)$ ceases to have any physical meaning at relatively low frequencies; taking the difference $\mu(\omega) - 1$ into account would be an unwarrantable refinement" (in the Russian original textbook it was worded even stronger: "illicit accuracy exceeding"). Landau's argument is based essentially on an assumption that magnetic susceptibility $\chi(\omega) = (\mu(\omega) - 1)/(4\pi)$ is only meaningful when the magnetization

current $c\vec{\nabla} \times \vec{M}$ (curl of magnetization $\vec{M} = (\vec{B} - \vec{H})/(4\pi)$) is large compared to the displacement current $\partial \vec{P}/\partial t$; the total current in the definition (1.1) is the sum of the two:

$$\vec{j} = \partial \vec{P}/\partial t + c\vec{\nabla} \times \vec{M}. \tag{1.8}$$

Here and everywhere in this Dissertation, it is assumed that conductivity is absorbed into complex permittivity $\epsilon = \epsilon' + i\omega/\sigma$; thus the displacement current also contains conduction current.

The claim of "no magnetism at optical frequencies" [LL84] was accompanied by a crude microscopic estimate leading to a strong inequality

$$\chi(\omega) \sim (\omega a/c)^2 \ll 1 \tag{1.9}$$

for atomic substances at optical frequencies, where $a \sim 2a_B \approx 1$ Å is the size of an atom.

Agranovich and Gartstein further quantified this argument in Ref. [AG06] by providing an estimate of magnetization of a homogeneous cylinder with dielectric and magnetic permeabilities ϵ, μ placed inside a solenoid of radius l. They came to an interesting conclusion: the "true" magnetic moment of a body associated with its $\mu(\omega)$ will exceed its "fake" magnetic moment related to electric displacement currents as long as

$$(\mu - 1)/\mu \gg \frac{1}{8}\left(\frac{\omega l}{c}\right)^2 (\epsilon - 1). \tag{1.10}$$

Combining this criterion with Landau's estimate (1.9) and the requirement of macroscopic size of the sample, $l \gg a_B$, they reproduced Landau's argument that the criterion for "true magnetism" (1.10) cannot be satisfied in atomic systems at visible frequencies, and thus optical magnetism is impossible.

To address this argument, we first note that in purely dielectric systems *all* magnetic moment (as defined by Eq. 1.1) comes from displacement current $\partial \vec{P}/\partial t = -i\omega \vec{P}$. Hence, magnetic susceptibility studied in this work is entirely "fake" in the sense of Ref. [AG06]. However, we argue that inequality (1.10) cannot be used to meaningfully discriminate between the "true" and "fake" magnetization even in conventional magnetic substances. It seems possible to violate the condition (1.10) even at relatively low frequencies in conventional materials, where the "legality" of μ has never been questioned (for example, if for some reason χ is extremely small and

ϵ is sufficiently large). For several reasons, it is impossible to separate the magnetic phenomena associated with displacement and magnetization currents. First, it is known that the magnetization current can be included into displacement current (regardless of their absolute values), if non-local response, i.e. spatial dispersion, is allowed [LL84]. After temporal and spatial Fourier transformations, this inclusion can be written as [LL84, Vin02, ASNZ04, AG06]

$$\epsilon_{tot}^{ij}(\omega, \vec{k}) = \epsilon_{electr}^{ij}(\omega, \vec{k}) + \frac{c^2 k^2}{\omega^2} \left(1 - \mu^{-1}(\omega)\right) \left(\delta_{ij} - \frac{k_i k_j}{k^2}\right), \qquad (1.11)$$

assuming, for simplicity, isotropic magnetic permeability $\mu(\omega)$. This inclusion of the entire electromagnetic response into dielectric response is possible at any frequencies, radio and optical alike.

Second, from microscopic viewpoint, the orbital part of magnetization in atomic systems comes from *electric currents*, as we noted above; it is hence analogous to the $\partial \vec{P}/\partial t$ contribution in classical electrodynamics. At the same time, in many cases it is impossible to separate the orbital ($\vec{L}$) contribution to magnetization from the spin ($\vec{s}$) part, rendering discrimination between two parts of magnetic moment meaningless. Third, from the most fundamental, quantum field theory, point of view, it was shown [BLP82] that the magnetization related to intrinsic magnetic moment of electrons (and their spin s) — probably the most real of all real magnetic moment densities — is a quantum mechanical current constructed from relativistic electron wave functions using Dirac γ-matrices: $j^\mu = e\bar{\psi}\gamma^\mu\psi$. We conclude that impossibility to separate on the fundamental level the spin-related current from orbital current does not invalidate the description of materials with magnetic permeability or makes the notion of μ less valuable to electromagnetic theory of materials. The real science behind the undoubtedly correct claim of "no optical magnetism in conventional materials" is the inequality (1.9).

Perhaps what was also implicit in Landau's remark on magnetic permeability, is the competition between magnetic-dipole (M1) and electric-quadrupole (E2) transitions [BLP82], which both lead to resonant terms in spatially-dispersive permittivity $\epsilon_{\text{eff}}(\omega, \vec{k})$ of comparable strength (see the note on p. 155 of Ref. [AG66]). This coincidence sometimes makes it difficult to clearly separate magnetic phenomena from effects of similar strength not describable by μ_{eff} (for discussion, see Ref. [AG06]). In this work, we will present two- and three-dimensional examples of

metamaterials where magnetic dipole phenomena cannot be confused with electric quadrupoles (EQ), because symmetry-related selection rules prohibit EQ transitions in MD resonances (Sec. 4.1 and Sec. 4.4).

Designing magnetic metamaterials for optical frequencies, unfortunately, has proven to be much more challenging than for microwaves. The real challenge comes from the necessity to keep the building blocks much smaller than wavelength. Microwave structures can be made extremely sub-wavelength using several standard microwave approaches to making a sub-wavelength resonator: enhancement of the resonator's capacitance by making its aspect ratios (e. g., ratio of the SRR's radius and gap size) high, inserting high-permittivity materials into SRR's gap, and so on. Simply scaling down NIMs from microwave to optical wavelengths does not work for two reasons.

First, to develop a $\lambda/10$ unit cell requires much smaller (typically, another factor 10) sub-cellular features such as metallic line widths and gaps. For $\lambda = 1$ μm that corresponds to 10nm features which are presently too difficult to fabricate. For example, the classic SRR has been scaled down to $\lambda = 3$ μm, but further wavelength reduction using the same design paradigm seems unpractical. Second, as the metal line width approaches the typical skin depth $l_{sk} \approx 25$nm, metal no longer behaves as an impenetrable perfect electric conductor (PEC). Optical fields penetrate into the metal, and the response of the structure becomes *plasmonic*.

These difficulties have not deterred the researchers from trying to fabricate and experimentally test magnetically-active and even negative index structures in the infrared [ZFP$^+$05, DEW$^+$05, SCC$^+$05, DEW$^+$06] and even visible [GGG$^+$05, CCY$^+$07] spectral regions. Because fabricating intricate metallic resonators on a nanoscale is not feasible, much simpler magnetic resonances such as pairs of metallic strips or wires [ZFP$^+$05, SCC$^+$05, DEW$^+$06] or metallic nanoposts [GGG$^+$05] have been used in the experiments. Unfortunately, so far there has been no success in producing *sub-wavelength* magnetically-active metamaterials in the optical range satisfying $a < \lambda/2n_d$, where n_d is the refractive index of a dielectric substrate or filler onto which magnetic materials are deposited. The reason for this is very simple [SU06]: in the absence of *plasmonic effects*, simple geometric resonators (such as pairs of metal strip or wires) resonate at the wavelength $\lambda \sim 2n_d L$, where L is the characteristic size of the resonator. In other words, "simple" metallic resonators are not sub-λ resonators.

Fortunately, metallic resonators can be miniaturized using *plasmonic effects* [Shv03b, SU04a, SU05, SU06]. In the optical regime metals can no longer be described as perfect electric conductors. Instead, they are best described by a frequency-dependent plasmonic dielectric permittivity $\epsilon(\omega) \equiv \epsilon' + i\epsilon''$. For low-loss metals such as silver, $\epsilon'' \ll |\epsilon'|$ and $\epsilon' \ll -1$. Therefore, there is a significant field penetration into metallic structures that are thinner than or comparable with the skin depth $l_{sk} = \lambda/2\pi\sqrt{-\epsilon'} \approx 25$nm. In metals $\epsilon(\omega)$ is determined by the Drude response of the free electron to the optical fields; metals are utilized in Chapter 4. In crystalline semiconductors, the dielectric function is determined by Drude-Lorentz response of optical phonons of the crystalline lattice; substances of this type are considered in Chapter 3.

1.2 History and applications of electromagnetic metamaterials

Since the rebirth of Veselago perfect lens idea in light of recently discovered metamaterials [PHRS99, SPV$^+$00], the number of publications on the matter and related issues (such as plasmonics, phononics, metamaterials, nano-photonics, nano-antennas, optical nano-circuit engineering, etc.) has sky-rocketed, and it continues to grow. Here, only selected publications that may be seen as important milestones in the field are highlighted.

One of the most well-publicized applications of electromagnetic metamaterials is negative refraction and related phenomena. The recent boom in EM metamaterial research was caused largely by a series of papers by John Pendry [Pen00], David Smith [SK00, SPV$^+$00] and their collaborators, where it was demonstrated, for the first time, how negative-index materials can actually be fabricated. Those authors were certainly not the first ones to consider negative index of refraction. Brief historical overviews of negative-index research have been recently published, e.g. by S. Tretyakov [Tre05] and V. Shalaev [Sha07]. It is pointed out in [Sha07] that negative phase velocity was discussed as early as in 1904 by scientific giants Arthur Schuster and H. Lamb. Professor L. I. Mandelshtam taught negative refraction as a plausible physical phenomenon at Moscow University in the early 1940's [Man50]. Another Russian scientist, G. D. Malyuzhinets considered implications of the backward-wave media on the Sommerfeld radiation boundary condition [Mal51]. Importantly, he

provided probably the first-ever physical model for a backward-wave medium. His construction was a one-dimensional LC-circuit transmission line; such structures and the methodology of RF circuit engineering are very actively pursued in the modern metamaterial literature [CI03, GE03, CI04, ESA05, YCI05]. Amongst other important publications on NIMs in mid-XX century we can point out D. V. Sivukhin's 1957 paper [Siv57] and V. E. Pafomov's 1959 paper [Paf59] where they showed that negative index of refraction can be implemented as a double-negative medium (DNM), i.e. a medium with simultaneously negative ϵ and μ, and R. A. Silin's 1959 paper [Sil59] describing periodic media (or photonic crystals, as we call them now) with negative dispersion.

Another milestone in NIM history was put by Prof. V. G. Veselago (Moscow Inst. Phys. Tech.) in 1967 [Ves62]. Veselago introduced now-popular terms "right-handed" and "left-handed" media, referring to the handedness of vector triplets $(\vec{E}, \vec{H}, \vec{k})$ in regular and negative-index media. He pointed to some of the counter-intuitive properties of left-handed media, including inverse Doppler effect, backward Čerenkov radiation and negative radiation pressure. Moreover, he discovered the "perfect lens": a flat slab of double-negative medium providing perfect relocation of field distributions from one plane (object) to another (image). Veselago's analysis, however, was based essentially on geometric (ray) optics. He did not prove an important property of his flat lens: that it actually "resolves" (in the sense explained in Chapter 3) spatial details much smaller than the wavelength of light. In fact, in an ideal superlens, there is no lower limit on the feature size; this curious mathematic fact and its physical explanation (surface waves) had to wait until 2000 to be discovered by J. Pendry, D. R. Smith and others [Pen00, SPV$^+$00].

The timely combination of the mathematical proof of perfect imaging [Pen00] and the experimental demonstration of negative-index structures [SPV$^+$00] caused a considerable public stir over metamaterial research. However, initial excitement with the "perfect lens" has largely decayed by the time this Dissertation was written. It was proven [SSR$^+$03, Mer04, PN05a] that any realistic losses in a NIM lens reduce super-resolution essentially back to the Abbe's resolution limit; this issue will be discussed in Chapter 3. Sub-wavelength spatial harmonics providing enhanced resolution in a realistic superlens survive only within limited distances from the source plane. Therefore, proof-of-principle studies of the original Veselago-Pendry-Smith superlens have essentially concluded by year 2007 with demonstration of deeply sub-

wavelength spatial resolution in the near field [FLSZ05, KUS06, TKU$^+$06], which is the subject of Chapter 3.

In response to the serious limitations in a realistic superlens, two approaches to overcoming these difficulties have been proposed and actively studied in the years 2001-2007. One approach is to overcome resistive damping in metamaterials by mixing them with active (gain) media [BS03, Law04, Law07, ST07, NZB$^+$06, PO06]. Multiple implementations of metamaterials with gain have been proposed, ranging from simple mixtures of laser dye molecules with NIMs [ST07, NZB$^+$06] or stacking layers of NIMs with layers of lasing media [RP03, SKRS44], to stimulated emission via surface-plasmon modes [Sir98, Tre00, BS03, SD89, NTF04, SGE05]. A comprehensive list of articles on this matter published by 2006 has been compiled by V. Shalaev in Ref. [Sha07]. He concluded that it should be feasible to use gain materials to compensate for the losses introduced by plasmonic nanostructures in NIMs. This conclusion is reaffirmed by the results of Section 4.3, and it motivates the studies of optical NIMs presented in this work.

Another approach to overcoming the difficulties of the original superlens is a novel phenomenon dubbed "hyperlensing" [JAN06]. A hyperlens of Refs. [SE06, JAN06] is a cylindrical, essentially two-dimensional structure filled with anisotropic *indefinite* medium [SKS04]. By indefinite medium we mean that the signs of at least one of its constitutive parameters, ϵ_{eff}, μ_{eff} or n_{eff}, has different signs for different polarizations of light (e.g., $\epsilon_{xx}\epsilon_{yy} < 0$); many of the metamaterials of Chapter 4 and the multi-layered superlens of Chapter 3 are indefinite media in certain frequency bands. Hyperlenses proposed in Refs. [SE06, JAN06] and implemented in Ref. [LLX$^+$07] use indefinite permittivity tensor with negative radial component and positive tangential component. The dispersion relation of light in indefinite medium is hyperbolic:

$$\frac{k_r^2}{\epsilon_\theta} - \frac{k_\theta^2}{|\epsilon_r|} = k_0^2; \tag{1.12}$$

hence the absolute value of the wavenumber $|\vec{k}|$ is not restricted by the wavenumber of light in vacuum $k_0 = \omega/c$. As a result, spatial Fourier harmonics with extremely small wavelengths $\lambda_k = 2\pi/|\vec{k}|$ can *propagate* in such media. The significance of the hyperlens is that it converts evanescent waves emanating from the object (which carry information about sub-wavelength features) into propagating waves and brings them to the surface, thus magnifying the object from sub-λ to supra-λ dimensions.

Since these waves are not evanescent (exponentially decaying), they need not be exponentially enhanced, as they must be in the original negative-index superlens. Hence the hyperlens is much less sensitive to resistive damping in metallic substances used for its fabrication [LLX$^+$07] than the superlens. An interesting combination of cylindrical geometry and multilayered superlensing dubbed "magnifying superlens" has been recently proposed and experimentally demonstrated [SHD07]. Another variant of the magnifying hyperlens, with surface corrugations converting from evanescent to propagating waves on the lens' outer surface, has been proposed by Liu, Zhang et al. [LDL$^+$07].

It has become obvious in the recent years that with electromagnetic metamaterials, some of the wildest mathematical constructions may become, to a limited extent, a physical reality. For instance, the above-mentioned indefinite medium is a model of Minkowski space-time, because one of the spatial coordinates plays the role of time. Mathematically, frequency-domain equations (Poisson or Helmholtz) effectively become hyperbolic (wave) equations. The idea of seeing anisotropic ϵ and μ tensors as metric tensors [LP06, MBW06] of a space-time manifold has proven to be extremely fruitful in the past two years, resulting in a new boom of publications on electromagnetic metamaterials [Leo06, PSS06, CPS$^+$06, SMJ$^+$06, GKLU07]. It was shown by Pendry et al. [PSS06] that it is possible to choose the tensors ϵ and μ in a coating around an object in such a way that the whole structure has exactly zero cross-section for all angles of incidence and all angles of scattering (see Fig. 1.1(right)). Their solution, dubbed *invisibility cloak*, is universal: it provides perfect concealment of objects of any size (compared with wavelength), any shape and arbitrary composition. The solution is essentially a concentric spherical shell with radii $R_o > R_i$ that combines impedance-matching property ($\epsilon = \mu$) with a conformal transformation that ensures proper bending of electromagnetic flux flow around the inner core:

$$\epsilon_{rr} \equiv \mu_{rr} = \frac{R_o}{R_o - R_i} \left(\frac{r - R_i}{r} \right)^2, \tag{1.13}$$

$$\epsilon_{\theta\theta} \equiv \epsilon_{\phi\phi} \equiv \mu_{\theta\theta} \equiv \mu_{\phi\phi} = \frac{R_o}{R_o - R_i}. \tag{1.14}$$

The inner surface of invisible shell is, in a sense, an event horizon [LP06]: no radiation can penetrate into or from the inner core, which is electromagnetically dis-

connected from the outside world. Depending on specific applications, this isolation can be seen as an advantage or drawback; for spying purposes a combination of an invisibility cloak with a one-way mirror that leaks some radiation into the hidden cavity (and perhaps actively compensates for this loss on the opposite side) would be a lot more useful [Ler05].

More recently, Pendry et al. have also provided the two-dimensional version [CPS+06] of their solution; cylindrical cloaking was immediately demonstrated experimentally for microwave radiation [SMJ+06]. It was further discovered [CCKS07] that an alternative "cloaking" solution exists in two dimensions which, in fact, requires no magnetic permeability tensor. The solution of Ref. [CCKS07] ensures perfect bending of electromagnetic flux, much the same way as in Ref. [CPS+06] and Fig. 1.1(right), although it is not precisely reflection-free or shadow-free. The latter two properties require perfect impedance matching between the cloaking device and ambient medium, which is practically impossible without manipulating the magnetic permeability μ (impedance of a wave is a ratio $\mu^{1/2}/\epsilon^{1/2}$). This motivates further studies of magnetic metamaterials, as they seem to be the only hope for implementing the perfect invisibility cloak [PSS06].

1.3 Statement of the problem

In this Chapter, we have explained the importance and novelty of engineering electromagnetic metamaterials. This motivates the studies of sub-wavelength phenomena in plasmonic or phonon-polaritonic structures presented in this work. The goal of the dissertation is essentially three-fold. First, we need to develop an analytic theory and a general framework for understanding and designing electromagnetic metamaterials. Second, we want to create some of the most challenging metamaterials that have not been convincingly demonstrated so far — double-negative metamaterials (DNMs) for optical frequencies, covering parts of spectrum from near-UV to mid-IR. Third, we want to demonstrate that at least one of the most exciting (and historically first) applications of DNMs — the superlens — is a meaningful scientific and technological tool enabling deeply sub-wavelength resolution. These problems are solved in Chapters 2–4. Concluding Chapter 5 provides a summary of results and outlines some of the unsolved questions that emerged in these studies.

Chapter 2

Quasistatic Perturbation Theory of Sub-wavelength Plasmonic and Polaritonic Crystals

In this Chapter, we introduce an effective medium theory of sub-wavelength metallic, semiconducting and dielectric nanostructures that encompasses their electric, magnetic and magneto-electric response at optical frequencies. Theory development is motivated by the recent surge of interest in electromagnetic metamaterials: nanostructured composites with unusual or naturally unavailable electromagnetic properties. Unlike numerous other studies, this work focuses on strongly sub-wavelength (unit cell size $a \ll \lambda/n$) structures inasmuch as non-subwavelength composites, in general, cannot be described with effective medium parameters. The theory starts from purely electrostatic description of non-magnetic composites and uses plasmon eigenfunctions as the basis. Magnetism and other retardation phenomena are taken into account as perturbations of electrostatic equations.

The theory consists of two major components: (1) definitions for effective medium parameters in terms of quasistatic electric fields, and (2) methodology for computing these fields in the form of eigenmode expansions. As a result, simple closed-form expressions for effective dielectric permittivity $\epsilon_{\text{eff}}(\omega)$ and magnetic

permeability $\mu_{\text{eff}}(\omega)$, as well as optional magneto-electric response functions, are obtained. This new theory is entirely general in the sense that it is applicable to nano-structures with arbitrary geometry of plasmonic (or polaritonic) inclusions. For a general geometry of inclusions, the theory is semi-analytical: numerical coefficients in analytical formulas are typically computed numerically from electrostatic eigenfunctions of the relevant plasmon states. This semi-analytical approach can be seen as an efficient characterization tool for electromagnetic metamaterial design: in most cases, only a few resonance eigenstates need to be found numerically in order to estimate the optical properties of a nanostructure in a wide frequency range. Several examples of negative permeability and negative index plasmonic metamaterials are used to illustrate the theory. Finally, theoretic description is validated by experimental data on extraordinary optical transmission through sub-wavelength hole arrays in crystalline silicon carbide films.

2.1 Motivation for theory development

Presently, the only sufficiently general method for theoretic characterization of electromagnetic metamaterials is by carrying out fully electromagnetic scattering simulations, obtaining complex transmission (t) and reflection (r) coefficients, and then calculating the effective parameters ϵ_{eff} and μ_{eff} of the metamaterial from r and t using inverse Fresnel-Airy formulas for a homogeneous magneto-dielectric slab, as described in a number of earlier works [SSMS02, MS03] and Section 4.2.4. Such direct approach is lacking the intuitive appeal and rigor of the earlier microwave work that provided semi-analytic expressions for both ϵ_{eff} [PHSY96] and μ_{eff} [PHRS99]. Moreover, the extracted parameters of a periodic structure exhibit various artifacts such as anti-resonances [KMSS03] that make their interpretation even less intuitive.

Recent progress has been made in rigorously calculating the quasistatic dielectric permittivity ϵ_{qs} of plasmonic nanostructures [SU04a, SU05, LFUS06, LFUS07] exhibiting optical magnetism. In fact, the frequency dependence of $\epsilon_{\text{qs}}(\omega)$ of an *arbitrary* periodic nanostructure can be reduced to a set of several numbers [SFB01, SBK04] (frequencies and strengths of various electric dipole resonances) that can be obtained by solving a generalized eigenvalue equation. However, there has been a very limited progress in calculating the magnetic permittivity of such structures. Only for several specific structures has $\mu_{\text{eff}}(\omega)$ been calcu-

18

lated [PSS03, ASE06, SSS06], usually under highly restrictive assumptions.

It would be highly desirable if a simple formula expressing $\mu_{\text{eff}}(\omega)$ in terms of several easily computable parameters could be derived. The increased complexity of new devices based on magnetic metamaterials [SMJ$^+$06] further highlights the need for such rapid and intuitive determination of $\mu_{\text{eff}}(\omega)$. Simply put, it is important to obtain rigorous expressions for $\mu_{\text{eff}}(\omega)$ that are similar in their form and complexity to those available for $\epsilon_{\text{qs}}(\omega)$. In addition, the formulas for $\epsilon_{\text{qs}}(\omega)$ themselves need further refinement. For example, when the size of a plasmonic nanostructures becomes a sizable fraction of the wavelength (as small as $\lambda/6$), the assumption of $\epsilon_{\text{eff}} \approx \epsilon_{\text{qs}}$ loses accuracy. One of the reasons is that the electric dipole resonances acquire a considerable electromagnetic red shift [MFZ05] that needs to be accounted for. The main objective of this Chapter is to derive, in the limit of $a \ll \lambda$, accurate formulas for $\epsilon_{\text{eff}}(\omega)$ and $\mu_{\text{eff}}(\omega)$.

2.2 Effective quasistatic dielectric permittivity of a plasmonic metamaterial

In this Section, we present the foundation of electromagnetic effective medium theory of sub-wavelength nanostructures: plasmon resonance theory of electric response in composite media. This theory consists of two basic components: (a) definitions of dielectric permittivity tensor, which contains full information about electric response of bulk nanostructures (subsection 2.2.1), and (b) solutions of electrostatic Poisson equation driven by external electric field in the form of plasmon eigenmode expansions (subsection 2.2.2). Our theory is a somewhat generalized formulation of the Bergman-Stroud theory of plasmon resonances in binary composite media [BS92, SFB01, SU04a].

2.2.1 Capacitance and dipole moment definitions of effective permittivity

In this subsection, several definitions of effective permittivity are introduced. It is shown analytically that in the quasistatic limit all of these definitions are mathematically equivalent forms of the same definition, which we call the "dipole density" definition. The deep-laid origin of this definition will be elucidated in

subsection 2.4.1.

The most simple and intuitive method of introducing the effective dielectric permittivity of a complex periodic plasmonic metamaterial is to imagine what happens when a single cell of such structure is immersed in a uniform electric field. To better illustrate the notion of effective permittivity, calculations in this subsection are simplified by assuming that the unit cell is a rectangular block of dimensions $a_x \times a_y \times a_z$ with the center at the origin of Cartesian coordinate system, xyz. The unit cell is assumed to consist of a plasmonic inclusion with a complex frequency-dependent dielectric permittivity $\epsilon(\omega)$ embedded into a dielectric host with the dielectric permittivity ϵ_d. The plasmonic inclusion does not have to be connected and it may intersect the unit cell boundary. We further assume in this subsection that the structure has three planes of symmetry (xy, xz and yz). In that case the effective permittivity tensor is diagonal: $\epsilon_{qs} = \mathrm{diag}(\epsilon_{qs}^{xx}, \epsilon_{qs}^{yy}, \epsilon_{qs}^{zz})$. This restriction will be lifted in subsection 2.2.2, where effective permittivity tensor is found in the most general form.

Applying a constant electric field $\vec{E}_0 = \vec{e}_x E_{0x} + \vec{e}_y E_{0y} + \vec{e}_z E_{0z}$ is equivalent to solving the Poisson equation for the potential ϕ:

$$\vec{\nabla} \cdot \left(\epsilon \vec{\nabla} \phi \right) = 0 \tag{2.1}$$

on the rectangular domain $V = [-a_x/2, a_x/2] \times [-a_y/2, a_y/2] \times [-a_z/2, a_z/2]$. The external electric field $\vec{E}_0$ determines the boundary conditions satisfied by ϕ: (1) $\phi(a_x/2, y, z) = \phi(-a_x/2, y, z) - E_{0x} a_x$, (2) $\phi(x, a_y/2, z) = \phi(x, -a_y/2, z) - E_{0y} a_y$, and (3) $\phi(x, y, a_z/2) = \phi(x, y, -a_z/2) - E_{0z} a_z$. We now view the unit cell of a metamaterial as a tiny capacitor immersed in a uniform electric field which is created by the voltage applied between its plates. For calculating ϵ_{qs}^{xx} assume that the voltage $V_0 = E_{0x} a_x$ is applied between its sides $x = -a_x/2$ and $x = a_x/2$, and that $E_{0y} = E_{0z} = 0$. From the potential distribution $\phi(x, y, z)$ the required surface charge density on the "capacitor plate" $x = -a_x/2$ is $\sigma(y, z) = (\vec{n} \cdot \vec{D}) = -\epsilon_d \partial_x \phi(-a_x/2, y, z)$. The total charge on the capacitor is $Q = \int_{-a_y/2}^{+a_y/2} dy \int_{-a_z/2}^{+a_z/2} dz \, \sigma(y, z)$. The opposite capacitor plate $x = a_x/2$ is oppositely charged. The capacitance of this capacitor,

$C \equiv \epsilon_{\text{qs}}^{xx}(a_y a_z)/a_x$ is thus given by $C = Q/V_0$, or

$$\epsilon_{\text{qs}}^{xx} = -\frac{\epsilon_d}{E_0 a_y a_z} \int_{-a_y/2}^{+a_y/2} dy \int_{-a_z/2}^{+a_z/2} dz \partial_x \phi(-a_x/2, y, z) \equiv$$
$$\frac{1}{E_0 a_y a_z} \int_{-a_y/2}^{a_y/2} dy \int_{-a_z/2}^{+a_z/2} dz D_x(x = -a_x/2, y). \qquad (2.2)$$

The $\epsilon_{\text{qs}}^{yy}$ component is determined similarly by applying the voltage $V_0 = E_{0y} a_y$ between the capacitor plates $y = -a_y/2$ and $y = a_y/2$. Constants $\epsilon_{\text{qs}}^{xx}$, $\epsilon_{\text{qs}}^{yy}$ and $\epsilon_{\text{qs}}^{zz}$ depend on the frequency ω because of the $\epsilon(\omega)$ dependence of the plasmonic permittivity. Therefore, extracting the frequency-dependent components of ϵ_{qs} tensor involves scanning the frequency ω, repeatedly solving (2.1) with the described boundary conditions, and applying the capacitance-based definition of ϵ_{qs} given by Eq. (2.2). We refer to this technique of extracting the electrostatic ϵ_{eff}-tensor as the "frequency scan" technique. As it turns out, there is a faster and more physically appealing approach to calculating $\epsilon_{\text{eff}}^{ij}(\omega)$, described in Sec. 2.2.2.

We note that the definition of quasistatic permittivity given by Eq. (2.2) coincides with the electromagnetic definition of ϵ_{eff},

$$\epsilon_{\text{eff}}^{xx} = \frac{(a_y a_z)^{-1} \int_{-a_y/2}^{a_y/2} dy \int_{-a_z/2}^{a_z/2} dz D_x(-a_x/2, y, z)}{a_x^{-1} \int_{-a_x/2}^{a_x/2} dx E_x(x, -a_y/2, -a_z/2)}, \qquad (2.3)$$

introduced earlier by Pendry, Smith et al. [PHRS99], which was derived [SP06] from the integral form of Maxwell's equations.

The capacitor model can be shown to be equivalent to another intuitive definition of ϵ_{qs} based on the dipole moment density. The total dipole moment of a unit cell $\vec{p} = \int_V \vec{P} \, dV$ (where $\vec{P} = \frac{\epsilon-1}{4\pi}\vec{E}$ is the polarization density) is linearly proportional to the external electric field $\vec{E}_0$. On the other hand, the dipole moment of a block of homogeneous medium with anisotropic permittivity tensor $\epsilon_{\text{qs}}^{ij}$ is $p_i = \frac{1}{4\pi} \left(\epsilon_{\text{qs}}^{ij} - \delta^{ij} \right) E_{0j}$. Therefore, ϵ_{qs} can be defined by requiring that

$$a_x a_y a_z(\epsilon_{\text{qs}}^{ij} - \delta^{ij}) E_{0j} \equiv \int dx \, dy \, dz \, (\epsilon - 1) \, E_i. \qquad (2.4)$$

21

Because $\int dx \, dy \, dz \, E_i = a_x a_y a_z E_{0i}$, this *dipole density* definition of ϵ_{qs} simplifies to

$$a_x a_y a_z \epsilon_{\mathrm{qs}}^{ij} E_{0j}^{(k)} \equiv \int dx \, dy \, dz \, D_i^{(k)} = \int dx \, dy \, dz \, \epsilon \, E_i^{(k)}, \qquad (2.5)$$

where the external field $E_{0j}^{(k)} \equiv E_0 \delta_{jk}$ applied to the unit cell produces the total internal field $\vec{E}^{(k)}$, and $k = 1, 2, 3$. The internal electric fields are computed by solving Eq. (2.1) subject to its $\vec{E}_0^{(k)}$-dependent boundary conditions. Equation (2.5) is equivalent to the capacitance-based definitions of ϵ_{qs} given by Eq. (2.2). Indeed, in periodic structures the flux of electric induction $\vec{D}$ in, for example, x-direction is conserved:

$$\partial_x \int_{-a_y/2}^{a_y/2} dy \int_{-a_z/2}^{a_z/2} dz D_x(x, y, z) = - \int_{-a_y/2}^{a_y/2} dy \int_{-a_z/2}^{a_z/2} dz \, (\partial_y D_y + \partial_z D_z) = 0, \quad (2.6)$$

because $\vec{D} = -\epsilon \vec{\nabla} \phi$ is divergence-free ($\vec{\nabla} \cdot \vec{D} = 0$) and periodic in coordinates y and z. In other words, the identity $\int D_x dx \, dy \, dz = a_x \int D_x dy \, dz$ holds, which completes the proof of equivalence between definitions (2.2) and (2.4) in the limit of vanishing phase shift per unit cell.

Owing to an identity

$$\int_V dV D_i = \oint_S dS \, x_i (\vec{D} \cdot \vec{n}), \qquad (2.7)$$

where $\vec{n}$ is the unit normal to the closed surface of integration $S = \partial V$ (unit cell boundary), Eq. (2.5) may also be presented in a surface integral form:

$$\epsilon_{\mathrm{qs}}^{ij} E_{0j}^{(k)} = \frac{1}{V} \oint_S dS \, x_i (\vec{D}^{(k)} \cdot \vec{n}), \qquad (2.8)$$

where $V = a_x a_y a_z$ is the volume of the unit cell. This surface integral indeed reduces to the surface charge on the capacitor plates. For example, for x-polarized external field ($k = 1$) we obtain

$$\oint_S dS \, x (\vec{D} \cdot \vec{n}) = (-a_x/2)(-Q) + (a_x/2)Q = a_x Q, \qquad (2.9)$$

providing another proof of equivalence between definitions (2.2) and (2.4). Note that Eq. (2.8) can be used for determining *all* (diagonal and off-diagonal) elements
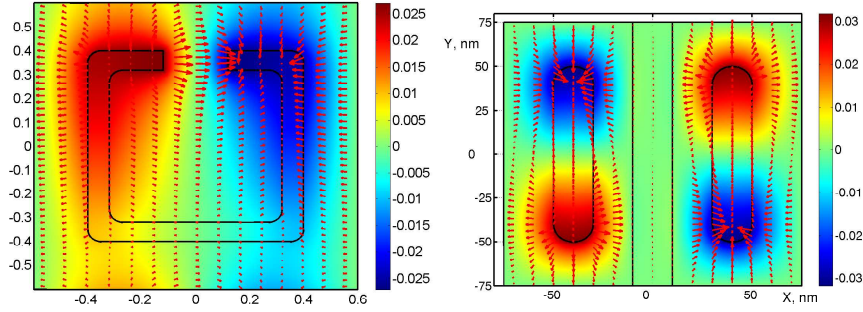
Figure 2.1: Potential distribution ϕ inside a lattice of (a) split rings (left), and (b) metal strips separated by a metal film (right) corresponding to electrostatic resonances responsible for the magnetic response. Arrows: $\vec{E} = -\vec{\nabla}\phi$. Electrostatic resonances occur at (a) $\epsilon_{res} \equiv -82$ ($\lambda = 1.5$ μm) for split rings, and (b) $\epsilon_{res} \equiv -8.8$ ($\lambda = 0.5$ μm) for strips, assuming that the plasmonic material is silver.

of tensor ϵ_{qs} of an arbitrary nanostructure (with or without inversion symmetry of a unit cell), because the number of unknown components of ϵ_{qs} is equal to the number of equations.

2.2.2 Electrostatic eigenvalues and eigenmode expansions

The frequency scan technique described in subsection 2.2.1 is a simple yet time consuming approach to calculating the quasistatic response of sub-wavelength metamaterials. Electrostatic eigenvalue (EE) approach [BS92, SFB01, SU04a] allows one to calculate this response for a wide range of frequencies by evaluating the position and strength of the electric dipole-active plasmon resonances in that range. As we shall see from examples below, there are only a few eigenmodes that contribute to ϵ_{qs}, making the EE approach extremely efficient. Additional theoretical insights (such as the Hermitian nature of ϵ_{qs} that is not evident from Eq. (2.5)) can be gained from the EE approach. In addition to reviewing some of the known facts about the EE approach [BS92, SFB01, SBK04] to calculating ϵ_{qs}, we extend the original theory of plasmon resonances to include plasmonic metamaterials with continuous plasmonic phase. Such structures have become increasingly important in the field of negative index materials (NIMs) since the introduction of the so-called *fishnet* structure [ZFP+05, DEW+06], as well as the SPOF structure [LFUS06, LFUS07, US07b, US07a].

One way of obtaining eigenvalue expansions is the *generalized eigenvalue differential equation* (GEDE) [BS92, SU04a]. Another, essentially equivalent, method is based on a *surface charge integral equation* (SCIE) [FM03, MFZ05]. The steps of the GEDE approach are briefly described here, with the details appearing elsewhere [SU04a, SU05]. We assume that a periodic nanostructure consists of two dielectric, non-magnetic materials: one with a frequency-dependent permittivity $\epsilon(\omega) < 0$ and another with permittivity ϵ_d. Local permittivity of such a structure is $\epsilon(\vec{r}, \omega) = \epsilon_d \left[1 - \frac{1}{s(\omega)}\theta(\vec{r})\right]$, where $\theta(\vec{r}) = 1$ in the subdomain $V_p \subset V$ representing the plasmonic inclusion and $\theta(\vec{r}) = 0$ in $V \backslash V_p$, and $s(\omega) = (1 - \epsilon(\omega)/\epsilon_d)^{-1}$ is the frequency label.

First, the GEDE

$$\vec{\nabla} \cdot \left[\theta(\vec{r})\vec{\nabla}\phi_n\right] = s_n \nabla^2 \phi_n \tag{2.10}$$

is solved for the real eigenvalues s_n. Spectral properties of the GEDE are discussed in detail in [BS92, SBK04] and references therein. Second, the solution of Eq. (2.1) is expressed as an eigenmode expansion [BS92]

$$\phi(\vec{r}) = \phi_0(\vec{r}) + \sum_{n>0} \frac{s_n}{s(\omega) - s_n} \frac{(\phi_n, \phi_0)}{(\phi_n, \phi_n)} \phi_n(\vec{r}), \tag{2.11}$$

where the scalar product is defined as $(\phi, \psi) = \int_V dV \theta \vec{\nabla}\phi^* \cdot \vec{\nabla}\psi$, and $\phi_0 = -\vec{E}_0 \cdot \vec{r}$ represents the uniform external field. Third, the quasistatic permittivity is calculated by substituting $\phi(\vec{r})$ from Eq. (2.11) into any of the equivalent definitions of ϵ_{qs}. For example, the dipole moment definition (2.4) leads to the following analytical expression for ϵ_{qs}:

$$\epsilon_{\text{qs}}^{ij}(\omega) = \epsilon_d \left(\delta_{ij} - \frac{V_p}{V} \frac{f_0^{ij}}{s(\omega)} - \frac{V_p}{V} \sum_{n>0} \frac{f_n^{ij}}{s(\omega) - s_n}\right), \tag{2.12}$$

where

$$f_n^{ij} = V_p^{-1}(\phi_n, x_i)(\phi_n, x_j)/(\phi_n, \phi_n) \tag{2.13}$$

are the electric dipole strengths of the nth resonance, normalized to the volume

$V_p = \int_{V_p} dV$ of the plasmonic phase contained within one unit cell, and

$$f_0^{ij} = \delta_{ij} - \sum_{n>0} f_n^{ij} \tag{2.14}$$

is the measure of the electric response of the continuous plasma phase. From the expression for f_n^{ij} we note that only dipole-active resonances having a non-vanishing dipole moment (ϕ_n, x_j) contribute to the dielectric permittivity. Example of such resonances is shown in Fig. 2.1(a) for the split rings (SR). But the electrostatic resonance of the SPOF structure shown in Fig. 2.1(b) is not dipole-active. It does not contribute to ϵ_{qs} but, as will be shown in Sec. 2.3.1, contributes to the magnetic permeability.

Application of the equivalent capacitance definition given by Eq. (2.8) leads to the same Eq. (2.12) with the same f_n^{ij}. However f_0^{ij} is obtained in a different (and more instructive) form:

$$f_0^{ij} = q^{ij} - \frac{1}{V_p} \sum_{n>0} \frac{(\phi_n, x_j)}{(\phi_n, \phi_n)} \oint_S dS \theta x_i \frac{\partial \phi_n}{\partial n}, \tag{2.15}$$

where $\partial/\partial n$ is the normal derivative, $q^{ij} = \frac{1}{V_p} \oint dS \theta x_i \frac{\partial x_j}{\partial n}$, and surface integration is carried out over the boundary of a unit cell. Combining Eqs. (2.14),(2.15) results in a generalized sum rule for plasmonic oscillators in nanostructures that contain a continuous plasmonic phase.

The non-negative quantity f_0 vanishes if the plasmonic phase of the metamaterial does not form a continuous path in the direction of the applied electric field, a path that would connect the "capacitor plates" and enable the current flow [Str79]. The new expression (2.15) for the residue f_0 provides analytical proof of this previously noted fact. We observe that the surface integrals in (2.15), as well as q^{xx}, vanish whenever the boundary of a unit cell does not cross the polaritonic phase. It is evident that a repeating unit cell can always be chosen in non-percolating polaritonic crystal so as to avoid any intersections with polaritonic particles, even though in densely packed crystals it might be necessary to choose a non-rectangular, non-convex unit cell different from the traditional Wigner-Seitz shape. Thus, the pole of ϵ_{qs} at $s = 0$ exists if and only if the negative-ϵ phase is continuous.

To illustrate the eigenmode expansion method, we chose the two-dimensional
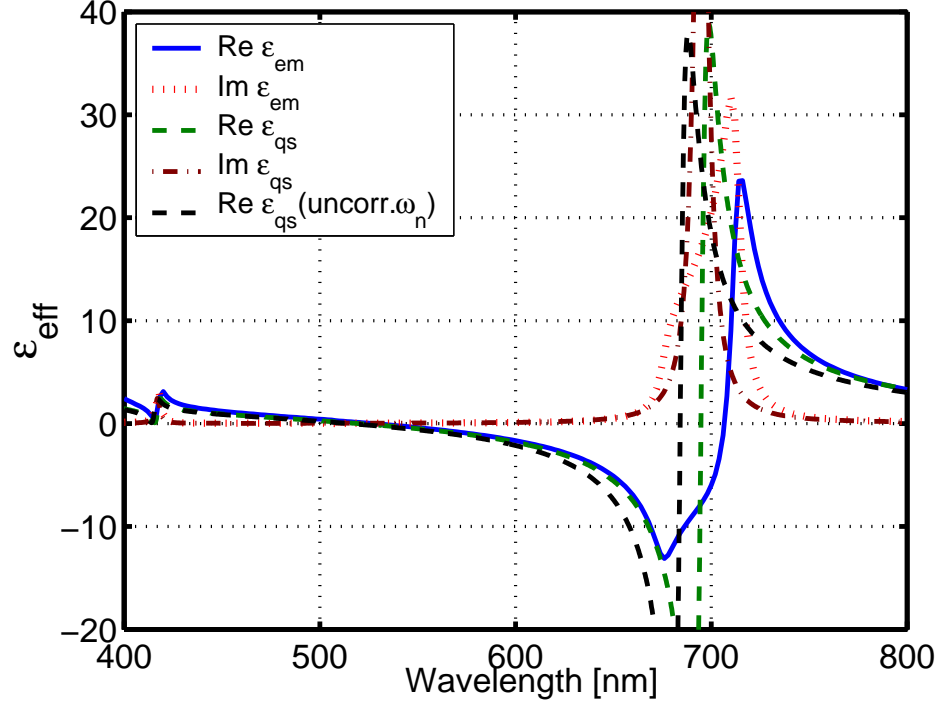
Figure 2.2: Effective dielectric permittivity $\epsilon_{\text{eff}}^{yy}$ of the SPOF (Sec. 4.3) structure (with the film in yz plane) calculated using two methods: electromagnetic EMPR procedure described in Sec. 4.2.4 (solid and dotted curves), and quasistatic formula (2.12) (dashed and dash-dotted). Red-shifted green dashed curve differs from the black dashed one by the frequency shift (2.76) discussed in Sec. 2.5. Structure parameters: periods $a_x = 100$ nm, $a_y = 75$ nm, strip width $w = 50$ nm, strip thickness $t_s = 15$ nm, film thickness $d_f = 5$ nm, strip separation in a pair $h = 15$ nm; plasmonic component: silver (Drude model with parameters from [GBSS98]); immersion medium: $\epsilon_d = 1$.

Strip Pair One Film (SPOF) [LFUS06, LFUS07, US07b, US07a] structure introduced in Sec. 4.3.The real and imaginary parts of the yy-component of ϵ_{qs} corresponding to electric field along the film are plotted as dashed and dash-dotted lines on Fig. 2.2, respectively. The green and black dashed lines show Re ϵ_{qs}^{yy} with and without the retardation correction to the frequency of the plasmon resonances. It is generally known [MFZ05] that frequencies of the optical resonances of finite-sized nanoparticles (with the typical spatial dimension w) are red-shifted from their electrostatic values because of the retardation effects proportional to $\eta^2 \equiv \omega^2 w^2/c^2$. As shown in Sec. 2.5, these shifts can be expressed as corrections to the frequency labels s_n: $s_n = s_n^{(0)} + s_n^{(2)}\eta^2$, where $s_n^{(0)}$ are the electrostatic resonances and $s_n^{(2)}$ are the retardation corrections computed in Sec. 2.5. To obtain any meaningful comparison between the electromagnetically-extracted values of ϵ_{eff} and the electrostatic ϵ_{qs}, these corrections must be included even for the structures as small as $\lambda/10$.

In the chosen range of frequencies, there are only two dipolar resonances that contribute to ϵ^{yy}; quasistatic curves in Fig. 2.2 are computed from the Eq. (2.12) with the following numerical coefficients: conduction pole residue $f_0^{yy} = 0.043$, electric resonance strengths $f_1^{yy} = 0.0045$, $f_2^{yy} = 0.0005$, and pole positions $s_n = s_n^{(0)} + s_n^{(2)}\eta^2$ with $s_1^{(0)} = 0.0426$, $s_2^{(0)} = 0.1630$ and $s_1^{(2)} = -0.007$, $s_2^{(2)} = -0.004$. The other component of ϵ_{qs} has no resonances between $\lambda = 500 - 800$ nm and remains approximately constant, $\epsilon_{qs}^{xx} \approx 1.2$ in the frequency range covered by Fig. 2.2. Quasistatic calculations of ϵ_{qs}^{yy} are compared with the $\epsilon_{\text{em}} \equiv \epsilon_{\text{eff}}$ of a single layer of SPOF extracted from the first-principles EM scattering simulations using the "standard" Effective Medium Parameter Retrieval (EMPR), described in Refs. [SSMS02, MS03, KMSS03] and Section 4.2.4. Electromagnetic simulations are performed using FEFD method implemented in the software package COMSOL Multiphysics [Com06]. Overall, agreement between ϵ_{em} and ϵ_{qs} is very good everywhere except near the strong absorption line associated with electric resonance at ≈ 700 nm. Inside that band ($680 - 720$ nm) the shape of ϵ_{em} strongly deviates from Drude-Lorentz resonance shape. We speculate that this irregularity of ϵ_{em} is related to the large phase shift per cell $\theta \equiv k_x a_x = \text{Re}\,[\sqrt{\epsilon_{\text{eff}}^{yy}}]\omega a_x/c$ neglected in the quasistatic approximation based on periodic electrostatic potentials. More accurate description of ϵ_{eff} should include spatial dispersion [AG06]. Development of an adequate theory of this phenomenon in sub-wavelength plasmonic crystals (SPCs) is under way.

2.3 Electromagnetic susceptibilities of plasmonic nanostructures

In Section 2.2 we have described several theoretical approaches to calculating $\epsilon_{\text{eff}} \approx \epsilon_{\text{qs}}$ for sub-wavelength nanostructures. A much more challenging problem is addressed in this Section: computing the magnetic permeability $\mu_{\text{eff}}(\omega)$. One of the intriguing results is that $\mu_{\text{eff}}(\omega)$ can be strongly dependent on the propagation direction for low-symmetry structures such as the recently described MSP (Sec. 4.2) and SPOF (Sec. 4.3) metamaterials.

In this Section, a simplified approach to the calculation of effective medium parameters is presented. We derive electric and magnetic polarizabilities of a single plasmonic "inclusion" (which may consist of more than one particle). Optical properties of periodic or random ensembles of identical inclusions (with the average distance between particles L much smaller than wavelength λ) can be estimated from single-particle polarizabilities using effective medium theories [LS97]. A more accurate and thus more complicated theory that explicitly takes periodicity of nanoparticle arrangement into account and intrinsically incorporates near-field interactions between adjacent cells will be developed in Section 2.4.

2.3.1 Electric and magnetic response to the lowest order in retardation parameter

In this subsection, we present a perturbation theory that uses electrostatic effective medium theory, formulated in Section 2.2, as the starting point. Unlike earlier two-dimensional treatments [FB05], this theory is applicable to both two- and three-dimensional structures. Calculations in this subsection are presented for three-dimensional plasmonic (or polaritonic) structures; expressions for two-dimensional systems are easily derived by replacing the measure of integration $dV \rightarrow a_z dx dy$, where a_z is an arbitrary "period" in the z-direction, which can be set to a unit length. The expansion parameter of this theory is the dimensionless retardation parameter $\eta = \omega a/c$. The goal of this subsection is to obtain a self-consistent analytic expression for electric and magnetic polarizabilities of a plasmonic nanostructure in the form of resonance expansions. For simplicity, we assume that the structure is an isolated particle or a finite collection of particles placed in transparent dielectric

28

medium with permittivity $\epsilon_d > 0$; the total volume of plasmonic phase, $\int_{V_p} dV$, is denoted V_p.

In conventional atomic crystals, low-frequency magnetism stems mostly from internal and orbital magnetic moments of electrons. In dielectric structures, including plasmonic metamaterials, magnetism originates from polarization and conduction currents; total local current equals $\vec{j}_{tot} = -i\omega(\epsilon - 1)\vec{E}/4\pi$ where the local complex permittivity ϵ also contains conductivity. These currents determine both electric and magnetic polarizabilities of a particle, χ_E and χ_M. We shall define these quantities in such a way that they vanish when the dielectric permittivity of the particle, $\epsilon(\omega)$ equals permittivity ϵ_d of surrounding medium. To calculate these *relative* polarizabilities, we use "excess" currents, $\vec{j}_{ex} = -i\omega(\epsilon - \epsilon_d)\vec{E}/4\pi$. Excess currents vanish outside of the plasmonic phase.

To describe the response of plasmonic inclusion, it is convenient to decompose electric and magnetic fields into "incident" and "scattered", i. e. $\vec{E} = \vec{E}_{in} + \vec{E}_{sc}$ and $\vec{H} = \vec{H}_{in} + \vec{H}_{sc}$, such that $\vec{E}_{sc}$ and $\vec{H}_{sc}$ vanish in the absence of plasmonic structure. For the incident fields, we use a plane wave in the uniform medium that surrounds plasmonic inclusion: $\vec{E}_{in} = \vec{E}_0 e^{i\vec{k}\cdot\vec{r}}$ and $\vec{H}_{in} = \vec{H}_0 e^{i\vec{k}\cdot\vec{r}}$, where $|\vec{k}| \equiv k = \sqrt{\epsilon_d}k_0$ and $k_0 = \omega/c$. The incident fields are transverse, and $\vec{H}_0 = \sqrt{\epsilon_d}[\vec{v} \times \vec{E}_0]$, where $\vec{v} \equiv \vec{k}/|\vec{k}|$ is the unit vector in the propagation direction. Thus the incident fields are purely solenoidal, $\vec{\nabla} \cdot \vec{E}_{in} = \vec{\nabla} \cdot \vec{H}_{in} = 0$.

The electric dipole moment of the particle (in excess to the uniform ambient medium) is defined as $\vec{p} = \int dV(\epsilon - \epsilon_d)\vec{E}/4\pi$. The magnetic dipole moment is calculated as $\vec{m} = \int dV \vec{M}$, where $\vec{M} = \frac{1}{2c}[\vec{r} \times \vec{j}_{ex}]$ is the magnetic polarization density. For a particle of a general shape, four electromagnetic polarizabilities can be introduced according to the linear relations between excited dipole moments and the amplitudes of incident fields:

$$p_i = \chi_E^{ij} E_{0j} + \chi_{ME}^{ij} H_{0j}, \tag{2.16}$$

$$m_i = \chi_{EM}^{ij} E_{0j} + \chi_M^{ij} H_{0j}. \tag{2.17}$$

Polarizabilities χ_α ($\alpha = E, ME, EM, M$) have dimensions of volume and are proportional to the volume V_p of the plasmonic inclusion. Note that the amplitude vector $\vec{E}_0$ (and, correspondingly, $\vec{H}_0$) of the incident wave can be complex in the general case of elliptic polarization.

Our goal is to determine the four tensors χ_α, each in the lowest order of the perturbation theory that treats retardation effects as corrections. Optical magnetism, that is, magnetic polarizability χ_M, appears in the $O(\omega^2)$ order of this perturbation theory [SU06, SSS06]. Magneto-electric polarizabilities χ_{ME} and χ_{EM} appear in the $O(\omega)$ order. Electric polarizability is determined mostly by electrostatic effects and is dominated by its zero-order part.

In accordance with this ordering, we calculate electric and magnetic dipole moments in the two lowest non-vanishing orders, namely, $\vec{p} = \vec{p}^{(0)} + \vec{p}^{(1)}$ and $\vec{m} = \vec{m}^{(1)} + \vec{m}^{(2)}$, and extract all the four polarizabilities in Eq. (2.16,2.17) from linear relations $\vec{p}^{(0)} = \chi_E \vec{E}_0$, $\vec{p}^{(1)} = \chi_{ME} \vec{H}_0$, $\vec{m}^{(1)} = \chi_{EM} \vec{E}_0$, and $\vec{m}^{(2)} = \chi_M \vec{H}_0$. We note that since $\vec{j}$ in the definition of magnetic moment $\vec{m}$ already has one factor of ω, to determine χ_M (and χ_{EM}) in the lowest order it suffices to calculate $\vec{E}$ with the first-order electromagnetic corrections.

The single-particle polarizability tensors can be used to calculate effective medium parameters of the medium that consists of ensembles of identical particles dispersed in a uniform dielectric substance with permittivity ϵ_d. A strongly inhomogeneous medium supports propagation of light waves over long distances in two cases: (a) when the size of individual scatterers is much smaller than the wavelength λ in surrounding medium, or (b) when the structure is periodic. Case (a) is known as the *effective medium regime*, while case (b) is referred to as the *Bloch-Floquet regime* or a photonic crystal regime. In the effective medium regime, appropriate quantities to describe the propagation of a plane wave are dielectric and diamagnetic susceptibilities of the compound medium. In general, for a linear medium there are four such (tensor) quantities. In the so-called Tellegen representation, they relate electric and magnetic induction with electric and magnetic field intensity [SL00]:

$$\vec{D} = \hat{\epsilon}_{\text{eff}} \vec{E} + \hat{\xi}_{\text{eff}} \vec{H},$$
$$\vec{B} = \hat{\mu}_{\text{eff}} \vec{H} + \hat{\zeta}_{\text{eff}} \vec{E}. \tag{2.18}$$

In the most general case where magneto-electric susceptibilities $\hat{\xi}_{\text{eff}}$, $\hat{\zeta}_{\text{eff}}$ do not vanish, the medium is called *bianisotropic* [SL00]. To the lowest order in the particle number density [LS97], single-particle polarizabilities are related to effective medium

30

parameters by linear relations

$$\epsilon_{\text{eff}}^{ij} = \epsilon_d \delta_{ij} + 4\pi \chi_E^{ij}/V, \tag{2.19}$$

$$\xi_{\text{eff}}^{ij} = 4\pi \chi_{ME}^{ij}/V, \tag{2.20}$$

$$\mu_{\text{eff}}^{ij} = \delta_{ij} + 4\pi \chi_M^{ij}/V, \tag{2.21}$$

$$\zeta_{\text{eff}}^{ij} = 4\pi \chi_{EM}^{ij}/V. \tag{2.22}$$

These identities can be found by comparing the total electric and magnetic moments inside a volume V that contains one plasmonic inclusion, with those of a block of homogeneous effective medium [LS97]. Here, volume V represents specific volume per particle in the case of random distribution, or the volume of a unit cell in a periodic structure. More accurate effective medium theories that account for the influence of surrounding effective medium on each particle in the ensemble [LS97] can be developed and will be reported elsewhere [US07a].

Now we proceed to evaluating the scattered fields, $\vec{E}_{sc}$, and subsequently, each of the four polarizability tensors. The scattered electric field $\vec{E}_{sc}$ can be decomposed into the potential and solenoidal parts, $\vec{E}_{sc} = \vec{E}_{pot} + \vec{E}_{sol} = -\vec{\nabla}\Phi_{sc} + ik_0\vec{A}_{sc}$, where $\vec{\nabla} \cdot \vec{A}_{sc} = 0$. Note that $\vec{A}_{sc}$ is related to the scattered magnetic field: $\vec{H}_{sc} = \vec{\nabla} \times \vec{A}_{sc}$. It can be demonstrated $\vec{A}_{sc}$ is first order in η, making the contribution of $\vec{A}_{sc}$ to $\vec{E}_{sc}$ second order in η. Therefore, the lowest-order (η^2) expression for χ_M can be found without directly computing $\vec{A}_{sc}$ or scattered magnetic fields, with a limitation discussed below using the example of a single sphere.

The potential part of $\vec{E}_{sc}$ is determined from $\vec{\nabla} \cdot \vec{D} = 0$, resulting in

$$\vec{\nabla}\epsilon\vec{E}_{pot} = -\vec{\nabla}\epsilon\vec{E}_{in} - \vec{\nabla}\epsilon\vec{E}_{sol} \equiv -\left(\vec{E}_{in} + ik_0\vec{A}_{sc}\right) \cdot \vec{\nabla}\epsilon, \tag{2.23}$$

where $k_0\vec{A}_{sc}$ can be neglected to order η^2. For completeness, we note that $\vec{A}_{sc}$ is computed, to the lowest order in η, as

$$-\nabla^2\vec{A}_{sc}^{(1)} = ik_0\epsilon\vec{\nabla}\Phi_{sc}^{(0)} - ik_0\left(\epsilon - \epsilon_d\right)\vec{E}_{in}^{(0)}. \tag{2.24}$$

Following the eigenvalue expansion formalism introduced by Bergman et

al.[BS92], Φ_{sc} is expanded as $\Phi_{sc}(\vec{r}) = \sum_{n>0} c_n \phi_n(\vec{r})$, where ϕ_n are electrostatic eigenfunctions of the GEDE with homogeneous boundary conditions $\phi_n = 0$ at infinity. This eigenmode expansion is justified because the full set of $\phi_n(x)$ functions is a complete basis in the space of solutions to Laplace equation [BS92] with the stated boundary conditions at infinity. The coupling coefficient c_n between $\vec{E}_{in}(\vec{r}) = \vec{E}_0 e^{i\vec{k}\cdot\vec{r}}$ and the nth plasmon eigenmode is found by applying the EE approach described in Sec. 2.2.2 to Eq. (2.23):

$$c_n = -\frac{s_n}{s(\omega) - s_n} \frac{\int (\vec{\nabla}\phi_n)\vec{E}_{in}\theta dV}{\int (\vec{\nabla}\phi_n)^2\theta dV} + O(\eta^2). \tag{2.25}$$

Expanding the plane wave $\vec{E}_{in} = \vec{E}_0 e^{ik(\vec{v}\cdot\vec{r})}$ in the powers of k up to the first order, we obtain $c_n = c_n^{(0)} + c_n^{(1)}$, where

$$c_n^{(m)} = -\frac{1}{m!}(ik)^m \frac{s_n}{s(\omega) - s_n} \vec{E}_0 \cdot \frac{\int (\vec{\nabla}\phi_n)(\vec{v}\cdot\vec{r})^m \theta dV}{\int (\vec{\nabla}\phi_n)^2\theta dV}, \, m = 0, 1. \tag{2.26}$$

The scattered field $\vec{E}_{sc}$ is now used to calculate $\vec{p}$ and $\vec{m}$, and, consequently, χ_α. For simplicity, we choose the center of mass of the plasmonic inclusion as the origin of coordinate system, such that $\int \vec{r}\theta dV = 0$. For the zeroth-order electric dipole moment, we obtain

$$\vec{p}^{(0)} = \int \frac{\epsilon - \epsilon_d}{4\pi} \left(\vec{E}_0 + \sum_{n>0} c_n^{(0)}(-\vec{\nabla}\phi_n) \right) dV =$$

$$= -\frac{V_p \epsilon_d}{4\pi s} \vec{E}_0 - \frac{\epsilon_d}{4\pi s} \sum \frac{s_n}{s - s_n} \frac{\int (\vec{\nabla}\phi_n)\theta dV \int (\vec{E}_0 \cdot \vec{\nabla}\phi_n)\theta dV}{\int (\vec{\nabla}\phi_n)^2\theta dV}. \tag{2.27}$$

After simple transformations and using $\frac{s_n}{s(s-s_n)} = \frac{1}{s-s_n} - \frac{1}{s}$, electric polarizability tensor is found:

$$\chi_E^{ij} = -\frac{V_p \epsilon_d}{4\pi} \left(\frac{f_0^{ij}}{s} + \sum_{n>0} \frac{f_n^{ij}}{s - s_n} \right), \tag{2.28}$$

where the dimensionless coefficients in the numerators are

$$f_n^{ij} = \frac{\int_{V_p} (\partial_i \phi_n)dV \int_{V_p} (\partial_j \phi_n)dV}{V_p \int_{V_p} (\vec{\nabla}\phi_n)^2 dV}, \tag{2.29}$$

$$f_0^{ij} = \delta_{ij} - \sum_{n>0} f_n^{ij}. \tag{2.30}$$

It is worth noting that effective permittivity of a particle ensemble calculated by substituting the quasistatic polarizability (2.28) into effective medium formula $\epsilon_{\text{eff}}^{ij} = \epsilon_d \delta_{ij} + 4\pi \chi_E^{ij}/V$ is precisely the same as the exact electrostatic result (2.12).

In the next order, electric dipole moment is given by

$$\vec{p}^{(1)} = -\frac{\epsilon_d}{4\pi s} \int_{V_p} \vec{E}^{(1)} dV = \frac{\epsilon_d}{4\pi s} \sum_{n>0} c_n^{(1)} \int_{V_p} \vec{\nabla} \phi_n dV. \tag{2.31}$$

The term with $\int_{V_p} \vec{E}_{in}^{(1)} dV$, where $\vec{E}_{in}^{(1)} = \vec{E}_0 i(\vec{k} \cdot \vec{r})$ is eliminated by the proper choice of the origin of coordinates (in the particle's center of mass). Expressing $\vec{E}_0$ through $\vec{H}_0$ as $\vec{E}_0 = \epsilon_d^{-1/2}[\vec{H}_0 \times \vec{v}]$, and using $k = k_0 \epsilon_d^{1/2}$, we find the coefficient of proportionality between $\vec{p}^{(1)}$ and $\vec{H}_0$:

$$\chi_{ME}^{ij} = -ik_0 \epsilon_d \frac{V_p}{4\pi} \left(\frac{G_0^{ij}}{s} + \sum_{n>0} \frac{G_n^{ij}}{s - s_n} \right), \tag{2.32}$$

where

$$G_n^{ij} = \frac{\int_{V_p} (\partial_i \phi_n) dV \int_{V_p} (\vec{v} \cdot \vec{r})(\vec{e}_j \cdot [\vec{v} \times \vec{\nabla} \phi_n]) dV}{V_p \int_{V_p} (\vec{\nabla} \phi_n)^2 dV}, \tag{2.33}$$

$$G_0^{ij} = -\sum_{n>0} G_n^{ij}. \tag{2.34}$$

Next, we calculate the magnetic moment of the plasmonic inclusion. In the first non-vanishing order,

$$\vec{m}^{(1)} = \frac{ik_0 \epsilon_d}{8\pi s} \int_{V_p} \vec{r} \times \vec{E}^{(0)} dV = -\frac{ik_0 \epsilon_d}{8\pi s} \sum_{n>0} c_n^{(0)} \int_{V_p} \vec{r} \times \vec{\nabla} \phi_n dV. \tag{2.35}$$

The term with $\int_{V_p} \vec{r} \times \vec{E}_0 dV$ is eliminated by our choice of coordinate center. After simple transformations, we find the coefficient of proportionality between $\vec{m}^{(1)}$ and $\vec{E}_0$:

$$\chi_{EM}^{ij} = ik_0 \epsilon_d \frac{V_p}{4\pi} \left(\frac{H_0^{ij}}{s} + \sum_{n>0} \frac{H_n^{ij}}{s - s_n} \right), \tag{2.36}$$

where

$$H_n^{ij} = \frac{1}{2} \frac{\int_{V_p} (\vec{e}_i \cdot [\vec{r} \times \vec{\nabla}\phi_n]) dV \int_{V_p} (\partial_j \phi_n) dV}{V_p \int_{V_p} (\vec{\nabla}\phi_n)^2 dV},$$ (2.37)

$$H_0^{ij} = -\sum_{n>0} H_n^{ij}.$$ (2.38)

In the next order, magnetic dipole moment is given by $\vec{m}^{(2)} = \frac{ik_0\epsilon_d}{8\pi s} \int_{V_p} \vec{r} \times \vec{E}^{(1)} dV$, where $\vec{E}^{(1)} = \vec{E}_0 ik(\vec{v} \cdot \vec{r}) - \sum_{n>0} c_n^{(1)} \vec{\nabla}\phi_n$. Expressing again $\vec{E}_0$ through $\vec{H}_0$, we find magnetic polarizability as the coefficient of proportionality between $\vec{m}^{(2)}$ and $\vec{H}_0$:

$$\chi_M^{ij} = -\frac{k_0^2 \epsilon_d V_p}{4\pi} \left(\frac{F_0^{ij}}{s} + \sum_{n>0} \frac{F_n^{ij}}{s - s_n} \right),$$ (2.39)

where

$$F_n^{ij} = \frac{1}{2} \frac{\int_{V_p} (\vec{e}_i \cdot [\vec{r} \times \vec{\nabla}\phi_n]) dV \int_{V_p} (\vec{v} \cdot \vec{r})(\vec{e}_j \cdot [\vec{v} \times \vec{\nabla}\phi_n]) dV}{V_p \int_{V_p} (\vec{\nabla}\phi_n)^2 dV},$$ (2.40)

$$F_0^{ij} = \frac{1}{2} \int_{V_p} (\vec{v} \cdot \vec{r}) \left[(\vec{v} \cdot \vec{r})\delta_{ij} - v_i x_j \right] dV/V_p - \sum_{n>0} F_n^{ij}.$$ (2.41)

2.3.2 Magnetic polarizability of a single sphere

Unlike f_0^{ij}, which vanishes in the case of an isolated particle due to the identity (2.15), the quantities F_0^{ij}, G_0^{ij} and H_0^{ij} may not vanish. The pole at $s = 0$ in expressions (2.32,2.36,2.39) is unphysical and indicates that the lowest-order (in frequency) expressions for χ_M, χ_{ME} and χ_{EM} should not be used in the limit of very large negative dielectric contrasts, i.e. when $0 < s(\omega) \ll 1$. In this regime, plasmonic particles behave as good conductors. Expulsion of magnetic field from plasmonic phase becomes so strong, that, in fact, scattered magnetic field $\vec{H}_{sc}$ is nearly equal in magnitude (and opposite in sign) to the incident magnetic field $\vec{H}_{in}$. Present theory treats $\vec{H}_{sc}$ as perturbation and is therefore inaccurate in this regime. This limitation manifests in Eq. (2.39) as an unphysical pole at $s = 0$. Its origin can be seen from Mie theory of a dielectric sphere.

For a sphere, all plasmon resonances have zero magnetic strength, $F_n^{ij} = 0$; this will become obvious from Eq. (2.54) in Section 2.3.4. Hence, the only remaining quantity in formula (2.39) is F_0^{ij}. Assuming that $\vec{k}||x$ and $\vec{H}_0||z$, and $\epsilon_d = 1$, we

find $F_0^{zz} = \int_{V_p} \frac{x^2}{2} dV/V_p = \frac{1}{30} 4\pi R^5/V_p$, where R is the radius of the sphere and $V_p = 4\pi/3R^3$. Our formula (2.39) gives $\chi_M \equiv \chi_M^{zz} = -k^2 V_p F_0^{zz}/s(\omega)$. Thus, we obtain $\chi_M/R^3 = \frac{1}{30}(\epsilon-1)(kR)^2$. The exact Mie result for the magnetic polarizability of a dielectric sphere in vacuum is

$$\frac{\chi_M}{R^3} = \frac{3ie^{-i\eta}}{2\eta^3} \frac{\cos\eta - \frac{1}{m}\cot m\eta \sin\eta - (1-\frac{1}{m^2})\sin\eta/\eta}{1 + \frac{i}{m}\cot m\eta + i(1-\frac{1}{m^2})/\eta}, \tag{2.42}$$

where $\eta = kR$ and $m^2 = \epsilon(\omega)$. Equation (2.42) can be simplified in two limiting cases: (a) $\eta \ll 1$ and arbitrary m, and (b) $|m^2| \gg 1$ and arbitrary η. The former expansion results in

$$\chi_M^{(a)}/R^3 = \frac{1}{30}(m^2 - 1)\eta^2 + O(\eta^4), \tag{2.43}$$

in agreement with Eq. (2.39). The latter expansion results in

$$\frac{\chi_M^{(b)}}{R^3} = \frac{3ie^{-i\eta}(\eta\cos\eta - \sin\eta)}{2\eta^3(\eta + i)}. \tag{2.44}$$

By taking the limit $\eta = kR \to 0$ in $\chi_M^{(b)}$, we recover the textbook result for magnetization of a perfectly conducting small sphere: $\chi_M^{(b)} = -1/2R^3$. Therefore, $\chi_M^{(a)}$ overestimates the magnetic polarizability of the sphere whenever $\eta \ll 1$ but $|m\eta| > 1$. The quasistatic theory developed here suffers from the same limitation. Nevertheless, the analytic expression for the magnetic polarizability χ_M of a plasmonic nanostructure given by Eq. (2.39) answers several conceptually important questions outlined below.

2.3.3 Dependence of the magnetic polarizability on the propagation direction

The magnetic strength F_n^{ij}, given by Eq. (2.40), may depend on the orientation of the wave vector $\vec{k}$ (or electric field $\vec{E}_0$) in the plane orthogonal to $\vec{H}_0$. Consequently, any component of magnetic polarizability χ_M^{ij} near a magnetic plasmon resonance can be anisotropic. This happens because the magnetic strength is a product of two factors: (i) coupling of the incident plane wave to a plasmon mode, and (ii) magnetic moment contained in the excited mode. While the latter is independent of the direction of $\vec{k}$ or $\vec{E}_0$, the former coupling is determined

35

by the inhomogeneity of the electric field $\vec{E}_0 e^{i\vec{k}\cdot\vec{r}}$ and, therefore, depends upon the orientation of the orthogonal pair $(\vec{k}, \vec{E}_0)$.

We use a two-dimensional structure, a metallic strip pair (see Sec. 4.2), to illustrate the anisotropy of scalar $\chi_M \equiv \chi_M^{zz}$ in optical metamaterials. This structure has attracted a great deal of attention as a magnetic component of NIMs [SU06, CKKS06]. Quasistatic values of the effective permeability from Eq. (2.39,2.21) (labeled as μ_{qs}) are compared with those (labeled as μ_{em}) extracted from the single-layer electromagnetic scattering simulations using Effective Medium Parameter Retrieval (introduced in Section 4.2.4). The two illumination geometries and the results are shown in Fig. 2.3. Unit cell dimensions are given in the caption to Fig. 2.3. Both quasistatic and electromagnetic results plotted in Fig. 2.3 demonstrate that the strength the magnetic plasmon resonance excitation depends strongly upon the direction of the wave vector $\vec{k}$ of the incident wave. Maximum deviation of μ_{eff} from unity is an order of magnitude larger when $\vec{k}$ is perpendicular to the strips. The high degree of anisotropy of μ_{eff} is related to the relatively low symmetry group (C_{2v}) of the two plasmonic strips.

Anisotropy of the scalar magnetic permeability μ_{zz} for optical metamaterials based on strip pairs allows one to conclude that, in principle, μ_{eff} introduced recently for optical frequencies does not have the same properties as the conventional permeability of magnetic bodies at low frequencies [AG06]. For example, it is implied in the definition of magnetic permeability that the magnetization of a body depends only on the direction of magnetic field, but not of the electric field. Magnetization of conventional diamagnetic substances does not depend, in the first approximation, on the direction or the intensity of electric field. At high frequencies, however, it is impossible to have the magnetic field without the electric; they are always acting together. In metal-dielectric structure, which respond strongly to electric fields, it is therefore not surprising that the orientation of external electric field is just as important as direction of incident magnetic field.

Fortunately, there exist situations when $\vec{E}$-dependence of optical permeability vanishes; they are studied in the next subsection.
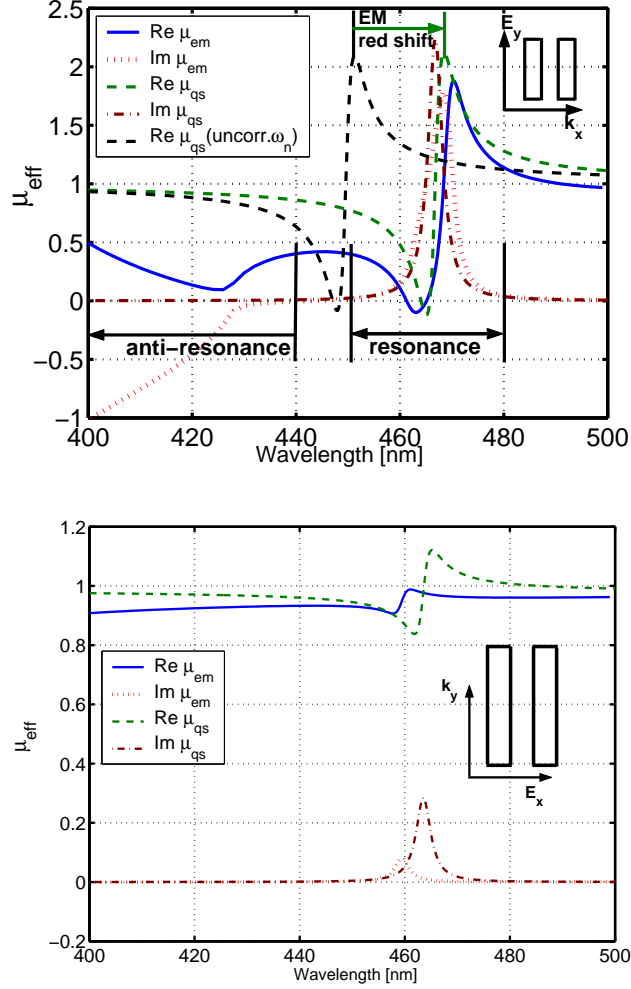
Figure 2.3: Effective magnetic permeability μ_{eff}^{zz} of the metallic strip pair (MSP) structure calculated using two methods: electromagnetic EMPR (solid and dotted curves), and the quasistatic result (2.39,2.21) (dashed and dash-dotted). Top: traditional strip orientation (strips along the incident $\vec{E}$ field); bottom: unit cell rotated by 90° (strips along the wave vector $\vec{k}$). Orientation of the strips and the incident electric field are shown in the insets. Green dashed curves incorporate the retardation frequency shift given by Eq. (2.76) in Sec. 2.5. For comparison, the black dashed curve is not corrected with that frequency shift. Structure parameters: periods $a_x = a_y = 100$ nm, strip width: $w = 50$ nm, strip thickness $t_s = 15$ nm, strip separation in the pair: $h = 15$ nm; strips are made of silver (Drude model with parameters from [GBSS98]) and embedded in vacuum ($\epsilon_d = 1$).

2.3.4 Magnetic polarizability of particles with discrete rotational symmetry

For plasmonic nanostructures with an axis of rotation the anisotropy of some components of χ_M^{ij} may disappear. For example, suppose that z-axis is an axis of rotational symmetry C_n of order $n \geq 3$, i.e. the particle is invariant with respect to a $2\pi/n$-radian rotation (in periodic systems, only $n = 3, 4, 6$ are allowed). Then it can be shown that the $\vec{v}$-dependent coefficients in F_n^{zz} for $\vec{v}\|\hat{x}$ and $\vec{v}\|\hat{y}$ are equal in magnitude but differ in sign: $\int x\frac{\partial\phi_n}{\partial y}\theta dV = -\int y\frac{\partial\phi_n}{\partial x}\theta dV$. Therefore, $\int x\frac{\partial\phi_n}{\partial y}\theta dV = \frac{1}{2}\int \left(x\frac{\partial\phi_n}{\partial y} - y\frac{\partial\phi_n}{\partial x}\right)\theta dV$, and all magnetic strengths F_n^{zz} as well as F_0^{zz} become isotropic:

$$F_n^{zz} = \frac{1}{4}\frac{(\int_{V_p}(\vec{e}_z\cdot[\vec{r}\times\vec{\nabla}\phi_n])dV)^2}{V_p\int_{V_p}(\vec{\nabla}\phi_n)^2dV}, \tag{2.45}$$

$$F_0^{zz} = \frac{1}{4}\int_{V_p}\left[\vec{r}^2 - z^2\right]dV/V_p - \sum_{n>0}F_n^{zz}. \tag{2.46}$$

Moreover, if the structure is isotropic in all directions (i.e., its symmetry group belongs to the cubic class), all electromagnetic polarizabilities become independent of $\vec{k}$-direction and form a symmetric set:

$$\chi_E^{ij} = -\epsilon_d\frac{V_p}{4\pi}\left(\frac{1}{s}\left(\delta_{ij} - \sum_{n>0}\mathfrak{p}_n^i\mathfrak{p}_n^j\right) + \sum_{n>0}\frac{\mathfrak{p}_n^i\mathfrak{p}_n^j}{s - s_n}\right), \tag{2.47}$$

$$\chi_M^{ij} = -k_0^2\epsilon_d\frac{V_p}{4\pi}\left(\frac{1}{s}\left(J_{ij} - \sum_{n>0}\mathfrak{m}_n^i\mathfrak{m}_n^j\right) + \sum_{n>0}\frac{\mathfrak{m}_n^i\mathfrak{m}_n^j}{s - s_n}\right), \tag{2.48}$$

$$\chi_{ME}^{ij} = -ik_0\epsilon_d\frac{V_p}{4\pi}\left(\frac{1}{s}\left(-\sum_{n>0}\mathfrak{m}_n^i\mathfrak{p}_n^j\right) + \sum_{n>0}\frac{\mathfrak{p}_n^i\mathfrak{m}_n^j}{s - s_n}\right), \tag{2.49}$$

$$\chi_{EM}^{ij} = -\chi_{ME}^{ji}, \tag{2.50}$$

where

$$\vec{\mathfrak{p}}_n = \frac{\int_{V_p}\vec{\nabla}\phi_ndV}{\left(V_p\int_{V_p}(\vec{\nabla}\phi_n)^2dV\right)^{1/2}}, \tag{2.51}$$

$$\vec{\mathfrak{m}}_n = \frac{1}{2} \frac{\int_{V_p} \vec{r} \times \vec{\nabla}\phi_n dV}{\left(V_p \int_{V_p} (\vec{\nabla}\phi_n)^2 dV \right)^{1/2}} \tag{2.52}$$

are the normalized electric and magnetic dipole moments of the plasmon states and $J_{ij} = \frac{1}{4} \int_{V_p} (\vec{r}^2 \delta_{ij} - x_i x_j) dV / V_p$ is a normalized inertia tensor of a plasmonic inclusion.

Considering the importance of the normalized dipole moments (2.51,2.52) contained in a plasmon eigenmode for the fast characterization of electromagnetic response of plasmonic metamaterials, we also present simplified expressions for $\vec{\mathfrak{p}}_n$ and $\vec{\mathfrak{m}}_n$, in which the volume integrations are reduced to surface integrals over the surface $S_p = \partial V_p$ of the plasmonic inclusion. Taking the volume integrals "by parts" and using $\vec{\nabla} \times \vec{r} \equiv 0$ and $\nabla^2 \phi_n \equiv 0$ in V_p, we find:

$$\vec{\mathfrak{p}}_n = \frac{\oint_{S_p} \vec{r} \frac{\partial \phi_n}{\partial n} dS}{\left(V_p \oint_{S_p} \phi_n \frac{\partial \phi_n}{\partial n} dS \right)^{1/2}}, \tag{2.53}$$

$$\vec{\mathfrak{m}}_n = \frac{1}{2} \frac{\oint_{S_p} [\vec{r} \times \vec{n}] \phi_n dS}{\left(V_p \oint_{S_p} \phi_n \frac{\partial \phi_n}{\partial n} dS \right)^{1/2}}, \tag{2.54}$$

where the normal derivative $\partial \phi_n / \partial n$ is evaluated on the plasmonic (inner) side of surface S_p. Expressions (2.53,2.54) are computationally more efficient than their volume equivalents (2.51,2.52). Moreover, it becomes apparent from (2.54) that, regardless of the multipolar order of the resonance ϕ_n, all electrostatic resonances of a single particle with spherical symmetry (e.g., a solid sphere or a concentric nanoshell) carry no magnetic moment, since $\vec{r} \times \vec{n} \equiv 0$ on a spherical surface. We have used this fact in Sec. 2.3.2.

Expression (2.48) shows that for sufficiently symmetric structures it is possible to introduce an isotropic χ_M, independent of the direction of applied electric field. A two-dimensional example of a plasmonic metamaterial with isotropic scalar μ_{eff} is a square array of plasmonic nanorods [SU04a, SU05, DUS07]; it is studied in detail in Sec. 4.1. An example of three-dimensionally *isometric* structure with fully isotropic permittivity and permeability is a tetrahedral plasmonic cluster introduced and studied using theoretic results of this Section in Sec. 4.4.

2.3.5 Electric and magnetic multipolar decompositions of the plasmon states

It has been observed earlier [SU05, SU06] that in the structures with a sufficiently high spatial symmetry only some plasmon resonances may have a non-vanishing magnetic moment given by Eq. (2.52). Such eigenmodes are sometimes referred to as *magnetic plasmon resonances* (MPR) [SSS06]. For example, if the structure has an inversion center, its electrostatic eigenfunctions ϕ_n can be either even or odd with respect to spatial inversion. It follows from the definitions of f_n^{ij} and F_n^{ij} that even modes have a vanishing electric strength while the odd modes have a vanishing magnetic strength. If inversion center is the only non-trivial element of symmetry, i. e. the structure's symmetry group is C_i, all even modes are magnetic resonances ($F_n \neq 0$) and odd modes — electric resonances ($f_n \neq 0$). For example, the electrostatic resonance of the SPOF structure shown in Fig. 2.1(b) has a finite magnetic strength proportional to η^2.

In structures with higher symmetries, electric and magnetic eigenmodes can be identified by their irreducible representation. It can be shown that electric strength f_n^{xx} may only be non-zero if the corresponding potential ϕ_n transforms under the same representation as the coordinate x (and similarly for f_n^{yy} and f_n^{zz}). For the magnetic strength F_n^{zz} to be non-vanishing, the potential ϕ_n must transform as an operator of rotation around z-axis (R_z), which is a component of a pseudovector. Standard character tables of the point groups of symmetry [KDWS63] provide the information necessary for assigning magnetic or electric dipole activity to various resonances.

Since the early days of the NIM structures based on strip pairs it was accepted that MPRs in two-dimensional structures with C_{2v} symmetry are electric quadrupoles (see Sec. 4.2 and Sec. 4.3). The fact that optical magnetic susceptibility is a phenomenon of order $(\omega d/c)^2$, where d is a characteristic size of a magnetic resonator, may seem suggestive that MPRs are electric quadrupoles in general. However, this generalization is incorrect: in structures with high symmetry, modes that carry magnetic dipole moment (2.52) are not necessarily electric quadrupoles. For example, it will be shown in Sec. 4.1 that in 2D plasmonic crystals with C_{4v} symmetry, such as square arrays of round nanorods, magnetic resonances are electric octupoles [SU04a] (azimuthal angular moment $M = 4$). In general, magnetic modes

40

Group	Electric resonance $(f_n^{xx,yy} \neq 0; f_n^{zz} \neq 0)$	Magnetic resonance and its LOEM $(F_n^{xx,yy} \neq 0; F_n^{zz} \neq 0)$
D_{3h}	$E'; A_2''$	$E''(J=2); A_2'(J=3)$
D_{4h}	$E_u; A_{2u}$	$E_g(J=2); A_{2g}(J=4)$
D_{6h}	$E_{1u}; A_{2u}$	$E_{1g}(J=2); A_{2g}(J=6)$
D_{3d}	$E_u; A_{2u}$	$E_g(J=2); A_{2g}(J=4)$
T_d	T_2	$T_1\ (J=3)$
O_h	T_{1u}	$T_{1g}\ (J=4)$
I_h	T_{1u}	$T_{1g}\ (J=6)$

Table 2.1: Examples of non-bianisotropic 3D point groups, their irreducible representations related to electric and magnetic resonances, and the Lowest-Order Electric Multipole (LOEM) of magnetic resonances.

in 2D crystals with C_{nv} symmetry are two-dimensional $2n$-poles ($n = 2, 3, 4, 6$). On the other hand, in two-dimensional C_n crystals without axes of reflection, magnetic modes are always electric quadrupoles regardless of n.

In more complicated cases, such as 3D crystals, information about the lowest-order non-vanishing electric multipole moment of an eigenmode may be found with help of point group theory [KDWS63]. For example, magnetic modes with non-vanishing F_n^{zz} turn out to be hexadecapoles ($J = 4, 2^J = 16$) in plasmonic crystals with point groups D_{4h}, D_{3d} and O_h. In hexagonal group D_{6h}, modes with $F_n^{zz} \neq 0$ are electric hexacontatetrapoles ($J = 6, 2^J = 64$). Examples of exceptions from the "MPR is a quadrupole" rule for 3D point groups are summarized in Table 2.1.

To provide a more general insight into the electromagnetic properties of plasmon eigenstates, we perform a systematic decomposition of all modes into electric and magnetic multipoles based on their rotational properties and inversion parity. Such decomposition arises from the observation that all 3-dimensional point groups are subgroups of the full group of the sphere $O(3) = SO(3) \bigotimes C_i$. Irreducible representations of the latter group are well-known [KDWS63]; they are characterized by the angular momentum $J = 0, 1, 2, \dots$ and inversion parity $P = \pm 1$. An electric 2^J-pole is a rank-J tensor with inversion parity $(-1)^J$. For example, the electric dipole is a vector that changes sign upon inversion. A magnetic 2^J-pole is a rank-J tensor of parity $(-1)^{J+1}$. For instance, the magnetic dipole does not change sign upon inversion and is a pseudovector. This identifies all irreducible representations of $O(3)$ as either electric or magnetic multipoles.

$\mathbf{T_d}$	Example function	Electric 2^J-poles	Magnetic 2^J-poles
A_1	1; x²+y²+z²; xyz	0, 3, 4, 6, ...	6, 9, 10, 12, ...
A_2	$R_x R_y R_z$	6, 9, 10, 12, ...	(0), 3, 4, 6, ...
E	$\{2z^2\text{-}x^2\text{-}y^2, x^2\text{-}y^2\}$	2, 4, ...	2, 4, ...
$\mathbf{T_1}$	$\{R_x, R_y, R_z\}$	3, ...	**1**, ...
$\mathbf{T_2}$	{x,y,z}	**1**, ...	3, ...

Table 2.2: Multipolar decomposition of irreducible representations of the symmetry group T_d. Ellipses (...) denote all multipoles higher than the last listed. R_α is the rotation operator (pseudovector). The non-physical magnetic monopole (pseudoscalar representation) given in parentheses cannot be constructed from electric charges. Dipoles ($J = 1$) are shown in bold face.

To illustrate this method, a complete multipolar decomposition of T_d group was performed; the results are presented in Table 2.2. The electric multipole part of Table 2.2 can be found in a variety of books on point groups [KDWS63]; the magnetic multipole analysis of plasmon eigenmodes reported here has not been performed prior to this work. From Table 2.2 we see that, for example, A_1-symmetric modes of a tetramer may contain electric monopoles and octupoles, and also magnetic 64-poles, but they must have vanishing electric quadrupole and magnetic dipole moments. Modes of T_1 symmetry may have non-vanishing magnetic dipole and electric octupole moments. Modes of type T_2 contain electric dipoles and magnetic octupoles. These results will be used in Sec. 4.4 for designing electromagnetic metafluids based on tetrahedral nanoclusters.

With regard to the method of multipole decomposition, it is interesting to note that in structures with inversion symmetry, all irreducible representations are organized into "dual" pairs: representations in each pair differ only by inversion parity and are labeled by the same symbol with an additional index g (*gerade*, inversion-even) or u (*ungerade*, inversion-odd). Since magnetic and electric multipoles of the same order have opposite parity, the magnetic multipole composition of each representation can be trivially obtained from electric multipole composition of the "dual" representation. For example, consider the largest of all 3D point groups: full icosahedral group I_h (Table 2.3); its relevance to metamaterial fabrication may be fully appreciated from Sec. 4.4. The fact that an even 4-fold degenerate representation G_g of icosahedral group I_h consists of electric 2^J-poles with $J = 2n$ ($n \geq 2$) translates into the fact that the odd representation G_u consists of magnetic 2^{2n}-

$\mathbf{I_h}$	Example function	Electric multipoles	Magnetic multipoles
A_g	1; x²+y²+z²	0,6,10,12,16,...(2n)	15,21,25,27
$\mathbf{T_{1g}}$	$\{R_x, R_y, R_z\}$	6,10,...(2n)	**1**,5,...(2n+1)
T_{2g}		8,...(2n)	3,...(2n+1)
G_g		4,...(2n)	3,7,...(2n+1)
H_g	$\{2z^2\text{-}x^2\text{-}y^2, x^2\text{-}y^2, xy, xz, yz\}$	2,...(2n)	5,...(2n+1)
A_u		15,21,25,27	(0),6,10,12,16,...(2n)
$\mathbf{T_{1u}}$	$\{x,y,z\}$	**1**,5,...(2n+1)	6,10,...(2n)
T_{2u}	$\{x^3,y^3,z^3\}$	3,...(2n+1)	8,...(2n)
G_u	$\{x(z^2\text{-}y^2),y(z^2\text{-}x^2),z(x^2\text{-}y^2),xyz\}$	3,7,...(2n+1)	4,...(2n)
H_u		5,...(2n+1)	2,...(2n)

Table 2.3: Multipolar decomposition (up to $J = 30$) of irreducible representations of the symmetry group I_h. Ellipses (...) denote all 2^J-poles higher than the last listed (of parity indicated in parentheses). Dipoles ($J = 1$) are shown in bold face. Irreps T_{2g}, G_g, A_u and H_u can be exemplified by polynomials of order > 3 (not shown).

poles ($n \geq 2$). Likewise, the presence of electric 2^{2n+1}-poles with $n = 1$ and $n \geq 3$ in G_u-symmetric modes implies that G_g modes also contain magnetic multipoles of the same orders. In groups without inversion center, the duality between electric and magnetic multipoles can be less trivial: in the T_d case (Table 2.2), it appears as duality between singlet modes ($A_1 \leftrightarrow A_2$), triplet modes ($T_1 \leftrightarrow T_2$) and self-duality of the doublet E.

In the structures without an inversion center, some eigenmodes may transform as both the coordinate x and rotation R_z, meaning that they contribute to both electric dipole moment p_x and magnetic moment m_z. Whenever such modes exist, the structure is termed *bianisotropic*: it may not be described with $\epsilon_{\text{eff}}(\omega)$ and $\mu_{\text{eff}}(\omega)$ tensors alone [SL00]. The simplest structure where such modes do exist is a particle without any symmetry at all (trivial C_1 group). Split rings (SR), as well as split-ring resonators (SRR), are examples of bianisotropic structures [MMREI02], and their electrostatic resonances shown in Fig. 2.1(a) contribute to both μ_{eff}^{zz} and $\epsilon_{\text{qs}}^{xx}$.

Our symmetry classification of electric and magnetic modes allows us to formulate the *necessary and sufficient condition for absence of bianisotropy*. A structure can only be bianisotropic (i.e., have non-vanishing electro-magnetic cross-polarizabilities) if there is an irreducible representation of its symmetry group that represents both a component of a real vector and a pseudovector. The presence of

inversion symmetry is a sufficient condition for non-bianisotropy, because it splits all modes into parity-even and parity-odd, thus prohibiting electric and magnetic dipole moments from being non-zero simultaneously. As seen from Table 2.2, tetrahedral group T_d is an example of a non-bianisotropic point group without inversion symmetry. Only the following point groups in 3 dimensions are non-bianisotropic: C_{nh} for $n \geq 2$, D_{nh} for $n \geq 2$ (including cylindrical group $D_{\infty h}$), D_{nd} for $n \geq 3$, $S_2 \equiv C_i$, S_{2n} for $n \geq 3$, and the four non-chiral cubic groups T_d, T_h, O_h, I_h. Many of these groups, namely, $C_{(2n+1)h}$, S_{4n} for $n \geq 2$, $D_{(2n+1)h}$, D_{2nd} for $n \geq 2$, and T_d, have no inversion center. These examples show that inversion symmetry is not a necessary condition for the artificial molecule to be non-bianisotropic.

An important subclass of bianisotropic structures are *chiral* (dissymmetric, enantiomorphic) structures. Chiral particles possess a property termed *handedness* or *enantiomorphism*: their mirror image is geometrically different from themselves. Chirality therefore requires that the structure does not have any symmetry planes or improper rotation axes; although a structure with mirror planes may still be bianisotropic. Chirality of the optical response of plasmonic nanostructures is characterized by non-vanishing *diagonal* components of tensors ξ_{eff}, ζ_{eff} (or polarizabilities χ_{ME}^{ii}, χ_{EM}^{ii}). Since averaging over orientations removes all components of tensors χ_{ME}, χ_{EM} except the diagonal ones, isotropic systems can still be chiral. The degree of chirality of their optical response is characterized by one scalar quantity, e.g. χ_{ME}^{zz} given by Eq. (2.49). It is interesting to note that chiral plasmonic particles can have a completely isotropic electromagnetic response even without averaging over orientations; this is the case when they belong to one of the three *chiral cubic groups*: tetrahedral T, octahedral O, or icosahedral I. Nanostructures of this type of symmetry are described by the full set of isotropic electromagnetic susceptibilities (2.47,2.48,2.49).

2.4   Perturbation theory of optical response for periodic plasmonic nanostructures

In this Section we develop a homogenization theory of *periodic* plasmonic metamaterials that encompasses both their averaged electric response (through the effective dielectric tensor $\epsilon_{\text{eff}}(\omega)$) and the effective magnetic permeability $\mu_{\text{eff}}(\omega)$. The theory extends in a perturbative manner the existing homogenization theory

of differential equations with periodic coefficients. One of the intriguing results is that the magnetic plasmon resonance, which corresponded to a pole of magnetic polarizability $\chi_M(\omega)$ in Section 2.3, becomes the zero (in lossless limit) of magnetic permeability $\mu_{\text{eff}}(\omega)$ when periodicity effects are taken into account. This theoretical finding is supported by numerical simulations of arrays of strip pairs introduced in Section 2.3.

2.4.1 Homogenization of electrostatic equations with periodic coefficients

In this subsection we review a multi-scale approach [Mil02, Zhi94, Ole96] to calculating the effective permittivity of a metamaterial, and reveal the mathematical origin for the dipole-density definition of ϵ_{eff} in periodic nanostructures. Also known as the homogenization theory of differential operators with periodic coefficients [Mil02, Zhi94, Ole96], this is the most vigorous approach to homogenizing a periodic metamaterial with a unit cell size a being much smaller than that of the typical variation scale Λ of the dominant electrostatic potential Φ. As in the previous sections, the key assumption leading to the electrostatic approximation is that $\omega a/c \ll \omega \Lambda/c \ll 1$. Under this set of assumptions, the frequency ω enters only as a parameter determining the dielectric permittivity of the plasmonic dielectric permittivity $\epsilon(\omega)$. As we show below, the results of this rigorous theory are in total agreement with a more intuitive "capacitor" model described in the previous section. The method is applicable to periodic structures in any number of dimensions.

The basis of the method is the two-scale expansion. Let $\vec{X}$ be the macroscopic coordinates enumerating the cells (large scale), and $\vec{\xi}$ the local coordinates (small scale). The fields depend weakly on $\vec{X}$ and strongly on $\vec{\xi}$. The potential $\phi(\vec{X}, \vec{\xi})$ and the local permittivity $\epsilon(\vec{\xi})$ are periodic in local coordinates $\vec{\xi}$; the latter can be restricted to one cell.

To quantify the difference between large and small scales, one introduces a small parameter $\tau = a/\Lambda$ and assumes that $\nabla_x = \nabla_\xi + \tau \nabla_X$. Naturally, τ is the expansion parameter of a perturbation theory series: $\phi(x) = \phi_0(X, \xi) + \tau \phi_1(X, \xi) + \tau^2 \phi_2(X, \xi) + O(\tau^3)$. The Laplace equation $\nabla_x \epsilon(x) \nabla_x \phi(x) = 0$ becomes

$$(\nabla_\xi + \tau \nabla_X)\epsilon(\xi)(\nabla_\xi + \tau \nabla_X)\phi(X, \xi) = 0. \qquad (2.55)$$

The goal of homogenization theory is to show that there exists a macroscopic potential $\phi_{macro}(X)$ that obeys Laplace-Poisson equation in a certain homogeneous, possibly anisotropic, medium. In doing so, both the rigorous definitions of $\phi_{macro}(X)$ and $\epsilon_{\text{eff}}^{ij}$ are discovered. This goal is achieved by expanding (2.55) in powers of τ. This gives

$$
\begin{aligned}
\nabla_\xi \epsilon(\xi) & \nabla_\xi \phi_0(X,\xi) + \\
+ \quad \tau \Big\{ & (\nabla_\xi \epsilon(\xi) + \epsilon(\xi)\nabla_\xi)\nabla_X \phi_0(X,\xi) + \\
+ \quad & \nabla_\xi \epsilon(\xi)\nabla_\xi \phi_1(X,\xi) \Big\} + \\
+ \quad & \tau^2 \Big\{ \nabla_X \epsilon(\xi)\nabla_X \phi_0(X,\xi) + \\
+ \quad & (\epsilon(\xi)\nabla_\xi + \nabla_\xi \epsilon(\xi))\nabla_X \phi_1(X,\xi) + \\
+ \quad & \nabla_\xi \epsilon(\xi)\nabla_\xi \phi_2(X,\xi) \Big\} = 0.
\end{aligned}
\tag{2.56}
$$

Terms with different powers of τ must vanish independently, which gives us three equations:

$$
\nabla_\xi \epsilon(\xi)\nabla_\xi \phi_0(X,\xi) = 0,
\tag{2.57}
$$

$$
(\nabla_\xi \epsilon(\xi) + \epsilon(\xi)\nabla_\xi)\nabla_X \phi_0(X,\xi) + \nabla_\xi \epsilon(\xi)\nabla_\xi \phi_1(X,\xi) = 0,
\tag{2.58}
$$

$$
\begin{aligned}
\nabla_X \epsilon(\xi) & \nabla_X \phi_0(X,\xi) + \\
+ (\epsilon(\xi)\nabla_\xi + \nabla_\xi \epsilon(\xi))\nabla_X \phi_1(X,\xi) & + \nabla_\xi \epsilon(\xi)\nabla_\xi \phi_2(X,\xi) = 0.
\end{aligned}
\tag{2.59}
$$

Their solution is carried out in three easy steps. First, eq. (2.57) is satisfied by choosing $\phi_0 = \phi_0(X)$ which is independent of ξ. This function $\phi_0(X)$ plays the role of macroscopic potential, as we shall see further. Second, $\phi_1(X,\xi)$ is expressed through the macroscopic gradients of ϕ_0:

$$
\phi_1(X,\xi) = -\frac{\partial \phi_0(X)}{\partial X_i}\phi_{sc}^{(i)}(\xi),
\tag{2.60}
$$

where $\phi_{sc}^{(i)}(\xi)$ ($i = 1, 2$ in 2D) are periodic basis functions that solve equations

$$
\nabla_\xi \epsilon(\xi)\nabla_\xi \phi_{sc}^{(i)}(\xi) = (\nabla_\xi \epsilon(\xi)) \cdot \vec{e}_i.
\tag{2.61}
$$

Equation (2.61) is called the auxiliary homogenization problem, and it is identical to the master equation (2.1) of the "capacitor" model. Indeed, eq. (2.61) is simply

$$\nabla_\xi \epsilon(\xi) \nabla_\xi (\phi_{sc}^{(i)}(\xi) - \xi_i) = 0, \tag{2.62}$$

in which we identify the "external" potential $\phi_{ext}^{(i)} = -\xi_i$ corresponding to a uniform electric field of unit amplitude polarized in the i-th direction. Their sum $\phi_{tot}^{(i)}(\xi) = \phi_{in} + \phi_{sc}$ satisfies (2.1).

Finally, the macroscopic equation for $\phi_0(X)$ is obtained by substituting ϕ_1 (2.60) into (2.59) and averaging over the local variable ξ:

$$\nabla_{X_i} \left\langle \epsilon(\xi)\delta_{ij} - (\epsilon(\xi)\nabla_{\xi_i} + \nabla_{\xi_i}\epsilon(\xi))\phi_{sc}^{(j)}(\xi) \right\rangle \nabla_{X_j}\phi_0(X) + \tag{2.63}$$

$$+ \langle \nabla_\xi \epsilon(\xi)\nabla_\xi \phi_2(X,\xi) \rangle = 0. \tag{2.64}$$

Full derivatives of periodic functions have zero average, and thus, the above equation reduces to $\nabla_{X_i} \epsilon_{\text{eff}}^{ij} \nabla_{X_j} \phi_{macro}(X) = 0$, where $\phi_{macro}(X) \equiv \phi_0(X) \equiv \langle \phi(X,\xi) \rangle$ and

$$\epsilon_{\text{eff}}^{ij} = \left\langle \epsilon(\xi)\delta_{ij} - \epsilon(\xi)\nabla_{\xi_i}\phi_{sc}^{(j)}(\xi) \right\rangle \equiv \left\langle \epsilon(\xi)\nabla_{\xi_i} \left(\xi_j - \phi_{sc}^{(j)}(\xi) \right) \right\rangle. \tag{2.65}$$

Here $\langle \cdot \rangle \equiv \int \cdot d\xi / \int 1 d\xi$. To identify this definition of ϵ_{eff} with the capacitor model, we note that $\vec{E}^{(j)}(\xi) = \nabla_\xi(-\phi_{sc}^{(j)}(\xi) + \xi_j)$ is the total electric field excited by external electric field $\vec{E}_0 = E_{0j}\vec{e}_j$ with unit amplitude $E_{0j} = 1$. Equation (2.65) is simply $\epsilon_{\text{eff}}^{ij} = \langle \epsilon(\xi)E_i^{(j)}(\xi) \rangle$, in exact agreement with eq. (2.5) and its equivalent forms.

2.4.2   Optical magnetism in periodic plasmonic structures

In Section 2.2 it was demonstrated that there are multiple ways to define ϵ_{eff}, and they all agree with each other in the sub-wavelength limit, $\eta \equiv \omega a/c \ll 1$. However, as the retardation parameter η becomes larger, discrepancy between the capacitance and dipole density definitions grows.

Similarly to the dielectric permittivity, *magnetic permeability* of a periodic structure can be defined in two ways. On one hand, there is a field averaging

definition [PHRS99, SVKS00]

$$\mu_{\text{eff}}^{zz} = \frac{(a_x a_y)^{-1} \int_{-a_x/2}^{a_x/2} dx \int_{-a_y/2}^{a_y/2} dy B_z(x, y, z = -a_z/2)}{a_z^{-1} \int_{-a_x/2}^{a_x/2} dx H_z(x = -a_x/2, y = -a_y/2, z)}, \tag{2.66}$$

analogous to the capacitance model (2.3).

On the other hand, one can calculate the magnetic dipole moment $\vec{m} = \int dx dy \vec{M}$ of a unit cell (per unit length in 2D), where $\vec{M} = \frac{1}{2c}[\vec{r} \times \vec{j}]$ is the magnetic polarization density, and postulate that

$$m_i = \frac{1}{4\pi} \left(\mu_{\text{eff}}^{ij} - \delta^{ij} \right) H_{0j}. \tag{2.67}$$

This gives a different definition of magnetic permeability, which was used in a number of works [SU06, SSS06, AG06]. While rigorous proof of their equivalence is yet to be published, it is known [SVKS00] that in the limit of small η definitions (2.66,2.67) of μ_{eff} agree.

It seems likely that a vigorous mathematical theory of magnetic homogenization will be based on a generalized multi-scale expansion technique described in Section 2.4.1. Recently, an important step in this direction has been made [FB05], which resulted in an eigenvalue expansion formula for $\mu_{\text{eff}}(\omega)$ of dielectric photonic crystals with high dielectric contrast, $\epsilon/\epsilon_d \gg 1$. Unfortunately, technique proposed in [FB05] is only applicable to *large and positive* dielectric contrasts. Plasmonic resonances, which occur in the $\epsilon/\epsilon_d < 0$ regime, cannot be found as the eigenvalues of Helmholtz equation used as the basis of that technique [FB05].

In this subsection, we present a perturbative homogenization theory that uses electrostatic plasmon eigenfunctions, which are known to provide a complete orthogonal basis in the appropriate linear space [BS92, SBK04], as the starting point. This theory is applicable to both two- and three-dimensional structures. The expansion parameter of this theory is the frequency ω, or rather the dimensionless retardation parameter $\eta = \omega a/c$. The goal of this Section is to obtain a general analytic expression for μ_{eff} of a periodic plasmonic nanostructure in the form of an eigenmode expansion similar to [FB05]. This way both the frequencies and strengths of approximately Lorentz-shaped resonances will be recovered.

When electrostatics is used as the base of a perturbation theory, it is easier

48

to start from the dipole density definition (2.67), which expresses μ_{eff} through the local quasistatic electric currents proportional to the electric field:

$$\vec{j} = \frac{\partial \vec{P}}{\partial t} = -\frac{i\omega}{4\pi}(\epsilon - 1)\vec{E}. \qquad (2.68)$$

Optical magnetism appears in the ω^2 order of this perturbation theory [SU06, SSS06]. Since the current expression (2.68) already has one factor of ω, to determine μ_{eff} in the lowest order it suffices to calculate $\vec{E}$ with the first-order electromagnetic corrections.

To isolate the role of electrostatic resonances, it is convenient to split electric and magnetic fields into "incident" and "scattered", i. e. $\vec{E} = \vec{E}_{in} + \vec{E}_{sc}$, such that $\vec{E}_{sc}$ would vanish in a homogeneous structure. To achieve this, we use the following ansatz: incident fields will be given by a plane wave in a homogeneous medium with wavenumber $\vec{k}$, i. e. $\vec{E}_{in} = \vec{E}_0 e^{i\vec{k}\cdot\vec{r}}$ and $\vec{H}_{in} = \vec{H}_0 e^{i\vec{k}\cdot\vec{r}}$. After the effective medium parameters ϵ_{eff} and μ_{eff} are expressed through $\vec{k}$, we will relate $\vec{k}$ with the frequency and effective medium parameters using the dispersion relation of transverse waves in a homogenized medium: $k = \sqrt{\epsilon_{\text{eff}}}\sqrt{\mu_{\text{eff}}}\omega/c$. This ansatz is somewhat similar to the Maxwell-Garnett homogenization theory, where individual particles to be homogenized are assumed to be immersed into an effective medium with some unknown ϵ_{eff} and μ_{eff}. Note that because incident fields satisfy Maxwell's equations in the homogenized medium, we have $\vec{H}_0 = Z_e^{-1}[\vec{n}_k \times \vec{E}_0]$, where $Z_e = \sqrt{\mu_{\text{eff}}}/\sqrt{\epsilon_{\text{eff}}}$ is effective impedance and $\vec{n}_k = \vec{k}/|\vec{k}|$ is the direction of phase velocity. From this point, we assume that $\vec{k}||\hat{x}$, $\vec{E}_0||\hat{y}$ and $\vec{H}_0||\hat{z}$. Therefore, $\mu_{\text{eff}} \equiv \mu_{\text{eff}}^{zz}$.

In order to find the scattered electric field $\vec{E}_{sc}$, we further decompose it into the potential and solenoidal parts, $\vec{E}_{sc} = \vec{E}_{pot} + \vec{E}_{sol} = -\vec{\nabla}\Phi_{sc} + ik_0\vec{A}_{sc}$, where $\vec{\nabla} \cdot \vec{A}_{sc} = 0$ and $k_0 \equiv \omega/c$. Vector potential $\vec{A}_{sc}$ is related to the scattered magnetic field: $\vec{H}_{sc} = (\mu_{\text{eff}} - 1)\vec{H}_{in} + \vec{\nabla} \times \vec{A}_{sc}$. It can be demonstrated that $\vec{A}_{sc}$ vanishes in the limit $\omega \to 0$, i.e. its perturbative expansion begins from the first order in ω. Contribution of $\vec{A}_{sc}$ to $\vec{E}_{sc}$ thus appears in the second order. It is the benefit of our approach that the lowest-order part of $\mu_{\text{eff}} - 1$ can be found without computing $\vec{A}_{sc}$ or magnetic fields. The potential part of $\vec{E}_{sc}$ is determined from $\vec{\nabla} \cdot \vec{D} = 0$, which gives Eq. (2.23) already used in Sec. 2.3; in that equation, $k_0\vec{A}_{sc}$ can be neglected in the first approximation.

In analogy with the work [FB05], we will represent Φ_{sc} in the form

49

$\Phi_{sc}(X,x) = \sum_n c_n(X)\phi_n(x)$, where ϕ_n are electrostatic eigenfunctions of the GEDE with periodic boundary conditions. Function $\Phi_{sc}(X,x)$ is periodic in the "local" coordinate x and depends upon the "macroscopic" coordinate X as the macroscopic fields, i. e. $\propto e^{ikX}$. Such expansion is justified because the full set of $\{\phi_n(x)\}$ functions is a complete basis in the space of periodic potential functions [BS92, SBK04]. The coupling coefficient c_n between $\vec{E}_{in} = \vec{E}_0 e^{ik(X+x)}$ and the nth plasmon eigenmode is found from (2.23) and is given by Eq. (2.25). Coefficients $c_n(X) = c_n(0)e^{ikX}$ absorb the phase shift per cell; it is sufficient to calculate them in the very first cell, i.e. at $X = 0$. Expanding the plane wave $\vec{E}_{in} = \vec{E}_0 e^{ikx}$ formally in powers of k up to the first order, we have $c_n = c_n^{(0)} + c_n^{(1)}$, where

$$c_n^{(m)} = -\frac{1}{m!}(i\sqrt{\epsilon_{\text{eff}}}\sqrt{\mu_{\text{eff}}}k_0)^m \frac{s_n}{s(\omega)-s_n}\vec{E}_0 \cdot \frac{\int(\vec{\nabla}\phi_n)x^m\theta dV}{\int(\nabla\phi_n)^2\theta dV}, \; m=0,1. \qquad (2.69)$$

Now that the scattered field $\vec{E}_{sc}$ is known, we use the dipole density definition (2.67) to calculate μ_{eff}. For simplicity, we assume that the structure has a center of inversion that coincides with the center of mass of a unit cell. Choosing it as the origin of coordinate system, we have $\int \vec{r}\theta dV = 0$ and $\int \vec{r}dV = 0$. This eliminates the term $\int(\epsilon-1)\vec{r}\times\vec{E}_0 dV$, and also guarantees that the dipole eigenmodes ϕ_n in Φ_{sc} excited by uniform field $\vec{E}_0$ do not carry magnetic moment, as explained below. Under these assumptions, $\mu_{\text{eff}} - 1 \propto k_0^2$.

Currents excited directly by $\vec{E}_{in}$ in (2.68) give a trivial diamagnetic contribution to μ_{eff}:

$$\Delta\mu_{diam} = \frac{k_0^2 \mu_{\text{eff}}}{2V}\left[(\epsilon_d-1)\int x^2 dV - \frac{\epsilon_d}{s}\int x^2\theta dV\right]. \qquad (2.70)$$

Quasistatic currents due to $\vec{E}_{sc} \approx -\vec{\nabla}\Phi_{sc}$ give the plasmon resonance part of the magnetic permeability:

$$\Delta\mu_{plasm} = -k_0^2\epsilon_d\mu_{\text{eff}}\sum_n \frac{F_n^{zz}}{s(\omega)-s_n} + k_0^2\epsilon_d\mu_{\text{eff}}\frac{1}{s}\sum_n F_n^{zz}, \qquad (2.71)$$

where we have introduced the magnetic strength of nth resonance, a quantity with
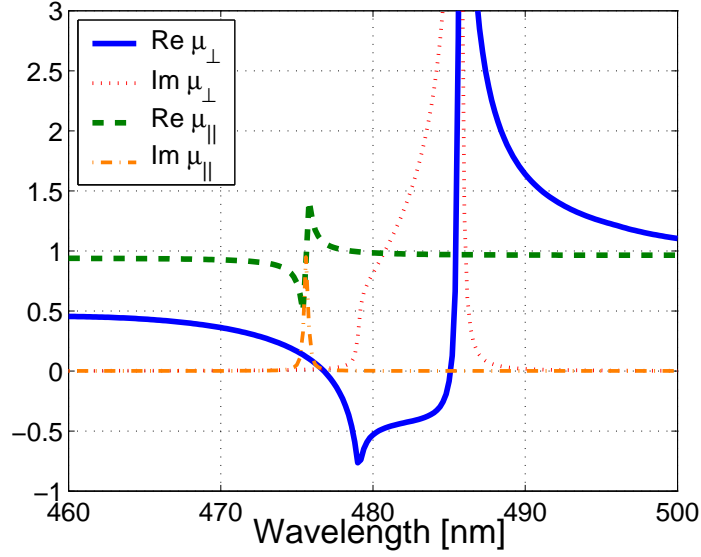
Figure 2.4: Effective magnetic permeability μ_{eff}^{zz} of the MSP structure calculated using EMPR procedure (Sec. 4.2.4). Solid and dotted curves: strips perpendicular to the wave vector $\vec{k}$ (and parallel to electric field $\vec{E}_0$ of the incident wave); dashed and dash-dotted curves: strips parallel to $\vec{k}$, perpendicular to $\vec{E}_0$. Note: magnetic cut-off (Re $\mu_{\text{eff}} = 0$) is polarization-independent. Structure parameters: periods $a_x = a_y = 100$ nm, strip width $w = 50$ nm, strip thickness $t_s = 15$ nm, strip separation in a pair $h = 15$ nm; plasmonic component: silver (dielectric function from [Pal85] with 100-fold reduced Im ϵ); immersion medium: $\epsilon_d = 1$.

dimension of area:

$$F_n^{zz} = \frac{1}{2} \frac{\int \left(x \frac{\partial \phi_n}{\partial y} \theta \right) dV \int \left(\vec{e}_z \cdot [\vec{r} \times \nabla \phi_n] \theta \right) dV}{V \int (\nabla \phi_n)^2 \theta dV}. \tag{2.72}$$

Finally, permeability is determined from $\mu_{\text{eff}} - 1 = \Delta \mu_{diam} + \Delta \mu_{plasm}$:

$$1 - \frac{1}{\mu_{\text{eff}}^{zz}} = \mu_d^{zz} - k_0^2 \epsilon_d \frac{F_0^{zz}}{s(\omega)} - k_0^2 \epsilon_d \sum_n \frac{F_n^{zz}}{s(\omega) - s_n}, \tag{2.73}$$

where $\mu_d^{zz} = k_0^2(\epsilon_d - 1)\langle \frac{x^2}{2} \rangle$ and $F_0^{zz} = \left(\langle \frac{x^2}{2} \theta \rangle - \sum_n F_n^{zz} \right)$.

Equation (2.73) differs from our earlier result (2.21,2.39,2.40) formally by a replacement $\mu_{\text{eff}} \rightarrow 1 - 1/\mu_{\text{eff}}$. This means, in particular, that, in the absence

51

of resistive losses (Im $\epsilon = 0$), the frequency of magnetic plasmon resonance ω_n, defined as $s(\omega_n) = s_n$, is the frequency of *magnetic cut-off* ($\mu_{\text{eff}} = 0$). To confirm this prediction and validate the theory, formula (2.73) is plotted in Fig. 2.4 for an array of strip pairs, introduced in Section 2.3. To isolate the magnetic cutoff, losses in metal (imaginary part of ϵ_{Ag}) were 100-fold reduced in simulations. As we have already seen in Section 2.3.3, magnetic strength of plasmon resonances F_n^{zz} in strip-pair structures strongly depends on the orientation of electric field; however, the frequency of plasmon resonance s_n does not. Therefore, if the formula (2.21) is valid for plasmonic crystals, the positions of magnetic resonances (defined by maxima of either Re μ_{eff} or Im μ_{eff}) should be the same for both polarizations; but if the periodicity-corrected formula (2.73) is valid, magnetic cut-off Re $\mu_{\text{eff}} = 0$ instead of magnetic resonance should be polarization-independent. It is evident from Fig. 2.4 that magnetic cut-off (Re $\mu_{\text{eff}} = 0$) is located at $\lambda = 476$ nm for both polarizations, while frequencies of magnetic resonance (or absorption lines) are polarization-dependent. Numerical simulations thus clearly demonstrate that the corrected formula (2.73) obtained from enhanced effective medium theory of this Section gives more adequate description of optical magnetism in periodic structures than single-resonator theory of Section 2.3.

Invariance of the magnetic cut-off frequency with respect to propagation direction (given by the Bloch wave vector $\vec{k}$) in sub-wavelength plasmonic crystals can be easily understood in terms of the photonic band structure. Indeed, magnetic cut-off frequency corresponds to the frequency of the Γ-point ($\vec{k} = 0$) on the dispersion surface of a photonic crystal. Therefore, if a branch of the dispersion surface can be described by effective medium parameters ($\epsilon_{\text{eff}}^{ij}$, μ_{eff}^{zz}) at all, μ_{eff}^{zz} must be zero at that frequency regardless of the polarization.

2.5   Electromagnetic red shifts of plasmonic resonances

In Sections 2.3 and 2.4 we have developed a quasistatic perturbation theory that gives approximate expressions for effective medium parameters of complex nanostructures. It was found that in the first order to the expansion parameter η (dubbed "retardation parameter"), magneto-electric coupling phenomena arise, and optical magnetism occurs in the second order. Optical magnetism is not the only second-order retardation phenomenon that can be described in the framework

of this theory. From Fig. 2.3(a) we observe that the frequency of the magnetic resonance determined from electromagnetic simulations (solid curve) is red-shifted with respect to the frequency of the corresponding electrostatic resonance (black dashed curve). It can also be seen from Fig. 2.2 that electric dipole resonances in FEFD simulations are red-shifted with respect to their electrostatic positions. Both shifts are explained in this Section as the retardation-induced corrections to the positions of the purely electrostatic plasmon resonances. The theory presented here is a volumetric reformulation and a slight generalization of a result found using surface charge integral equation (SCIE) [MFZ05]. General formulas of this Section cover arbitrary geometries in any number of dimensions (including 2D and 3D) and may also account for periodicity and interactions between adjacent cells in plasmonic metamaterials.

Retardation-related frequency shifts of plasmon resonances are always red (regardless of their multipolar nature) and can be understood physically as follows. Quasistatic currents associated with electric fields of electrostatic resonances induce magnetic fields via Ampere's law. These magnetic fields generate secondary electric fields according to the Faraday's law. The latter contribute to the Poisson equation $\vec{\nabla} \cdot \epsilon \vec{E} = 0$, causing shifts in electrostatic eigenvalues. While such frequency shifts have been calculated earlier for isolated plasmonic nanoparticles, they have never been calculated for periodic plasmonic metamaterials. These shifts have been derived earlier from the SCIE formalism; here, we use the GEDE formalism and a generalization of the standard perturbation theory (formulated in Section 2.7) to obtain new analytic expressions for retardation shifts. These results are not limited to isolated inclusions; red shifts in periodic collections of particles can be calculated by utilizing periodic boundary conditions. In this Section, V represents either a unit cell of a periodic structure, or the entire space (for isolated particles).

We use the results of the perturbation theory sketched in Sec. 2.4. To the lowest order in η and in the close vicinity of the nth plasmonic resonance (i.e., at $s \approx s_n^{(0)}$, where $s_n^{(0)}$ is the purely electrostatic eigenvalue of the Eq. (2.10)), the vector potential induced by the nth electrostatic resonance is found from Eq. (2.24):

$$\vec{A}_{sc}^{(1)}(\vec{r}) = ik_0 \int_V dV' G(\vec{r} - \vec{r}')\epsilon(\vec{r}')\vec{\nabla}\phi_n(\vec{r}'), \tag{2.74}$$

where $\epsilon = \epsilon_d \left(1 - \frac{1}{s_n^{(0)}}\theta\right)$, and $G(\vec{r} - \vec{r}')$ is the Green's function of Poisson equation with appropriate boundary conditions on ∂V. Thus computed vector potential $\vec{A}_{sc}^{(1)}$ contributes to Poisson equation:

$$\vec{\nabla}\theta\vec{\nabla}\Phi + k_0^2\epsilon_d\vec{\nabla}\theta \cdot \int_V dV' G(r,r')\left(1 - \frac{1}{s_n^{(0)}}\theta\right)\vec{\nabla}\Phi = s_n\nabla^2\Phi. \qquad (2.75)$$

This is a generalized linear eigenvalue problem with integro-differential operator. Treating the integral term as a perturbation, (see Section 2.7), corrections to electrostatic eigenvalues $s_n^{(0)}$ can be shown to be:

$$s_n^{(2)} = k_0^2\epsilon_d s_n^{(0)} \oint_{S_p} dS\phi_n(r)\vec{n} \cdot \int_V G(\vec{r} - \vec{r}')\left(1 - \frac{1}{s_n^{(0)}}\theta(\vec{r}')\right)\vec{\nabla}\phi_n(\vec{r}')dV' \times$$

$$\left(\int_V (\vec{\nabla}\phi_n)^2\theta dV\right)^{-1}, \qquad (2.76)$$

where $\oint dS$ is a surface integral over a closed surface S_p of the plasmonic inclusion (which reduces to a contour integral for 2D crystals). The renormalized s_n is calculated as $s_n = s_n^{(0)} + s_n^{(2)}$.

Volume integral in Eq. (2.76) can be reduced to a surface integration over the surface S_p of plasmonic inclusion using the following technique. Equation (2.24) can be re-written back in its original, curl-curl form (omitting the drive term with $\vec{E}_{in}$):

$$\vec{\nabla} \times [\vec{\nabla} \times \vec{A}_{sc}^{(1)}] = ik_0\epsilon\vec{\nabla}\Phi_{sc}^{(0)}. \qquad (2.77)$$

An equation of the form $\vec{\nabla} \times [\vec{\nabla} \times \vec{A}] = \vec{F}$ can be solved by applying the following identity twice:

$$\vec{\nabla} \times \vec{A}(\vec{r}) = \int_V dV'\vec{\nabla}'G(\vec{r},\vec{r}') \times \vec{F}(\vec{r}') = -\int_V dV'G(\vec{r},\vec{r}')[\vec{\nabla}' \times \vec{F}(\vec{r}')]. \qquad (2.78)$$

Introducing the auxiliary vector function [MFZ05]

$$\vec{a}(\vec{r},\vec{r}'') = -\int_V dV'G(\vec{r}',\vec{r}'')\vec{\nabla}'G(\vec{r},\vec{r}') \equiv -\vec{\nabla}\int_V dV'G(\vec{r} - \vec{r}'')G(\vec{r} - \vec{r}'), \qquad (2.79)$$

we find the vector potential generated by a single plasmon eigenmode ϕ_n:

$$\vec{A}_{sc}^{(1)}(\vec{r}) = ik_0 \int_V dV' \vec{a}(\vec{r}, \vec{r}') \times \left[\vec{\nabla}' \times \epsilon \vec{\nabla}' \phi_n\right] = \frac{ik_0 \epsilon_d}{s_n^{(0)}} \cdot \qquad (2.80)$$

$$\cdot \oint_{S_p} dS' \vec{a}(\vec{r}, \vec{r}') \times \left[\vec{n}' \times \vec{\nabla}' \phi_n(\vec{r}')\right]. \qquad (2.81)$$

Consequently, the correction to electrostatic eigenvalue is found:

$$s_n^{(2)} = k_0^2 \epsilon_d \left(\oint_{S_p} dS \phi_n(\vec{r}) \vec{n} \cdot \oint_{S_p} dS' \vec{a}(\vec{r}, \vec{r}') \times [\vec{n}' \times \vec{\nabla}' \phi_n(\vec{r}')] \right) \cdot \qquad (2.82)$$

$$\cdot \left(\oint_{S_p} \phi_n \frac{\partial \phi_n}{\partial n} dS \right)^{-1} \qquad (2.83)$$

where the normal derivative $\partial \phi_n / \partial n$ is evaluated on the plasmonic side of surface S_p. A particular case of this formula has been previously reported for isolated three-dimensional particles [MFZ05].

Despite substantial progress in calculations of periodic Green's functions [Mar00], closed-form expressions for double- or triple-periodic G in two or three dimensions are not known. However, there exists one simple yet exact result for a 2D Green's function in the limit $a_y \gg a_x$ [Mar00]:

$$G_2(\vec{r} - \vec{r}') = \frac{1}{2a_x} \left(\frac{(y-y')^2}{a_y} - |y-y'| + \frac{a_y}{6} \right) -$$

$$-\frac{1}{4\pi} \ln\left[1 - 2e^{-2\pi|y-y'|/a_x} \cos(2\pi|x-x'|/a_x) + e^{-4\pi|y-y'|/a_x}\right]. \qquad (2.84)$$

The function (2.84) is periodic only in the x-direction. It is therefore applicable only for $|y - y'| \ll a_y$, i.e. when plasmonic inclusions are much thinner in the y-direction than the period ($w_y \ll a_y$). For periodic metamaterials based on "current loops" (strip pairs, horse shoes, etc.), interaction between consecutive layers of resonators is usually insignificant, and the function (2.84) provides reasonable approximation. When the condition $w_x \ll a_x$ is satisfied, one can use expression (2.84) with interchanged variables $x \leftrightarrow y$, $a_x \leftrightarrow a_y$. When both dimensions are small, $w_{x,y} \ll a_{x,y}$, a symmetrized (in x, y) version of Eq. (2.84) is used.

Retardation frequency shifts of selected electric and magnetic resonances are illustrated on Fig. 2.2 and Fig. 2.3, respectively. Frequency shifts are calculated

using Eq. (2.76) with the Green's function given by Eq. (2.84). It is apparent that the quasistatic Eqs. (2.12,2.73) with frequency corrections corresponding to $s_n = s_n^{(0)} + s_n^{(2)}$ (green dashed curves on Fig. 2.2,2.3) are in much better agreement with the electromagnetic ϵ_{eff} and μ_{eff} than the unperturbed electrostatic eigenvalues $s_n^{(0)}$ (black dashed curves).

2.5.1 Analytic calculation of retardation effects for a circular cylinder

In this Section we verify the new formula (2.83) analytically in the case of an infinitely long circular cylinder. For a single cylinder, electromagnetic scattering problem can be solved analytically without making assumptions about the wavelength-to-diameter ratio (van de Hulst theory). For a plane wave scattering off a cylinder, Mie-van de Hulst expansion coefficients are

$$a_n = \frac{J_n'(mx)J_n(x) - mJ_n(mx)J_n'(x)}{J_n'(mx)H_n(x) - mJ_n(mx)H_n'(x)}, \tag{2.85}$$

$$b_n = \frac{-\frac{2im}{\pi x}}{J_n'(mx)H_n(x) - mJ_n(mx)H_n'(x)}, \tag{2.86}$$

where $x \equiv k_0 R$ is the dimensionless size parameter of the cylinder, $m = \sqrt{\epsilon(\omega)}$ is the refractive index inside the cylinder, and $H_n \equiv H_n^{(1)} \equiv J_n + iY_n$ is the Hankel function of the first kind. Without loss of generality, we assume that the medium outside the cylinder is vacuum ($\epsilon_d = 1$).

Exact frequencies of all plasmon resonances can be found as zeros of the denominators of either a_n or b_n. Plasmon resonances are characterized by their multipolar order n. Resonant permittivities ϵ_n can be found analytically in the limit of small $k_0 R$ using Laurent series for Bessel and Hankel functions:

$$\epsilon_n = -1 - \frac{(k_0 R)^2}{n^2 - 1} + O(k_0 R)^3, \; n \geq 2, \tag{2.87}$$

$$\epsilon_1 = -1 - \left(\frac{1}{4} - \gamma_E + \frac{\pi i}{2} - \ln\frac{k_0 R}{2}\right)(k_0 R)^2 + O(k_0 R)^3, \tag{2.88}$$

where $\gamma_E \approx 0.577215665$ is the Euler-Mascheroni constant.

All plasmon resonances collapse to $\epsilon = -1$ in the electrostatic limit ($k_0 R \rightarrow$

0). Consequently, electrostatic eigenvalue $\epsilon^{(0)} = -1$ is the only eigenvalue of the circular cylinder, and it is infinitely degenerate. In general, degeneracy of unperturbed eigenvalues requires proper diagonalization of the unperturbed problem, leading to the so-called secular perturbation theory. However, non-secular theory is still applicable when perturbation $\hat{V}$ satisfies

$$\langle m|\hat{V}|n\rangle = 0 \;\forall m, n : s_m = s_n. \tag{2.89}$$

Fortunately, electromagnetic perturbation does possess this property: it does not mix plasmon resonances with different multipole orders.

Our formula (2.83) can be applied analytically to all plasmon modes of a cylinder, except in the special case of dipolar modes ($n = 1$), as we shall see immediately. Vector function $\vec{a}$ in (2.83) is given for a single 2D scatterer by

$$\vec{a}_{2\infty}(r, r') = -\frac{1}{4\pi}(\vec{r} - \vec{r}')\left(\ln\left|\vec{r} - \vec{r}'\right| + C\right), \tag{2.90}$$

where C is an arbitrary constant. The value of this arbitrary constant does not affect frequency corrections (2.83) for any resonances except those that carry dipolar moment: indeed, a variation of this constant induces a change in $s_n^{(2)}$

$$\frac{\partial}{\partial C}s_n^{(2)} = -\frac{k_0^2}{4\pi}\oint ds\phi_n^{(0)}(r)\vec{n} \cdot \oint ds'(\vec{r} - \vec{r}') \times [\vec{n}' \times \nabla\phi_n^{(0)}(r')] \cdot$$
$$\left(\oint \phi_n^{(0)}\frac{\partial\phi_n^{(0)}}{\partial n}ds\right)^{-1}, \tag{2.91}$$

which is proportional to the electric strength f_n of this resonance. Therefore, for dipolar modes of an *isolated two-dimensional* particle the formula (2.83) does not give a definite value. The case of dipolar modes in 2D is clearly special, because, as we see from van de Hulst theory result (2.88), dipolar eigenfrequencies are complex even in the lossless case. This hurdle originates from the fact that electric dipole radiation scales as ω^2 in two dimensions — same as the order of corrections that we are calculating perturbatively. In 3D, electric dipole radiation appears in order ω^3 and does not influence second-order corrections $s_n^{(2)}$. Neither does it influence 2D double-periodic arrays of scatterers: there is no radiative losses (associated with Sommerfeld boundary condition at infinity) in fully periodic systems.

We now proceed to direct evaluation of the formula (2.83). In polar coordinates (r, θ), the potential of the $2n$-polar electrostatic resonance inside the cylinder can be written as

$$\phi_n^{(0)}(r, \theta) = (r/R)^n \sin n\theta, \; r \leq R. \tag{2.92}$$

For example, dipolar eigenmode ($n = 1$) is simply $\phi_1^{(0)} = y/R$. Due to rotational invariance of the cylinder, sines in $\phi_n^{(0)}$ can be replaced with cosines without affecting the final result. The normalization factor equals

$$\oint \phi_n^{(0)} \frac{\partial \phi_n^{(0)}}{\partial n} ds = n \int_0^{2\pi} d\theta \sin^2 n\theta = n\pi. \tag{2.93}$$

Radius-vector equals $\vec{r} = R(\cos\theta\hat{x} + \sin\theta\hat{y})$. The unit vectors of normal and tangent directions on the circle are given by $\vec{n}(\theta) = \cos\theta\hat{x} + \sin\theta\hat{y}$ and $\vec{t}(\theta) = -\sin\theta\hat{x} + \cos\theta\hat{y}$. We note that $\vec{r} - \vec{r}' = 2R\sin\frac{\theta-\theta'}{2}\vec{t}(\frac{\theta+\theta'}{2})$ and $\vec{n}(\theta') \times \vec{\nabla}\phi_n^{(0)}(\theta') = \frac{1}{R}\hat{z}\frac{\partial\phi_n^{(0)}}{\partial\theta'}$. With the aid of identity

$$\vec{n}(\theta) \cdot [2R\sin\frac{\theta - \theta'}{2}\vec{t}(\frac{\theta + \theta'}{2}) \times [\vec{n}(\theta') \times \nabla\phi(\theta')]] =$$
$$= -\sin(\theta - \theta')\frac{\partial\phi_n^{(0)}}{\partial\theta'}\hat{z} \tag{2.94}$$

we finally obtain

$$s_n^{(2)} = \frac{1}{4\pi}(k_0 R)^2 \int_0^{2\pi} d\theta \int_0^{2\pi} d\theta' \sin n\theta \cos n\theta' \sin(\theta - \theta') \cdot$$
$$\cdot \ln\left|\tilde{C}\sin\frac{\theta - \theta'}{2}\right|. \tag{2.95}$$

We have verified analytically that for $n = 2, 3, 4, 6$ these integrals give $s_n^{(2)} = -\frac{(k_0 R)^2}{4(n^2-1)}$, regardlessly of the value of $\tilde{C} \neq 0$. Corrections to $\epsilon_n^{(0)}$ are expressed through $s^{(2)}$ linearly:

$$\epsilon_n^{(2)} = \frac{\partial\epsilon}{\partial s_n^{(0)}}s_n^{(2)} = (s_n^{(0)})^2 s_n^{(2)} = \frac{1}{4}s_n^{(2)}. \tag{2.96}$$

Perturbed resonant permittivities are thus $\epsilon_n = -1 - (k_0 R)^2/(n^2 - 1) + O(k_0 R)^3$, in agreement with the exact result (2.87).

2.6 Application of the theory: extraordinary transmission through sub-wavelength hole arrays in SiC membranes

In this Section, it is shown that perforated SiC membranes can be used for engineering optical properties of metamaterials in the infrared. The complex-valued frequency-dependent effective dielectric permittivity $\epsilon_{\text{eff}}(\omega)$ of a single membrane can be controlled by the size and spacing between the holes. Regions of the anomalous dispersion and strong absorption described by $\epsilon_{\text{eff}}(\omega)$ have been identified and related to the excitation of even-parity surface phonon polaritons of a smooth SiC film. The effective permittivity description has been validated by comparing transmittance and absorbance of the film obtained from $\epsilon_{\text{eff}}(\omega)$ with that calculated using first principles electromagnetic simulations. Theoretical predictions of the enhanced transmission and absorption in the perforated film have been verified experimentally using FTIR micro-spectroscopy. For the first time, the dependance of enhanced transmission and absorption on the incidence plane of the incoming radiation has been studied.

A sub-wavelength hole in a metallic screen is one of the simplest objects in nano-optics. The calculation of light transmission through a single hole in a thin, perfectly conducting screen was one of the first analytically solved problems in sub-wavelength optics. Bethe's famous result [Bet44] indicated that the transmission coefficient through a sub-λ hole is extremely low: it rapidly decays with the hole diameter D as $(D/\lambda)^6$, where λ is the wavelength of light. This low transmission considerably diminished the perceived utility of a nano-hole as a nano-photonic device. However, a real metallic screen is neither perfectly conducting nor infinitely thin. Nor must the nanoholes be isolated: they can form periodic or quasi-periodic arrays. A new surge of interest in nanoholes followed the remarkable discovery by Ebbesen and collaborators [ELG$^+$98] of extraordinary optical transmission (EOT) through sub-λ periodic hole arrays. The original experiments were done using optically thick substrates for which the extraordinary transmission is most dramatic: no light is transmitted through the films in the absence of holes but, contrary to Bethe's prediction, a rather significant transmission was observed when the sub-wavelength hole array was present. A number of analytic tools based on EOT are already under

development [GE07], including refractive index sensors [TPF06], infrared absorption spectroscopy [CWR$^+$06] sensors, and multispectral biosensors [SMM$^+$06].

The enhanced transmission was attributed to resonant excitation of surface plasmons. The role of surface plasmons in the enhanced transmission was questioned in a number of consequent publications [CL02, LT04] and still remains a subject of some controversy. The main reason for this controversy is that several complicated phenomena are playing out in EOT experiments. In addition to surface plasmons, more conventional diffractive and interference phenomena such as waveguide resonances [MMGVL$^+$01, CL02], Wood's anomalies, and quasi-bound modes [dAGMS05] were shown to contribute to (or in some instances be the sole cause of) the extraordinary transmission. For example, extraordinary transmission has been observed at THz and even microwave frequencies for which surface plasmons do not exist [RSBK03, LHS04]. It was later theoretically demonstrated [PMMGV04] that holes and other perforations in a thick perfectly conducting metal (which do not support the "true" surface plasmons) can support the so-called "spoof plasmons." In an optical experiment similar to the original EOT work, all these effects (surface plasmons, "spoof plasmons," Wood's anomalies, waveguide resonances) occur at the same time because the EOT wavelength is very close to the Wood's anomaly: $\lambda \approx \sqrt{\epsilon_d} L$, where L is the array's periodicity and ϵ_d is the dielectric permittivity of the substrate that supports the metal film.

In this Section, we describe a series of experiments (supported by theoretical calculations and first-principles electromagnetic simulations) enabling us to clearly separate EOT due to diffractive effects from the EOT due to the excitation of surface polaritons (SPs). Here, the general term *polariton* refers to either plasmon polaritons or phonon polaritons. First, the perforated films are optically thin, ruling out "spoof polaritons." Second, all measurements are carried out in the mid-infrared part of the spectrum, with the films made of silicon carbide (SiC). SiC is a low-loss polaritonic material that has a negative dielectric permittivity $\epsilon(\omega)$ for a range of frequencies referred to as the *reststrahlen* band. Therefore, the surface polaritons responsible for mid-IR EOT are the surface phonon polaritons (SPPs). Because SiC films are thin ($\lambda_{\mathrm{skin}} \equiv \lambda/4\pi\sqrt{|\epsilon|} > H$), the SPPs responsible for EOT are double-sided polaritons, i.e., they exist on both SiC–vacuum interfaces. Third, the high-index substrate is eliminated by using air-bridged (suspended) SiC membranes, thereby ensuring that EOT is observed far from the grazing-angle

(Wood's) anomalies at the substrate-film interface. This enables us to observe EOT in the sub-wavelength regime ($D \ll \lambda$ and $L < \lambda$) where only SPPs and not diffractive effects can be responsible for EOT.

Using polarized FTIR micro-spectroscopy and detecting both transmitted and reflected radiation, we demonstrate, in adjacent frequency ranges, extraordinary optical transmission and absorption of the incident radiation. Our theoretical calculations and numerical simulations show that both phenomena are caused by the excitation of quasi-electrostatic SPPs. It is shown that a perforated film can be described as a *metamaterial* with the effective permittivity $\epsilon_{\text{eff}} = \epsilon_r + i\epsilon_i$ strongly modified by the excitation of SPPs. Armed with ϵ_{eff}, transmission and reflection coefficients T and R can be determined using Fresnel formulas for a dielectric slab. Regions of the enhanced transmission and absorption are related, respectively, to the lowering of $|\epsilon_r|$ and increase of ϵ_i.

We show that SPPs supported by the perforated film give rise to the poles of the ϵ_{eff} which becomes substantially different from $\epsilon(\omega)$ of the smooth SiC film in the vicinity of SPP resonances. The effective permittivity description is enabled by the sub-wavelength nature of the perforated membranes. We demonstrate that only the slow surface polaritons (SSPs) whose in-plane electric field is even with respect to the mid-plane of the film contribute to the effective permittivity. The role of SPPs in EOT can be phenomenologically interpreted as Fano [GvEW03, SVV03] resonances. The first-principles explanation of the enhanced transmission and absorption using a quasistatic $\epsilon_{\text{eff}} \equiv \epsilon_{\text{qs}}$ developed in this Chapter removes the phenomenological aspect of the interpretation based on Fano resonances. In addition, we theoretically show that two types of SPPs are supported by the hole arrays in a polaritonic membrane: localized surface polaritons (LSPs) and delocalized SSPs. The LSPs are shown to exist inside the frequency band corresponding to $-1 < \epsilon(\omega) < 0$, where they cannot decay into propagating SPPs.

2.6.1 Effective optical constants of hole arrays in the quasistatic approximation

In this Section we apply theoretical techniques introduced in Section 2.2 to a simple three-dimensional metamaterial: a square array of circular holes in a thin film. Our approach relies on the quasistatic approximation which assumes that a

patterned metamaterial (such as, in our case, SiC film perforated by a hole array) can be described by a quasistatic dielectric permittivity $\epsilon_{\text{qs}}(\omega)$ obtained by solving an electrostatic problem [BS92, SFB01, SU04a] of the material's response to an imposed electric field $\vec{E}_0(\vec{r}, t) = \vec{E}_0 e^{-i\omega t}$. To characterize this system, we use a combination of the frequency scan (Section 2.2.1) and eigenmode expansion (Section 2.2.2) techniques, as described below. The method plasmon resonance has been successfully applied in the past to periodic sub-λ crystals consisting of interpenetrating positive-ϵ dielectrics [BD92], or non-connected polaritonic inclusions [SU04a]. To our knowledge, this is the first application of this method to the system with *continuous polaritonic* (negative-permittivity) phase, which supports *delocalized surface phonon-polaritons*. These delocalized surface polaritons are responsible for the extraordinary optical transmission observed in experiments conducted by Korobkin et al. [UKI+07, KUI+07, KUI+06], as will become obvious from discussions in subsections 2.6.2-2.6.3.

Owing to the periodicity and symmetry of the perforated membrane, it is sufficient to solve electrostatic Eq. (2.1) inside the unit cell. Because we are mostly concerned with the small incidence angle transmission, only the in-plane component of the permittivity tensor will be of interest. Therefore, $\vec{E}_0 = E_0 \vec{e}_x$, where the film is parallel to the x-y plane, will be assumed.

Since our structure has three orthogonal planes of symmetry ($x = 0$, $y = 0$ and $z = 0$), the dielectric tensor is diagonal. Moreover, $\epsilon_{\text{qs}}^{xx} \equiv \epsilon_{\text{qs}}^{yy}$, because z is the 4-fold axis of symmetry:

$$\epsilon_{\text{qs}}^{xx} = \epsilon_{\text{qs}}^{yy} \equiv \epsilon_{\text{qs}}(\omega) = 1 - \frac{f_0}{s(\omega)} - \sum_{n>0} \frac{f_n}{s(\omega) - s_n}, \qquad (2.97)$$

where $f_n = |(\phi_n, x)|^2 / [V(\phi_n, \phi_n)]$ $(n > 0)$ is the electric dipole strengths of the nth resonance, and $f_0 = V_p/V - \sum_{n>0} f_n$.

Note that in the limit of the smooth film $f_0 = 1$, $f_n = 0$ for $n > 0$, and $\epsilon_{\text{qs}}(\omega) \equiv \epsilon(\omega)$. While the oscillator strengths f_n $(n > 0)$ can be computed numerically from their corresponding eigenfunctions ϕ_n, calculating f_0 requires a detailed knowledge of all f_n's (or ϕ_n's).

An alternative method of calculating f_0 and f_n's is to directly solve Eq. (2.1) assuming a uniform electric field $\vec{E}_0$, and then to substitute the solution $\phi(\vec{r})$ into Eqs. (2.4) or (2.2) defining $\hat{\epsilon}_{\text{qs}}$. We used the commercial finite-element solver COM-
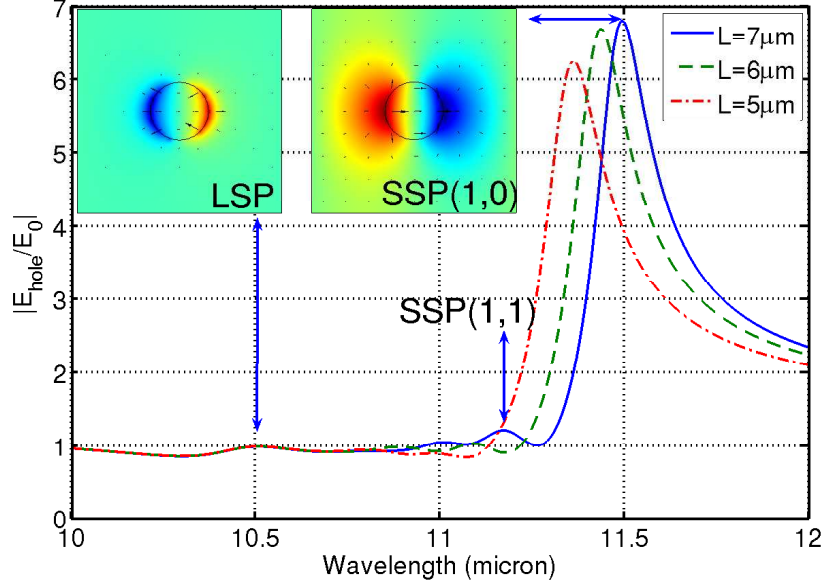
Figure 2.5: Volume-averaged electric field enhancement inside a hole in a SiC film. Sample: $H = 458$ nm SiC film perforated with a $L = 7$ μm square array of $D = 2$ μm round holes (blue solid line). Insets: ES potential profile at the resonances: (left) LSP resonance, and (right) SSP(1, 0) resonance. Green dashed line: $L = 6$ μm, red dash-dotted line: $L = 5$ μm.
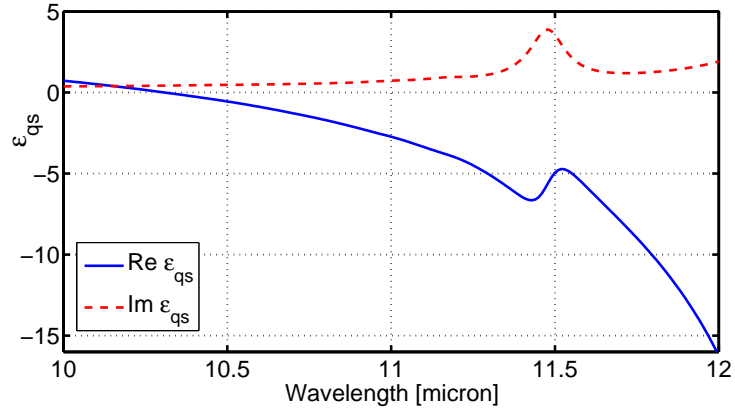
Figure 2.6: Effective quasistatic permittivity of a perforated SiC film (electrostatic FEM simulation). Sample: $H = 458$ nm SiC film perforated with a $L = 7$ μm square array of $D = 2$ μm round holes.

SOL to calculate the quasistatic response of a perforated films for experimentally relevant parameters. Because the most dramatic results were obtained for the samples with thickness $H = 458$ nm, period $L = 7$ μm, and hole diameter $D = 2$ μm, all theoretical calculations (except the ones shown in Figs. 2.5 and 2.9 where the period and hole diameter varied) were done for these specific dimensions of the hole array. Also, the following expression for the dielectric permittivity of a doped (with a finite conductivity σ) SiC film has been used:

$$\epsilon_{\text{SiC}}(\omega) = \epsilon_\infty \frac{\omega^2 - \omega_{LO}^2 + i\Gamma\omega}{\omega^2 - \omega_{TO}^2 + i\Gamma\omega} + \frac{i\sigma}{\omega}, \qquad (2.98)$$

where $\omega_{LO} = 972$ cm^{-1} ($\lambda_{LO} = 10.288$ μm), $\omega_{TO} = 796$ cm^{-1} ($\lambda_{TO} = 12.563$ μm), $\Gamma = 5.25$ cm^{-1}, $\sigma = 346.2$ cm^{-1}, and $\epsilon_\infty = 4.71$ were found to give the best fit to the experimental transmission data for the unperforated membrane.

Real and imaginary parts of $\epsilon_{\text{qs}}(\omega)$ are plotted in Fig. 2.6. The strongest electrostatic resonance can be clearly identified as the maximum of Im $[\epsilon_{\text{qs}}(\omega)]$. The extracted $\epsilon_{\text{qs}}(\omega)$ can be fitted to Eq. (2.97) to determine the dipole oscillator strengths f_0 and f_n as well as their spectral positions ω_n corresponding to $s(\omega_n) = s_n$. The following values of the electrostatic eigenvalues s_n and electric dipole strengths f_n of the dominant dipole resonances were found to be: $s_0 = 0$ ($\epsilon_0 = -\infty$) with $f_0 \approx 0.88$, $s_1 \approx 0.1241$ ($\epsilon_1 \approx -7.058$) with $f_1 \approx 0.041$ (the strongest resonance), $s_2 \approx 0.1958$ ($\epsilon_2 \approx -4.107$) with $f_2 \approx 0.0054$, $s_3 \approx 0.255$ ($\epsilon_3 \approx -2.922$) with $f_3 \approx 0.0036$, and $s_4 \approx 0.666$ ($\epsilon_4 \approx -0.50$) with $f_4 \approx 0.0049$.

To better identify different contributing resonances of the structure, we have calculated electric field E_{hole} (averaged over the volume of a hole) in response to ac electric field E_0, as a function of frequency. The ratio of E_{hole}/E_0 is plotted in Fig. 2.5 for a fixed hole diameter $D = 2$ μm and variable period L. Four enhancement spikes corresponding to resonances of $\epsilon_{\text{qs}}(\omega)$ can be identified for all periods. By comparing Figs. 2.5 and 2.6 we note that some of the resonances that manifest in the field enhancement pictures (second and third from the right in Fig. 2.5) barely contribute to the effective dielectric permittivity ϵ_{qs}. That is due to several factors, for example, high localization of the enhanced fields or cancelation between the fields in different parts of the structure, or even the enhancement of the *orthogonal* component of the electric field. These effects can be appreciated from the potential plots for different resonances in Fig. 2.8. More detailed discussion of the electrostatic
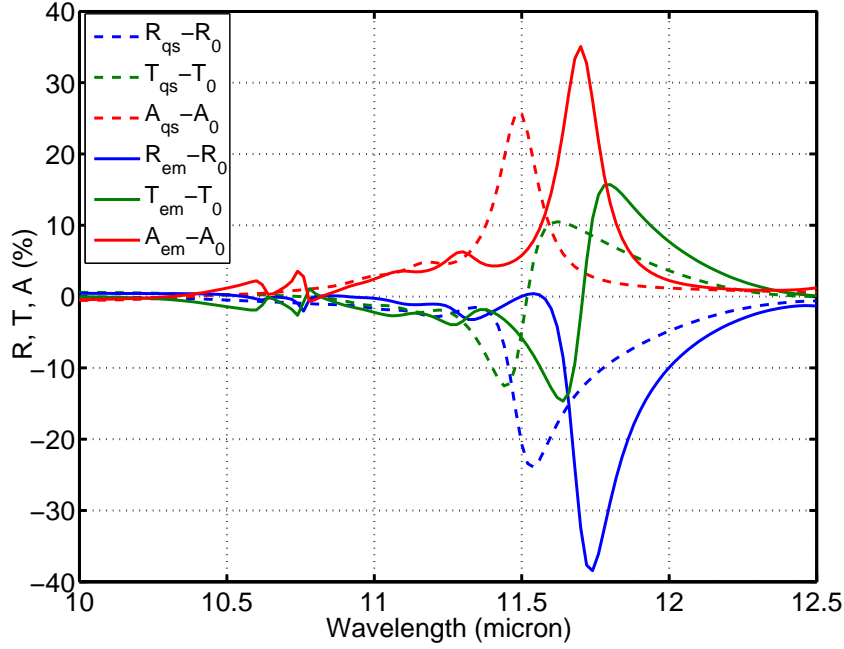
Figure 2.7: Theory: reflectance (R, blue lines), transmittance (T, green lines) and absorbance (A, red lines) of a perforated SiC film, relative to the same quantities of a smooth film. Solid lines: first-principles FEFD simulation of EM wave scattering; dashed lines: theoretical estimate based on ϵ_{qs} (see Fig. 2.6).

resonances is found in Sec. 2.6.2.

Once the effective permittivity $\epsilon_{qs}(\omega)$ is known, one can estimate the transmission (T) and reflection (R) coefficients of the sub-wavelength array using well-known formulas for a homogeneous slab. At normal incidence, these formulas read:

$$T = \left| \frac{(1 - r_1^2)e^{ik_0(n-1)H}}{1 - r_1^2 e^{2ik_0 nH}} \right|^2, \quad R = \left| \frac{r_1(1 - e^{2ik_0 nH})}{1 - r_1^2 e^{2ik_0 nH}} \right|^2, \tag{2.99}$$

where $n = \sqrt{\epsilon_{qs}}$, $k_0 = \omega/c$ and $r_1 = (1 - n)/(1 + n)$.

We have calculated transmittance T and absorbance $A = 1 - R - T$ of the perforated film, subtracted the corresponding quantities for the non-perforated film (ϵ_{qs} replaced by ϵ_{SiC}), and plotted the corresponding differential quantities in Fig. 2.7. The absorption spike (red dashed line) is caused by the peak of $Im[\epsilon_{qs}]$ at

$\lambda = \lambda_1 \approx 11.45$ μm in quasistatic approximation, and corresponds to the resonant frequency. The transmission maximum occurs because of the decrease of the absolute value $|\text{Re}[\epsilon_{qs}]|$ (with the rise of $\text{Re}[\epsilon_{qs}] < 0$) at $\lambda = \lambda_{max} \approx 11.6$ μm, as seen in Fig. 2.6. In agreement with Lorentz theory of resonant response, this rise of $\text{Re}[\epsilon_{qs}] < 0$ takes place below the resonance frequency. Enhanced transmission predicted from ϵ_{qs} thus occurs for $\lambda_{max} > \lambda_1$ — slightly red-shifted from enhanced absorption band. Because spacing between the holes ($L = 7$ μm) is nearly comparable with the wavelength ($\lambda \sim 11$ μm), the quasistatic ϵ_{qs} is only an approximate description of the perforated film. Therefore, fully electromagnetic (EM) calculations of T and A were executed using the finite-element frequency domain (FEFD) solver COMSOL. The results displayed in Fig. 2.7 (solid lines) show qualitative agreement with the ϵ_{eff}-based calculation, with the exception that all transmission and absorption maxima are slightly red shifted. This red shift is a previously noted [MFZ05] effect explained by the EM corrections to the purely ES response of sub-λ polaritonic structures.

To summarize the theoretical results presented in Fig. 2.7, we have found that extraordinary transmission through optically thin perforated SiC membranes can be explained using the concept of the effective dielectric permittivity of the sub-wavelength metamaterial. As Fig. 2.6 indicates, sub-λ holes introduce a significant (and disproportionate to their overall surface area of under 6%) correction to the dielectric permittivity of the smooth film creating strong resonant features in $\epsilon_{qs}(\omega)$. The strongest modification occurs in the imaginary part of ϵ_{qs}. The physical origin of this modification is the excitation of electrostatic (or quasi-electrostatic when $L/\lambda \sim 1$) resonances. The prominent reduction of the absolute value $|\text{Re}[\epsilon_{qs}]|$ due to the excitation of the strongest resonance results in the prediction of an additional transmittance of 15% — more than twice the geometric area of the holes. Even more dramatically, absorbance is predicted to increase by 35% (from less than 1%). These theoretical predictions are fully confirmed by our experiments as detailed in Sec. 2.6.3. Below we investigate the nature of quasi-electrostatic resonances that have been shown above to shape the transmission and absorption properties of sub-λ hole arrays in SiC films and relate them to the better known SPPs supported by smooth films.

2.6.2 Connection of resonances of a perforated film to surface polaritons of a smooth film

Surface polaritons have been suspected of playing an important role in EOT ever since its discovery [ELG$^+$98]. Polarization and dispersion properties of SPs responsible for transmission resonances have been subsequently explored experimentally [BMD$^+$04, AvEW03, TPF06] and theoretically [GvEW03, SVV03] for thick films, and their connection to the SPs of smooth (unperforated) films has been noted. The connection is made by wavenumber matching: resonances of a perforated film with period L are commonly related to SPs of a smooth film with the in-plane wavenumbers $k_{(m,n)} = \left| \frac{2\pi}{L}(m\hat{x} + n\hat{y}) \right| \equiv \frac{2\pi}{L}\sqrt{m^2 + n^2}$, where m and n are integers. Resonant effects such as enhanced transmission and absorption [BMD$^+$04] are expected to occur at frequencies close to those of the smooth film surface polaritons $\omega_{SP}(k_{(m,n)})$. For optically thick films, the k-dependent SP frequency is given by an implicit formula: $ck\sqrt{1 + \epsilon^{-1}(\omega_{SP})}$; a slightly more complicated formula for the frequency of *slow surface polaritons* must be used for thin films. The in-plane component of the electric field of the SSP is even with respect to the mid-plane of the film. In the electrostatic limit ($L \ll \lambda$), $\omega_{SP}(k)$ is given implicitly by $\epsilon(\omega_{SP}(k)) = -\tanh^{-1}(kH/2)$.

When the size of the holes becomes of the same order as the period, resonance frequencies are likely to get significantly shifted from their smooth-film values of $\omega_{SP}(k_{(m,n)})$. This frequency shift has been noted in a number of experiments [GTG$^+$98, SGZdF01, GvEW03] and attributed to scattering of SPs into light. We find that in the sub-wavelength (quasi-electrostatic) regime there is another reason for the red shifting of the EOT maximum: the electrostatic resonances are hole-size dependent, explained in detail below. First, we have solved the GEDE equation to obtain several electrostatic resonances, shown in Fig. 2.8. The lowest frequency SSPs can be identified as modified by the presence of a large-hole SSP(1,0) and SSP(1,1). Qualitatively, this identification can be made by the visual inspection of Figs. 2.8(a,b), where the electrostatic potential and electric field in the mid-plane of the perforated film are shown.

To make this identification more quantitative, we have decomposed the electrostatic potential into 2D sin / cos Fourier series. The strongest ES resonance, shown in Fig. 2.8(a), is dominated by the Fourier component $\sin(kx)$, where
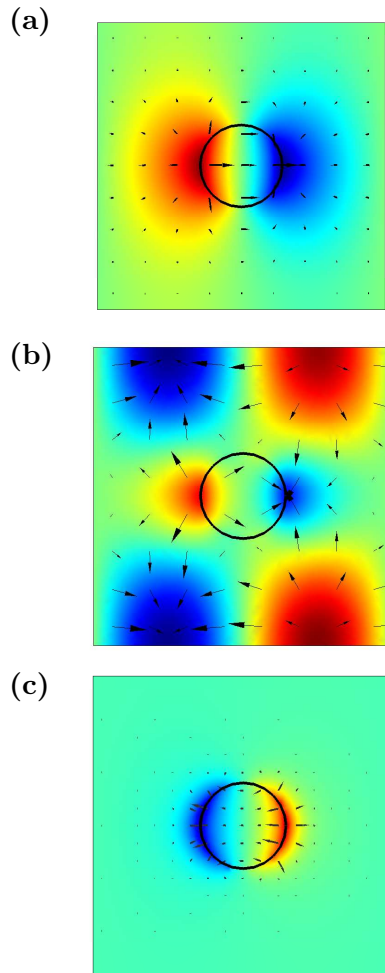
Figure 2.8: Electrostatic potential and electric field profiles in the mid-plane of qua-sistatic dipolar eigenmodes of a perforated film (same as in Fig. 2.6). (a) Delocalized resonance corresponding to SSP(1,0); (b) SSP(1,1); (c) single-hole resonance (LSP).

$k = 2\pi/L$, thus justifying its identification with the SSP(1,0) of the smooth film. The second strongest resonance, shown in Fig. 2.8(b), has a dominant Fourier component $\sin(kx)\cos(ky)$ corresponding to the SSP(1,1), although it is appreciably hybridized with higher order SSPs. The third strongest resonance, visible in Fig. 2.5 (not shown in Fig. 2.8), is a mixture of several Fourier components $\sin(mkx)\cos(nky)$ with $m = 1, 2$ and $n = 0, 1, 2$. Mixing between different smooth film polaritons is thus more prominent for shorter-wavelength modes. It appears that surface polaritons with the wavelength comparable to or less than the hole diameter D are more strongly hybridized due to the presence of the holes. The ES resonances of the perforated film—originating from SSPs of the smooth film—occupy a significant volume of the film, and, more importantly, their frequency is clearly period-dependent (see Fig. 2.5); therefore, we refer to these ES resonances as delocalized SSPs. Frequencies of all delocalized resonances (field enhancements due to the three strongest are shown in Fig. 2.5) are located in the spectral region where $\text{Re}[\epsilon_{\text{SiC}}] < -1$. This is expected because this spectral interval corresponds to *propagating* slow surface polaritons.

We have investigated frequency dependence of delocalized resonances on the hole diameter D. Resonance positions corresponding to $D = 0$ (smooth film) were obtained by interpolation. Noting that $\text{Re}\,[\epsilon]$ is a monotonic function of the frequency ω and using $\text{Re}\,[\epsilon(\omega)]$ as a frequency label, we have used GEDE to compute the spectral positions of the electrostatic delocalized resonances (green dashed lines in Fig. 2.9) SSP(1,0) and SSP(1,1). A significant red shifting of the strongest electrostatic SSP(1,0) resonance is observed: $\Delta\epsilon^{(ES)} \approx -2$ as the hole diameter increases from $D = 0$ (smooth film) to $D = 2\ \mu$m (perforated film). From the first-principles FEFD simulations we have also calculated the values of $\text{Re}\,[\epsilon]$ as a function of the hole diameter for which an absorption peak is observed (blue solid curve). Even for the smooth film, electromagnetic resonances are red shifted with respect to their electrostatic counterparts because the array period $L = 7\ \mu$m is comparable to the wavelength, and the electrostatic calculation is only approximately valid. The red shift between the electrostatic and electromagnetic resonances increases as holes get larger, partly due to quasistatic retardation effects quantified in Sec. 2.5 and, in part, due to radiation from the holes [SGZdF01, GvEW03] (in Sec. 2.5 there was no radiation, because the structures were assumed periodic or uniform in all directions). According to the FEFD simulations, for $D = 2\ \mu$m holes the amount of
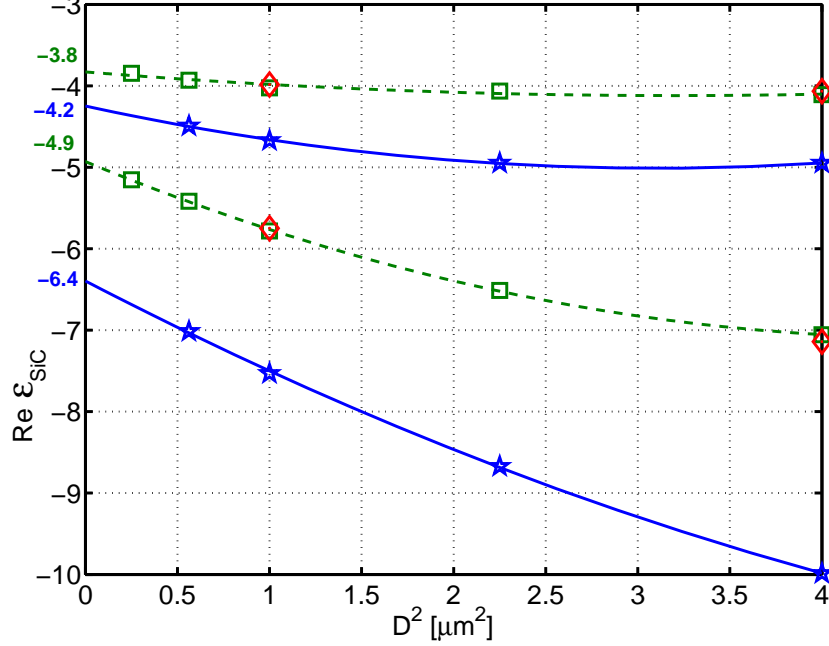
Figure 2.9: Position of delocalized resonances $SSP(1,0)$ and $SSP(1,1)$ as a function of hole diameter D. Squares – position of absorption lines in quasistatic 3D simulations (interpolated with dashed curves), diamonds – electrostatic GEDE simulations; stars – absorption lines in EM FEFD simulations (interpolated with solid curves). Extrapolation to $D = 0$ is also shown.

red shift of the SSP(0,1) resonance from its smooth film values is $\Delta\epsilon^{(EM)} \approx -3.6$. Comparing $\Delta\epsilon^{(EM)}$ to $\Delta\epsilon^{(ES)}$, we conclude that only about one half of the red shift of the absorption peak from the position of the smooth film $SSP(1,0)$ resonance can be attributed to retardation effects. The second half is a purely electrostatic effect that occurs due to hybridization of the electrostatic SSP resonances in the presence of a large hole.

No identification with one of the smooth film SSPs can be made for the LSP resonance at $\lambda = 10.5~\mu$m shown in Fig. 2.5. In fact, this surface wave resonance, highly localized near the hole perimeter, can be thought of as an even-parity "defect state" created by the presence of a single hole in a negative-ϵ film. Because the frequency range for which $-1 < \epsilon(\omega) < 0$ is a stop-band for even-parity propagating SPs, the even-parity LSP can exist in this frequency range alone. Because of the

localized nature of the LSP, its frequency is insensitive to the proximity of other holes (i.e., to the period L) but is sensitive to the aspect ratio of the hole and even to the radius of curvature of hole edge. As may be seen in Fig. 2.5, frequencies of the three red resonances ($\lambda > 10.6$ μm) are located in the $\text{Re}[\epsilon_{\text{SiC}}] < -1$ band and are all dependent on L. On the contrary, the blue resonance ($\lambda_{\text{loc}} \approx 10.5$ μm) belongs to the $-1 < \text{Re}[\epsilon_{\text{SiC}}] < 0$ range and is period-independent. Another striking difference between the red and blue resonances is that the former are very delocalized, while the latter is strongly localized near the hole (see the two insets to Fig. 2.5).

To summarize, we have theoretically explained transmission and absorption anomalies of sub-wavelength hole arrays by introducing the effective permittivity of a perforated membrane with a complex frequency dependence caused by resonant coupling to surface phonon polaritons. Two types of phonon polariton resonances are theoretically uncovered: (i) delocalized modes related to slow surface polaritons (SSPs) of a smooth film, and (ii) a localized surface polariton (LSP) of a single hole in the spectral range complementary to that of SSPs. We have also discussed the red shift of the transmission/absorption maximum through a perforated film with large holes from the position corresponding to the frequency of a smooth film SSP. This diameter-dependent shift comes from the combination of two factors: (a) a purely electrostatic effect of the resonant frequency shift of a perforated film, and (b) a purely electromagnetic effect of radiation through a finite-diameter hole combined with SSP retardation in a finite-size unit cell. The relative importance of (b) increases with the hole diameter.

2.6.3 Experimental verification of the theory: spectroscopy of perforated SiC membranes

In this Section experimental measurements of the EOT and enhanced optical absorption (EOA) in sub-wavelength array of holes drilled in air-bridged (suspended) SiC films is described. All experiments are done in the mid-infrared frequency range (7 μm $< \lambda < 16$ μm) which encompasses the *reststrahlen* band of SiC inside which $\epsilon < 0$. The FTIR micro-spectroscope used in this study collects all transmitted and reflected light, enabling us to separately compute scattered and absorbed fractions of the incident light in a manner similar to an earlier study [BMD+04] of a hole array in a metal screen. The high accuracy of our measurements and the utilization

of an infrared polarizer enables us to separate the peaks of EOT and EOA for both s and p polarizations. Moreover, by rotating the stage on which the perforated film is positioned, the incidence plane of the beam with respect to the rows of the array could be changed for each polarization. This additional flexibility enables us, for the first time, to experimentally demonstrate a high (up to a factor of two) anisotropy with respect to different orientations of the incidence plane. Even for the appreciably sub-λ arrays ($L = 7$ μm, $\lambda \approx 12$ μm) used in this study, this high anisotropy is observed for fairly small ($\approx 20°$) incidence angles. Depending on the incidence plane orientation, absorption spectra are shown to exhibit single- or double-peaked transmission spectra.

Using the dielectric permittivity $\epsilon(\omega)$ of SiC given by Eq. (2.98) with experimentally determined optical constants, we compared theoretical (from the first-principles FEFD simulations) and measured reflection $R(\lambda)$, transmission $T(\lambda)$, and absorption $A(\lambda) = 1 - R - T$ coefficients. The results obtained for an s-polarized incident beam with the incidence plane corresponding to $\varphi = 0°$ (parallel to rows of holes) are plotted in Fig. 2.10 for the 7-μm-period array of 2-μm-diameter holes. Incidence angle $\theta = 22°$ was assumed for numerical simulations. Given finite spread in θ and φ for realistic experimental conditions, the agreement between theory and experiment is good. Both $T(\lambda)$ and $R(\lambda)$ exhibit characteristic kinks at the frequencies corresponding to excitation of SPPs. The shapes of these kinks is reminiscent of Fano resonances. They represent interference between radiation transmitted through the film (continuum state) with the radiation re-emitted by SPPs through the holes (discrete state). In most experiments to date, identification of the continuous and discrete states was elusive [CGC05], mostly because of the close proximity between Wood's anomalies and SPP resonances. In our experiment there is no ambiguity in identifying the dominant continuum state due to optical transparency of the film. Nor is the identification of slow surface polaritons as discrete states ambiguous because they are well separated from Wood's anomalies. In fact, our spectra are taken for the 10.5 μm $< \lambda <$ 12.5 μm *reststrahlen* frequency band of SiC inside which $\epsilon_{SiC} < 0$. Wood's anomalies corresponding to $\lambda \approx L = 7$ μm are clearly outside of the spectral range of our experiments.

Experimental results shown in Fig. 2.10 (solid lines) demonstrate that transmission peaks correlate with the absorption peaks (as has been previously noted [BMD$^+$04]) because both are related to the excitation of SPPs. In full

agreement with FEFD simulation results shown in Fig. 2.10 (dashed lines) and theory presented above, the transmission peak is red shifted from the absorption peak. To our knowledge, this is the first experimental observation of this frequency shift.
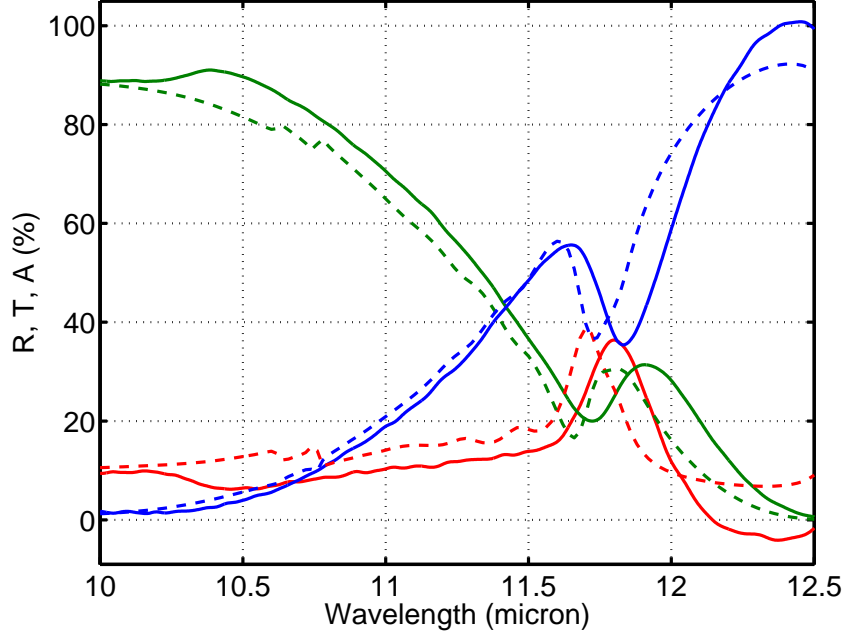
Figure 2.10: Reflection, transmission, and absorption spectra in blue, green, and red, respectively, for the 7-μm-period array of 2-μm-diameter holes under s-polarized light and with $\varphi = 0$ sample orientation. The experimental FTIR results (solid, courtesy D. Korobkin and B. Neuner III) are in agreement with simulation results (dashed).

While most hole array studies involve *optically thick* (several times thicker than the skin depth) films, our *optically thin* samples allow non-vanishing transmission without any perforations. Although it was generally believed that optical thinness allows for transmission significant enough to deem holes unnecessary [GE07], Fig. 2.10 demonstrated that holes modify transmission spectra to such an extent that optical thinness is not a detriment. This modification occurs in a specific spectral range where surface polaritons are excited. To quantify the role of the holes, spectra of smooth SiC membranes located next to the perforation windows were measured and subtracted from the corresponding hole array spectra.
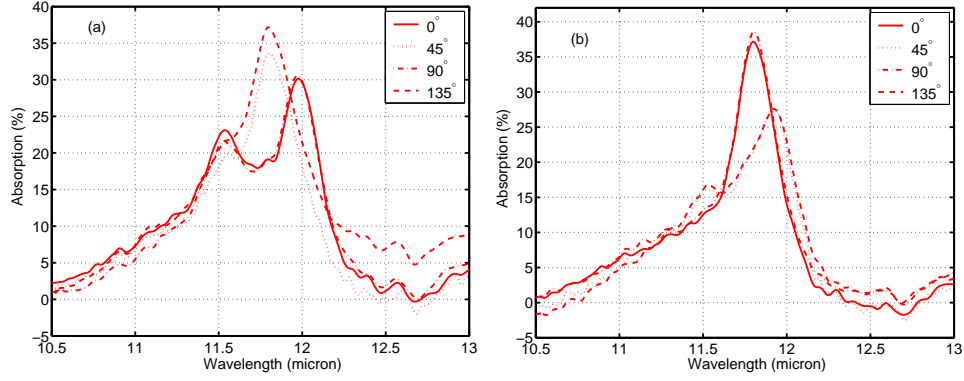
Figure 2.11: Absorption spectra for the 7-μm-period array of 2-μm-diameter holes under (a) p-polarized radiation and (b) s-polarized radiation with non-perforated film spectra subtracted. To study angular anisotropy, the sample was rotated in the x-y plane in increments of 45° from 0° to 135°. Data courtesy D. Korobkin and B. Neuner III.

Spectra were taken under various conditions: s- and p-polarized IR radiation was used, and the sample was rotated in the x-y plane in 45° increments from 0° to 135°. The results in Fig. 2.11 and Fig. 2.12 are displayed in a manner to show angular anisotropy at fixed polarizations. It is seen that spectra change considerably when the sample is rotated from a parallel to diagonal orientation. For the p-polarized radiation with the incidence plane parallel to rows or columns ($\varphi = 0°$ or $\varphi = 90°$) both absorption (Fig. 2.11(a)) and transmission (Fig. 2.12(a)) exhibit double-peaked spectra. Qualitatively, this is related to the fact that the radiation, incident at an angle θ, can strongly couple to two SSPs with $k_\pm^{SSP} = 2\pi/L \pm \sin\theta\omega/c$. When the sample is rotated by 45°, the two peaks are too close to each other to be clearly distinguished. An opposite trend is observed in s-polarization as shown in Fig. 2.11(b) and Fig. 2.12(b): for $\phi = 0°, 90°$ there is a single absorption/transmission peak which splits into two when the sample is rotated by 45°. As expected, the $A(\lambda)$ and $T(\lambda)$ spectra are invariant with respect to a 90° rotation as confirmed by all plots within Fig. 2.11 and Fig. 2.12—a reassuring sign that the array holes were precisely placed to form a symmetric, evenly spaced lattice. Through the aforementioned 90° sample symmetry, an absorption or transmission spectrum will alternate between one and two peaks with rotation; this effect could be used in spectral filtering applications and for the identification and alignment of

74
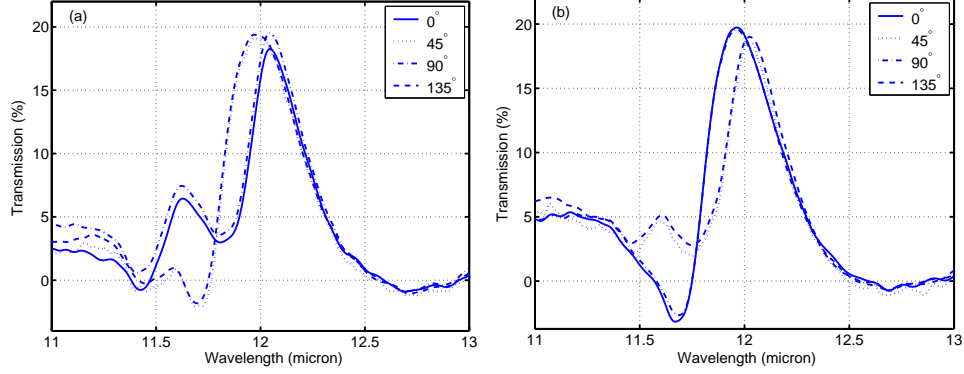
Figure 2.12: Transmission spectra for the 7-μm-period array of 2-μm-diameter holes under (a) p-polarized radiation and (b) s-polarized radiation with non-perforated film spectra subtracted. To study angular anisotropy, the sample was rotated in the x-y plane in increments of 45° from 0° to 135°. Data courtesy D. Korobkin and B. Neuner III.

sample orientation.

Another interesting and potentially useful property of perforated hole arrays is their extraordinary birefringence with respect to light polarization. For a given sample orientation ($\varphi = 0°$ in Fig. 2.13 and $\varphi = 45°$ in Fig. 2.14) transmission and absorption spectra are plotted for s- and p-polarizations and compared with the corresponding numerical simulations. For both sample orientations, we find that a very significant birefringence in transmission of order $|T_s - T_p| \approx 20\%$ can be obtained for the two polarizations. That is significantly higher than the birefringence from the unperforated film (about 5%). Enhanced s/p polarization birefringence can be explained using the qualitative band diagram of SPPs [BMD+04]. Such enhanced birefringence will manifest itself in polarization conversion (e.g., from linear to elliptical) if the incident polarization is a superposition of s and p polarizations. Experimental indications of polarization rotation have already been found in earlier experiments [AvEW03, TPF06], although the connection to s–p polarization birefringence has not been made.

Experimental results shown in Fig. 2.13(a) and Fig. 2.14(a) show a very good qualitative agreement when compared to their simulation counterparts shown in Fig. 2.13(b) and Fig. 2.14(b). For the $\varphi = 0°$ sample orientation, s-polarized light results in a strong single absorption/transmission peak, splitting to twin peaks
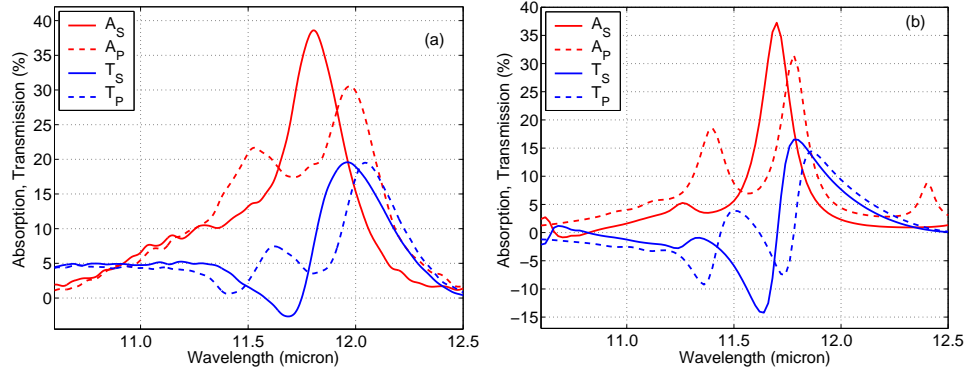
Figure 2.13: Absorption and transmission spectra from (a) experiments and (b) simulations for s and p polarization at $0°$ sample orientation with non-perforated film spectra subtracted. Absorption peak splitting, observed when changing from s to p polarization, is clearly seen in (a) and (b) with similar split peak-to-peak magnitude and frequency differences. Electromagnetic simulations (b) clearly agree with measured spectra (a) for both s and p polarizations. Data courtesy D. Korobkin and B. Neuner III.

with p-polarized light, seen in Fig. 2.13. The peak splitting in Fig. 2.13(a) found experimentally is verified by simulations and shown in Fig. 2.13(b) with similar split peak-to-peak magnitude and frequency differences. Peak splitting in p polarization and the lack thereof in s polarization has been noted earlier [BMD$^+$04] for thick metallic films.

We also find a significant s–p polarization birefringence for the $\varphi = 45°$ sample orientation. Although the quantitative agreement between the experimental and theoretical results for the sample orientation of $\varphi = 45°$ shown in Fig. 2.14(a) and (b), respectively, is less impressive than that for the $\varphi = 0°$ sample orientation Fig. 2.13(a) and (b), the qualitative agreement is quite good. Both the primary and much smaller secondary absorption/transmission peaks in both polarizations are seen in experiments and simulations. The primary peaks in A_P and T_P are shifted to frequencies higher than those of A_S and T_S, an experimental result (Fig. 2.14(a)) reproduced through simulation (Fig. 2.14(b)). While the peak magnitude difference between A_P and A_S in Fig. 2.14(a) is not seen in Fig. 2.14(b), the frequency shift of 0.12 μm occurs in both experiments and simulations. Numerical difference between electromagnetic simulations and experimental results can be caused by several reasons: uncertainty in the dielectric function of perforated SiC, significant spread
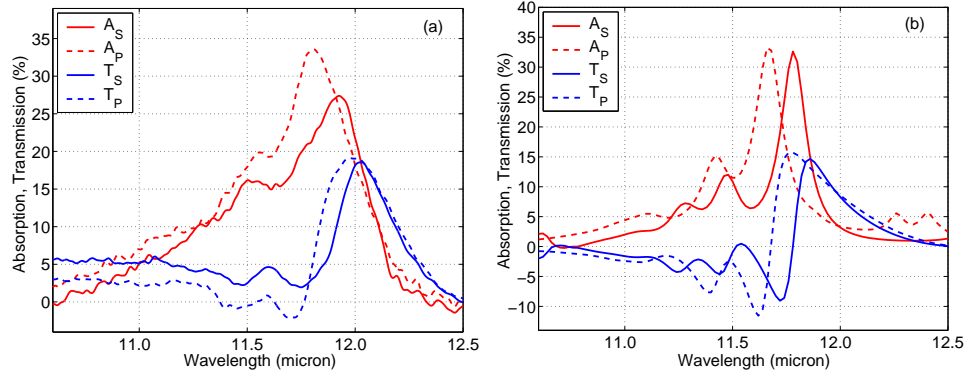
Figure 2.14: Absorption and transmission spectra from (a) experiments and (b) simulations for s and p polarization at $45°$ sample orientation with non-perforated film spectra subtracted. While the main s and p polarization absorption peak magnitudes differ in (a) but not (b), both sets display a similar frequency shift and maintain similar relative shapes. Data courtesy D. Korobkin and B. Neuner III.

in the angles of incidence at the sample, and insufficiently precise decomposition of optical spectra into s and p polarization caused by uncertainties of the beam propagation inside the FTIR device. Future experiments with infrared laser sources will allow us to better control angles of incidence and polarization and improve quantitative agreement with the theory.

In conclusion, we have theoretically and experimentally investigated the phenomenon of enhanced optical transmission (EOT) in mid-infrared through a square array of sub-wavelength round holes milled in an optically thin polaritonic (SiC) membrane. We have theoretically demonstrated and experimentally verified that EOT is accompanied by a slightly blue shifted absorption peak corresponding to enhanced optical absorption (EOA). Both EOT and EOA were shown to be caused by the excitation of quasi-electrostatic resonances of the film that can be traced to even-parity surface phonon polaritons of the smooth film. Enhanced absorption and transmission as high as nearly 40% each have been shown for the arrays in which holes occupied only 6% of the total area. Such high absorbance indicates that perforated SiC films can be used as highly efficient tunable thermal radiation source.

The major differences of our experiments from the earlier EOT experiments are as follows: (a) optically thin *phonon-polaritonic* films (SiC) are used; (b) SiC

films are suspended (air-bridged, i.e., there is no underlying substrate); and (c) the hole array is essentially sub-wavelength (the ratio of the period L and diameter D to wavelength λ are $L/\lambda \approx 0.6$ $D/\lambda \approx 0.2$). This choice of the experimental parameters enabled us, for the first time, to definitively eliminate diffraction and interference effects (Wood's anomalies, "spoof polaritons," waveguide resonances, and quasi-bound modes) as being responsible for EOT/EOA, and to demonstrate that both phenomena are caused by the excitation of surface phonon polaritons. Because of the sub-wavelength nature of the perforated hole array, we have been able to model it as a metamaterial described by the effective (quasistatic) dielectric permittivity obtained using electrostatic simulations. For the first time, we have investigated the dependence of EOT and EOA on both incident wave polarization (s and p) and incidence plane orientation with respect to the rows of the holes. The high degree of anisotropy with respect to the incidence plane orientation has been demonstrated and theoretically explained. Strong polarization dependance can be utilized in polarization converters while strong anisotropy can be used as a diagnostics of the film orientation in sensing applications.

2.7 Appendix: Perturbation theory of the generalized linear eigenvalue problem $Lu = \lambda Ru$

In this Section, we develop general perturbation theory for a generalized linear eigenvalue problem, such as, for example, electrostatic eigenvalue equation 2.1. Only the first order corrections are derived here, to be used in calculations of electromagnetic retardation effects in Chapter 2.

Consider a linear equation of the form

$$(L_0 + V_L)\phi - \lambda(R_0 + V_R)\phi = f, \tag{2.100}$$

where λ is a parameter, f is external drive (independent of ϕ), and V_L, V_R are small perturbations of operators L_0 and R_0, respectively. All these operators are integro-differential operators defined on a certain domain D. The functions ϕ belong to a certain linear space $\Sigma(D)$, which characterizes the physical boundary conditions imposed upon ϕ. Assuming that perturbations V_L, V_R are of the same order and proportional to the same small parameter, conventional perturbation theory

in this parameter can be developed, under the following circumstances. Suppose that solutions of the unperturbed eigenvalue problem $L_0\phi = \lambda R_0\phi$ comprise a full and *orthogonal* basis in $\Sigma(D)$, denoted $\{\phi_n^{(0)}\}$, such that $L_0\phi_n^{(0)} = \lambda_n^{(0)} R_0\phi_n^{(0)}$ and $\int_D \phi_m^{(0)} R_0\phi_n^{(0)} dV = \delta_{mn}\int_D \phi_n^{(0)} R_0\phi_n^{(0)} dV$. In that case, it is possible to determine the solutions of the driven problem solely from knowledge of these unperturbed eigenfunctions $\{\phi_n^{(0)}\}$.

Let us begin with the non-driven case, $(L_0 + V_L)\phi = \lambda(R_0 + V_R)\phi$. Perturbed eigenfunctions are expanded in the basis $\{\phi_n^{(0)}\}$:

$$\phi_n = \sum_m (\delta_{nm} + \alpha_{nm})\phi_m^{(0)}, \tag{2.101}$$

where α_{nm} are of the same order as V_L and V_R. For our purpose, we need only corrections linear in V_L and V_R. The eigenvalue λ_n is expanded similarly: $\lambda_n = \lambda_n^{(0)} + \lambda_n^{(1)} + O(V_L^2)$. Omitting simple algebra, we give only the final result. First-order correction to the eigenvalue is given by

$$\lambda_n^{(1)} = \frac{\int_D \phi_n^{(0)}(V_L - \lambda_n^{(0)} V_R)\phi_n^{(0)} dV}{\int_D \phi_n^{(0)} R_0\phi_n^{(0)} dV}, \tag{2.102}$$

and first-order corrections to the eigenfunctions are given by

$$\phi_n^{(1)}(r) = \sum_{m\neq n} \frac{\phi_m^{(0)}(r)}{\lambda_n^{(0)} - \lambda_m^{(0)}} \frac{\int_D \phi_m^{(0)}(V_L - \lambda_n^{(0)} V_R)\phi_n^{(0)} dV}{\int_D \phi_m^{(0)} R_0\phi_m^{(0)} dV}. \tag{2.103}$$

These expressions are derived under implicit assumption that the unperturbed spectrum $\lambda_n^{(0)}$ contains no degenerate eigenvalues. They are valid even when degenerate eigenvalues are present, as long as perturbations V_L, V_R do not mix eigenfunctions belonging to the same eigenvalue. In that case, indefinite ratios $\frac{\int_D \phi_m^{(0)}(V_L - \lambda_n^{(0)} V_R)\phi_n^{(0)} dV}{\lambda_n^{(0)} - \lambda_m^{(0)}} = 0/0$ should be omitted from summation. Fortunately, electromagnetic perturbations to electrostatic equations possess the full symmetry of the electrostatic problem, which is stored in the function $\epsilon(r)$. Consequently, they do not induce coupling between eigenmodes that are degenerate because of the geometric symmetry of $\epsilon(r)$.

The solution to the driven problem is also expanded in the basis $\{\phi_n^{(0)}\}$:

$$\phi = \sum c_n \phi_n^{(0)}, \tag{2.104}$$

where $c_n = c_n^{(0)} + c_n^{(1)} + O(V_L^2)$. After some simple algebra we get

$$c_n^{(0)} = \frac{\int_D \phi_n^{(0)} f dV}{(\lambda_n^{(0)} - \lambda) \int_D \phi_n^{(0)} R_0 \phi_n^{(0)} dV}, \tag{2.105}$$

and

$$c_n^{(1)} = -c_n^{(0)} \frac{\int_D \phi_n^{(0)} (V_L - \lambda_n^{(0)} V_R) \phi_n^{(0)} dV}{(\lambda_n^{(0)} - \lambda) \int_D \phi_n^{(0)} R_0 \phi_n^{(0)} dV}. \tag{2.106}$$

Up to the first order in perturbation, we thus obtain

$$c_n \approx c_n^{(0)} + c_n^{(1)} = \frac{\int_D \phi_n^{(0)} f dV}{(\lambda_n^{(0)} - \lambda) \int_D \phi_n^{(0)} R_0 \phi_n^{(0)} dV} \left(1 - \frac{\lambda_n^{(1)}}{\lambda_n^{(0)} - \lambda} \right). \tag{2.107}$$

From the physics viewpoint, corrections $\lambda_n^{(1)}$ to eigenvalues correspond to frequency shifts of externally driven resonances. It is therefore desirable to present solutions of the driven problem in the form that includes resonant denominators with corrected frequencies of the resonances. Noticing that

$$\frac{1}{\lambda_n^{(0)} + \lambda_n^{(1)} - \lambda} = \frac{1}{\lambda_n^{(0)} - \lambda} \left(1 - \frac{\lambda_n^{(1)}}{\lambda_n^{(0)} - \lambda} \right) + O(V_L^2), \tag{2.108}$$

we achieve this goal by writing the solution in the desired form

$$\phi(r) = \sum_n \phi_n^{(0)}(r) \frac{\int_D \phi_n^{(0)} f dV}{\left((\lambda_n^{(0)} + \lambda_n^{(1)}) - \lambda \right) \int_D \phi_n^{(0)} R_0 \phi_n^{(0)} dV}. \tag{2.109}$$

Chapter 3

Sub-wavelength Resolution with a Flat Superlens

In the previous Chapter, we have developed a theory of sub-wavelength photonic, plasmonic and polaritonic structures, with the emphasis on their resonances and behavior in the long-wavelength limit. This theory provides a general framework for description, analysis and engineering of electromagnetic nanostructures. Development of such a theory is motivated partly by this Chapter, which deals with one of the most exciting applications of electromagnetic nanostructures: sub-wavelength resolution via the "superlensing" phenomenon.

In this Chapter, a novel approach to making a superlens in the infrared frequency band is described. Materials with negative dielectric permittivity ϵ are utilized in this approach. Those could be either plasmonic (metals) or polaritonic (semiconductors) in nature. A possible application of the negative-epsilon superlens devised here is laser-driven near field nanolithography. Theoretically, any plasmonic or polaritonic material with negative $\epsilon = -\epsilon_d$ sandwiched between dielectric layers with $\epsilon_d > 0$ can be used to significantly decrease the feature size. It is shown that a thin slab of SiC is capable of focusing the mid-IR radiation of a CO_2 laser to several hundred nanometers, thus paving the way for a new nano-lithographic technique: Phonon Enhanced Near Field Lithography in Infrared (PENFIL). Although an essentially near-field effect, this resolution enhancement can be quantified using far-field measurements. Numerical simulations supporting such experiments are presented.

Several objectives are fulfilled in this Chapter. For the first time, sub-micron super-resolution is realized at the mid-infrared frequency produced by a CO_2 laser. Thanks to our choice of the relatively long operating wavelength, we were able to fabricate an ultra-thin SiO_2-SiC-SiO_2 superlens that satisfies the small retardation [SP02]. This demonstration paves the way for various nano-lithographic applications that can take advantage of the widely available and highly efficient CO_2 laser. It also proves that the resolution of at least 1250 nm $\approx \lambda/9$ has been achieved. Thus, this demonstration goes beyond the previously accomplished resolution of the order of a wavelength [MBW04] and even beyond the resolution $\lambda/6$ recently reported by X. Zhang et al.[FLSZ05] in the UV regime.

This Chapter is organized as follows. Section 3.1 provides introductory notes on sub-wavelength imaging. Basic elements of the theory of near-field imaging with flat "superlenses" are presented in Section 3.2, which also introduces our implementation of a near-field superlens. Section 3.3 describes our original design of a far-field diagnostic that reveals formation of an image with strongly sub-wavelength features. Section 3.4 presents a few optical measurements from the proof-of-principle experiments that support the theory presented in Sections 3.2 and 3.3.

3.1 Introduction: imaging with a flat superlens

The wave nature of light places a stringent limit, known as the Abbe resolution limit [BW80], on the resolution of a microscope: the minimal feature size that can be detected by any conventional (far-field) optical system, with acceptance angle α, immersed in a host medium with dielectric permittivity ϵ_h, is $\Delta = 1.22\lambda/(2\sqrt{\epsilon_h}\sin\alpha)$, where λ is the wavelength of light.

Another well-known example of the resolution limit due to diffraction of light is a sub-wavelength diffraction grating with a period D. When illuminated by a laser beam with the wavelength $\lambda > D$, such diffraction grating produces only one (zeroth) diffraction order in the far field. All other diffraction orders $|m| \geq 1$ are evanescent with the decay constants $\chi_v^m = 2\pi|m|/D$. That implies that after a distance $\Delta x > D/2\pi$ all information about the diffraction grating is lost, and a hypothetic light-sensitive screen placed in the image plane at a distance Δx behind the grating is going to be uniformly illuminated. Restoring the information about

the grating (or, equivalently, making the intensity in the image plane non-uniform) requires amplifying evanescent diffraction orders.

While resolution can be enhanced beyond the canonical $\lambda/2$ limit by using high-ϵ_h materials (as it is done in liquid or solid immersion microscopy [MK90]), the truly impressive gains in resolution may require unconventional materials and approaches. One approach is the construction of electromagnetic *metamaterials*.

Metamaterial is a general term referring to man-made composites of natural materials which have the desirable properties unavailable in the naturally occurring materials. There has been a particular interest in engineering *electromagnetic* properties of metamaterials that enable unconventional approaches to controlling light propagation. For example, metal-dielectric composites have been used to enhance light intensity for nonlinear spectroscopic applications [Sha00], induce very strong nonlinear effects [BYBS99], design highly reflective [WPS95] or selectively transmissive [BS98, ZWCS05] mirrors.

The most fascinating metamaterials contain natural ingredients with both positive and negative dielectric permittivity ϵ. For example, a sub-wavelength diffraction pattern of a periodic slits array has been reproduced in the imaging plane (on a photoresist) using a dielectric/silver stack [MBW04, FLSZ05]. Enhanced transmission through a slab of negative ϵ material sandwiched between two layers of positive ϵ material has been recently demonstrated [ZWCS05].

Another, even more exotic example of metamaterials are the so-called double-negative (or left-handed) materials [Pen00, SPV$^+$00, SSS01, PGL$^+$03, HBC03]. Double-negative metamaterials (DNMs) utilize combinations of various resonant elements [PHSY96, PHRS99], which create negative dielectric permittivity and magnetic permeability. The possibility of accessing the sub-wavelength resolution using the so-called *superlens* [Pen00, SP02] is the most challenging and technologically rewarding application of the double-negative materials (DNMs).

The advent of a new class of Negative Index Materials [SPV$^+$00, Pen00] (NIMs) generated a significant optimism for enabling sub-wavelength resolution in optical systems. NIMs are artificial materials that have a *negative index of refraction*: Re $n_{\text{eff}} < 0$. The sign of refractive index is, by definition, the sign of projection of the phase velocity upon the group velocity:

$$\text{signRe } n_{\text{eff}} = \text{sign}(\vec{v}_{ph} \cdot \vec{v}_{gr}). \tag{3.1}$$

83
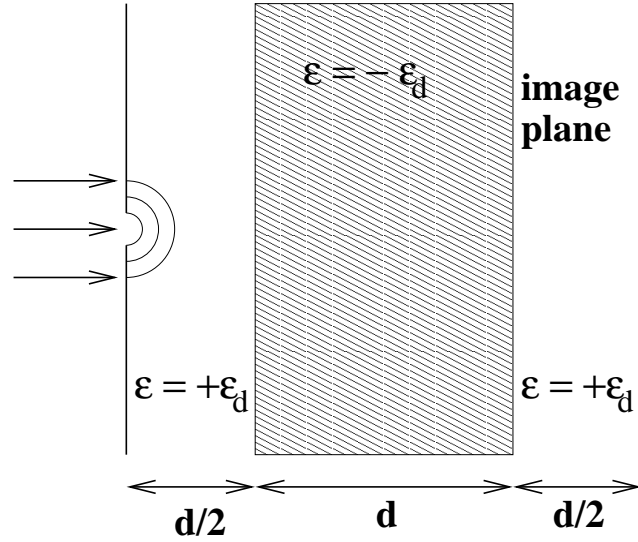
Figure 3.1: Schematic of a near-field lens: a thin slab of material with $\epsilon \approx -1$ is used to image a narrow (sub-wavelength) slit in a screen illuminated by a long-wavelength laser source.

It can be shown that DNMs are a subclass of NIMs: transverse waves in a isotropic double-negative medium have oppositely directed wave vector $\vec{k}$ and Poynting flux $\vec{P} = \frac{1}{8\pi}[\vec{E} \times \vec{H}]$, which corresponds to negative index. The notion of NIM is broader than DNM, because refractive index can be defined even in metamaterials where effective medium description is impossible. Non-homogenizable metamaterials with well-defined effective index include non-subwavelength photonic crystals (PhC).

A negative-index slab supports surface waves that can be externally excited, for example, by an evanescent diffraction order of an illuminated sub-wavelength diffraction grating. Under special conditions that will be explained below these surface modes can become exponentially increasing inside the NIM slab as a function of the distance from the interface between the ordinary and negative index media. This spatial growth can compensate for the exponential decay (evanescence) of those waves in an ordinary material. Thus a slab of NIM material designed to resolve spatial features much smaller than the wavelength of light has been dubbed a "perfect lens" [Pen00] (see schematics of a flat lens in Fig. 3.1). The super-resolution of a "perfect lens" is entirely due to the excitation of such surface waves.

Unfortunately, double-negative and negative-index materials do not occur in

nature and must be engineered as metamaterials. Successful experimental demonstrations of the negative refraction in the microwave frequency range have been recently published [SPV$^+$00, PGL$^+$03, HBC03]. However, despite several theoretical advances [PSS03, SU04a], NIMs in the highly desirable infrared or optical frequency ranges have been elusive so far. Conventional photonic crystals have been shown to produce images that still make a significant fraction of $\lambda/2$. To make a step in the direction of strongly sub-wavelength resolution, we demonstrate in Subsection 4.1 that a *sub-wavelength plasmonic crystal* (SPC) supports double-negative modes, and can be potentially used for making a superlens. Several designs of double-negative metamaterials are engineered in Chapter 4.

As soon as the fundamental role of surface waves in the "perfect lens" was realized, and enormous challenges in creating the "true" double-negative Veselago lens were faced, two side branches of the superlens research have formed. In one branch, researchers hoped that negative index of refraction, regardless of its mechanism, can be used to implement the "perfect lens". This hope was founded on two facts: (i) in the limit of geometric optics, index of refraction determines paths of light rays unambiguously in homogeneous media (through eikonal equation), and (ii) rays of light experience negative refraction on the interface between positive and negative index media. Since the notion of refractive index is broader than that of effective permittivity, impedance or permeability, it is possible to create complex media (e.g., photonic crystals) displaying both negative index and negative refraction on flat interfaces. According to this school of thought, achieving negative magnetic permeability at optical frequencies is unnecessary or even irrelevant, since the notion of permeability can be dropped.

The second branch of research abandoned the hope for "perfect imaging" by means of negative refraction (which is, strictly speaking, a far field phenomenon), and focused on the role of surface polaritons in sub-wavelength near-field imaging. Surface polaritons exist on interfaces with negative dielectric contrast ($\epsilon_2/\epsilon_1 < 0$). Again, there is no need for "optical magnetism": magnetic permeability need not be negative or even well-defined.

As a big disappointment, it was quickly realized that the lack of optical NIMs would not be the only obstacle in creating the perfect lens. Even more significantly, losses severely limit the thickness of a flat negative-index lens [SSR$^+$03, Mer04, PN05a]. Specifically, it has been recently demonstrated [PN05a] that, when realistic

85

material losses are accounted for, the resolution enhancement by the "perfect lens" is limited to the near-field zone.

In the near-field zone the two types of waves, P-polarized (with magnetic field parallel to the NIM interface) and S-polarized (with electric field parallel to the NIM interface) decouple from each other. Electrostatics largely governs the behavior of the P-polarized waves [Pen00], and the value of μ becomes irrelevant to surface wave excitation. Therefore, one does not need to employ NIMs for making a "perfect" near-field lens. Naturally occurring materials with $\epsilon < 0$ can be used instead. Low-loss negative ϵ materials include metals (mostly Ag and Au) and polar crystals (ZnSe, GaP, SiC) [Kit76]. The original proposal for a "perfect lens" [Pen00], as well as the improved calculations [SP02], advanced the idea of using a low-loss metal with $\epsilon \approx -1$ for significant improvement of the near-field resolution. We refer to the phenomenon of improving the near-field resolution by a slab of material with $\epsilon < 0$ as *near-field superlensing*. This phenomenon was recently experimentally demonstrated in the ultraviolet band [FLSZ05] with a 35 nm-thick silver film, and a resolution of about $\lambda/6$ has been claimed. More recently, near-field superlensing has been experimentally demonstrated in the mid-infrared band [TKU$^+$06]; the latter experiment provided a direct proof of a ground-breaking $\lambda/20$ resolution of single two-dimensional objects such as holes.

The significance of a near-field superlens is that it improves spatial resolution of near-field imaging. In other words, for a given distance between the imaged object and the imaging plane, a superlens creates a sharper (higher spatial resolution) image than that created without its assistance. Conversely, the superlens enables increasing the distance between the source and the imaging plane while maintaining spatial resolution. A realistic superlens *does not* "beat the diffraction limit" because such limit only exists in the far field.

Resistive losses is not the only factor limiting the resolution of a near-field superlens. Another important factor [SP02] is retardation, i. e. the finite thickness of the lens compared with the wavelength of light. Retardation effect dominates over losses whenever the inequality $\sigma/\epsilon_d < \epsilon_d \omega^2 d^2/c^2$ is satisfied [Shv03a], where $\epsilon \equiv -\epsilon_d + i\sigma$ is the complex dielectric permittivity of a negative-ϵ material surrounded by a regular dielectric with permittivity ϵ_d. Several recent experiments [MBW04, FLSZ05] used a relatively low loss silver as a negative-ϵ material, and were securely within the limits of this inequality. Therefore, retardation was the

dominant resolution-limiting factor. Theoretical calculations demonstrate [SP02] that, in the retardation-limited case, uniform amplification of a broad range of transverse wavenumbers works properly only for very thin superlenses, $\omega d/c < 0.3$. For thicker superlenses there is still a significant amplification coefficient $T(k_y)$ of the large transverse wavenumbers k_y in the image in comparison with the un-assisted near field image. However, $T(k_y)$ is not a flat function of k_y. Therefore, such a super-lens can only be used for imaging objects of small transverse feature size separated from each other by a much larger distance.

In Section 3.2, we describe an implementation of a planar superlens for mid-infrared spectral range (around 11μm) based on a three-layered structure of sub-micron thickness, $SiO_2/SiC/SiO_2$, in which the polaritonic material SiC has a negative dielectric permittivity in the restrahlen band between the frequencies of the transverse and longitudinal optical phonons. The fabricated superlens consists of a 400 nm thick film of SiC inserted between two 200nm thick SiO_2 dielectric layers. Far-field diagnostics of superlensing based on measuring transmission coefficients through the metal-coated superlens has been implemented using a tunable CO_2 laser and Fourier Transform Infrared (FTIR) micro-spectroscopy. This work breaks the new ground for developing metamaterials in the mid-IR part of the electromagnetic spectrum that is of considerable interest for medicine and biology [WIG01]. Strong interest in mid-IR free-space communications coupled with the recent breathtaking progress in quantum cascade lasers [CPM$^+$02] provides yet another incentive to the development of metamaterials in mid-IR. Another attraction of using polaritonic materials with the negative ϵ in mid-IR (e. g., SiC, ZnSe, TiO_2) is that their electromagnetic properties can be readily tuned by applying an external electric field [TIZS91, LWM$^+$05].

3.2 Theory and simulations of the near-field superlens

It was noted previously by several theorists that planar slabs of materials with $\epsilon < 0$ can be used instead of negative-index metamaterials for enhancing the near-field image [SP02, FLYZ03, Shv03a]. Materials with $\epsilon(\omega) < 0$ in a limited frequency range are common in nature. For example, free electrons in metals account for their negative dielectric permittivity: $\epsilon \equiv \epsilon_b - \omega_p^2/\omega(\omega + i\gamma) < 0$ for $\omega < \omega_p/\sqrt{\epsilon_b}$. Here ω_p is the plasma electron frequency, $\epsilon_d > 0$ is the frequency-independent dielectric

87

contribution of bound electrons, and γ is the damping rate. For example, for silver $\epsilon_b = 5$, $\hbar\omega_p = 9.1\text{eV}$, and $\hbar\gamma = 0.02\text{eV}$. Another class of the so called polaritonic materials (SiC, ZnSe, GaP, etc.) exists for which $\epsilon < 0$ occurs for frequencies in the far to mid-IR band. The frequency-dependent dielectric permittivity of these crystals is given by the approximate formula

$$\epsilon = \epsilon_\infty \frac{\omega^2 - \omega_{LO}^2 + i\Gamma\omega}{\omega^2 - \omega_{TO}^2 + i\Gamma\omega}, \tag{3.2}$$

where ω_{TO} and ω_{LO} are the frequencies of the transverse and longitudinal optical phonons, respectively. The finite phonon lifetime is accounted for by the damping constant Γ in Eq. (3.2). For example, for SiC $\omega_{LO} = 972\text{cm}^{-1}$, $\omega_{TO} = 796\text{cm}^{-1}$, $\epsilon_\infty = 6.5$ and $\Gamma = 5\text{cm}^{-1}$. The so called restrahlen band $\omega_{TO} < \omega < \omega_{LO}$ for which $\epsilon < 0$ is typically in mid to far infrared for polaritonic materials (PM's). The low damping rate of optical phonons makes PMs attractive for developing enhanced near-field lenses in the mid to far-infrared range.

Enhancing the near field image, thereby improving its spatial resolution, is important for developing new nano-lithographic tools. In this Section, we describe a new nanolithographic tool, Phonon Enhanced Near Field Infrared Lithography (PENFIL) that utilizes a thin (about 400 nm) film of SiC sandwiched between two thin layers (about 200 nm each) of SiO_2. By tuning the high-power radiation of a CO_2 laser to the wavelength ($\approx 11.1\mu\text{m}$) for which $\epsilon_{SiC} = -\epsilon_{SiO2}$, a 100nm wide slit on the front side of the $SiO_2/SiC/SiO_2$ sandwich can be accurately imaged onto its backside side by a laser beam normally incident on the front side. A thin layer of thermoresist deposited on the backside the sandwich can thus be patterned on a 1200-nm scale using a high power CO_2 laser beam. This super-resolution corresponding to $\lambda/100$ is accomplished by a purely near-field effect: strong coupling to the broad wavenumber range of surface phonon polaritons at the SiO_2/SiC interface. Below we also demonstrate how, by adding an additional set of narrow slits on the backside of the $SiO_2/SiC/SiO_2$ sandwich, the transmission coefficient through the structure can be correlated to the existence of the above mentioned near-field effect.

Below we review the theory of near-field superlensing as applied to the $SiO_2/SiC/SiO_2$. The principle of enhanced near-field imaging using thin slabs of a negative-ϵ material $\epsilon \approx -\epsilon_d$ inserted between low-loss dielectric with permittivity ϵ_d

is shown in Fig. 3.1. A single sub-wavelength slit (or a periodic array of slits spaced by $D \ll \lambda$) of width $\Delta y \ll \lambda$ located at $x = 0$ is illuminated by a normally incident laser, and is imaged onto the focal plane behind the film. It follows from Fig. 3.1 that the focal distance of a superlens is equal to the thickness of the polaritonic material d. We assume that the imaging wave is p-polarized, i. e. the non-vanishing field components are B_z, E_x, and E_y. Magnetic field B_z in the object plane can be decomposed into planar waves:

$$B_z(x = 0, y) = \int_{-\infty}^{+\infty} dk A_k e^{iky},$$

where $A(k)$ is the wave amplitude which is non-vanishing up to $k = k_{max}$. In the case of a periodic array of slits the integral turns into a sum of the harmonics of $k_D = 2\pi/D$: $A(k) = \sum_{m=-\infty}^{+\infty} A_m \delta(k - mk_D)$, where m is the diffractive order. It will be assumed that all $|m| \geq 1$ diffractive orders are non-propagating (evanescent).

Given the magnetic field distribution at the slit $B_z(y, x = 0)$, magnetic field in the image plane $B_z(y, x = 2d)$ is given by

$$B_z(y, x = 2d) = \int_{-\infty}^{+\infty} dy' B_z(y', x = 0)G(y - y'). \tag{3.3}$$

The Green's function $G(y - y')$ is given by [SSR$^+$03, Shv03a, Mer04, PN05a]

$$G = (2\pi)^{-1} \int_{-\infty}^{+\infty} dk \ T(k)e^{iky}, \tag{3.4}$$

where

$$T(k) = \frac{4(\chi_d/\epsilon_d)(\chi_p/\epsilon) \exp{(-\chi_d d)}}{(\chi_p/\epsilon + \chi_d/\epsilon_d)^2 \exp{(\chi_p d)} - (\chi_p/\epsilon - \chi_d/\epsilon_d)^2 \exp{(-\chi_p d)}}, \tag{3.5}$$

and the evanescence constants in the regular and polar materials are, respectively, $\chi_d = \sqrt{k^2 - \epsilon_d \omega^2/c^2}$ and $\chi_p = \sqrt{k^2 - \epsilon \omega^2/c^2}$. Perfect restoration of the image is only possible for $\epsilon = -\epsilon_d$ and $\chi_p = \chi_d$. For non-magnetic materials ($\mu = 1$) $\chi_p > \chi_d$. Therefore, $T(k)$ cannot be equal to unity for all k's. The expression for $T(k)$ can be simplified in the most relevant here limit of $|k| \gg |\epsilon_d|\omega/c$ and $\epsilon = -\epsilon_d + i\sigma$:

$$T(k) \approx \frac{4e^{-2kd}}{(\bar{\sigma} - i\epsilon_d \omega^2/k^2 c^2) + 4e^{-2kd}}, \tag{3.6}$$
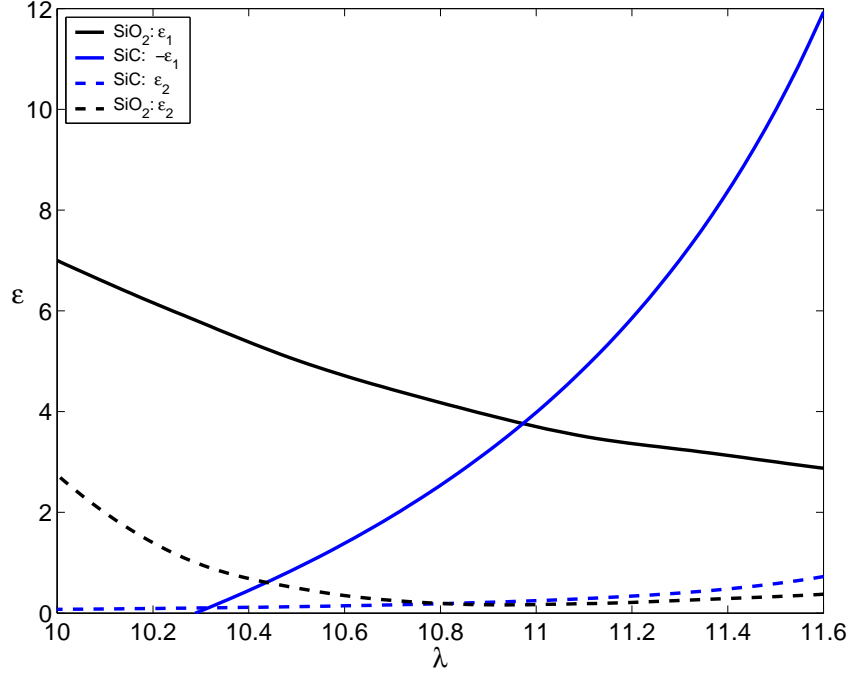
Figure 3.2: Dielectric permittivities $\epsilon = \epsilon_1 + i\epsilon_2$ of SiO_2 and SiC (see legend) as a function of the laser wavelength λ measured in microns.

where $\bar{\sigma} = \sigma/\epsilon_d$ characterizes losses in the negative-ϵ material. If both positive and negative-ϵ materials are lossy, $\bar{\sigma}$ is the sum of the losses in both materials. Note that losses (proportional to $\bar{\sigma}$) and retardation (proportional to $\epsilon_d\omega^2/k^2c^2$) cumulatively cause $T(k)$ to deviate from unity. Because the highest resolved wavenumber $k \propto 1/d$, retardation dominates when $\bar{\sigma} \ll \epsilon_d\omega^2 d^2/c^2$.

Dielectric permittivities of SiC and SiO_2 are plotted as a function of the laser wavelength λ inside the tunability range of a CO_2 laser in Fig. 3.2. Dielectric permittivity of SiO_2 was interpolated from Ref. [Pal85], and that of SiC was computed from Eq. (3.2) with parameters [SKW59, OC82] $\omega_{LO} = 972$cm^{-1}, $\omega_{TO} = 796$cm^{-1}, $\epsilon_\infty = 6.5$ and $\Gamma = 5$cm^{-1}.

Accessing the wavelengths in the $10.7 < \lambda < 11.4\mu$m range requires using a ^{13}C ^{16}O$_2$ gas filling. Rapid increase in the real and imaginary parts of $\epsilon = \epsilon_1 + i\epsilon_2$ of SiC towards the longer wavelengths corresponds to the transverse optical phonon resonance at $\lambda \approx 12.6\mu$m while a similar increase of $\epsilon_{1,2}$ of SiO_2 towards shorter

wavelengths corresponds to the resonance at $\lambda \approx 9\mu$m. Fortunately, there exists a wavelength $\lambda \approx 11\mu$m for which $\epsilon_1^{\text{SiC}} = -\epsilon_1^{\text{SiO}_2} = -3.76$ and ϵ_2 are very small for both materials. Dissipation limits the resolution of surface wave enhanced imaging [SP02, Shv03a] if $|\epsilon_2/\epsilon_1| \gg \epsilon_d \omega^2 d^2/c^2$, where d is the width of the negative ϵ slab. For the subsequent simulations we choose the width of the SiC to be $d = 400$nm, and the opposite limit holds: $(\epsilon_2^{\text{SiO}_2} + \epsilon_2^{\text{SiC}})/\epsilon_1^{\text{SiO}_2} = 0.1$ but $\omega^2 d^2/c^2 \times \epsilon_1^{\text{SiO}_2} \approx 0.2$. Therefore, the SiC thickness limits the resolution [Mer04].

Eq. 3.6 demonstrates that while a far-field "perfect lens" is not achievable given realistic material losses, improvement in near-field resolution is possible [PN05a]. As an object to be imaged onto the focal plane we have chosen a periodic set of slits of the width $\Delta y = 500$nm spaced by a period $D = 2.5\mu$m. Because the first evanescent diffraction maximum decays by one e-folding after a distance $L = D/2\pi$, a convincing demonstration of superlensing requires that the lens' thickness $2d > L$. In the absence of near-field superlensing, an electromagnetic wave transmitted through the periodic array of slits in the object plane turns into a planar wave propagating normally to the lens after a distance L behind the object plane. Therefore, the focal plane is uniformly illuminated if the laser frequency $\omega = 2\pi c/\lambda$ does not satisfy the superlensing condition $\text{Re}[\epsilon(\omega)] = -\text{Re}[\epsilon_d]$. Non-uniform illumination can occur under two conditions: (a) superlensing, and (b) excitation of the slab resonances of the slab superlens. We use computer simulations to demonstrate the strongly resonant nature of the superlensing phenomenon and to illustrate the three vastly different frequency regimes: superlensing at $\lambda = 11\mu$m; excitation of the slab resonance at $\lambda = 10.7\mu$m; and total loss of resolution (uniform illumination of the focal plane) at $\lambda = 11.25\mu$m.

Superlensing at $\lambda = \lambda_0 = 11\mu$m is demonstrated in Fig. 3.3. Strong field enhancement at the right SiO$_2$/SiC boundary is indicative of evanescent wave amplification by the superlens. Image of the slit is formed on the back side of the lens (SiO$_2$/vacuum boundary). Profiles of the electric field amplitude behind the screen (solid line) and in the focal plane (dashed line) are shown in Fig. 3.3(bottom). While the sharp sparks behind the metal screen are not resolved in the focal plane (they are represented by a very large wavenumber k, such that $T(k)$ is small), the overall width of the slit is captured. It is apparent from Fig. 3.3(bottom) that the adjacent slits separated by $D = 2.5\mu$m are well resolved. The actual FWHM of the slit image is better than $D/2$ which corresponds to the spatial resolution better than $\lambda/8$. It

is also noteworthy that, apart from the spikes corresponding to "sparking" at the edges of the slit, the shape of the electric field behind the screen mimics that of the slit. This is an indication of very small reflections from the superlens because, otherwise, the field profile near the metal screen would have been modified by the reflected wave. Incidentally, small reflection coefficient has been predicted [Shv03a] in the superlensing regime. Therefore, Fig. 3.3(bottom) contains two indication of superlensing at $\lambda = \lambda_0$: (a) FWHM of the slit image in the focal plane is significantly smaller than the slit spacing D, and (b) apart from the spikes at the sharp edges of the screen, electric field profile behind the screen sharply reproduces that of a slit.
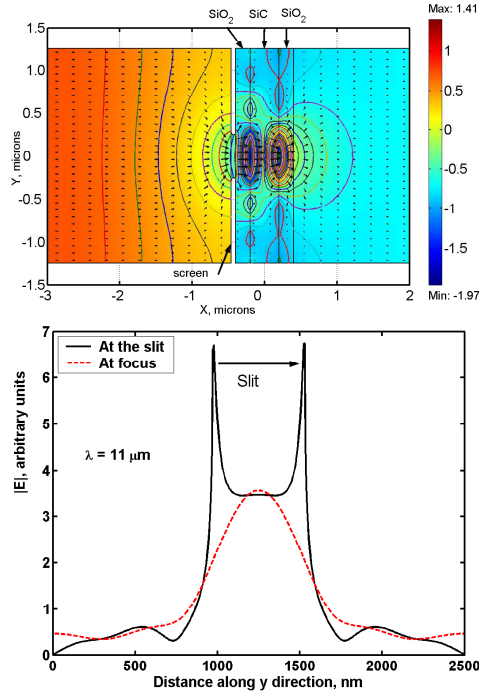
Figure 3.3: Superlensing at $\lambda = 11\mu$m. Top: Color-coded magnetic field strength B_z and $B_z =$ const isocontours and Poynting vectors (arrows) in and around the $SiO_2/SiC/SiO_2$ superlens illuminated by a normally incident from the left p-polarized electromagnetic wave. Bottom: Electric field magnitude $|\vec{E}|$ in the object plane behind the screen ($x = -400$nm, solid line) and in the focal plane ($x = 400$nm, dashed line). Spikes in the object plane are due to "sparking" at the edges of the slit. SiO_2 regions: $-400 < x < -200$ nm, SiC region: $-200 < x < 200$ nm.
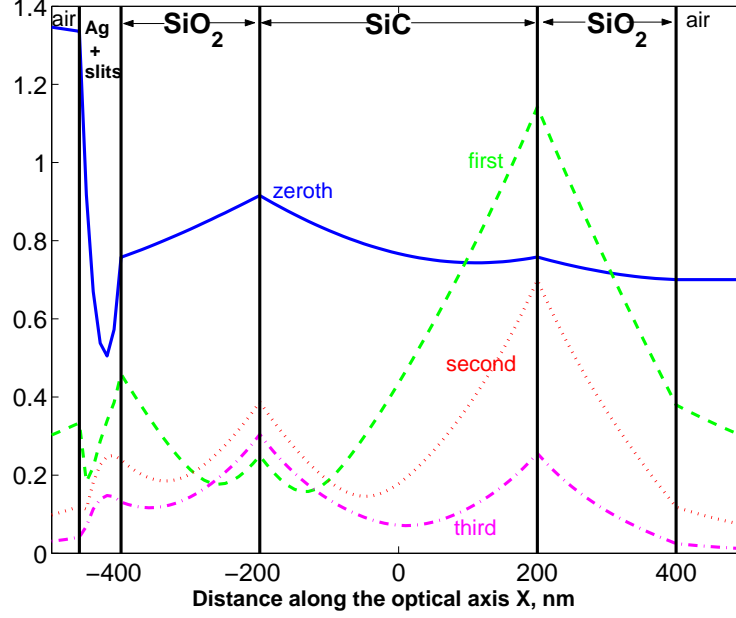
Figure 3.4: Evolution of transverse Fourier harmonics of $B_z(x = \text{const}, y)$ along the optical axis x in a superlens excited by a screen with periodic array ($D = 2.5\mu\text{m}$) of slits ($0.5\mu\text{m}$ wide), at the superlensing frequency ($\lambda = 10.972\mu\text{m}$). Dielectric constants used are $\epsilon_{SiC} = -3.76 + 0.24i$ and $\epsilon_{SiO_2} = 3.76 + 0.17i$. The first and second harmonics are dominated by the exponentially growing terms in the negative dielectric slab ($-200 < x < 200$ nm). The boundaries of SiC and SiO_2 layers are indicated by thick solid lines.

To better illustrate the image formation in this superlens, we have numerically solved (using FEFD method implemented in Femlab [Com03]) the problem of a three-layered structure excited by an incident plane wave passing through a periodic array of slits made in a silver screen (Fig. 3.4). The fields after the screen can be decomposed into Fourier harmonics which evolve as $e^{\pm i\sqrt{\epsilon k_0^2 - k^2}x}$ along the optical axis, where $k_0 = 2\pi/\lambda$ is the vacuum wavenumber. Within the layer of negative dielectric, there are both exponentially growing and exponentially decaying waves. Even though we do not have a rigorous solution of this essentially 5-layered problem, we know that when a slab with dielectric constant ϵ is surrounded by medium with dielectric constant ϵ_d, the ratio of magnetic fields on the opposite sides of the slab

93

equals[Shv03a]

$$\frac{A_k(x = d/2)}{A_k(x = -d/2)} = \frac{2(\chi_p/\epsilon)e^{-\chi_p d}}{(\chi_p/\epsilon + \chi_d/\epsilon_d) + (\chi_p/\epsilon - \chi_d/\epsilon_d)e^{-2\chi_p d}}, \; k = 2\pi m/D. \quad (3.7)$$

At the superlensing frequency we have by definition $|\epsilon + \epsilon_d| \ll 1$, and the harmonic enhancement can become large:

$$\frac{A_k(x = d/2)}{A_k(x = -d/2)} \approx \frac{2\epsilon_d}{\epsilon + \epsilon_d} e^{-2\pi md/D}, m = 1, 2, 3... \quad (3.8)$$

at least for small m, but it decreases exponentially with the order of Fourier harmonics m. In our case, $\epsilon_d \approx 3.76$, $\epsilon + \epsilon_d \approx 0.4i$, $d/D = 0.16$, which gives the estimate of the amplitude enhancement ≈ 7 for $m = 1$, ≈ 2.5 for $m = 2$ and ≈ 0.9 for $m = 3$, in qualitative agreement with the Fig. 3.4. This analysis illustrates how the super-resolution is obtained in this structure, and convinces us that at least the first harmonic, which is responsible for resolving the features about $D/2$ in size, is enhanced exponentially in the SiC layer.
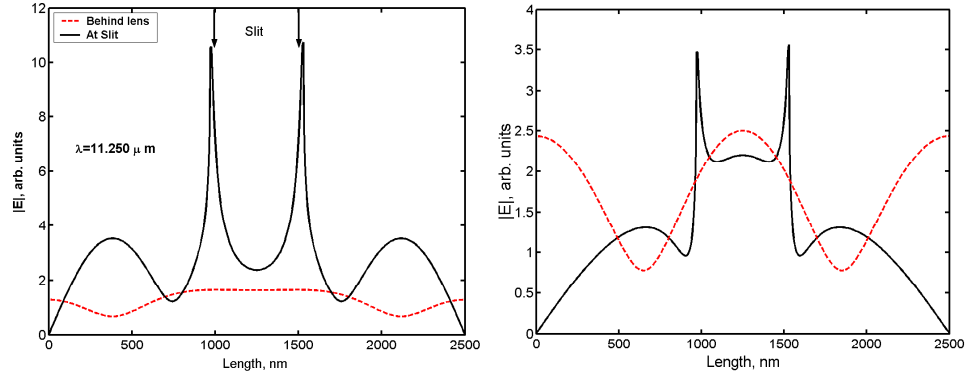
Figure 3.5: Absence of the superlensing for two representative wavelengths $\lambda = \lambda_1$ (left) and $\lambda = \lambda_2$ (right). Total electric field $|\vec{E}|$ is plotted behind the metal screen (solid lines) and in the focal plane (dashed lines). For $\lambda_1 = 11.25$ spatial resolution in the focal plane is lost: electric field profile in the focal plane is almost uniform. For $\lambda_2 = 10.7\mu$m the electric field profile in the focal plane is strictly sinusoidal indicating a slab resonance.

Superlensing is a resonant phenomenon strongly dependent on the radiation frequency ω because $\mathrm{Re}[\epsilon(\omega)] \approx -\mathrm{Re}[\epsilon_d]$ must be satisfied. We illustrate the absence

of superlensing for $\lambda \neq \lambda_0$ by two examples: $\lambda = \lambda_1 \equiv 11.25\mu$m and $\lambda = \lambda_2 \equiv 10.7\mu$m. Total electric field $|\vec{E}|$ is plotted behind the screen and in the focal plane in Fig. 3.5 for $\lambda = \lambda_1$ and $\lambda = \lambda_2$. For $\lambda = \lambda_1$ we find (see Fig. 3.5[left]) that $|\vec{E}|$ is almost uniform in the focal plane indicating the lack of superlensing. Spatial information about the periodic slit array is lost in the focal plane because evanescent diffractive orders $|m| \geq 1$ are not amplified by the $SiO_2/SiC/SiO_2$ lens, and the only non-evanescent $m = 0$ diffractive order results in a uniform illumination of the focal screen. Another indication of the lack of superlensing is a significant reflection from the $SiO_2/SiC/SiO_2$ lens that manifests itself in a strongly distorted field distribution behind the screen. For $\lambda = \lambda_2$ we also find (see Fig. 3.5[right]) that the profile of $|\vec{E}|$ in the focal plane does not resemble the image of a single slit. The almost perfectly sinusoidal dependence of $|\vec{E}|$ on y is caused by the excitation of the electromagnetic resonance of the $SiO_2/SiC/SiO_2$ lens [SP02]. We have chosen the two non-resonant wavelengths λ_1 and λ_2 sufficiently outside of the superlensing region that our simulations have shown to be in the $10.85\mu m < \lambda < 11.05\mu m$ range.

The difference between the superlensing case of $\lambda = \lambda_0$ (Fig. 3.3) and the two representative non-superlensing cases of $\lambda = \lambda_{1,2}$ (Fig. 3.5) is sufficiently striking to convince us that superlensing is a real near-field effect that can be diagnosed by careful measurements of the field profile in the focal plane. Unfortunately, these near-field measurements can be fairly challenging because they may require a sub-micron spatial resolution.

We have also simulated transmission of mid-IR radiation through the SiO_2-SiC-SiO_2 superlens *without* the image-forming metal screen (Fig. 3.6). The purpose of this numerical experiment is to verify the recent prediction [ZWCS05] that a negative-ϵ material can become totally transmissive when encased inside a positive-ϵ dielectric. Although Fabry-Perot resonances of dielectric slabs, resulting in 100% transmission, are very well known, it is quite remarkable that total transmission can be achieved with sub-wavelength sandwich-like structures. The key to this effect is that an electromagnetic wave propagating normally to the material interface of a sub-wavelength structure and polarized parallel to the interface experiences an average dielectric permittivity given by the effective medium theory [Asp82]:

$$\epsilon_\parallel(\omega) = (d_1\epsilon_1 + d_2\epsilon_2)/(d_1 + d_2). \tag{3.9}$$

Here $d_{1,2}$ and $\epsilon_{1,2}$ label the thicknesses and dielectric permittivities of the two materials comprising the sub-wavelength sandwich. Total transmission through the structure is expected if $\epsilon_\parallel = 1$. This phenomenon cannot be realized for most materials: if $\epsilon_{1,2} > 1$, then $\epsilon_\parallel > 1$. For polar materials with $\epsilon_2 < 0$ there exists, however, a particular frequency ω_1 for which $\epsilon_\parallel(\omega_1) = 1$. The physical basis for the enhanced transmission is that the reflection from the negative-ϵ material is exactly canceled by the reflection from the positive-ϵ coating.
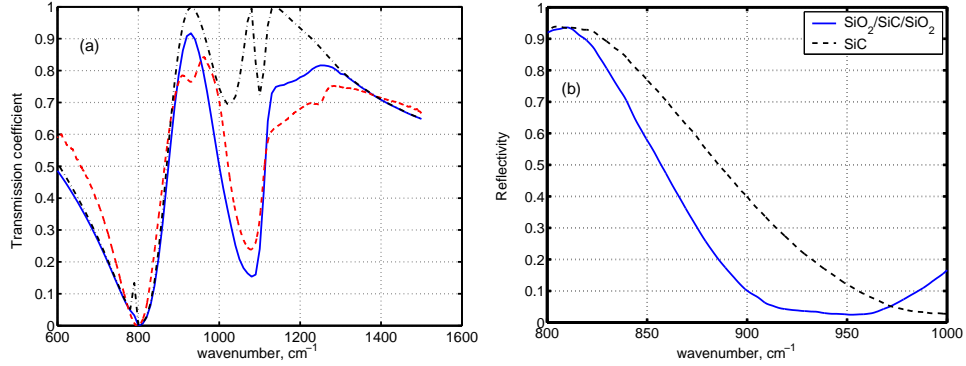
Figure 3.6: (a) Transmission through a three-layer SiO_2(200nm)-SiC(400nm)-SiO_2(200nm) nanostructure. Dot-dashed line indicating perfect transparency at $\omega_1 = 931\text{cm}^{-1}$: simulation result, losses in SiO_2 and SiC are neglected. Solid line: simulation result, losses are included. Dashed line: experimental measurements using FTIR microscope. (b) Reflection from a 400nm SiC film (dashed line) and a SiO_2(200nm)-SiC(400nm)-SiO_2(200nm) composite film. Addition of the 400nm (or $\lambda/25$) SiO_2 coating reduces the reflection coefficient by a factor 6 at $\omega = 930\text{cm}^{-1}$.

Enhanced transmission was numerically simulated by assuming that $\epsilon_1 \equiv \epsilon_{SiO_2}$ [Pal85], $\epsilon_2 \equiv \epsilon_{SiC}$ from Eq. (3.2), and $d_1 = d_2 = 400$ nm. The results of the numerical simulation of the EM wave incident on the three-layer structure are shown in Fig. 3.6. Neglecting material losses in SiO_2 and SiC by retaining only the real part of the dielectric permittivity yields a dashed-line curve indicating total transmission at $\omega_1 = 930\text{cm}^{-1}$. This transmission maximum is expected to be experimentally observable because, at that frequency, losses in SiC and SiO_2 are small. The other two higher frequency transmission maxima are located close to phonon resonances of SiO_2, where $\text{Re}(\epsilon_{SiO_2}) < 0$ and $\text{Re}(\epsilon_{SiC}) > 0$. These transmission maxima are not expected to be observable because of the very high losses in SiO_2. Indeed, when the imaginary parts of the dielectric permittivities are included, the transmission

curve represented by the solid line has a single well-formed maximum at $\omega = \omega_1$. The peak transmission falls short of 100% to about 92% because of the finite losses. The experimentally measured transmission curve (dashed line) indeed closely tracks the numerically simulated solid line. The small dip near the expected transmission maximum appears to be caused by sample contamination resulting in absorption.

3.3 Far-field detection of superlensing: design of the proof-of-principle experiments
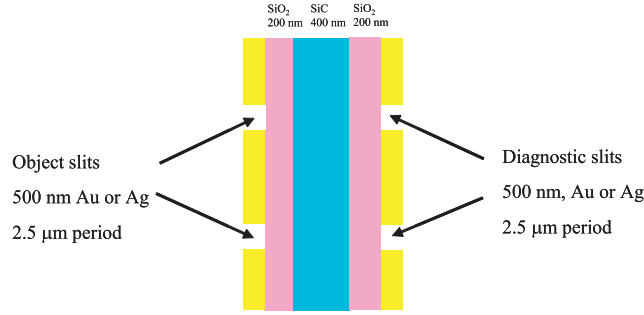
Figure 3.7: $SiO_2/SiC/SiO_2$ superlens with two sets of slits: image-forming Object Slits and Diagnostic Slits. Only Sample IN for which Diagnostic Slits are directly opposite to the Object Slits is shown. In the Sample OUT Diagnostic Slits are laterally displaced by $D/2 = 1.25\mu$m.

Simulation results of Section 3.2 indicate that superlensing is a real near-field phenomenon that can be diagnosed by careful measurements of the field profile in the focal plane. Unfortunately, these near-field measurements can be challenging in mid-IR part of the spectrum. For example, one cannot employ photoresist [MBW04, FLSZ05], as it is typically done in UV, because low-energy infrared photons do not affect it. Near field scanning optical microscopy (NSOM) has also been relatively undeveloped in mid-IR until recently [TKU$^+$06]. Our solution is a new far-field diagnostic of image localization. In this Section we present numerical calculations demonstrating how transmission through a double set of nano-slits (one set on the front and another on the back side of the $SiO_2/SiC/SiO_2$ superlens) can serve as a reliable proof of superlensing at $\lambda = 10.97\mu$m, and a valuable test bed for studying the sensitivity of superlensing to the laser wavelength.
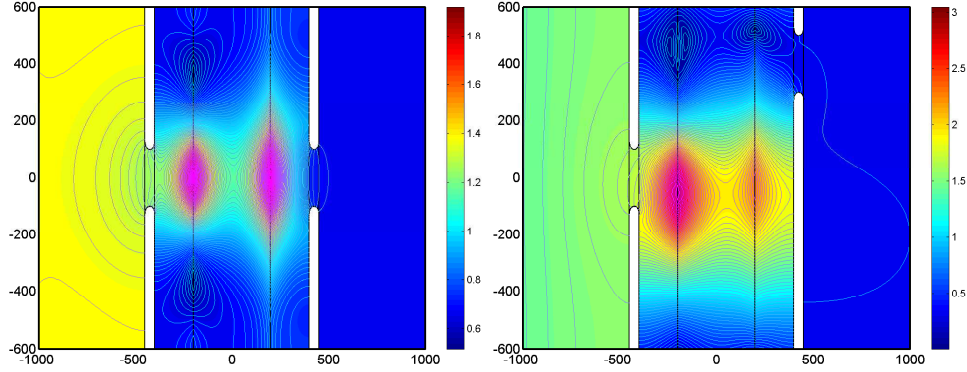
Figure 3.8: Resonant transmission through a double set of nanoslits. Case IN (left): diagnostic slit in front of the object slit. Case OUT (right): diagnostic slit displaced laterally by $D/3 = 400$ nm. Other parameters: same as in Fig. 3.3.

To devise a far-field diagnostic of superlensing we added a second metallic screen on the back side (focal plane) of the $SiO_2/SiC/SiO_2$ lens. A periodic set of *diagnostic slits* is cut in the screen. The slits are identical in width Δy and period D to those on the front side of the lens. We consider two kinds of diagnostic slits: in-phase (cut exactly across the lens from the image-forming slits) and out-of-phase (laterally displaced in y-direction from the image-forming slits). The $SiO_2/SiC/SiO_2$ lens with in-phase (out-of-phase) slits will be referred to as the IN (OUT) Samples, respectively. The IN sample is shown in Fig. 3.7. Let us denote the frequency-dependent transmission coefficient through the IN Sample as $T_{in}(\omega)$ and through the OUT Sample as the $T_{out}(\omega)$.

The IN and OUT samples were numerically simulated. In Case IN the diagnostic slit is positioned directly opposite the object slit, so that the image of the object slit fits inside the diagnostic slit as shown in Fig. 3.8 (left). Hence, a relatively high transmission through the two sets of slits is expected. Indeed, the transmittance is $T_{in} = 44.5\%$. In Case OUT shown in Fig. 3.8 (right) the diagnostic slit is laterally displaced by $D/3 = 400$ nm. As evident from Fig. 3.8 (right), the metal screen of the diagnostic grating obscures the image of the first slit. Hence, the expected transmittance is low. Indeed, it is found to be only $T_{out} = 9.7\%$, yielding the transmission contrast of $T_{in}/T_{out} = 4.6$ for these two cases. Both simulations were done for the resonant $\lambda = 10.97\mu$m.

To demonstrate that such a high transmission contrast is the consequence of superlensing, we have carried out transmission simulations for cases IN and OUT using a different laser wavelength achievable by a CO_2 laser, $\lambda = 11.262\mu$m. For that wavelength, $\epsilon^{\text{SiC}} = -6.55 + 0.37i$ and $\epsilon^{\text{SiO}_2} = 3.29 + 0.24i$, and no superlensing effect is expected. Transmission coefficients for the two cases are $T_{in} = 30\%$ and $T_{out} = 35\%$, respectively. So, indeed, the displacement of the diagnostic slit has very little effect on transmission in the absence of superlensing. This decrease in the transmission contrast for the two slit positions was to be expected. Indeed, when the two sets of slits are separated by the vacuum region, the transmission for coincident slits (Case IN) is $T_{in} = 77.5\%$ while for the displaced slits $T_{out} = 77.2\%$.
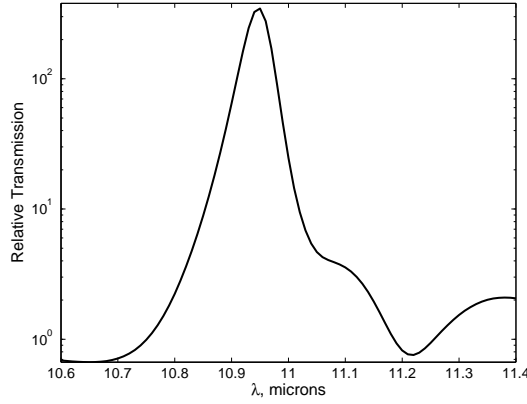
Figure 3.9: Theoretical calculation of the ratio of transmissions through IN and OUT Samples. Lateral shift between slits in the OUT sample is $D/2$. Large peak at $\lambda_0 \approx 11\mu$m indicates superlensing.

It is easy to see why $T_{in}(\omega)/T_{out}(\omega)$ carries information about superlensing. In the absence of superlensing (for example, for $\lambda = \lambda_1$) an electromagnetic wave that penetrates through the object slits into the lens consists of multiple diffractive orders. However, after a distance $\Delta z = D/(2\pi)$ only the fundamental $m = 0$ diffractive order survives as all other diffractive orders are evanescent. Therefore, the second metal screen (in the focal plane of the lens) is uniformly illuminated as shown in Fig. 3.5(left). Consequently, the relative phase of the diagnostic slits with respect to the object ones is irrelevant, and $T_{in}(\omega_1) \approx T_{out}(\omega_1)$. The situation drastically changes for near the superlensing wavelength $\lambda = \lambda_0$. Because the superlens focuses radiation transmitted through a given slit directly in front of that

slit as shown in Fig. 3.3, the relative position of the diagnostic slits with respect to the image-forming object slits becomes crucial. Specifically, it is natural to expect that transmission through the IN Sample is going to be much higher than through the OUT Sample at the superlensing wavelength. The ability of a superlens to amplify evanescent diffractive orders makes the transmission coefficient through the structure dependent on the relative lateral positions of the object and diagnostic slits.

Numerical simulations confirm these simple qualitative arguments. The frequency-dependent ratio T_{in}/T_{out} (this time for lateral displacement $D/2$) is plotted as a function of the laser wavelength in Fig. 3.9. A sharp peak at $\lambda \approx 10.97\mu$m signals superlensing. Away from that point $T_{in}/T_{out} \sim 1$. To summarize, we have designed a simple far-field test of superlensing that requires measuring the ratio of transmission amplitudes for Samples IN and OUT. This diagnostic is remarkable in that it uses far field measurements for diagnosing a near-field effect.

3.4 Experimental evidence of superlensing: far-field spectra

In Section 3.3, we have devised a spectroscopic far-field diagnostic of superlensing by producing periodic arrays of sub-micron slits on both surfaces of the superlens as shown in Fig. 3.7. One set of *image-forming* slits creates localized sources while the other set of *diagnostic* slits is used for collecting the transmitted light. Spatial localization of the image is confirmed by varying the lateral position of the diagnostic slits.

To confirm the predictions of the theory and demonstrate formation of subwavelength images, Korobkin et al. [KUZS05, KUS06] have fabricated several samples with diagnostic IN an OUT double sets of slits (Figures 3.10, 3.11). By using a broadly tunable FTIR microscope, they measured reflection and transmission coefficients of the superlensing structures designed in Sections 3.2, 3.3, covering a wide band around the polaritonic resonance in SiC and the superlensing resonance of the structure with resolution 1 cm^{-1}. Fabrication of the superlens and experimental procedures are described in detail in Refs. [KUZS05, KUS06].

Fig.3.12 shows transmission through the 200 nm SiO$_2$/400nm SiC/200nm SiO$_2$ structure for the symmetric IN and half-period shifted OUT groove positions.
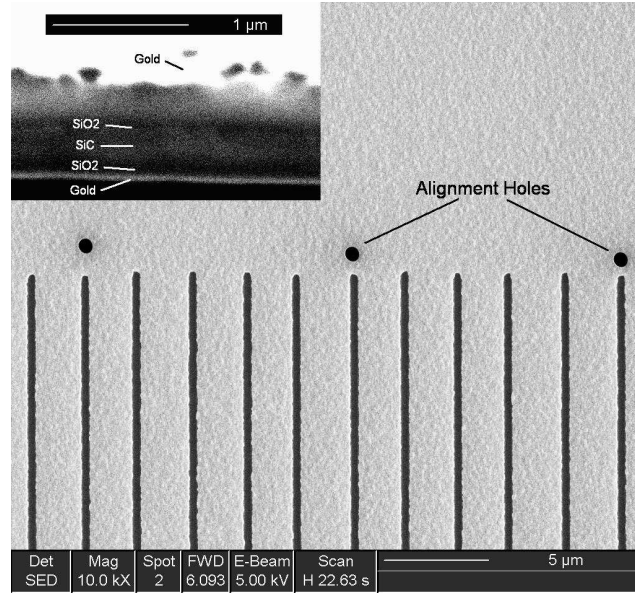
Figure 3.10: Left upper corner: SEM image of a segment of $SiO_2/SiC/SiO_2$ membrane covered with a 60nm thick gold film on both sides. The plane of view is tilted by $52°$. Bottom: periodic array of slits produced in the gold film using ion milling. Image courtesy D. Korobkin.

One can see that the curves are dramatically different only in the vicinity of the superlensing wavenumber. The ratio of those two curves is shown in Fig.3.13 (black solid curve). The maximum ratio is reached at $k_{peak} = 924 \pm 0.5$ cm^{-1}.

As a control experiment, it was demonstrated that superlensing in its originally conceived form [Pen00] requires a symmetric superlens, i.e. that the amounts of the positive and negative ϵ materials must be the same. When the amounts of SiO_2 and SiC are not equal, the superlens does not work. To demonstrate that we have measured $T_{in}(\omega)$ and $T_{out}(\omega)$ for a sample that consists of the Au(60nm)-SiO_2(400 nm)-SiC(400 nm)-SiO_2(400nm)-Au(60nm) layers. The ratio T_{in}/T_{out} that serves as a diagnostics of superlensing was plotted in Fig. 3.13 as a dashed pink line. The difference between the cases of the symmetric and non-symmetric superlenses is dramatic: the non-symmetric superlens does not exhibit the spike associated with the superlensing. The experiment of Korobkin and Neuner III did not only confirm the superlensing effect in mid-IR, but also demonstrated its highly resonant nature.
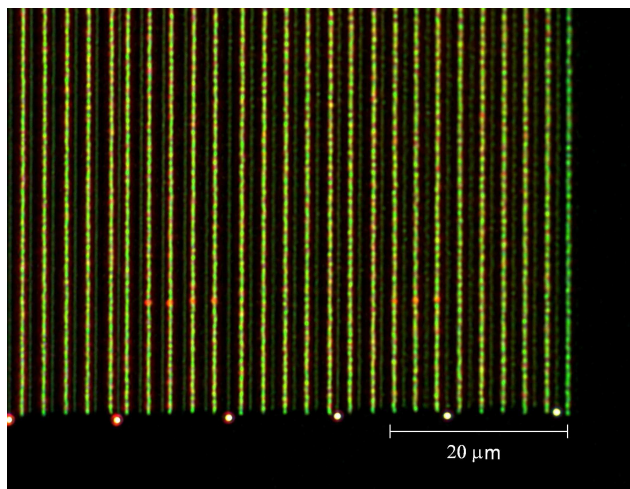
Figure 3.11: Optical transmission microscope image (x100 objective) of the diagnostic structure with half-period shifted slit arrays on both sides of the superlens. Darker lines between bright lines represent the slits on the other side. Image courtesy D. Korobkin and B. Neuner III.

None of the earlier demonstrations of superlensing [MBW04, FLSZ05] demonstrated such strong frequency dependence of superlensing.

3.5 Conclusions

In conclusion, we have experimentally demonstrated that a nanoscale metamaterial consisting of SiC (negative permittivity crystal) and SiO_2 (positive permittivity dielectric) can be used as a near-field superlens in mid-IR capable of significantly enhancing near field resolution. Superlensing manifests itself in imaging a sub-micron slit cut in a metal screen with a resolution exceeding the usual near-field resolution.

A novel far-field diagnostic of superlensing has been developed theoretically and implemented experimentally using a tunable CO_2 laser and a spectral FTIR microscope. By studying transmission through the superlens over a broad range of mid-IR frequencies ($600 < \omega < 1500 \text{cm}^{-1}$), we demonstrated that superlensing is a highly resonant phenomenon occurring in the vicinity of the frequency ω_0 for which the resonance condition $\text{Re}\epsilon_{SiC}(\omega_0) = -\text{Re}\epsilon_{SiO_2}(\omega_0)$ is satisfied. Because
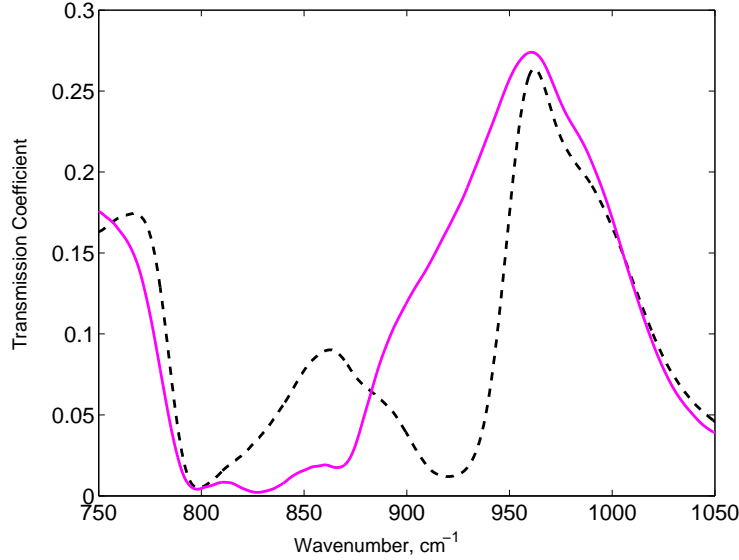
Figure 3.12: FTIR measurements of transmission through the IN (pink solid curve) and OUT (black dashed curve) samples. Data courtesy D. Korobkin.

the transverse shift of the second set of slits causes full loss of transparency, this diagnostics confirms that the constructed dielectric superlens has resolution of at least 1250 nm $\approx \lambda/9$ at $\lambda \approx 11\mu$m.

We have also demonstrated that a three-layer sub-wavelength structure consisting of positive and negative permittivity materials behaves as a metamaterial with an effective dielectric permittivity given by the effective medium theory. This was experimentally proven by us by demonstrating the enhanced transmission through the structure whose effective dielectric permittivity is tuned to that of vacuum. This work paves the way to designing metamaterials with desirable electromagnetic properties in mid-IR. We envision, for example, using electrically tunable negative-ϵ materials, such as TiO_2, as ingredients for electrically controlled metamaterials.

It is interesting to note that after this theoretic work and proof-of-principle experiments were concluded in 2006, deeply sub-wavelength resolution with infrared light was demonstrated with the designed superlens by the Nano-Photonics Group at the Max-Planck-Institute for Biochemistry, Germany [TKU+06]. Figure 3.14 shows near-field infrared SNOM images of three rows of holes that range in diameter

103
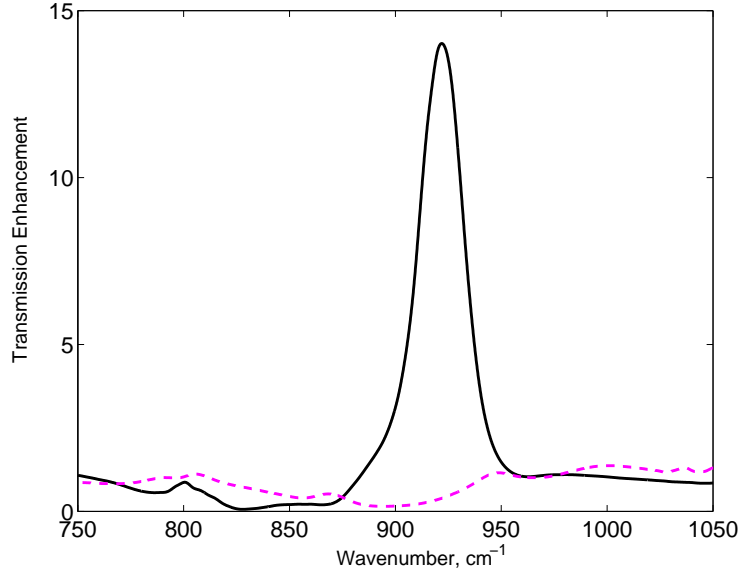
Figure 3.13: Ratio of the transmission coefficients through the IN and OUT Samples as a function of the laser wavelength. Black solid curve: the "right" superlensing structure (200/400/200 nm), pink dashed curve: a structure with "wrong" thickness ratio (400/400/400 nm). Data courtesy D. Korobkin.

from 1200 nm (bottom row) to 860 nm (middle row) and 500 nm (top row). This demonstration has proven that this superlens is capable of resolving essentially two-dimensional objects (circular holes), which is a major improvement relative to earlier superlens demonstrations that utilized 1D gratings (as described in Sec. 3.4). In addition, deeply sub-wavelength (up to $\lambda/20$) resolution was obtained, for the first time, on a series of 2D objects (holes) spaced from each other by only $\lambda/5 \sim 2~\mu$m. This ground-breaking accomplishment validates theoretic work and test-bed experiments discussed in this Chapter.
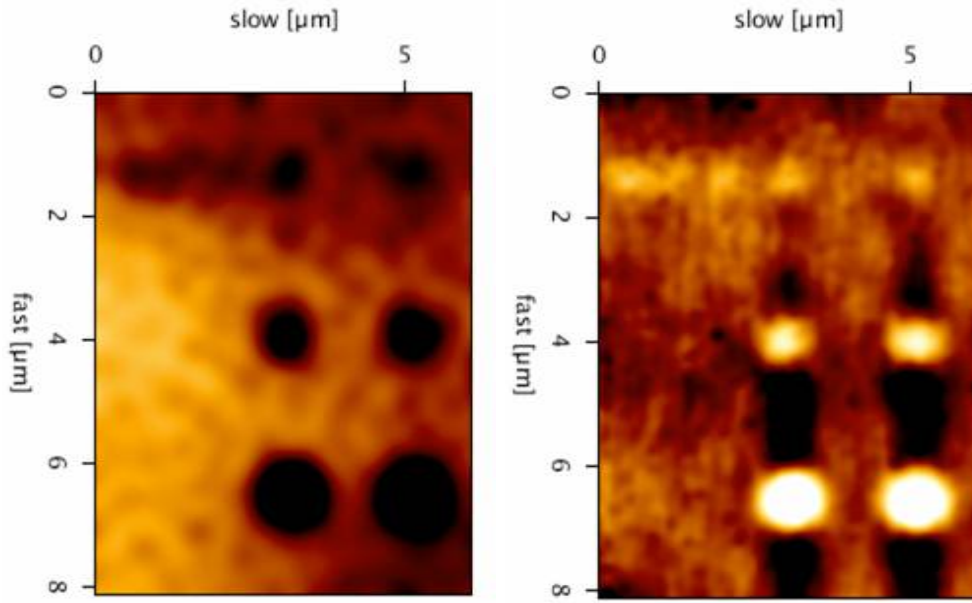
Figure 3.14: Scanning near-field optical microscopy (SNOM) through a 880-nm-thick superlens structure designed in this Chapter. Left: infrared amplitude in the image plane at $\lambda = 10.85$ μm. Right: infrared phase contrast at $\lambda = 11.03$ μm. Images courtesy T. Taubner and R. Hillenbrand.

Chapter 4

Engineering Negative-Index Metamaterials for the Flat Superlens

The ability of periodic dielectric structures to significantly alter the propagation of light has been realized with the introduction of a photonic crystal [Yab87, Joh87, JMW95, Yab94]. To maximize the effect of the structure on the dispersion properties of propagating electromagnetic waves, the crystal period is typically of the order of the light wavelength. Light propagation is affected in several ways: through creation of the stop-bands (band gaps) separating adjacent propagation bands, group velocity reduction near the propagation band edge, generation of cavity states localized near a defect [JMW95], polarization-dependent birefrigence [SMCH03], and extreme anisotropy with respect to propagation direction [US03, US05b]. Applications of dielectric photonic crystals (PhC) include low-loss fibers [CMK$^+$99], microcavity lasers [PLS$^+$99], band-edge quantum cascade lasers, cavity quantum electrodynamics, and development of novel quarter waveplates [SMCH03].

Several even more exotic applications of dielectric PC's have been recently suggested: development of the so-called left-handed (or negative index) materials, flat photonic lenses, and sub-wavelength imaging [LJJP03] capable of exceeding the diffraction limit. Since the resolution of any PC-based lens is limited by the crystal period [SSR$^+$03], beating the diffraction limit requires using a PC with a sub-wavelength period [OP02]. In addition to dielectric PhCs, a new class of metal-

lic photonic crystals (MPC) has recently drawn attention because of their wide bandgap for short wavelengths [Mor00] and the ability to act as efficient filters of electromagnetic radiation [MM93, HL97]. Even more exciting electromagnetic phenomena occurring in MPCs are the existence of left-handed waves [SPV$^+$00] which can be used for sub-wavelength imaging [Pen00] and extreme field enhancement by arrays of metallic nanorods [GSSW04] which can be used for surface-enhanced Raman scattering (SERS). Since all these applications require sub-wavelength scale MPCs, it is important to understand and classify the types of electromagnetic waves supported by such structures.

Moreover, in the optical/UV frequency range metals behave very differently than at the longer wavelengths. Because of the strong (plasma-like) frequency dependence of the metallic dielectric permittivity $\epsilon(\omega)$ in that frequency range, metallic inclusions are referred to as *plasmonic*. Accounting for the dispersion of $\epsilon(\omega)$ becomes necessary, even further complicating an already challenging task of calculating the detailed photonic bands of a PC. To address this challenge, we develop a new technique for calculating dispersion properties of sub-wavelength plasmonic crystals (SPC). This technique is based on the assumption $\omega d/c \ll 1$, where d is the crystal period and c is the speed of light in vacuum. However, we go beyond the traditional electric dipole approximation [BS92, SFB01] and demonstrate how higher-multipole plasmonic resonances can produce magnetic moments of a plasmonic inclusion and give rise to electromagnetic waves with a negative magnetic permeability. When metals are used as negative ϵ inclusions, the typical lattice period that satisfies the "sub-wavelength" criterion is under 50 nm. Therefore, metallic SPCs are necessarily nanostructured. Because the focus of this work is on plasmonic structures, the metallic inclusions will be occasionally referred to as nanorods or nanoparticles.

In this Chapter, we examine several geometries of sub-wavelength plasmonic crystals and in each case, determine if (and how) the structural parameters of such crystals can be chosen to create a double-negative, negative-index band. In two out of four considered geometries, we succeed in finding bands with negative index of refraction. Section 4.1 introduces a two-dimensional SPC consisting of closely-packed metallic cylinders placed in a dielectric matrix. In Section 4.2, another geometrically simple and easy-to-fabricate SPC is studied: arrays of metallic strip pairs (MSP). It is shown that despite initial hopes, this structure cannot be both deeply

107

subwavelength and exhibit negative index at the same time. Problems associated with simple MSP metamaterial are successfully resolved in Sec. 4.3, which introduces a novel, easy-to-fabricate Strip Pair One Film (SPOF) structure. Proof is provided that SPOF metamaterial can exhibit negative index of refraction even in a deeply subwavelength ($a/\lambda = 7$) regime. This Chapter concludes with Section 4.4, which describes an experimentally realizable nanoparticle colloid exhibiting magnetic resonances in strongly sub-wavelength regime. We believe that this Section is an indication that the extremely challenging task of fabricating negative-index *liquids* (or gels) can be solved in the near future.

4.1 Plasmonic nanorod array as a negative-index metamaterial

In this Section we demonstrate how electromagnetic properties of periodic two-dimensional sub-wavelength plasmonic structures consisting of closely-packed inclusions of materials with negative dielectric permittivity ϵ in a dielectric host with positive ϵ_h can be engineered using the concept of multiple electrostatic resonances. Fully electromagnetic solutions of Maxwell's equations reveal multiple wave propagation bands, with the wavelengths much longer than the nanostructure period. It is shown that some of these bands are described using the quasistatic theory of the effective dielectric permittivity ϵ_{qs}, and are independent of the nanostructure period. An additional propagation band characterized by a negative magnetic permeability develops when a magnetic moment is induced in a given nano-particle by its neighbors. Imaging with sub-wavelength resolution in that band is demonstrated.

Electrostatic resonances of isolated nanoparticles occur when a metallic or dielectric particle with a negative frequency-dependent dielectric permeability $\epsilon(\omega) < 0$ is imbedded in a dielectric host (including vacuum) with a positive dielectric permeability $\epsilon_h > 0$. The wavelengths λ of the incident electromagnetic radiation that resonate with a small particle of a characteristic size $d \ll \lambda$ depend on the particle shape and the functional dependence of $\epsilon(\omega)$. By changing the shape and internal composition [JWH$^+$03] of nanoparticles resonances can be shifted to the wavelength optimized for a particular application. Close proximity of other small particles can also strongly affect the resonances. We explore this proximity effect in order to engineer electromagnetic properties of *periodic* arrays of metallic parti-

cles. Because the particle size R and separation d are significantly smaller than the radiation wavelength in vacuum $\lambda \equiv 2\pi c/\omega$, we call these crystals Sub-wavelength Plasmonic Crystals (SPC).

By numerically solving Maxwell's equations, we identify two classes of waves supported by an SPC: (a) hybridized Dipole Modes (DM) that are characterized by a quasistatic period-independent dielectric permittivity $\epsilon_{\mathrm{qs}}(\omega)$, and (b) hybridized Higher-Multipole Modes (HMM) that depend on the crystal period d. Two types of DMs are identified: almost dispersionless (non-propagating) collective plasmons (CPL) satisfying the $\omega(\vec{k}) \equiv \omega_i^{(c)}$ dispersion relation (where $\omega_i^{(c)}$ are multiple zeros of ϵ_{qs}), and propagating collective photons (CPH) satisfying the $\vec{k}^2 c^2 = \omega^2 \epsilon_{\mathrm{qs}}(\omega)$ dispersion relation. The mean-field dielectric permittivity ϵ_{qs} calculated from the quasistatic theory [BS92, SFB01] is found to be highly accurate in predicting wave propagation even for SPCs with the period as large as $\lambda/2\pi$. DM wave propagation bands are "sandwiched" between multiple resonance $\omega_i^{(r)}$ and the cutoff $\omega_i^{(c)}$ frequencies of the SPC.

The new HMM propagation bands are discovered inside the frequency intervals where $\epsilon_{\mathrm{qs}} < 0$ and, by the mean-field description, propagation is prohibited. HMM bands should not be confused with the usual high order Brillouin zones of a photonic crystal because the latter do not satisfy the $d \ll \lambda$ condition. One HMM band defines the frequency range for which the sub-wavelength photonic crystal behaves as a double-negative metamaterial (DNM) that can be described by the negative effective permittivity $\epsilon_{\mathrm{eff}} < 0$ and permeability $\mu_{\mathrm{eff}} < 0$. Magnetic properties of the DNM are shown to result from the induced magnetic moment inside each nanoparticle by high-order multipole electrostatic resonances of its neighbors. It is shown that a thin slab of such DNM can be employed as sub-wavelength lens capable of resolving images of two slits separated by a distance $\ll \lambda$. We will concentrate on two-dimensional SPCs only.

4.1.1 Propagation bands in a two-dimensional SPC

For the remainder of this Section we concentrate on transverse magnetic (TM), also known as p-polarized, electromagnetic waves propagating in the $x - y$ plane of a two-dimensional photonic crystal. Photonic crystal is assumed to be a square array with period d of cylindrical inclusions (rods of radius R infinitely

extended in the $z-$direction) with dielectric permittivity ϵ imbedded in a host material with dielectric permittivity $\epsilon_h \equiv 1$, as shown on the inset of Fig. 4.1. The non-vanishing EM field components are H_z, E_x, and E_y. Propagation bands can be obtained by solving the nonlinear eigenvalue equation for H_z:

$$-\vec{\nabla} \cdot \left(\frac{1}{\epsilon(\omega, \vec{x})} \vec{\nabla} H_z \right) = \frac{\omega^2}{c^2} H_z, \tag{4.1}$$

where H_z satisfies phase-shifted boundary conditions at the edges of the elementary cell:

$$H_z(d/2, y) = e^{ik_x d} H_z(-d/2, y), \ \ H_z(x, d/2) = e^{ik_y d} H_z(x, -d/2) \tag{4.2}$$

The electric field of the wave is given by $\vec{E}(\vec{x}) = -i[c/\omega\epsilon(\vec{x})]\vec{e}_z \times \vec{\nabla} H_z$. The dielectric permittivity $\epsilon(\omega, \vec{x})$ is assumed to be piecewise constant: $\epsilon(\omega, \vec{x}) = \epsilon(\omega)\theta(\vec{x}) + \epsilon_h[1 - \theta(\vec{x})]$, where $\theta(\vec{x})$ is a Heaviside function equal to 1 inside the plasmonic cylinder and 0 outside. Solving Eq. (4.1) yields the dispersion relation ω vs. $\vec{k} = k_x\vec{e}_x + k_y\vec{e}_y$, where $-\pi/d < k_x, k_y < \pi/d$. Due to band folding, multiple Brillouin zones (propagation bands) separated by stop-bands are revealed. Thus $\omega^{(n)2}$, where n labels the Brillouin zones (BZ), is a multi-valued function of $\vec{k}$ and crystal period d. The band edge $\vec{k} = 0$ (Γ-point) corresponds to periodic boundary conditions on H_z.

There is an important difference in the electromagnetic properties of dielectric (with frequency-independent $\epsilon(\omega) \equiv \epsilon_i$) and plasmonic (with $\epsilon(\omega) \equiv 1 - \omega_p^2/\omega^2$) photonic crystals in the limit of $d \to 0$. For small $|\vec{k}| \ll \pi/d$ EM waves propagating through the former can be described using the effective medium $d-$independent dielectric permittivity ϵ_{eff} only for the lowest BZ. For the upper BZs wave frequencies scale inversely proportionally with d. On the other hand, there are two classes of waves supported by a plasmonic PC:

(i) Non-resonant waves (dipole modes) which exist far from electrostatic resonances, and are described by the dispersion relation $k^2 = \epsilon_{\text{eff}}(\omega)\omega^2/c^2$, where for $d \to 0$ $\epsilon_{\text{eff}} = \epsilon_{\text{qs}}(\omega)$. The quasistatic dielectric permittivity $\epsilon_{\text{qs}}(\omega)$ is calculated using the conventional QSED theory [BS92, SFB01] as explained in Sec. 4.1.3.

(ii) Higher-multipole resonances with the dispersion relation $\omega \equiv \omega(k^2 d^2)$. Although these waves are predominantly electrostatic, they can excite a finite magnetic moment inside the plasmonic inclusions. These profound differences between

dielectric and plasmonic periodic structures are caused by the *electrostatic resonances* introduced in Section 4.1.2.

In the rest of the Section we concentrate on the specific SPC shown as an inset in Fig. 4.1: a square lattice of round ($R = 0.45d$) almost-touching *plasmonic* cylinders with the frequency-dependent dielectric permittivity $\epsilon(\omega) = 1 - \omega_p^2/\omega^2$ characteristic of collisions-free electron gas described by the Drude model. The cylinders are separated by the lattice period $d = c/\omega_p$.

4.1.2 Electrostatic resonances in SPCs

For a sub-wavelength rod the right-hand side of Eq. (4.1) can be neglected as long as $\omega^2 d^2/c^2 \ll 1$ (because $\nabla H_z \sim H_z/d$). Hence, the total magnetic field satisfying Eq. (4.1) can be expressed as $H_z = H_{\text{qs}} + H_1$, where H_{qs} satisfies the generalized nonlinear eigenvalue equation (for a real number $\epsilon(\omega)$ and, therefore, implicitly for ω):

$$- \vec{\nabla} \cdot \left(\epsilon^{-1} \vec{\nabla} H_{\text{qs}} \right) = 0, \tag{4.3}$$

where H_{qs} satisfies the phase-shifted boundary conditions described by Eq. (4.2). Equation 4.3 is an eigenvalue equation only in the sense of having non-trivial solutions only for certain values of ϵ. The $\vec{k}$-dependent eigenvalues $\epsilon_j^{(r)}$ of the Eq. (4.3) form a discrete spectrum ($j \in \mathbb{N}$), and the superscript (r) denotes the resonance. The constant $\epsilon_j^{(r)}$ combined with material dispersion $\epsilon(\omega)$ defines the mode frequency $\omega_j^{(r)}$ which can be used to calculate H_1 assumed to be a small correction (of order $\omega^2 d^2/c^2$) to H_{qs}. The inhomogeneous equation for H_1 is

$$- \vec{\nabla} \cdot \left(\epsilon^{-1} \vec{\nabla} H_1 \right) = \frac{\omega^2}{c^2} H_{\text{qs}}, \tag{4.4}$$

where H_1 also satisfies Eqs. (4.2).

It can be shown that the EM waves with frequencies close to $\omega_j^{(r)}(\vec{k})$ are predominantly electrostatic. Indeed, the electric field $\vec{E} = -i[c/\omega\epsilon]\vec{e}_z \times \vec{\nabla} H_z$ can be separated into the electrostatic and solenoidal components: $\vec{E} = \vec{E}_{es} + \vec{E}_{sol}$, where

$$\vec{E}_{es} = -i[c/\omega\epsilon]\vec{e}_z \times \vec{\nabla} H_{\text{qs}} \tag{4.5}$$

and

$$\vec{E}_{sol} = -i[c/\omega\epsilon]\vec{e}_z \times \vec{\nabla}H_1. \tag{4.6}$$

From $|H_{\text{qs}}| \gg |H_1|$ it follows that $|E_{\text{qs}}| \gg |E_{sol}|$. It is straightforward to show that $\vec{\nabla} \times \vec{E}_{es} = 0$, so that the electric field is indeed predominantly electrostatic. Thus, it can be expressed as the gradient of an electrostatic potential ϕ: $\vec{E}_{\text{qs}} = -\vec{\nabla}\phi$. Because in the electrostatic limit Maxwell's equations simplify to $\vec{\nabla} \cdot (\epsilon\vec{E}) = 0$, two equations for ϕ and H_z are simultaneously satisfied for a sub-wavelength plasmonic crystal:

$$-\vec{\nabla} \cdot \left(\epsilon^{-1}\vec{\nabla}H_{\text{qs}}\right) = 0 \quad \text{and} \quad -\vec{\nabla} \cdot \left(\epsilon\vec{\nabla}\phi\right) = 0. \tag{4.7}$$

Equations (4.7) will be used in Section 4.1.4 to derive a useful duality relationship between resonances and cutoffs of electromagnetic waves propagating in an SPC. Note that the electrostatic assumption can only be used in close proximity of the resonant frequencies $\omega_j^{(r)}$. Away from resonances a different procedure described in Section 4.1.3 must be used to describe the propagation of EM waves in an SPC. The perturbative calculation of H_1 according to Eq. (4.4) also loses validity away from the electrostatic resonances.

Electrostatic resonances for the specific SPC are calculated for a range of propagation wavenumbers $\vec{k}$ inside the Brillouin zone by solving the eigenvalue equation (4.7) for ϕ. For computational convenience Eq. (4.7) is recast in the form of

$$\vec{\nabla} \cdot \left[\theta(\vec{x})\vec{\nabla}\phi_i\right] = s_i\nabla^2\phi_i, \tag{4.8}$$

where ϕ_i are the potential functions corresponding to electrostatic resonances satisfying the periodically phase-shifted boundary conditions analogous to Eq. (4.2), and $s_i = (\omega_i^{(r)}/\omega_p)^2$. The dependence of s_i on the wavenumber is presented in Fig. 4.1, where the inset shows four unit cells of the SPC. The wavenumber $\vec{k}$ is labeled in Fig. 4.1 according to the standard convention: $\Gamma - X$ direction is along the $x-$axis and $\Gamma - M$ along the diagonal of the SPC. The finite elements code FEM-LAB [Com03] was used to solve Eq. (4.8). All eigenvalues were computed to at least fourth decimal accuracy as verified by successive refinements of the computational mesh.

Different curves represent different families of resonances labeled according to their symmetry at the Γ-point ($\vec{k} = 0$). For example, the resonance labeled as
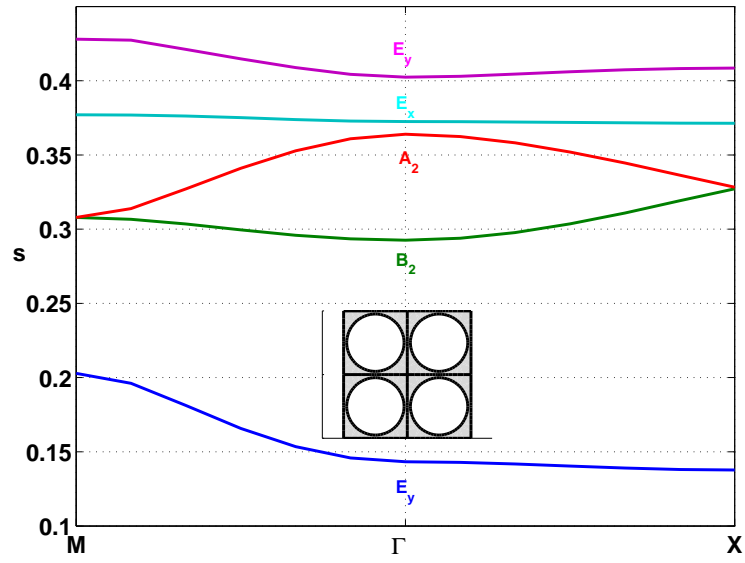
Figure 4.1: Electrostatic resonances of the square lattice SPC consisting of almost touching plasmonic cylinders with $R/d = 0.45$ (shown as inset). Vertical axis: $s = 1/[1 - \epsilon(\omega)] \equiv \omega^2/\omega_p^2$, horizontal axis: wavenumber. Scanned eigenvalue range: $0 < s < 0.45$

B_2 is a quadrupole: its lowest azimuthal dependence is $\phi_i^{(B_2)} \propto \sin 2\theta$ at the Γ-point. Azimuthal dependencies of some of the other resonances are: $\phi_i^{(A_2)} \propto \sin 4\theta$ (octupole), $\phi_i^{(E_x)} \propto \cos \theta$, and $\phi_i^{(E_y)} \propto \sin \theta$ (dipoles). Angular dependencies of the E-modes is given for $\vec{k} = \delta k \vec{e}_x$, where $\delta k d$ is infinitesimal. Resonances labeled as E_y and E_x are special because they have a non-vanishing dipole moment, and describe the modes resonantly excited by a uniform $\vec{E} = E_0 \vec{e}_y$ or $\vec{E} = E_0 \vec{e}_x$ fields, respectively. E_x and E_y are hybridized dipole resonances while the others (e. g. A_2 and B_2) are higher-multipole resonances (HMR). Note that the wavenumber enters Eq. (4.7) only through the boundary conditions, and only through the combinations $k_x d$ and $k_y d$. Therefore, the dispersion relations for all resonances have the ω vs. $|\vec{k}| d$ dependencies, and, therefore, are period-dependent.

It would be tempting to assume that the propagation curves in Fig. (4.1) calculated in the vanishing period limit $\omega^2 d^2/c^2 \ll 1$ accurately describe *all* waves propagating in a finite-d SPC. This turns out not to be the case. Electrostatic calculation is accurate only in close proximity of electrostatic resonances. Away from those resonances the electrostatic assumption is invalid, and other modes emerge. For instance, by numerically solving the full electromagnetic Eq. (4.1), we have identified a propagating mode below the lowest In frequency) electrostatic E_y resonance ($s < 0.14$). That mode merges with the E_y curve for $|\vec{k}| \gg 1/d$.

It is also found, based on the group theoretical analysis of Eq. (4.1) explained in Sec. 4.1.5, that the electromagnetic modes form a doublet at the $\Gamma-$point corresponding to the E_x resonance. The degeneracy is removed for finite $\vec{k} = k_x \vec{e}_x$, and the doublet is split into lower and higher frequency modes. The low-frequency mode of the doublet referred to as a bulk plasmon (BP) is $x-$ polarized, practically dispersionless, and has the propagation properties almost identical to the electrostatic E_x mode. The high-frequency mode referred to as the plasmon polariton (PP) is $y-$ polarized and occupies a much wider frequency range than the BP: between the E_x and E_y resonances. For large $|\vec{k}| \gg 1/d$ the PP's frequency approaches that of the E_y resonance, and the dispersion curve of the PP merges with that of E_y. The $x-$ and $y-$polarized electromagnetic waves are strictly frequency-degenerate at the $\Gamma-$point, whereas the approximate electrostatic calculation in Fig. (4.1) gives a misleading impression that they are not. Both BP and PP are hybridized dipole modes because, as shown in Sec. 4.1.3, their fields can be expanded as a sum of hybridized dipole resonances.

Other propagating electromagnetic modes of a finite-period SPC are not frequency-degenerate at the $\Gamma-$point. Those modes indeed are the hybridized higher-order multipole resonances. Even for finite sized nanoparticles HMR's dispersion relations are very accurately described by the dispersion curves shown in Fig. 4.1. Electromagnetic properties of HMR bands are period-dependent because ω depends on $|\vec{k}|d$.

4.1.3 Quasistatic electric dipole theory of SPC

Away from multipolar electrostatic resonances a well-established methodology exists for characterizing the frequency-dependent electromagnetic properties of a nano-structure. This is done by introducing a frequency-dependent quasistatic dielectric permittivity $\epsilon_{qs}(\omega)$ of a nanostructure [BS92, SFB01], as described in detail in Section 2.2. We refer to this approach as the quasistatic electric dipole (QSED) theory because it takes into account only hybridized dipole resonances of the nano-structure. For the frequencies sufficiently distanced from higher-multipole resonances this is a justifiable assumption: dipole scattering by individual particles dominates over the multipolar scattering.

From the theory of quasistatic permittivity presented in Section 2.2 it follows that only the resonances with a non-vanishing dipole moment at the Γ-point contribute to $\epsilon_{qs}(\omega)$. For example, the E_y resonances from Fig. (4.1) contribute to ϵ_{qs} while the A_2, B_2, and E_x do not. We conjecture, and later verify, that the quasistatic dielectric permittivity $\epsilon_{qs}(\omega)$ calculated from Eqs. (2.12,2.13) can be used for deriving the dispersion characteristics of $y-$polarized electromagnetic waves propagating in $x-$direction.

The dipole strengths can be significantly simplified for a square lattice of round plasmonic rods. Because the square lattice is invariant with respect to the transformations of the C_{4v} point group [Lyu60], all periodic solutions transform according to one of the irreducible representations (irreps) of C_{4v}: four singlets (commonly labeled as A_1, A_2, B_1, and B_2) and one doublet E. The electrostatic eigenfunctions with a non-vanishing dipole moment $\phi_i^{(E)}$ and $\tilde{\phi}_i^{(E)}$ have the symmetry of E. By symmetry, inside a given rod each $\phi_i^{(E)}$ can be expanded as the sum of multipoles:

$$\phi_i^{(E)}(r,\theta) = \sum_{l=0}^{\infty} A_i^{(2l+1)}(r/R)^{2l+1}\sin{(2l+1)}\theta. \tag{4.9}$$

Because ϵ is a piecewise constant function of the radius, and $\nabla^2\phi_i = 0$ inside and outside of the rod, for any ϕ_i we can simplify

$$\nabla^2\phi_i = \delta(r - R) \times [\partial_r\phi_i(r = R + 0) - \partial_r\phi_i(r = R + 0)]. \tag{4.10}$$

By continuity of $\epsilon(r)\partial_r\phi_i$ we can further simplify

$$\nabla^2\phi_i = \delta(r - R)(\epsilon_i - 1)\partial_r\phi_i(r = R - 0). \tag{4.11}$$

Using the multipole expansion inside the rod one finds that the dipole strength is proportional to the dipole component of $\phi_i^{(E)}$:

$$f_i = \left(A_i^1\right)^2 / \sum_{l=0}^{\infty}(2l + 1)\left(A_i^{2l+1}\right)^2. \tag{4.12}$$

For the plasmonic structure analyzed here there are three significantly strong hybridized dipole resonances: $(s_1 = 0.1433, f_1 = 0.8909)$, $(s_2 = 0.4025, f_2 = 0.064)$, and $(s_3 = 0.6275, f_3 = 0.0366)$. In general, there are infinitely many hybridized dipole resonances, most of them clustering around the singular point of $s_i = 1/2$ (or $\omega_i = \omega_p/\sqrt{2}$) which corresponds to the resonance of an *isolated* plasmonic rod. In Section 2.2, a generalized sum rule for electric oscillators was proven. In the case of disconnected plasmonic inclusions such non-touching cylinders, the quantity f_0 vanishes, and the sum rule reduces to

$$\sum_{n=1}^{\infty} f_n = 1. \tag{4.13}$$

Because numerically $\sum_{n=1}^{3} f_n = 0.992$, we are justified in neglecting weaker dipole resonances and using the strongest three in Eq. (2.12) for calculating $\epsilon_{qs}(\omega)$. The potential functions $\tilde{\phi}_i$ of the three strongest dipole resonances (corresponding to the electric field in $x-$direction) are shown in Fig. 4.2(a-c). The first resonance is primarily dipolar ($\propto \cos\theta$) while the second one has a significant sextupolar ($\propto \cos 3\theta$) component. Thus, the close proximity of the rods in the lattice results in a strong hybridization of the odd multipoles with the dipole. Moreover, the hybridized dipole resonances $\omega_1^{(r)} = 0.38\omega_p$, $\omega_2^{(r)} = 0.63\omega_p$, and $\omega_3^{(r)} = 0.79\omega_p$ occur at the frequencies *controllably* different (through the R/d ratio) from that
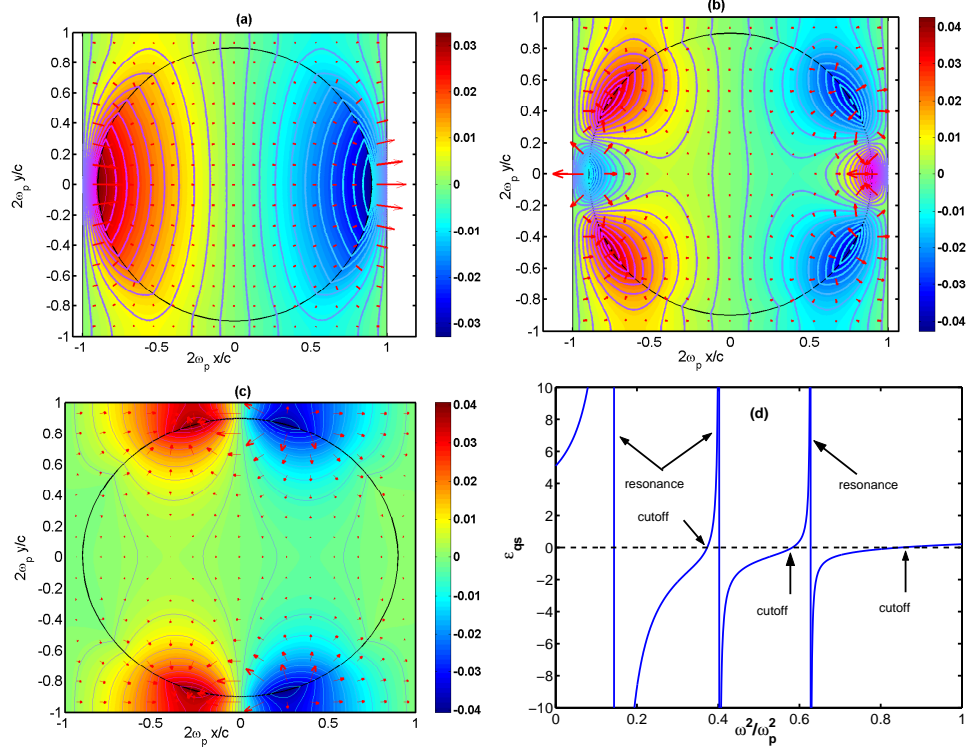
Figure 4.2: (a-c) The potential functions of the three strongest hybridized dipole resonances of the SPC with parameters from Fig. (4.1), in the order of decreasing dipole strength (contours) and the corresponding electric field (arrows). (d) Quasistatic dielectric permittivity ϵ_{qs} vs. ω calculated from Eq. (2.12) using the three strongest resonances.

of an isolated rod, $\omega^{(r)} = \omega_p/\sqrt{2}$. Red-shifting of the strongest dipole resonance of a nanoparticle due to close proximity of other nanoparticles has been observed experimentally [MJB00].

The corresponding quasistatic dielectric permittivity ϵ_{qs} is plotted in Fig. 4.2(d) as a function of the frequency ω. Infinities of ϵ_{qs} correspond to electrostatic dipole resonances. In calculating $\epsilon_{qs}(\omega)$ we have neglected the finite damping in the plasmonic rods. If damping is accounted for, the infinities of ϵ_{qs} are removed. Another set of special frequencies $\omega_i^{(c)}$ are the cut-off frequencies for which $\epsilon_{qs}(\omega_i^{(c)}) = 0$. For the structure analyzed here there are three such frequencies: $\omega_1^{(c)} = 0.61\omega_p$, $\omega_2^{(c)} = 0.77\omega_p$, and $\omega_3^{(c)} = 0.93\omega_p$. Note that ϵ_{qs} is

independent of the SPC periodicity scale d and is only dependent on the geometry (i. e. R/d). Therefore, the quasistatic ϵ_{qs} approach is the effective medium theory which neglects the internal structure the SPC.

4.1.4 Duality theorem for SPC: relation between cut-off and resonance frequencies

We have discovered that for a highly-symmetric square lattice the cut-off and resonance frequencies are related to each other by a simple formula: for each resonance frequency $\omega_j^{(r)}$ there exists a cutoff frequency $\omega_i^{(c)}$ for which $\epsilon(\omega_i^{(c)}) = 1/\epsilon(\omega_j^{(r)})$. Numerical calculation of the zeros of ϵ_{qs} from Eq. (2.12) accurately confirms the duality principle. Below the duality principle in an SPC is rigorously derived. This principle is a combination of a known duality theorem of two-dimensional electrostatics [Kel64] with rotational invariance of C_{4v} lattice (or any lattice with C_n axes of symmetry, $n = 3, 4, 6$).

First we review a related duality principle for the resonances of an isolated plasmonic nano-cylinder of an arbitrary shape. Recall that Eqs. (4.7) are simultaneously satisfied for the electrostatic potential ϕ and magnetic field H_{qs}. Because the electric field is *normal* to $\phi = $ const lines and *along* the $H_{qs} = $ const lines, Eqs. (4.7) simply illustrate that in electrostatics there are two equivalent descriptions of the electric field: using potentials and field lines. Both H_{qs} and ϕ must vanish far away from the cylinder. It follows from Eqs. (4.7) that if a resonance is supported by a rod of an arbitrary transverse shape for $\epsilon = \epsilon_1$, then there exists another resonance for $\epsilon_2 = 1/\epsilon_1$ [FM03]. For the resonances with $\epsilon = \epsilon_1$ and $\epsilon = \epsilon_2$ electric field lines and potential iso-contours are simply interchanged. Hence, the duality principle for isolated nano-rods: all electrostatic resonances occur for frequency pairs (ω_1, ω_2) such that $\epsilon(\omega_1) = \epsilon_1$ and $\epsilon(\omega_2) = 1/\epsilon_1$.

Symmetry considerations must be used for deriving a duality relation for a two-dimensional SPC. Let's assume that an electrostatic resonance is found for $\epsilon = \epsilon_1$ for a $y-$polarized electric field. The corresponding potential eigenfunction ϕ_1 is a solution of Eq. (4.7) and satisfies the following homogeneous conditions at the unit boundaries $(x, y) = (\pm d/2, \pm d/2)$: (a) ϕ_1 and its derivatives are periodic; (b) $\phi_1(y = \pm d/2) = 0$; (c) $\partial_x \phi_1(x = \pm d/2) = 0$. By symmetry, another eigenfunction $\tilde{\phi}_1$ obtained by a $90-$degree spatial rotation of ϕ_1 also satisfies Eq. (4.7). Next, consider

a pair of magnetic field functions $H_z^{E_x} = \phi_1$ and $H_z^{E_y} = \tilde{\phi}_1$, and the frequency ω_2 such that $\epsilon(\omega_2) = 1/\epsilon_1$. It follows from Eq. (4.7) that $H_z^{E_x}$ and $H_z^{E_y}$ both satisfy Eq. (4.1) in the quasistatic limit of $\omega^2 d^2/c^2 \ll 1$. Moreover, the periodic boundary conditions satisfied by $(H_z^{E_x}, H_z^{E_y})$ indicate that the pair are the magnetic fields of the BP and PP at the cut-off point of $\vec{k} = 0$ (see Eq. (4.2)). Therefore, ω_2 is the cut-off frequency. The inverse is also true: if the cut-off frequency is ω_3, than there is a resonance at ω_4 such that $\epsilon(\omega_4) = 1/\epsilon(\omega_3)$.

Using a frequency-dependent label $s(\omega) = 1/(1 - \epsilon(\omega))$ (which reduces to $s(\omega) = \omega^2/\omega_p^2$ for the plasmonic dielectric permittivity $\epsilon(\omega) = 1 - \omega_p^2/\omega^2$), the duality condition can also be expressed as $s(\omega_i^{(r)}) + s(\omega_j^{(c)}) = 1$ (which reduces to $\omega_i^{2(r)} + \omega_j^{2(c)} = \omega_p^2$ for the plasmonic ϵ). We have verified that indeed, with high accuracy, $\omega_1^{(r)2} + \omega_3^{(c)2} = \omega_p^2$, $\omega_2^{(r)2} + \omega_2^{(c)2} = \omega_p^2$, and $\omega_3^{(r)2} + \omega_1^{(c)2} = \omega_p^2$ for the particular plasmonic structure considered in this Section.

4.1.5 Correspondence between electromagnetic and quasistatic bands associated with electric dipoles

Symmetry considerations are very useful in classifying the electromagnetic modes supported by an SPC. The square lattice of the SPC is invariant with respect to the transformations of the C_{4v} point group [Lyu60]. Symmetry arguments can be most readily applied to the highly symmetric Γ-point of the electromagnetic bands corresponding to $\vec{k} = 0$. The eigenmodes of Eq. (4.1) satisfy the periodic boundary conditions at the Γ-point. Thus these periodic solutions transform according to one of the irreducible representations (irreps) of C_{4v}: four singlets (commonly labeled as A_1, A_2, B_1, and B_2) and one doublet E. The Γ-point solutions can also be labeled according to their irreps. Only the doublet E has a non-vanishing dipole moment. Therefore we expect that some of the solutions of Eq. (4.1) are non-degenerate at the $\Gamma-$point (singlets) while others are doubly-degenerate (doublets).

By numerically solving Eq. (4.1) some of the representative propagation bands have been computed for a range of frequencies $0 < \omega < 0.7\omega_p$ and propagation wavenumbers $\vec{k} = k\vec{e}_x$. The resulting ω vs. k dispersion relations are marked by symbols (circles and triangles) in Fig. (4.3). The lowest propagation band (circles) starts at the origin and approaches what appears to be a resonance. Electric field of the propagating mode is primarily in y-direction, and the resonant frequency is
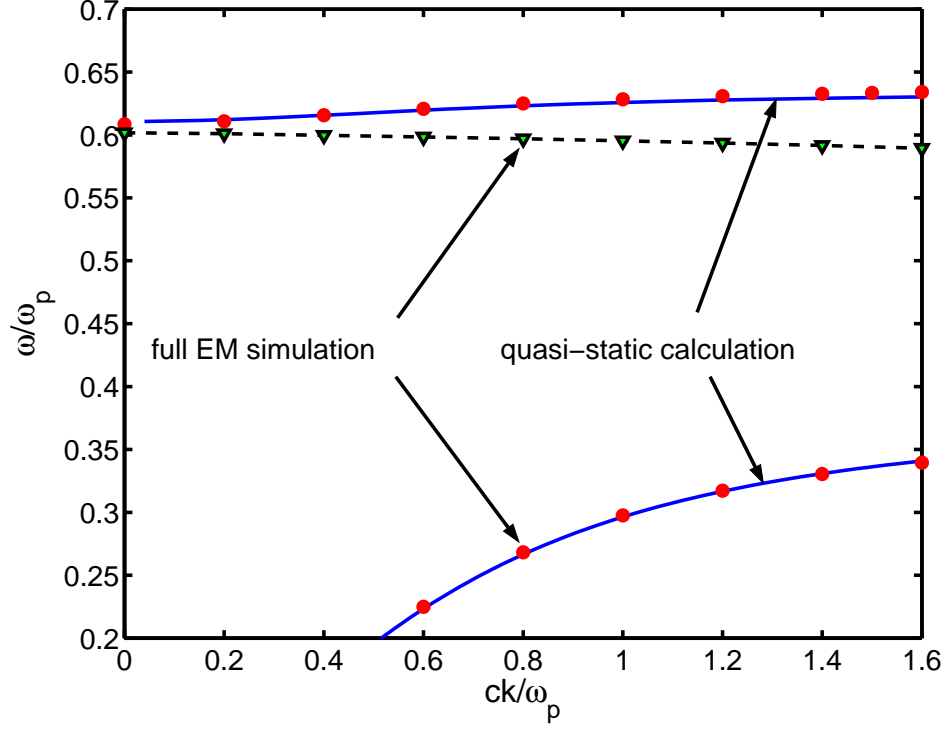
Figure 4.3: Propagation bands in an SPC with parameters from Fig. 4.1 and $d = c/\omega_p$. Circles and triangles: calculated by solving Eq. (4.1). Solid lines: predictions of the quasistatic electric dipole theory, $k = \sqrt{\epsilon_{qs}}\omega/c$.

close to that of the lower E_y resonance ($\omega = 0.37\omega_p$) in Fig. (4.1) at the Γ-point. The two frequencies cannot be expected to exactly coincide because the SPC period, while sub-wavelength, is still finite: $d = c/\omega_p$.

The upper propagation band starts at $\omega \approx 0.61\omega_p$, where it turns out to be a doublet consisting of (i) a non-propagating collective plasmon BP with $\omega(k) \approx 0.61\omega_p$ (not shown due to its flatness in frequency), and (ii) a propagating PP whose dispersion is shown by circles in Fig. (4.3). The frequency of the BP coincides with that of the E_x resonance in Fig. (4.1). That is so because EM fields of the BP are largely electrostatic ($|E_x| \gg |H_z|$) for all values of k. The propagation band of the PP is very narrow: $0.61\omega_p < \omega < 0.63\omega_p$; it is bounded from above by a resonance at $\omega = 0.63\omega_p$ which coincides with that of the upper E_y resonance in Fig. (4.1) at the Γ-point. As explained in Sec. 4.1.3, for small $k \ll \pi/d$ these

two propagation bands are sufficiently far away from electrostatic resonances to be accurately described by the scale-independent effective dielectric permittivity $\epsilon_{\text{qs}}(\omega)$ calculated using QSED theory. The results of the full electromagnetic calculation (circles) closely follow the theoretical curves $k = \sqrt{\epsilon_{\text{qs}}}\omega/c$.

The middle propagation band (marked by triangles) corresponds to the electrostatic resonance A_2 shown in Fig. (4.1). Wave dispersion in this band cannot be derived from ϵ_{qs} because of its proximity to the octupole resonance. Note that for the A_2-symmetric band we have $\partial\omega/\partial k < 0$: its group and phase velocity oppose each other. Such behavior is also found in negative refractive index meta-materials which are characterized by the negative effective permittivity $\epsilon_{\text{eff}} < 0$ and permeability $\mu_{\text{eff}} < 0$ [SPV$^+$00]. Section 4.1.7 explains the origin of the negative effective magnetic permeability of this wave.

4.1.6 Transverse and longitudinal modes associated with quasistatic permittivity

Propagation properties of electromagnetic waves through any medium (including an SPC) characterized by the effective medium $\epsilon_{\text{eff}}(\omega)$ can be obtained by solving the Maxwell's equations in the medium for space-averaged quantities $\vec{\mathcal{H}}$ and $\vec{\mathcal{E}}$ [LL84]:

$$\vec{\nabla} \times \vec{\mathcal{E}} = \frac{i\omega}{c}\mu_{\text{eff}}\vec{\mathcal{H}}, \quad \vec{\nabla} \times \vec{\mathcal{H}} = -\frac{i\omega\epsilon_{\text{eff}}}{c}\vec{\mathcal{E}}, \tag{4.14}$$

where the electromagnetic field is assumed to be harmonic in time.

The prescription for calculating the averaged fields for a three dimensional photonic crystal has been introduced elsewhere [OP02, PHRS99]. Modifications to those procedures were made in order to adapt them to the two-dimensional problem at hand. Specifically, we assumed that the elementary cell is a cube with the height d in the $z-$direction. Because all physical quantities (electric and magnetic fields) are $z-$independent, surface integrals over the faces parallel to z are reduced to line integrals. For two dimensions, and assuming that the elementary cell of the SPC is centered at the origin, the averaged $\vec{\mathcal{E}}$ and $\vec{\mathcal{D}}$ are defined as $\mathcal{E}_y = d^{-1}\int_{-d/2}^{+d/2} dy\, E_y(x = -d/2, y)$, $\mathcal{E}_x = d^{-1}\int_{-d/2}^{+d/2} dx\, E_x(x, y = -d/2)$, $\mathcal{D}_y = d^{-1}\int_{-d/2}^{d/2} dx E_y(x, y = -d/2)$, $\mathcal{D}_x = d^{-1}\int_{-d/2}^{d/2} dy E_x(x = -d/2, y)$. Since away from electrostatic resonances SPC does not exhibit magnetic properties, it is assumed that $\mu_{\text{eff}} = \mathcal{B}_z/\mathcal{H}_z \equiv 1$, where $\mathcal{B}_z = d^{-2}\int dA H_z(x, y)$, $\mathcal{H}_z = H_z(x = -d/2, y = -d/2)$ [PHRS99].

For small $|\vec{k}| \ll 1/d$ the standard definition of $\epsilon_{\text{eff}} = \mathcal{D}_x/\mathcal{E}_x = \mathcal{D}_y/\mathcal{E}_y$ exactly coincides with that of ϵ_{qs}. Therefore, $\epsilon_{\text{qs}}(\omega)$ computed from Eq. (2.12) replaces ϵ_{eff} in Eqs. (4.14). Assuming a planar wave with a wavenumber $\vec{k}$, it is found from Eq. (4.14) that two distinct classes of modes are supported by the medium: (a) longitudinal modes with $\vec{\mathcal{E}} \parallel \vec{k}$, and (b) transverse modes with $\vec{\mathcal{E}} \perp \vec{k}$. We refer to the longitudinal waves as bulk plasmons (BP) and the transverse ones as plasmon polaritons (PP). The dispersion relation for a BP is $\omega(\vec{k}) \equiv \omega_i^{(c)}$. Thus the cut-off frequencies also coincide with those of the BPs. For example, $\omega_1^{(c)}$ almost exactly coincides with the frequency (evaluated at the Γ-point) of the longitudinal resonance E_x shown in Fig. 4.1. The small difference is due to the finite ratio of d/λ. The dispersion relation for a PP is $|\vec{k}|^2 = \epsilon_{\text{qs}}\omega^2/c^2$.

The frequency bands between the cut-offs and resonances define the non-resonant propagation bands of the PP's. From Fig. 4.2(d), there are four propagation bands (where $\epsilon_{\text{qs}} > 0$) predicted by the quasistatic theory for $\omega < \omega_p$. The first propagation band is fairly broad, extending from $\omega = 0$ to $\omega_1^{(r)} = 0.38\omega_p$. The second band is very narrow: between $\omega_1^{(c)} = 0.61\omega_p$ and $\omega_2^{(r)} = 0.63\omega_p$. This band is "sandwiched" between two electrostatic resonance curves shown in Fig. 4.1: longitudinal resonance E_x and transverse resonance E_y. Two modes exist inside the band: a BP with $\omega(\vec{k}) = \omega_1^{(c)}$ and a PP. These propagation bands are also revealed by the full electromagnetic simulation of Eqs. (4.1,4.2), and are shown in Fig. 4.3 (circles) to be in a very good agreement with the prediction of the QSED theory (solid lines). The third, also very narrow, propagation band is between $\omega_2^{(c)} = 0.77\omega_p$ and $\omega_3^{(r)} = 0.79\omega_p$, and it also supports a non-propagating BP and a propagating PP. The fourth band extends upwards in frequency from $\omega_3^{(c)} = 0.93\omega_p$. None of the four propagation bands are revealed by the approximate electrostatic calculation which resulted in the band structure shown in Fig. 4.1.

4.1.7 Propagation bands associated with negative magnetic permeability: origin of negative refraction

In Section 4.1.3 electromagnetic properties of the SPC for frequencies sufficiently distanced from higher multipole resonances were described using the quasistatic electric dipole theory. The justification for QSED theory is that the dipole scattering of incident electromagnetic waves by individual nanoparticles dominates

over high-multipole scattering. This is not the case for frequencies very close to those of electrostatic multipole resonances [AKSV99]. For those frequencies multipolar scattering is resonantly enhanced, and can dominate over the dipolar scattering. That the QSED theory may be inadequate for describing all propagating modes in an SPC becomes apparent by noting that the propagation band marked by triangles in Fig. (4.3) belongs to the frequency range where $\epsilon_{\mathrm{qs}} < 0$. Therefore, in the vicinity of the A_2 electrostatic resonance QSED description breaks down, and the resonant frequency broadens into a frequency band with a finite group velocity $\vec{v}_g = \partial\omega/\partial\vec{k}$.

Moreover, we show that an SPC can also exhibit a finite magnetization, i.e. $\vec{\mathcal{B}} \neq \vec{\mathcal{H}}$. Whether or not finite magnetization exists depends on the azimuthal dependence of the resonant field. Here we concentrate on the A_2 resonance. Recall that in the vicinity of electrostatic resonance $H_z = H_{\mathrm{qs}} + H_1$, where H_{qs} is responsible for the electrostatic (potential) portion of the electric field, and H_1 is perturbatively calculated using Eq. (4.4). Although the electric field near resonance is mostly electrostatic, it possesses a non-vanishing solenoidal component:

$$\vec{E} = -\vec{\nabla}\phi + \vec{S}, \tag{4.15}$$

where $\vec{S}$ is a purely solenoidal field $\vec{\nabla} \cdot \vec{S} = 0$, and ϕ, $\vec{S}$ satisfy

$$\vec{\nabla} \times \vec{S} = i\frac{\omega}{c}H_{\mathrm{qs}}\vec{e}_z \quad \text{and} \quad -\nabla^2\phi \approx i\frac{c}{\omega}\vec{e}_z \cdot \left(\vec{\nabla}\epsilon^{-1} \times \vec{\nabla}H_{\mathrm{qs}}\right). \tag{4.16}$$

It is this small (to order $\omega^2 d^2/c^2$) solenoidal part of the electric field that is responsible for the magnetic properties of an SPC. Those magnetic properties can manifest themselves as the negative magnetic permeability in the vicinity of an electrostatic resonance, and give rise to the negative refractive index [SPV$^+$00].

The magnetic permeability μ_{eff} is affected because the A_2 mode carries the electric current which produces a finite magnetic moment. The electrostatic $\vec{E}$−field of the mode inside the plasmonic rod is derived from the electrostatic potential

$$\phi = \sum_{n=1}^{\infty} \Phi_n^{(A_2)} \left(\frac{r}{R}\right)^{4n} \sin 4n\theta. \tag{4.17}$$

Electric field lines correspond to the iso-contours of the quasistatic magnetic field

123

given by

$$H_{\text{qs}} = \sum_{n=1}^{\infty} H_n^{(A_2)} \left(\frac{r}{R}\right)^{4n} \cos 4n\theta. \tag{4.18}$$

The expansion coefficients $\Phi_n^{(A_2)}$ and $H_n^{(A_2)}$ are found numerically by solving Eqs. (4.7) with periodic boundary conditions. Although we label electromagnetic modes according to the spatial symmetry of their electrostatic potential, note from Eqs. (4.17,4.18) that the electrostatic potential and the magnetic field transform according to the A_2 and A_1 irreducible representations, respectively. This is a general property of a square (and hexagonal) SPC's: ϕ and H_{qs} belong to the complimentary irreducible representations.

The monopole term $H_0^{(A_2)}$ does not contribute to the electrostatic field in the quasistatic limit. However, for a finite particle size there is a non-vanishing solenoidal electric field according to Eqs. (4.15,4.16). By the Stokes' theorem, the azimuthal electric field inside the particle is found from $2\pi r E_\theta = i(\pi r^2)H_0^{(A_2)}\omega/c$ to be $E_\theta = i(\omega r/2c)H_0^{(A_2)}$. The corresponding electric current in the plasmonic rod is given by $J_\theta = -H_0^{(A_2)}\omega^2 r/2c^2 \times (\epsilon - 1)$. This current produces a magnetic moment density $\vec{M} = (1/2c)\langle \vec{r} \times \vec{e}_\theta J_\theta \rangle$, where the average is taken over the unit cell. After straightforward algebra one gets

$$M = (pH_0^{(A_2)}/16\pi)(1 - \epsilon)\omega^2 R^2/c^2. \tag{4.19}$$

The magnitude of the induced magnetic moment depends on two factors: the particle size (through the $\omega^2 R^2/c^2$ term) and the inter-particle proximity (through the value of $H_0^{(A_2)}$ which rapidly decreases as the function of R/d).

Importantly, Fig. 4.3 reveals that there is another propagation band (diamonds) in the frequency range for which no propagation is expected due to $\epsilon_{\text{qs}} < 0$. Note that the mode's group velocity $v_g = \partial\omega/\partial k < 0$ opposes its phase velocity – an indication that we are dealing with a DNM. For $\vec{k} = 0$ this mode's H_z has the symmetry of the A_1 irrep of the symmetry group C_{4v}, and can be expanded inside a given plasmonic rod as

$$H_z(r,\theta) = \sum_{k=0}^{\infty} A^{(4k)} \left[I_{4k}(\omega\sqrt{-\epsilon}r/c)/I_{4k}(\omega\sqrt{-\epsilon}R/c) \right] \cos(4k\theta), \tag{4.20}$$

where I_l is the modified Bessel function of order l. Because there is no dipole component in H_z, the A_1 mode does not contribute to the quasistatic permittivity ϵ_{qs}. We therefore refer to this and other singlet modes as the higher-order multipole resonance (HMR) bands. For the SPC at hand, the largest term in the expansion is the octupole term $A^{(4)}$, and the next largest is the monopole term $A^{(0)}$ that is responsible for the magnetic moment induced in the photonic structure as explained earlier. Therefore, the mode is an HMR, with predominantly $m = 4$ component.

We have calculated the effective permittivity ϵ_{eff} and permeability μ_{eff} using the procedure explained in Sec. 4.1.6. Both ϵ_{eff} and μ_{eff} have been calculated for a range of wavenumbers $\vec{k} = k\vec{e}_x$ and the corresponding frequencies $\omega(k)$. For $kd \ll \pi$ it follows from the analyticity of $\omega(\vec{k})$ that the frequency depends only on $|\vec{k}|$ and not on its direction. For $k_0 = 0.6/d$ and $\omega_0 = 0.6\omega_p$ (or $n_{\text{eff}} = -1$) we numerically computed that $\mu_{\text{eff}} = -2.35$ and $\epsilon_{\text{eff}} = -0.427$. Therefore, at this frequency our SPC can be viewed as a double-negative material. This is consistent with the negative group velocity of the A_2 wave. Note that the hybridized monopole/octupole resonance affects not only the magnetic permeability of the SPC, but also the dielectric permittivity: the effective medium calculation using Eq. (2.12) yields $\epsilon_{qs}(\omega_0) = -0.65$ that is significantly different from ϵ_{eff}.

4.1.8 Sub-wavelength resolution with SPC slab in a double-negative propagation band

DNM-based flat superlenses capable of sub-wavelength imaging have been proposed [Pen00]. The condition for superlensing is that the DNM with the dielectric permittivity $\epsilon < 0$ is embedded in a host medium with $\epsilon_h = -\epsilon$. We have tested a six-period thick plasmonic SPC for the superlensing effect by embedding it inside the hypothetic host with $\epsilon_h = 0.55$. This particular choice of $-\epsilon_{\text{eff}} < \epsilon_h < -\epsilon_{qs}$ was not optimized, and is one among the several that showed superlensing. To verify the sub-wavelength resolution, we simulated the distribution of the magnetic field $|\vec{E}|$ behind a screen with narrow slits of width $\Delta_y = \lambda/5$ separated by a distance $2\Delta_y$. As depicted in Fig. 4.4, where only two slits are shown, a planar wave with frequency $\omega = 0.6\omega_p$ is incident on the screen from the left. A six-period long plasmonic SPC of width $D = 0.6\lambda$ is positioned between $0 < x < D$. The distribution of $|\vec{E}|$ in the $x - y$ plane is shown in Fig. 4.4(a). Also, in Fig. 4.4(b) $|\vec{E}|$ is plotted in two

125
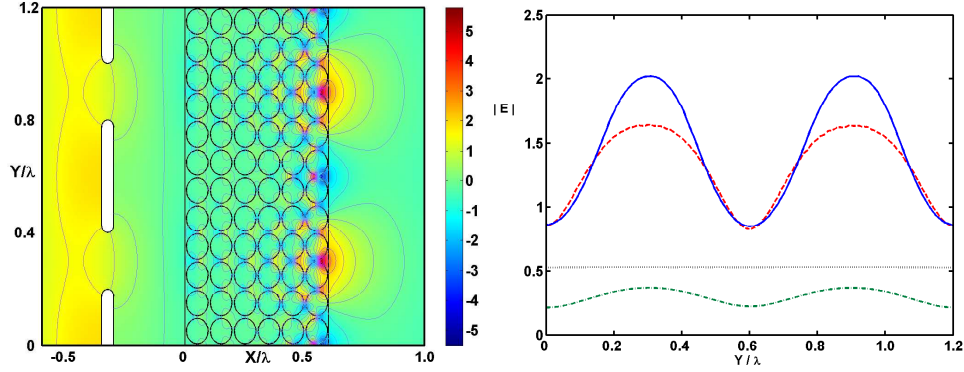
Figure 4.4: (a) Left: Magnetic field distribution behind an illuminated periodic slit array, with a six-period SPC, parameters as in Fig. 4.2. (b) Right: $|\vec{E}|$ in the object plane (blue solid line); in the image plane for $\omega_0 = 0.6\omega_p$, without damping (red dashed line) and with damping characteristic of silver (green dot-dashed line); in the image plane for $\omega = 0.606\omega_p$ (black dotted line).

cross-sections: the object plane right behind the screen (at $x = -D/2 + \lambda/10$, solid line), and in the image plane (at $x = 3D/2 - \lambda/10$, dashed line). Object plane is slightly displaced from the screen to avoid $\vec{E}$-field spikes at the slit edges. The two sub-wavelength slits are clearly resolved. Increasing the incident frequency by just 1% (outside of the DNM band) results in the complete loss of resolution in the image plane (dotted line).

Even small material losses can have a strong effect on the resolution [SSR$^+$03]. While the DNM band for the plasmonic SPC is quite narrow, $[\omega(k = 0) - \omega(k = \pi/d)]/\omega(k = 0) = 0.055$, it is still broader than the collisional linewidth for some plasmonic materials. For example, for silver $\epsilon = \epsilon_b - \omega_p^2/\omega(\omega + i\gamma)$, where $\epsilon_b \approx 5$, $\omega_p = 9.1$ eV, and $\gamma = 0.02$ eV [JC72]. Fig. 4.4(b) (dash-dotted line) confirms that, although finite damping $\gamma/\omega_p = 0.002$ reduces the field amplitude in the image plane, it does not affect the image contrast.

We have found numerically that an electromagnetic wave with the frequency inside the A_2 band incident from vacuum onto an SPC can couple into the crystal with very little reflection. Moreover, we observed strong enhancement of the field amplitude inside the crystal. The band flatness in a plasmonic SPC translates into very sharp excitation resonances, and large enhancements of the incident field. This enhancement is caused by the very low group velocity of the A_2 band. In

126

Section 4.1.9 we speculate how the flatness of this band and its proximity to the plasmon polariton band (see Fig. 4.4(b)) can be employed to improve the surface-enhanced Raman scattering, which relies on resonantly enhanced structure response at the incident and Raman-shifted re-emitted frequencies.

4.1.9 Applications of SPC to surface-enhanced Raman scattering (SERS)

Close proximity of the two flat propagation bands of a two-dimensional SPC shown in Fig. (4.3) (labeled by circles and triangles) may be useful for surface-enhanced Raman scattering (SERS) [MJB00]. Arrays of closely-spaced nanoparticles are known to cause a significant enhancement of the local fields with respect to the incident laser field: $R = E_{\text{local}}/E_{\text{inc}} \gg 1$ [GSSW04, LSB04, GVP96]. This enhancement is caused by coupling to the narrow electrostatic (plasmon) resonance. The narrower is the resonance ($\delta\omega = \omega_1/Q$, where $Q \gg 1$ is the quality factor), the higher is the enhancement. Molecules placed in the region of the enhanced incident field with the frequency ω_1 re-emit at the Raman-shifted frequency $\omega_2 = \omega_1 - \Omega_v$, where Ω_v is the vibrational frequency of interest. The spectacular enhancements of the Raman signal observed in the experiments [MJB00] are related to the fact that electromagnetic fields at both ω_1 and ω_2 are enhanced by the structure. Only in that case the enhancement of the Raman signal scales as R^4. The field enhancement R is proportional to Q. The exact proportionality coefficient can substantially exceed unity for the nanoparticles with sharp features (for example, prisms with sharp corners or almost-touching nanospheres).

The implication of both the emitted and absorbed light being inside the resonance curve is that $\omega_1 - \omega_2 < 1/Q$, or that $Q < \Omega_v/\omega_1$. Because the Raman enhancement scales as R^4, the largest electromagnetic enhancement is proportional to $(\omega_1/\Omega_v)^4$. This estimate puts an upper limit on the vibrational frequencies that can be detected with SERS while still enjoying the enhancement benefits. For example, for $\Omega_v = 1000\text{cm}^{-1}$ and $\omega_1 = 30,000$ cm^{-1} (corresponding to $\lambda_1 = 350$ nm) the electromagnetic Raman signal enhancement is only of order 10^6. Although higher enhancements have been reported, they are primarily found in the narrow gap between dimer-forming nanoparticles [MJB00]. If the separation between the Stokes and fundamental frequencies is larger than ω_1/Q, these dramatic enhancements of

the Raman signal cannot be realized.

Our suggestion is to employ two well separated propagation bands each of which is very flat. If each of the bands has the spectral width of $(\delta\omega_1)$ and $(\delta\omega_2)$, and the frequency separation between the bands is $\Omega_v \gg (\delta\omega_{1,2})$, then these two bands can be employed for detecting the vibrational frequency Ω_v. Band separation can be easily tuned by changing the rods' radii R and, possibly, their shapes. The magnitude of the signal enhancement is governed by the width of each individual band $\delta\omega_{1,2}$) while the detected vibrational frequency is governed by the separation between the bands. One example of such closely located flat bands is shown in Fig. 4.3 (two upper bands marked by triangles and circles).

4.2 Negative-index metamaterials based on metallic strips

Electromagnetic properties of two-dimensional metallic nano-structures in the optical frequency range are studied. One example of such structure is a periodic array of thin metallic strip pairs. Magnetic response of these structures is studied, as is the closely related emergence of the negative index of refraction (NIM) propagation bands. The presence of such bands is found to critically depend on the proximity of electric and magnetic dipole resonances. It is demonstrated that the frequencies of those resonances are strongly dependent on the ratio of the structure thickness and the plasmonic skin depth. Electromagnetic structures that are much thicker than the plasmonic wavelength are shown to exhibit standard broad antenna resonances at the wavelength roughly twice the strip length. As the structures are scaled down to resonate in the visible/mid-infrared, electrostatic resonances determine electromagnetic properties of such materials.

4.2.1 Motivation: quest for easy-to-fabricate optical metamaterials

Meta-materials is a general term referring to man-made composites which have the desirable properties unavailable in the naturally occurring materials. Extending the range of materials' *electromagnetic* properties is currently the main driving force behind the development of meta-materials. For example, it has recently been demonstrated that meta-materials containing split ring resonators can

have a negative magnetic permeability $\mu < 0$ in the microwave [PHRS99] and even THz [YPF$^+$04] frequency ranges. When additional elements, such as continuous conducting wires [PHSY96], are introduced into an elementary cell of a meta-material, both dielectric permittivity and magnetic permeability can be made negative [SPV$^+$00]. Such negative index materials (NIMs) with $\varepsilon < 0$ and $\mu < 0$ are particularly promising because of the possibility of making a "perfect" lens with the sub-wavelength spatial resolution [Pen00]. NIMs can be very useful for many other microwave and optical applications [PGL$^+$03, CI03, YCI05, AE04, PN05b] as well.

Developing NIMs for optical frequencies, however, has proven to be challenging. Although there are naturally occurring materials (metals, polaritonic materials such as SiC, ZnSe, MnO in mid-infrared) with the negative ϵ, using the scaled-down version of the original split-ring resonator is more challenging due to fabrication issues. For example, the original double split ring concept [PHRS99] was replaced by the simplified single split ring resonator (SRR) [LEW$^+$04] to demonstrate magnetic response in the infrared part of the spectrum. Even further simplifications of the unit cell may be necessary to develop magnetic response at near-infrared/visible frequencies. As the resonant structures are simplified, there is less opportunity for increasing their capacitance and inductance by making their aspect ratios (e. g., ratio of the SRR's radius and gap size) high. Hence, increasing the ratio of the resonant wavelength λ to the cell periodicity L becomes more difficult. It is the high λ/L ratio that distinguishes a true meta-material from its more common cousin, photonic crystal [Yab87, Joh87].

Another limitation of the split-ring resonator was recently recognized: because it does not have an inversion symmetry, electromagnetic resonances cannot be classified as purely electric dipole or magnetic dipole resonances. Consequently, both electric and magnetic responses are strongly excited at the same frequency unless significant modifications of the structure [MMREI02] are made. Therefore, it can be difficult to experimentally distinguish between the two. This was experimentally demonstrated at infrared frequencies [LEW$^+$04] by exciting the magnetic resonance of a split ring in the illumination geometry that had the incident and induced magnetic fields orthogonal to each other. This property of non-centrosymmetric structures is known as bianisotropy. Electromagnetic wave propagation in bianisotropic structures is substantially different than that in NIMs [MMREI02]. On the other hand, electromagnetic modes of centro-symmetric structures can be classified ac-

cording to their spatial symmetry as electric dipolar, electric quadrupolar, magnetic dipolar, etc. Thus, one can identify frequency ranges where the structure has either electric or magnetic response.

In order to realize NIMs at high (optical) frequencies, there is a need to consider electromagnetic materials with the unit cell satisfying the following conditions: (a) fabrication simplicity, (b) inversion symmetry (to avoid bi-anisotropy), (c) availability of both magnetic and electric resonances in close frequency proximity of each other, and (d) small elementary cell size compared to the wavelength. We will consider the simplest metallic structures, metallic strip pairs, and demonstrate using numerical simulations how the negative index property emerges from electric and magnetic resonances. We will show how sub-wavelength infrared resonances of these structures naturally occur as the structures become thinner. These resonances are electrostatic in nature, and their resonant frequency is determined by the shape of the structure and the frequency-dependent dielectric permittivity of the metal. The transition from geometric resonances (dependent on both the shape and the scale of the structure) to plasmonic (electrostatic) resonances (shape-dependent, scale-independent) occurs when the smallest dimension of the structure becomes smaller than the skin depth.

4.2.2 Negative refraction with perfectly conducting strip pairs

The concept of a resonance is fundamental to understanding and designing meta-materials. This is especially true when very exotic electromagnetic properties of a metamaterial are desired, such as, for example, a negative magnetic permeability. For example, the approximate formula for the magnetic permeability of a meta-material consisting of SRRs [PHRS99] reads

$$\mu_{\text{eff}} = 1 - \frac{F\omega^2}{\omega^2 - \omega_M^2 + i\omega\Gamma},\tag{4.21}$$

where F is the fractional area of a unit cell occupied by the SRR, ω_M is the magnetic resonance frequency, and Γ is the resistive loss coefficient. The filling factor F is typically kept small to avoid strong interaction between adjacent unit cells. Therefore, $\mu_{\text{eff}}(\omega) < 0$ only for ω's in the close vicinity of the magnetic resonance frequency ω_M. A similar expression [PS04] exists for a periodic meta-

material consisting of wire elements into which cuts are periodically introduced:

$$\epsilon_{\text{eff}} = 1 - \frac{\omega_p^2 - \omega_E^2}{\omega^2 - \omega_E^2 + i\omega\Gamma}, \quad (4.22)$$

where ω_p is the characteristic "plasma" frequency and ω_E is the cut-wire resonance frequency. Except for a very specific and often practically challenging case of uninterrupted wires ($\omega_E = 0$), negative ϵ_{eff} exists in the immediate proximity of the electric resonance at $\omega = \omega_E$. Thus it can be argued that developing a NIM may require finding a resonant structure that has adjacent electric and magnetic resonances.

Luckily, the simplest structure exhibiting nearby resonances consists of two thin metallic strips placed next to each other. A layer of such metallic strips (vertically stacked on top of each other) is shown in Fig. 4.5. For computational simplicity and to facilitate qualitative understanding, the strips are assumed to be infinitely extended in the $z-$direction. All calculations below assume that the fields are not varying in the $z-$direction as well. A P-polarized electromagnetic wave with non-vanishing E_x, E_y, and H_z field components incident on the layer can excite both electric and magnetic resonances. Because no resonances are expected to be excited by the S-polarized electromagnetic wave, our calculations are restricted to P-polarization.

Magnetic resonance is excited because the magnetic field H_z of the incident wave is normal to the plane of the strip pair. The double-strip structure has the center of inversion symmetry. This symmetry ensures that the structure is not bi-anisotropic: electric and magnetic resonances occur at different frequencies. The magnetic resonance can thus only be excited by the magnetic field perpendicular to $x - y$ plane. It cannot be excited by the electric field alone (with magnetic field in the $x - y$ plane) as it is the case with bi-anisotropic structures [GBM02, KKK$^+$04]. In any case, the assumption of field invariance along the $z-$direction precludes us from modelling such a case.

To determine and characterize possible resonances of a perfectly conducting metallic strip pair (MSP), we have numerically calculated the transmission coefficient $T(\omega)$ of a P-polarized electromagnetic wave normally incident on a single layer of vertically stacked MSPs as a function of the incident wave frequency ω. MSP layer geometry is defined by the following parameters: $H/L_y = 0.64$, $W = D = H/8$.
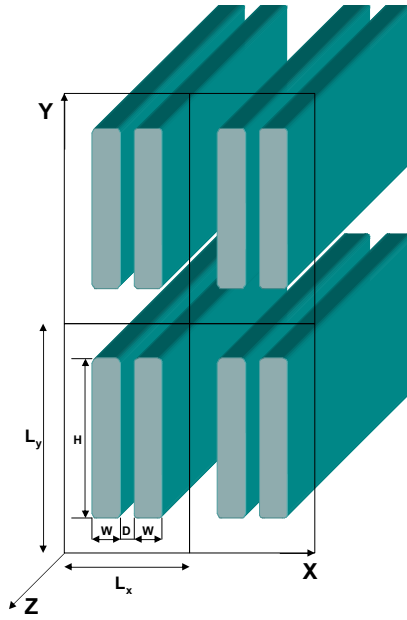
Figure 4.5: Two horizontally spaced layers of vertically stacked pairs of metallic strips. Layers are infinitely extended in $y-$direction with periodicity L_y. Separation between strips is D, height and width of each strip is H and W, respectively.

Here L defines the spatial scale, and L_y is the periodicity in y−direction. The simulation was done using a commercial finite elements code FEMLAB [Com03] that solves a two-dimensional *fixed frequency* Helmholtz equation for the magnetic field H_z:

$$- \nabla^2 H_z = \frac{\omega^2}{c^2} H_z, \tag{4.23}$$

where the following boundary conditions are satisfied: (a) $\partial_n H_z = 0$ at the metal surface (here ∂_n is the normal derivative), (b) $\partial_x H_z + i\omega H_z/c = 2i\omega H_0$ at $x = -L_B$, and (c) $\partial_x H_z - i\omega H_z/c = 0$ at $x = L_B$. Here ∂_n is the normal derivative at the metal surface, H_0 is the amplitude of the electromagnetic wave incident on the structure from the left, and $x = \pm L_B$ are the computational domain boundaries. Boundary condition (c) corresponds to the source-free radiative boundary condition. Boundary condition (b) corresponds to the radiative boundary condition with an external source. For all simulations $\omega < 2\pi c/L$ making the single-layer structure a sub-wavelength diffraction grating. The computational domain was chosen large enough so that the evanescent diffractive orders are negligibly small: $L_B = 5L$.

The assumption that MSP is a perfect conductor is accurate only when the strip thickness W is much larger than the skin depth of the incident light. For most metals this translates into $W \gg 20$nm for infrared frequencies. Most recently reported experimental results (see, for example, Reference [LEW$^+$04]) on detecting magnetic response in the infrared do indeed fall under the "perfect conductor" category. The plot of $T(\omega)$ shown in Fig. 4.6(left) exhibits two pronounced transmission dips. The first dip at $\omega L/c \equiv \omega_E^{(1)} L/c \approx 2.7$ is very broad and relatively shallow. Plotting the fields structure (electric and magnetic fields) at that frequency reveals its electric dipole nature: the bottom (top) caps of both metallic strips are positively (negatively) charged. Magnetic field between the strips is essentially zero because electric current in both strips flows in the same direction.

The high-frequency dip at $\omega L/c \approx 4.6$ is both narrower and deeper: transmission reduces to numerically undetectable level. Note that this dip occurs when $H/\lambda \approx 0.44$ (where $\lambda = 2\pi c/\omega$ is the light wavelength), corresponding to the well-known half-wavelength antenna resonance. The structure of the fields is, however, much more complicated at that frequency than at the $\omega_E^{(1)}$ frequency. To understand the structure of the fields better, a leaky mode analysis (LMA) was developed. LMA enables us to extract resonances of the structure by assuming that the electromag-
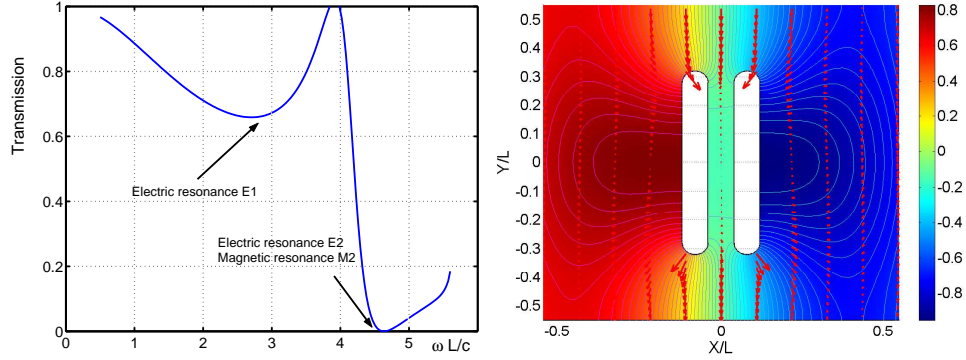
Figure 4.6: (Left) Transmission coefficient through a single (in x-direction) layer of perfectly conducting metallic strip pairs (MSP) shown in Fig. 4.5. MSP's parameters: $L_y = L$, $H/L = 0.64$, $W = D = H/8$. The two transmission dips correspond to the excitation of a broad electric dipole resonance E1 (at $\omega_E^{(1)} L/c \approx 2.7$) and a closely-spaced electric and magnetic dipole resonances E2 and M2 (at $\omega_{E,M}^{(2)} L/c \approx 4.6$). (Right) Electric field (arrows) and magnetic field isocontours corresponding to $\omega_E^{(1)}$.

netic fields concentrated in the vicinity of the structure is weakly coupled to the outgoing radiative mode. By imposing the source-free radiative boundary conditions at $x = \pm L_B$ (where $L_B \gg L$), the complex frequencies $\omega \equiv \omega_r - i\omega_i$ of the leaky modes can be extracted. Radiative losses are characterized by ω_i while the real mode frequency is ω_r.

4.2.3 Leaky mode analysis of magnetic and electric resonances

Natural frequencies of the leaky modes of a single layer of MSP's are found by solving Eq. (4.23) as an eigenvalue equation for a complex frequency $\omega \equiv \omega_r - i\omega_i$, subject to the source-free radiative boundary conditions. Only weakly leaking modes with $\omega_i \ll \omega_r$ were studied. Specifically, the following boundary conditions have been imposed: $\partial_x H_z + i\omega_r H_z/c = 0$ at $x = -L_B$ and $\partial_x H_z - i\omega_r H_z/c = 0$ at $x = L_B$. Because the boundary conditions are dependent on the frequency of the leaky mode we are seeking by solving the eigenvalue Eq. (4.23) for ω, we have used an iterative procedure. First, a trial $\omega_r^{(1)}$ is chosen and the complex eigenvalue $\omega^{(1)}$ is obtained. Then the real part of $\omega^{(1)}$ is chosen as $\omega_r^{(2)}$, and the process is repeated
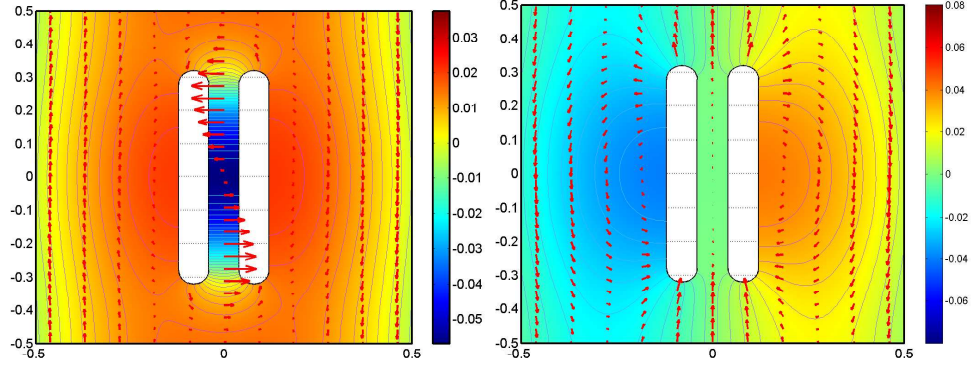
Figure 4.7: Leaky mode profiles corresponding to the magnetic dipole resonance at $\omega_M^{(2)} L/c = 4.68 - 0.43i$ (left) and $\omega_E^{(2)} L/c = 4.73 - 0.49i$ (right). MSP geometry is the same as in Fig. 4.6. Electric field strength and direction is shown by proportionate arrows. Iso-contours and coloring correspond to the magnetic field.

until convergence is reached after N iterations: $\text{Re}\left(\omega^{(N)}\right) = \omega_r^{(N)}$. The iterative sequence typically converged after fewer than 10 iterations.

The numerically computed eigenfrequencies are $\omega_M^{(2)} L/c = 4.68 - 0.43i$ and $\omega_E^{(2)} L/c = 4.73 - 0.49i$. Their identification as magnetic and electric dipole resonances, respectively, is done by inspecting electric and magnetic field profiles of the respective eigenmodes shown in Fig. 4.7. The field structure of the electric dipole resonance in the right Fig. 4.7 is the same as in Fig. 4.6(right), and is identified as the electric dipole resonance. Field distribution corresponding to $\omega = \omega_M^{(2)}$ shown in the left Fig. 4.7 is qualitatively different. Inspection of the charge distribution on the metal surface indicates that the electric dipole moment of the MSP is equal to zero. That is because the charge distribution possesses an inversion symmetry. However, the quadrupole electric moment and the magnetic dipole moment are not vanishing. The latter is finite because the currents are flowing in the opposite direction in the two MSP-forming strips. The non-vanishing of the magnetic moment can also be seen in Fig. 4.7(left) by inspecting a strong enhancement of the magnetic field in the region between the metallic strips.

Two important lessons can be learned from this single-layer LMA. First, it confirms that the electric and magnetic resonances occur at different frequencies due to the inversion symmetry of the MSP. Second, this example illustrates that,

135
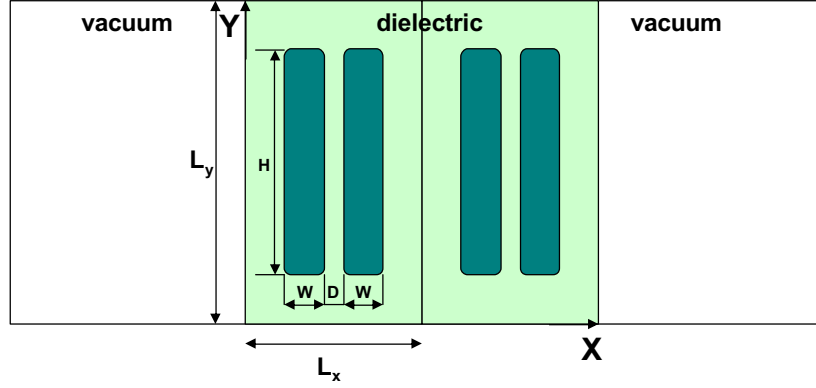
Figure 4.8: Two horizontal layers of vertically stacked pairs of metallic strips embedded in a dielectric with $\epsilon_d = 4$. Layers are infinitely extended in $y-$direction with periodicity L_y. Geometric parameters: $L_x = 0.64L$, $L_y = 0.8L$, $H/L = 0.64$, $W = D = H/8$.

while the frequencies of the two resonances are not identical, they do occur in a relatively close proximity of each other. Therefore, one can expect that there is a finite frequency interval where both $\epsilon_{\text{eff}} < 0$ and $\mu_{\text{eff}} < 0$ for an infinitely extended in both x and y directions (multi-layer) structure. An important downside of the MSP-based design of a NIM is that the resulting meta-material is not strongly sub-wavelength: $L/\lambda \approx 0.75$ at the magnetic resonance. That is due to the extreme simplicity of the MSP structure: none of the capacitance-increasing techniques used in the design of an SRR [PHRS99] have been employed here. On the other hand, the simplicity of the MSP structure makes it attractive for deployment as a building block of a visible/near-IR NIM. The structure can be made sub-wavelength due to the emergence of the plasmonic resonances as the strip width W becomes smaller. This approach to miniaturization of the unit cell to the sub-λ level is described in Section 4.2.5.

4.2.4 Demonstration of negative index in MSP metamaterial using Effective Medium Parameter Retrieval (EMPR)

A sub-wavelength negative index meta-material can be designed by embedding metallic strip pairs in a high-ϵ dielectric and taking advantage of the proximity

of the electric and magnetic resonances demonstrated in Section 4.2.3. Specifically, we model a NIM consisting of periodically repeated, with horizontal and vertical periods $L_x = 0.64L$ and $L_y = 0.8L$, MSP's. The sketch is given in Fig. 4.8. Here L is a geometric scale of the meta-material in terms of which its parameters (periodicity, the shape of its constituent MSP) are expressed. MSP's are assumed to be embedded in a high dielectric permittivity material with $\epsilon_d = 4$. Embedding MSP's in a dielectric serves two goals: (i) lowering the resonant frequency by approximately $\sqrt{\epsilon_d}$, and (ii) defining a sharp clearly defined interface between vacuum and NIM. The effective impedance $Z_{\text{eff}}(\omega)$ and refractive index $n_{\text{eff}}(\omega)$ can be extracted from the reflection and transmission coefficients $r(\omega)$ and $t(\omega)$ through a slab of thus constructed meta-material with thickness Δ [SSMS02, MS03]:

$$Z_{\text{eff}}(\omega) = \pm\sqrt{\frac{t^2 - (1-r)^2}{t^2 - (1+r)^2}}, \tag{4.24}$$

$$n_{\text{eff}}(\omega) = \frac{\ln Y(\omega)}{i\omega\Delta/c}, \tag{4.25}$$

where

$$X \equiv \cos(n_{\text{eff}}\omega\Delta/c) = (1 - r^2 + t^2)/(2t), \tag{4.26}$$

$$Y \equiv e^{in_{\text{eff}}\omega\Delta/c} = X \pm \sqrt{X^2 - 1}. \tag{4.27}$$

The signs in expressions (4.24) and (4.27) are chosen such that the conditions $\text{Re}(Z_{\text{eff}}) > 0$ and $\text{Im}(n_{\text{eff}}) > 0$ are satisfied [MS03].

The transmission/reflection coefficients $t(\omega)$ and $r(\omega)$ are *complex* numbers containing both the phase and amplitude information (unlike the the transmission amplitude $T \equiv |t|^2$ plotted in Fig. 4.6(left) for a single layer of MSP's in vacuum). We have used the standard approach developed earlier [SSMS02, MS03] for extracting an unambiguous refractive index by varying the slab thickness. In our case, varying $\Delta \equiv NL$ is equivalent to varying the number of elementary unit layers N. This number is varied from $N_{min} \geq 1$ to $N_{max} > N_{min}$ with unit increment, so that the phase ϕ_N of the complex exponent in Eq. (4.27) for N layers does not change by more than π when one switches from N layers to $N + 1$. In photonic crystals, this assumption always holds, because the x-component of the Bloch wavenumber $k_{Bloch} \equiv n_{\text{eff}}\omega/c$ cannot exceed π/L_x in magnitude, so that $|k_{Bloch}L_x| \leq \pi$, and thus
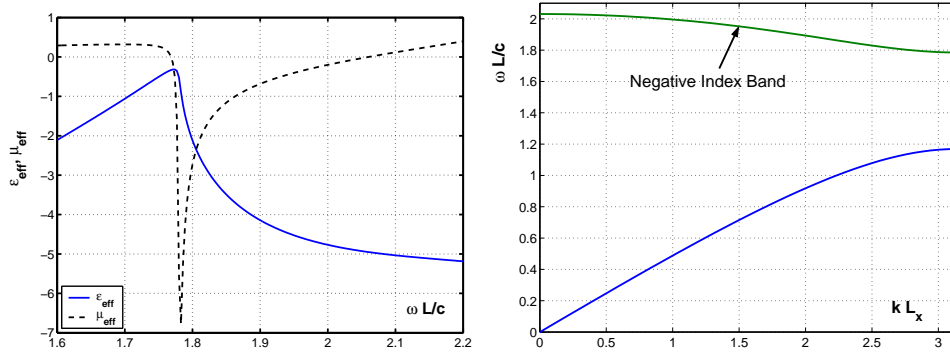
Figure 4.9: Left: Extracted dielectric permittivity ϵ and magnetic permeability μ_{eff} for a NIM consisting of a square lattice of metallic strip pairs (MSP) embedded in a $\epsilon_d = 4$ dielectric. Right: Band diagram ω vs k exhibiting a negative index band. Wave vector $\vec{k} = k\vec{e}_x$ directed along $x-$direction. MSP's geometric parameters: $L_x = 0.64L$, $L_y = 0.8L$, $H/L = 0.64$, $W = D = H/8$.

the phase $\phi_N = k_{Bloch}NL_x + \psi_0$ can not change by more than π. This property of periodic structures allows one to eliminate phase jumps greater than π and to draw a smooth, nearly linear curve ϕ_N vs. N. This curve is used to extract ψ_0. After subtraction of $\phi_c = 2\pi[\psi_0/(2\pi)]$ from ϕ_N (brackets denote rounding to nearest integer) each point of the curve $\phi_N - \phi_c$ represents the actual value of $n_{\text{eff}}(N)N\omega L_x/c$, where n_{eff} is the effective refraction index of the structure with N layers. If all $n_{\text{eff}}(N)$ are approximately the same, the meta-material behaves as a homogeneous effective medium. This assumption has been tested and found to be satisfied for all structures described here.

The effective dielectric permittivity and magnetic permeability are related to Z_{eff} and n_{eff} as $\epsilon_{\text{eff}} = n_{\text{eff}}/Z_{\text{eff}}$ and $\mu_{\text{eff}} = n_{\text{eff}}Z_{\text{eff}}$. Numerically extracted ϵ_{eff} and μ_{eff} are plotted in Fig. 4.9. Reflection and transmission coefficients were obtained for an electromagnetic wave incident along the $x-$direction on a meta-material slab. Therefore, the extracted ϵ_{eff} is the ε_{yy} component of the effective dielectric permeability tensor ε. Because the structure is clearly anisotropic (x and y directions are not equivalent), only wave propagation in the $x-$ direction is considered. The negative index is exhibited only along that direction.

From Fig. 4.9(left) follows that the extracted values of ϵ_{eff} and μ_{eff} of such meta-material are both negative in the vicinity of $\omega = 2c/L$. Therefore, this

meta-material is expected to support electromagnetic waves with a negative refractive index. To demonstrate the presence of a negative index band, the band structure of the meta-material was calculated by imposing phase-shifted periodic boundary conditions [Shv03b] at the left and right cell boundaries: $H_z(x = 0, y) = \exp(ikL_x)H_z(x = L_x, y)$ and $\partial_x H_z(x = 0, y) = \exp(ikL_x)\partial_x H_z(x = L_x, y)$. The wavenumber k satisfies $0 < k < \pi/L_x$ condition. Solving Eq. (4.23) as an eigenvalue equation for ω yields the dispersion curve ω vs k plotted in Fig. 4.9(right). The second propagation band indeed has a negative refractive index because its group velocity opposes its phase velocity: $\partial\omega/\partial k < 0$.

One drawback of the present NIM design is that the unit cell of this meta-material is only marginally sub-wavelength: $L_x/\lambda = 0.2$. Even this modest miniaturization of a unit cell is accomplished by embedding the MSP's in a high-ϵ material. While such materials can be found in near and mid-infrared (for example, $\epsilon_{Si} = 12$), they are less common in the visible. The solutions of Eq. (4.23), with perfectly conducting boundary conditions at the metal surface, are *scalable,* i. e. determined by a single dimensionless parameter $\omega L/c$ for a given geometry of the MSP layer. Therefore, making a strongly sub-wavelength MSP-based NIM in the optical range is as hard (or harder, given the absence of suitable high-ϵ dielectrics) as in the microwave range. A different approach must be used. One such approach described below is to take advantage of the *plasmonic* resonances of an MSP.

4.2.5 Plasmon resonances of ultra-thin MSPs

The concept of using electrostatic resonances for inducing optical magnetism was recently [Shv03b, SU04a, SU05] introduced by us. In those papers electrostatic resonances of periodic plasmonic nanostructures have been employed to induce magnetic properties due to close proximity of adjacent nanowires. Higher multipole electrostatic resonances were shown [SU05] to hybridize in such a way as to induce magnetic moments in individual nanowires. Strong electrostatic resonances of regularly shaped nanoparticles (including nanospheres and nanowires) occur for $-2 < \epsilon_R < -1$, where $\epsilon_m(\omega) \equiv \epsilon_R(\omega) + i\epsilon_I(\omega)$ is the frequency-dependent dielectric permeability of the metal from which the MSP is made.

The drawback of such designs [Shv03b, SU04a] is that if metal is used in such a meta-material, negative index is found only for the frequencies at which resistive
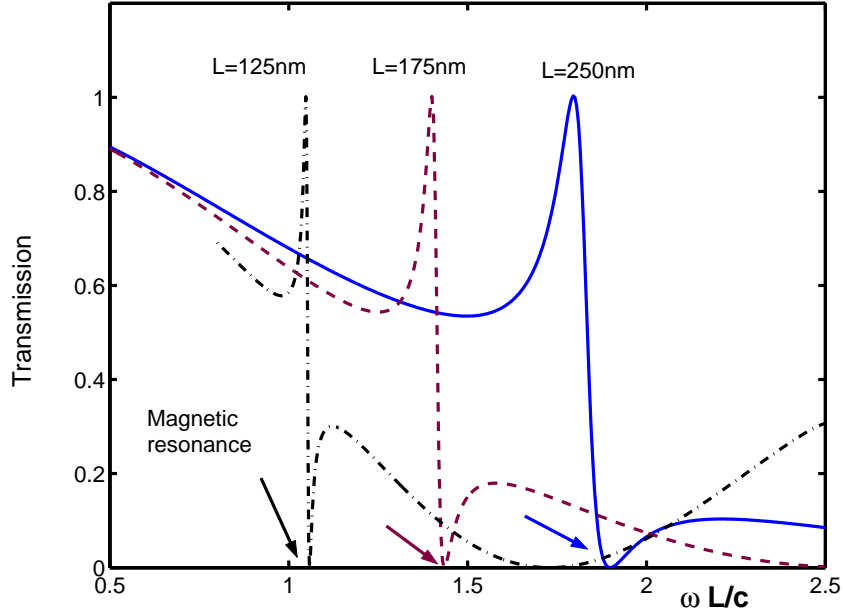
Figure 4.10: Frequency dependence of the transmission coefficient through a single layer of plasmonic MSP's spaced in vacuum by $L_y = 0.8L$. Geometric parameters of the MSP: $H/L = 0.64$, $W = D = H/8$. Solid line: $L = 250$nm, dashed line: $L = 175$nm, dot-dashed line: $L = 125$nm.

damping is high: if $-2 < \epsilon_R < -1$, then ϵ_I is comparable to ϵ_R. Qualitatively, this occurs because of inter-band transitions in metals. Moving away from inter-band transitions (and corresponding high losses) requires reducing the frequency ω and, therefore, increasing the absolute value of $\epsilon_R(\omega)$. Making the structures resonate at the frequency ω such that $\epsilon_R(\omega) \ll -1$ requires moving from simple shapes (cylinder, sphere, etc.) to more complicated geometric shapes characterized by extreme aspect ratio values. For example, it is known [NPRH03] that gold nanoshells with a dielectric core/metall shell structure resonate at a much lower frequency than pure gold nanoparticles if the thickness of the gold shell is much smaller than the core radius. As demonstrated below, MSP's shown in Fig. 4.5 exhibit electrostatic resonances for $\epsilon_R \ll -1$ if $H \gg W, D$.

The fundamental wave equation that must be solved for the magnetic field

H_z is

$$-\vec{\nabla} \cdot \left(\frac{1}{\epsilon} \vec{\nabla} H_z \right) = \frac{\omega^2}{c^2} H_z, \qquad (4.28)$$

where $\epsilon(x, y, \omega)$ is a frequency and position-dependent function: $\epsilon \equiv \epsilon_m(\omega)$ inside the metallic strips and $\epsilon \equiv 1$ outside the strips. Here $\epsilon_m(\omega)$ is the material-dependent dielectric permittivity. For most metals $\epsilon_m = 1 - \omega_p^2/\omega(\omega + i\Gamma)$ is a good approximation obtained on the basis of the Drude model. Below we use the typical for many metals (but specific to Au) material constants: $c/\omega_p = 23$nm and $\Gamma/\omega_p = 3 \times 10^{-3}$. Equation (4.28) replaces Eq. (4.23) which assumed that a metal is a perfect conductor. Both equations give the same result if the skin depth $l_{sk} \sim c/\omega_p$ is much smaller than the metal thickness W.

We refer to metallic structures with characteristic thickness $W \leq c/\omega_p$ as *plasmonic*. An array of plasmonic MSPs presented a very different medium to an incident electromagnetic wave than an array of perfectly conducting MSPs described in Section 4.2.2. Because of the dependence of ϵ_m on the frequency, these structures are no longer scalable – unlike the perfectly conducting MSP's. For example, if the transmission coefficient $T_0 = T(\omega_0)$ through the layer of MSP's is observed for a characteristic structure size L_0, then one cannot expect that $T(S\omega_0) = T_0$ for a scaled down structure with a characteristic size $L = L_0/S$. Scalability of perfectly conducting MSP's presents a serious disadvantage for making a sub-wavelength NIM: no matter how small is the unit cell, NIM behavior is observed at a proportionally short wavelength. The question posed by us here is: does the lack of scaling for realistic (plasmonic) MSPs at the optical frequencies enable a sub-wavelength NIM, or does it make the structures disproportionately large? Below we demonstrate that the lack of the simple scaling enables sub-wavelength meta-materials. However, the same MSP-based design that reveals negative index behavior when the unit cell is large (and the wavelength long) may not reveal such behavior for scaled-down unit cells.

To investigate the lack of scalability in plasmonic structures we simulated transmission through a single layer of MSP's spaced in vacuum by $L_y = 0.8L$. For three different structures with $L = 250$nm, $L = 175$nm, and $L = 125$nm the transmission coefficient is plotted in Fig. 4.10 as a function of the dimensionless parameter $\omega L/c$. The same perfectly matched boundary conditions at $x = \pm L_B$ and periodic boundary conditions at $y = \pm L_y/2$ were applied as in the simulations

described in Section 4.2.2. The difference is that Eq. (4.28) is solved instead of Eq. (4.23) and that a finite-permittivity material with $\epsilon_m(\omega)$ is assumed inside the MSP's instead a perfect conductor. For this simulation we have neglected the very small damping constant $\Gamma \ll \omega$. Two important differences between the perfectly conducting and plasmonic case are apparent when comparing any one of the three curves in Fig. 4.10 to Fig. 4.6(left). First, transmission dips (magnetic dipole resonances) in the plasmonic case are much sharper. We have verified that the dips indeed correspond to the excitation of magnetic resonances by inspecting the magnetic field distribution. Indeed, magnetic field is strongly concentrated inside the MSP as shown in Fig. 4.7(left). Second, the normalized frequencies corresponding to the magnetic resonance are smaller in the plasmonic case: $\omega_M^{(2)} L/c \approx 1.05$ for the $L = 125$nm plasmonic case vs $\omega_M^{(2)} L/c = 4.7$ for the perfectly conducting case. Because resistive damping is neglected in our plasmonic simulations, the sharpness of the resonance is indeed related to the lower normalized frequency: optically small objects with $L \ll \lambda$ experience low radiative damping.

Comparison between the three curves in Fig. 4.10 also shows that thinner structures are more sub-wavelength. This proves that the plasmonic structures are not scalable. In fact, reducing the scales size of the structure by a factor 2 (from $L = 250$nm to $L = 125$nm) reduces the normalized resonance frequency $\omega_M^{(2)} L/c$ by an almost equal factor. This implies that as the structures become very small, the resonant wavelength reaches a certain saturation value. Miniaturizing the structures further makes them progressively more sub-wavelength. Therefore, the non-scalability of the magnetic resonances of plasmonic MSPs is *advantageous* for designing sub-wavelength meta-materials.

It is instructive to note that the widths of the MSPs in the three cases shown in Fig. 4.10 are, in the descending order, $W = 20, 15, 10$nm. Therefore, all three MSPs are thinner than the skin depth $l_{sk} \sim c/\omega_p = 23$nm. It is in this regime of ultra-thin metallic structures that the electrostatic effects are expected to become prominent. To demonstrate that plasmonic effects indeed become dominant for the three structure sizes considered here, it is instructive to calculate the real values of $\epsilon_m(\omega_M^{(2)})$ at the magnetic resonance frequencies. Those are: $\epsilon_m = -31$ for $L = 250$nm, $\epsilon_m = -27$ for $L = 175$nm, and $\epsilon_m = -25$ for $L = 125$nm. Evidently, as the structures shrink, the ϵ_m reaches some fixed value. This effect is consistent with the observation that shrinking the structure size does not affect the resonant
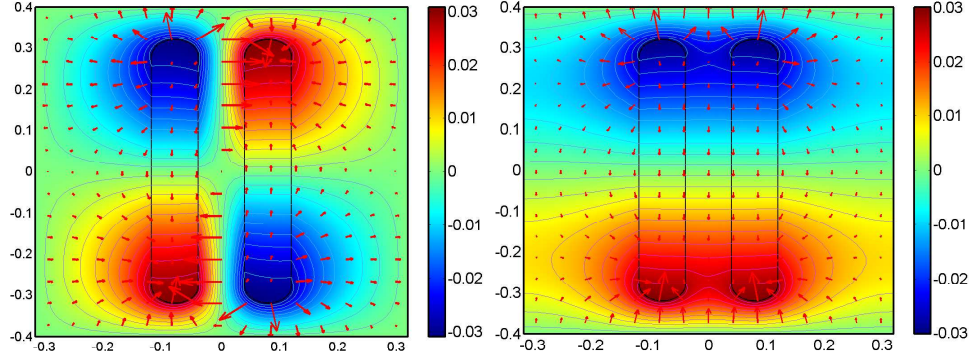
Figure 4.11: Left: Magnetic resonance at $\epsilon_1 = -22.75$, right: electric resonance at $\epsilon_2 = -9.9$. Contours: lines of equal potential Φ_i. Resonances are computed for a periodic meta-material with $L_x = 0.64L$, $L_y = 0.8L$, $H/L = 0.64$, $W = D = H/8$.

frequency. Below the magnetic resonance in sub-wavelength MSPs is shown to be electrostatic in origin.

4.2.6 Plasmon resonances in quasistatic approximation

In the limit of $\omega L/c \ll 1$ the right hand side of Eq. (4.28) representing the retardation effects can be neglected, yielding $\vec{\nabla} \cdot \left(\epsilon^{-1} \vec{\nabla} H_z \right) = 0$. This equation is equivalent [SU04a, SU05] to assuming that the electric field is purely electrostatic: $\vec{E} \equiv \vec{E}_{ES}$, $\vec{\nabla} \times \vec{E}_{ES} = 0$, or $\vec{E}_{ES} = -\vec{\nabla}\Phi$, where Φ is the electrostatic potential.

The Poisson's equation in the medium satisfied by Φ is

$$\vec{\nabla} \cdot \left(\epsilon \vec{\nabla} \Phi \right) = 0, \tag{4.29}$$

where, as in Eq. (4.28), $\epsilon \equiv \epsilon(x, y, \omega)$ is the function of space. Equation (4.29) can be solved as a generalized eigenvalue equation for the positions of electrostatic resonances s_i, as described in detail in Section 2.2. For a lossless plasmonic material, the relationship between eigenvalues s_i and eigenfrequencies ω_i is particularly simple:

$$s_i = \omega_i^2/\omega_p^2. \tag{4.30}$$

Thus, small values of s_i correspond to low frequencies and large negative values of the corresponding $\epsilon_m(\omega_i)$.

Bearing in mind that we are interested in describing the y-polarized wave propagation in a periodic structure, $\Phi_i(y = \pm L_y/2) = 0$ and $\Phi_i(x = -L_x/2) = \Phi_i(x = L_x/2)$ boundary conditions [SU05] were used. The finite elements code FEMLAB [Com03] was used to solve Eq. (4.8). Thus obtained resonances can be classified according to the symmetry of the potential function Φ with respect to symmetry group transformations of the unit cell. For example, the electric quadrupole resonance shown in Fig. 4.11(left) corresponding to $s_1 = 0.042$ (or $\epsilon_1 \equiv \epsilon_{EQ} = -22.75$) is even with respect to spatial inversion and odd with respect to mirror reflections in $y - z$ and $x - z$ planes. The electric dipole resonance shown in Fig. 4.11(right) has an odd inversion symmetry, and odd(even) mirror symmetry with respect to reflection in $x - z$ ($y - z$) planes. This resonance occurs at $s_2 = 0.09$ (or $\epsilon_2 \equiv \epsilon_{ED} = -9.9$). As was earlier demonstrated [SU04a], resonances with such spatial symmetry contribute to the quasistatic dielectric permittivity ε_{yy}. Electric dipole resonant frequency ω_{ED} corresponds to divergent (or very large, in the case of finite resistive losses) dielectric permittivity. This is easy to see by inspecting the potential distribution in Fig. 4.11(right). The potential difference between $y = +L_y/2$ and $y = -L_y/2$ planes is equal to zero. However, the electric field flux through those planes (which is proportional to the electric charge) is finite. Therefore, the capacitance of such a capacitor and, correspondingly, the effective dielectric permittivity, are infinite. The electric quadrupole resonance at the lower frequency ω_{EQ} does not contribute to the dielectric permittivity. But, as shown below, when small but finite retardation effects are retained, this resonance acquires a magnetic dipole component.

These FEM modeling results highlight yet another important property of plasmonic strip pairs: electrostatic resonances occur at the frequencies corresponding to a large negative value of ϵ_m. This is an important distinction from the electrostatic resonances at $\epsilon_m \sim -1$ of regularly shaped (circular [SU04a] or triangular [Shv03b]) plasmonic structures studied by us earlier: large values of $|\epsilon_m|$ occur at lower frequencies where absorption due to interband transitions is small.

An important finding of the electrostatic analysis is that electric and magnetic dipole resonances occur at rather different wavelengths. This is in sharp contrast to the case of perfectly conducting MSPs, where the two resonances are at very close frequencies. The assumption of perfect conductivity is valid only for the structures that are much thicker than the skin depth: $W \gg \lambda_{sk}$. Using the above

example of an ultra-thin structure and the tabulated values of ϵ_m for gold, it is found that the electric quadrupole (and the related to it magnetic dipole) resonance occurs at $\lambda = 770$nm while the electric dipole resonance is at $\lambda = 590$nm. This large difference results in the disappearance of the negative index band in the miniaturized MSP-based structure. Thus, even though the MSP-based meta-material with a large unit cell can exhibit a NIM band as shown in Fig. 4.9(right), a scaled-down structure does not necessarily support such a band.

4.2.7   Magnetic moment at the electric quadrupole resonance

It is rather remarkable that the frequency ω_{EQ} of the electric quadrupole resonance calculated by simulating our system in the electrostatic approximation corresponds to $\epsilon_m = -22.75$. As was shown in Section 4.2.5, the magnetic resonance moves from $\epsilon_m = -31$ for $L = 250$nm to $\epsilon_m = -27$ for $L = 175$nm, and to $\epsilon_m = -25$ for $L = 125$nm as the MSPs are getting progressively smaller. These values are remarkably close to $\epsilon_m(\omega_{EQ})$ at the electric quadrupole resonance frequency, suggesting that there is a natural connection between the two. Below we demonstrate that indeed, the electric quadrupole acquires a finite magnetic moment when the retardation effect (finite value of $\omega L/c$) is accounted for. A somewhat related effect was described for a U-shaped nano-antenna using a different approach [SS04, SSS06].

We start by separating the total magnetic and electric fields into $H_z = H_{\mathrm{qs}} + H_1$ and $\vec{E} = \vec{E}_{ES} + \vec{S}$, where $\vec{E}_{ES} = ic\epsilon^{-1}\vec{\nabla} \times \vec{H}_{\mathrm{qs}}/\omega$ and $\vec{S} = ic\epsilon^{-1}\vec{\nabla} \times \vec{H}_1/\omega$. Physically, this separation means that the electric field is divided into the electrostatic ($\vec{E}_{ES} = -\vec{\nabla}\Phi$) and solenoidal ($\vec{\nabla} \cdot \vec{S} = 0$) parts. Magnetic field is split up into the quasistatic H_{qs} satisfying $\vec{\nabla} \cdot \left(\epsilon^{-1}\vec{\nabla}H_{\mathrm{qs}}\right) = 0$ and the electromagnetic H_1 parts. The quasistatic magnetic field is small to order $\omega L/c$ compared with the electrostatic electric field: $|H_{\mathrm{qs}}| \sim (\omega L/c)|\vec{E}_{ES}|$. The electromagnetic component H_1 satisfies, to first order in $\omega^2 L^2/c^2$, Eq. (4.4) from Sec. 4.1.2, i.e. $\vec{\nabla} \cdot \left(\frac{1}{\epsilon}\vec{\nabla}H_1\right) = \frac{\omega^2}{c^2}H_{\mathrm{qs}}$. Therefore, H_1 is even smaller that H_{qs}: $|H_1| \sim \omega^2 L^2/c^2|H_{\mathrm{qs}}|$; H_1 is neglected in what follows. Magnetic field $\vec{H}_{\mathrm{qs}} = \vec{e}_z H_{\mathrm{qs}}$ can be calculated from $\vec{\nabla} \times \vec{H}_{\mathrm{qs}} = -i\omega\epsilon\vec{E}_{ES}/c$. The peak amplitude of the magnetic field $|H_{\mathrm{qs}}|$ can be evaluated by noting that, from the $\vec{\nabla} \times \vec{E}_{ES} = 0$, the vertical component of the electrostatic field E_y inside the metal strips is related to the peak horizontal electric field E_x at the

145

caps of the strips through $|E_y| = |E_x|D/H$. Therefore, $|H_{\text{qs}}| \sim (\omega W D/cH)|\epsilon_m||E_x|$. Thus, $|H_{\text{qs}}| \ll |E_x|$ because $W \ll H$, $D \ll H$, and, by assumption, $\omega H/c < 1$.

Effective magnetic permeability of a meta-material differs from unity due to induced magnetic moments. The electric current pattern through the MSPs at the quadrupole resonance is clearly such that the currents flow in opposite directions through the adjacent strips. It would be a mistake, however, to assume that the entire current contributes to the generation of the magnetic moment. In determining the contribution of the induced electric current in the MSP to the magnetic moment, it is essential to keep in mind that the current pattern contains both the magnetic dipole and electric quadrupole [VA99]. The quadrupole part originates from the electrostatic field and does not contribute to the magnetic moment. The magnetic dipole portion of the current originates from the solenoidal component of the electric field $\vec{S}$ that can be calculated [SU05] from H_{qs}:

$$\vec{\nabla} \times \vec{S} = i\frac{\omega}{c}H_{\text{qs}}\vec{e}_z, \tag{4.31}$$

and $\vec{\nabla} \cdot \vec{S} = 0$. The magnitude of $\vec{S}$ inside the strips is estimated as

$$|\vec{S}| \sim (\omega W/c)\,|\bar{H}_{\text{qs}}|, \tag{4.32}$$

where $|\bar{H}_{\text{qs}}|$ is the peak value of H_{qs} between the strips. The magnetic moment density is given by $\vec{M} = (1/2c)\langle \vec{r} \times \vec{J}_S \rangle$, where $\vec{J}_S = -i\omega(\epsilon_m - 1)\vec{S}$ represents the solenoidal component of the electric field and the $\langle ... \rangle$ stands for averaging over the unit cell. For the MSP it is estimated that

$$|\vec{M}| \sim p|\epsilon_m - 1|\left(\omega^2 W D/c^2\right)|\bar{H}_{\text{qs}}|, \tag{4.33}$$

where $p = 2WH/(L_xL_y)$ is the fractional area of the unit cell occupied by the MSPs. This qualitative estimate highlights the fact that magnetic properties of plasmonic nanostructures are indeed proportional to the retardation effects and, therefore, scale as the square of the frequency.

146

4.2.8 Conclusions

Electromagnetic properties of two-dimensional meta-materials consisting of an array of metallic strips pairs (MSPs) are investigated using electromagnetic simulations. Simulated transmission through a single layer of MSPs show that electromagnetic resonances corresponding to electric and magnetic dipole resonances can be excited. Large MSPs such that the strip thickness significantly exceeds the skin depth can be modeled as perfect conductors. Perfectly conducting MSPs are shown to possess electric and magnetic dipole resonances which are very close in frequency. This property of MSPs is used to demonstrate a sub-wavelength negative index meta-material based on MSPs. These resonances are related to the well-known antenna resonances occurring at the wavelength approximately equal to twice the strip height H. A new approach to making a strongly sub-wavelength MSP-based meta-material is demonstrated. This approach involves reducing the size of the unit cell to the point at which plasmonic (electrostatic) resonances of MSPs become dominant. Two types of electrostatic resonances, dipole and quadrupole, are investigated. The quadrupole resonance is shown to contribute to magnetic moment of the meta-material and, therefore, to result in the optical magnetism.

4.3 Deeply sub-wavelength negative-index metamaterials combining metallic strips and films

In this Section, an optical negative index metamaterial with deeply sub-wavelength unit cells is introduced. Because of its sub-wavelength nature, this NIM operates in effective medium regime, and thus it can be characterized by meaningful ϵ_{eff} and μ_{eff}. It is demonstrated that ϵ_{eff} retains its physical meaning even in the negative-index band, thus proving that this NIM is also a doubly-negative metamaterial (DNM). The DNM can operate in the near infrared and visible spectra and may be manufactured using standard nanofabrication methods. The structure's unit cell comprise a continuous optically thin metal film sandwiched between two identical optically thin metal strips separated by a small distance form the film. The incorporation of the middle thin metal film avoids limitations of metamaterials comprised of arrays of paired wires or strips (patches) to operate for large wavelength-to-period ratios. Extensions of the presented two-dimensional structure

147

to three dimensions by using square patches are straightforward and will enable more isotropic metamaterials that exhibit negative refraction for all polarizations and angles of incidence.

4.3.1 Introduction and motivation

Metamaterials are artificial composite materials that possess electromagnetic properties not found in natural substances or structures. Doubly negative metamaterials (DNM) are metamaterials that are characterized by permeability, permittivity, and index of refraction simultaneously having negative real parts [Ves62]. Due to their unique electromagnetic properties, DNMs have a number of important potential applications including the construction of perfect lenses [Pen00, SSM+04], transmission lines [YCI05], and antennas [AE04, EZ05, ZH01].

First practical realizations of DNM were introduced in the microwave and then THz regimes [JKL+06, KS03, SSS01, SU06, SWM+05]. For example, microwave and THz DNMs were constructed from periodic unit cells comprising split ring resonators and straight wires [SSS01]. In these DNMs the split ring resonators and wires support strong magnetic and electric resonance that result in frequency bands of negative permittivity and permeability that can be tuned to overlap. Extending the operational spectrum of DNMs to optical frequencies is an important ongoing task among physical and engineering communities.

However, realizations of DNMs in the optical and, especially, near-infrared (IR) and visible spectra are challenging. For instance, it has been demonstrated that scaling of the split ring resonator based metamaterials to the visible regime fails for realistic metals due to the saturation of the magnetic resonance frequency and increased loss [ZKK+05]. Recently, several structures have been suggested to operate as DNMs in the optical regime [SWM+05, SCC+05, ZFP+05, DEW+06]. These optical DNMs can be classified into two types. One type incorporates arrays of plasmonic rods (Sec. 4.1)or spheres [ASE06] of subwavelength size forming two- and three-dimensional DNMs. The operation of these structures is based on the existence of quasistatic resonances supported by subwavelength particles when the frequency of operation approaches the plasma frequency of the particles in the ambient environment. Unfortunately, due to this property, such DNMs will not operate in spectral ranges extended to near-IR. Moreover, these designs may lead

to excessively high losses for realistic materials and cannot be easily realized using standard nanofabrication techniques.

The second type of optical DNMs represents several variations of pairs of patterned thin metal films, including arrays of paired strips (Sec. 4.2), paired wires, staples, and paired perforated plates [SWM$^+$05, SCC$^+$05, ZFP$^+$05, DEW$^+$06]. The operation of these structures is based on the existence of plasmonic resonances of magnetic and electric type supported by cavities formed between the pairs of particles. These structures allow a greater flexibility in tuning their electromagnetic properties and they can be manufactured using standard nanofabrication techniques. However, none of these structures were shown to operate in a wide spectral range from near-IR to visible. Moreover, all these structures comprise unit cells that are only marginally subwavelength (with the vacuum wavelength to period ratio being around 2.5) when the frequency of operation is in the near-IR or visible parts of the spectrum. For instance, it was shown in Section 4.2 that arrays of MSPs (and, hence, arrays of paired wires and patches) cannot support overlapping frequency bands of magnetic and electric resonances when the wavelength-to-period ratio is large. This restriction represents a major limitation for these structures to be considered in effective medium regime. Indeed, it is well known that a structure can be regarded as a quasi-homogeneous metamaterial only when its unit cell is much smaller than the wavelength of operation scaled to the effective index of refraction. Otherwise, the behavior of light is dominated by diffraction and Bragg scattering phenomena.

In this Section we introduce a novel DNM structure that modifies the MSP structure described in Sec. 4.2 by adding a thin metal film in the middle plane between the strips. We show that this simple modification entirely avoids the limitations of the simple MSP structure. The new design provides the following unique properties and features:

- tunable operation in a wide optical spectral range from near-IR to visible,

- true metamaterial design consisting of a periodic unit cells of size much smaller than the effective wavelength of operation, and

- design compatible with standard nanofabrication techniques.

The introduced DNM structure is modeled analytically and numerically to elucidate the physics behind its operation as well as to provide simple means to tune its

effective permittivity, permeability, and index of refraction.

4.3.2 Description of the SPOF geometry

Consider a composite metamaterial consisting of a periodic array of unit cells as shown in Fig. 4.12. The structure is uniform in the y dimension. The unit cells are arranged periodically in the x and z directions with periods L_x and L_z, respectively. The structure comprises a finite number of m_l layers in the z direction and an infinite number of unit cells in the x direction. Every layer comprises an infinite metal film of thickness d_f and an infinite array of metal strip pairs (MSPs) of width w and thickness d_s (Fig. 4.12). In the z dimension, the strips are arranged in pairs symmetrically with respect to the unit cell symmetry plane ($z = 0$). Because the unit cell contains one film and a pair of strips, we refer to this structure as the Strip Pair One Film (SPOF) metamaterial. This name was chosen to distinguish it from an alternative NIM design that contains two films and two strips per unit cell [CKKS06].

The distance between the bottom face of the top strip and the top face of the bottom strip equals $2h$. The strips and the film are assumed to be made of same metal characterized by a relative permittivity with Re $\epsilon_m < 0$ in the optical frequency regime (e.g., silver or gold). It is assumed that d_s, d_f, h, L_x and L_z are all much smaller than the (free-space) wavelength of illumination λ. In addition, d_s and d_f are assumed to be smaller than w, such that possible charge and current gradients in the strips and the film occur primarily in the horizontal (x) dimension. The whole metallic structure is embedded into a homogeneous dielectric material with permittivity ϵ_d of a total thickness $H = m_l L_z$. In this Section, harmonic time dependence $\propto e^{i\omega t}$ of electromagnetic fields is assumed and suppressed in what follows. Under this convention for complex field phasors, passive materials are characterized by negative imaginary part of ϵ and μ.

As shown below, the presence of the middle metal film avoids the limitations of the double-strip (double wire or patch) structure in achieving simultaneously negative ϵ_{eff} and μ_{eff} in deeply subwavelength optical regime. Moreover, it will be shown that for a TM polarization (magnetic field being along the y axis) and for special combinations of the structure parameters and frequency of illumination, the structure in Fig. 4.12 is equivalent to a slab made of a DNM characterized
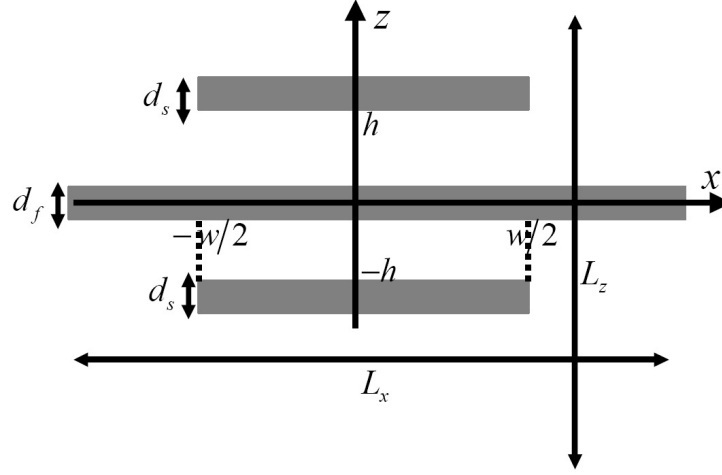
Figure 4.12: Schematic of the Strip Pair One Film (SPOF) structure.

simultaneously by negative real parts of the effective permittivity, permeability, and index of refraction. It is noted that the introduced array of strips is a 2D counterpart of a 3D structure comprising doubly periodic arrays of rectangular or square patches, and therefore the results presented here are directly extendable to more general 3D configurations leading to DNMs with properties nearly independent of light polarization and plane of incidence.

4.3.3 Electric and magnetic resonances in SPOF structure

The structure in Fig. 4.12 can be viewed as a periodic array of cavities formed in the volumes between the strips that support resonances, i.e. source-free fields. Understanding the behavior of these resonances is essential for unraveling the optical properties of the structure. Luckily, the SPOF system is one of a few sub-wavelength geometries that has been described analytically [LFUS06, LFUS07]. Under several assumptions that hold for thin metallic films and strips used to construct NIMs in near-IR or the visible range, Lomakin et al. [LFUS06, LFUS07] obtained closed-form expressions for frequencies of all relevant electric and magnetic resonances in SPOF metamaterial. To describe the resonances of a unit cell, a well-known cavity model can be adapted from electromagnetic analysis of patch antennas [JH89] and modified to take into account plasmonic effects, i.e. the penetration of the fields into

151

thin metal films. Results of Lomakin et al. [LFUS06, LFUS07] are condensed in this paragraph, as they enable profound understanding of MSP-based metamaterials and some of the findings of Sec. 4.2.

Due to the unit cell symmetry around $z = 0$, the structure supports resonances for which magnetic field has either even or odd parity with respect to the $z = 0$ plane. First, consider the resonances with even magnetic field symmetry: $H_y(-z) = H_y(z)$. For this symmetry, no current flows in the central film, and hence the film has no effect on resonances of this type. In contrast, the currents in the top and bottom strips are strong and they flow in opposite directions, forming a current loop (closed by pure displacement currents between the tips) and leading to strong magnetic response. The magnetic field of the magnetic resonances is given approximately by

$$\vec{H} = \hat{y}A(\omega_m, z)\sin(\pi q(x - w/2)/w), \tag{4.34}$$

where q is an integer counting the number of field oscillations in the x direction within strip width w ($q = 1$ for the lowest resonance), $A(\omega_{magn}, z)$ is an even function of z, and ω_m is the magnetic resonance frequency satisfying the following dispersion relation obtained by matching the fields outside and inside the cavity:

$$Y_s^{strip} + Y_z(1 - i\cot k_z h) = 0, \tag{4.35}$$

where $k_z \equiv \sqrt{\epsilon_d(\omega_m/c)^2 - (\pi q/w)^2}$ and $Y_z \equiv \omega_m\epsilon_d/(ck_z)$.

To obtain an approximate expression for the frequency of magnetic resonance (ω_m) in this regime, Lomakin et al. [LFUS06, LFUS07] assume that $|k_z h| \ll 1$, and $\omega_m \ll \pi cq/(w\sqrt{\epsilon_d})$; these assumptions are justified by the solution found. Assuming also that metal dielectric function is approximated by a lossless Drude model, $\epsilon_m(\omega) \approx -\omega_p^2/\omega^2$, it is demonstrated [LFUS06, LFUS07] that

$$\omega_m \approx \omega_p\pi q\sqrt{\frac{d_s h}{\epsilon_d w^2}}. \tag{4.36}$$

This expression shows that the structure in Fig. 4.12 supports magnetic resonances even when the cavity has a subwavelength size. Moreover, Eq. 4.36 shows that the resonant frequency no longer depends solely on the length of resonators (as it is the case with PEC antenna resonances), but rather it is determined by the

shape and the material properties of the composites. In fact, properties of deeply sub-wavelength metal-dielectric structures with optically thin elements are (almost) independent of length. The physical reason for this scale invariance is that the fields inside the resonator are essentially quasistatic and can be described to the zero order approximation by either electrostatic potential ϕ (see Chapter 2) or by the stream function ψ (defined as $\vec{E} = \hat{y} \times \nabla \psi$, see Sec. 4.1 and Ref. [SU04a]); the latter is proportional to the magnetic field H_y.

In resonances with odd magnetic field symmetry, currents in the top and bottom strips flow in the same direction thus resulting in electric dipole response caused by non-zero average dipole moment; these resonances are referred to as electric resonances. Since the symmetry does not prohibit currents in the central symmetry plane, they do flow in the continuous central film and affect the modal field structure of electric resonances significantly.

For this type of resonances, Lomakin et al. [LFUS06, LFUS07] give an analytic dispersion equation, which unfortunately cannot be resolved in closed form using elementary functions without making drastic approximations. However, it can be proven using the analytic dispersion equation that it has two solutions $\omega_e^{(1,2)}$ for each value of the integer q, corresponding to frequencies of the electric resonances of order q. The two lowest-frequency electric resonances correspond to $q = 1$. It was found [LFUS06] that these frequencies satisfy inequalities

$$\omega_e^{(1)} < \omega_m < \omega_e^{(2)}. \tag{4.37}$$

Moreover, in the limit of optically thin film (characterized by small absolute value of sheet impedance $Y_s^{film} = ik_0(\epsilon_m - 1)d_f$), the following strong inequality holds:

$$\omega_m \ll \omega_e^{(2)}. \tag{4.38}$$

As $|Y_s^{film}|$ (and optical thickness) increases, $\omega_e^{(2)}$ decreases towards ω_m, and in the limit $|Y_s^{film}| \to \infty$ we have $\omega_m = \omega_e^{(2)}$. Such behavior allows the second electric and first magnetic resonance bands to partially overlap. As was noted by Lomakin et al. in Ref. [LFUS06], the second electric resonance at $\omega_e^{(2)}$ is similar to the electric resonance supported by MSP structures without continuous films. The main difference between MSP and SPOF brought about by the central film is therefore the existence of the lower-frequency electric resonance at $\omega_e^{(1)}$; this

resonance allows the negative-ϵ_{eff} and negative-μ bands to overlap even when the film and strips are substantially thinner than the skin depth of metal.

Recalling that the unit cell size of the structure in Fig. 4.12 is subwavelength, the structure can be described by its effective permeability and permittivity, as described in Chapter 2. Due to symmetry planes, it can be characterized by diagonal permeability and permittivity tensors $\epsilon_{\text{eff}}^{ij}$ and μ_{eff}^{ij}. For the TM excitation considered here, the relevant tensor components are μ_{eff}^{yy}, $\epsilon_{\text{eff}}^{xx}$ and $\epsilon_{\text{eff}}^{zz}$. For normal incidence ($\vec{k} = k\hat{z}$), only components $\epsilon_{\text{eff}}^{xx}$ and μ_{eff}^{yy} matter: they determine both the refractive index $n_{\text{eff}} = \sqrt{\epsilon_{\text{eff}}^{xx}}\sqrt{\mu_{\text{eff}}^{yy}}$ and effective impedance $Z_{\text{eff}} = \sqrt{\mu_{\text{eff}}^{yy}}/\sqrt{\epsilon_{\text{eff}}^{xx}}$ of metamaterial surface. It is these components $\epsilon_{\text{eff}}^{xx}$ and μ_{eff}^{yy} that become negative near the frequencies $\omega_e^{(1)}$ and ω_m, respectively.

It is important to note that the negative-ϵ_{eff} and negative-μ bands in SPOF can be tuned nearly independently in a very wide range from near-IR to visible. To create a negative index of refraction at a desired wavelength, one may first choose structural parameters w, d_s and h to tune ω_m. Then the film thickness d_f can be chosen so as to bring the electric resonance frequency $\omega_e^{(1)}$ close to ω_m. This second step is possible because the magnetic resonance is very weakly dependent of d_f.

It should also be noted that the location of the continuous film in the central symmetry plane between the strips is critical for preserving the properties of this NIM. Displacing the film to a different location may corrupt the NIM band significantly as the even and odd resonances become combined resonances of indeterminate parity. Moreover, the structure becomes generally bianisotropic: to describe it in effective medium regime, it may be necessary to introduce an additional constitutive parameter responsible for magneto-electric coupling between magnetic (H_y) and electric (E_x) field components.

On the other hand, displacement of strips in each unit cell with respect to each other does not destroy the center of inversion, reducing the overall point group of symmetry from C_{2v} to C_i. Fortunately, resonances in C_i-symmetric are still classified as either electric or magnetic. This circumstance helps preserve the modal structure of the unperturbed resonances of symmetric SPOF upon strip misalignment in a pair, which is a common problem for nano-fabrication. In addition, C_i symmetry prohibits bianisotropy, hence preserving the notion of constitutive parameters ϵ_{eff}, μ_{eff} and their connection to electric and magnetic dipole resonances, as described in Chapter 2.

4.3.4 Numerical demonstration of negative index in SPOF meta-material

To demonstrate negative index of refraction in the SPOF structure, we performed a series of numerical FEM simulations in the frequency domain. The effective permeability, permittivity, and index of refraction can be obtained from EMPR procedure (introduced in Sec. 4.2.4). In all simulations we used SiO_2 as an embedding dielectric with the dielectric constant value of $\epsilon_d = 2.25$. The metal was assumed to be gold whose dielectric function is approximated by a Drude model with parameters cited in Ref. [DEW$^+$06].

Figure 4.13(a) shows the magnitudes of normal incidence, zeroth diffraction order transmission coefficient T_0 for a single layer ($m_l = 1$) in the absence of the central film (blue curves) and for central film thicknesses $d_f = 6.5$ nm (green) and $d_f = 8.5$ nm. Other structural parameters are listed in figure caption.

In the absence of the central film (for pure MSP), two non-overlapping electric and magnetic resonances are obtained at $\lambda_e^{(0)} = 350$ nm and $\lambda_m = 600$ nm, respectively. In the presence of the middle film, for smaller film thickness ($d_f = 6.5$ nm), three separate resonance dips are observed around $\lambda_e^{(2)} = 435$ nm, $\lambda_m = 640$ nm, and $\lambda_e^{(1)} = 800$ nm corresponding to electric, magnetic, and electric resonances, respectively. As d_f increases, the two longer wavelength (magnetic and electric) resonances approach each other, and at $d_f = 8.5$ nm they are very close to each other around $\lambda = 680$ nm. The longest wavelength resonance for $d_f = 0$ and the middle resonance for $d_f > 0$ in Fig. 4.13(a) clearly correspond to bands of negative μ_{eff} in Fig. 4.13(b). The longest wavelength resonances for $d_f > 0$ in Fig. 4.13(a) correspond to bands with Re $\epsilon_{\text{eff}} < 0$ in Fig. 4.13(c).

From the obtained results it is evident that in agreement with Sec. 4.2, no bands with simultaneously negative Re μ_{eff} and Re ϵ_{eff} are obtained when the central film is absent. As predicted by the cavity model and analysis above, inserting a film into the symmetry plane of MSP structure enables double-negative bands and consequently, negative index of refraction.

To better understand the nature of two resonances (λ_m and $\lambda_e^{(1)}$) causing negative refraction, we calculated the field distributions in quasistatic approximation, using recipes of Chapter 2. Figure 4.14 shows the field distribution corresponding to magnetic and electric resonances within the cavity with the same parameters as
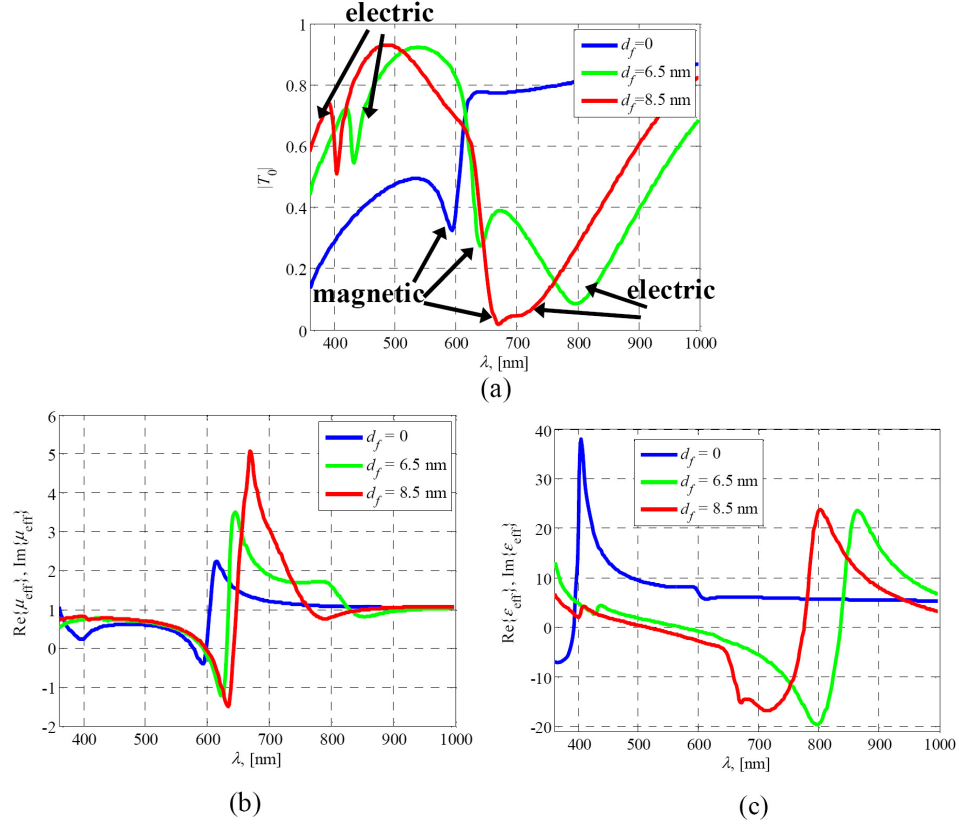
Figure 4.13: Transmittance and extracted constitutive parameters versus the thickness of the central film, d_f. (a) Magnitude of the zeroth order transmission coefficient $|T_0|$; (b) effective permeability μ_{eff} ; (c) effective permittivity ϵ_{eff}. Fixed structural parameters: $L_x = 100$ nm , $w = 50$ nm, $d_s = 15$ nm. The three sets of structures differ by the following parameters: (1) $d_f = 0$ and $h = 7$ nm ($L_z = 44.5$ nm), (2) $d_f = 6.5$ nm and $h = 10.25$ nm ($L_z = 50.5$ nm), (3) $d_f = 8.5$ nm and $h = 11.25$ nm ($L_z = 52.5$ nm). The bands with $\epsilon_{\text{eff}} < 0$ and $\mu_{\text{eff}} < 0$ are almost separated for $d_f = 6.5$ nm, but overlap for $d_f = 8.5$ nm.

156
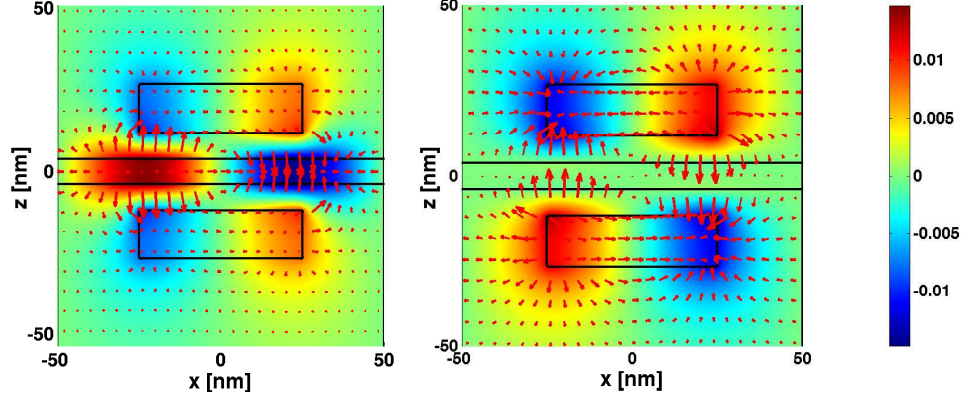
Figure 4.14: Electrostatic potential and electric field profiles corresponding to the lowest-frequency electric (left) and lowest-frequency magnetic (right) resonances of the SPOF metamaterial with parameters listed in Fig. 4.13 and $d_f = 8.5$ nm (set 3). Magnetic resonance is associated with electric quadrupole plasmon resonance.

those used in Fig. 4.13(a) for $d_f = 8.5$ nm (set 3). In full accordance with electromagnetic cavity model, resonance identified as electric ($\lambda_e^{(1)}$) has x-odd, z-even quasistatic potential ϕ plotted in Fig. 4.14 in color. Therefore, it corresponds to an x-polarized electric dipole resonance. The resonance identified as magnetic (λ_m) has quadrupolar (odd-odd) symmetry of electrostatic potential, and therefore its stream function ψ (and magnetic field) is even-even. From the results in Figs. 4.13, 4.14 it is evident that the structure in Fig. 4.12 indeed can operate as a DNM having a deeply subwavelength unit cell with a wavelength-to-period ratio of about 7, and that the cavity model predictions are valid.

To verify that the phenomena leading to DNM operation are quasistatic in their physical nature, we have plotted in Fig. 4.15 the effective permittivity obtained via two methods: using EMPR procedure described in Sec. 4.2.4, and using quasistatic theory presented in Sec. 2.2. It is evident that the quasistatic approximation captures the behavior of ϵ_{eff} very well. Note that the position of the resonance extracted from fully electromagnetic simulations is red shifted form its electrostatic value because of the finite retardation effects proportional to $(\omega L)^2$, as described in Sec. 2.5.

Figure 4.16 shows that the structure in Fig. 4.12 can be tuned to operate as

157
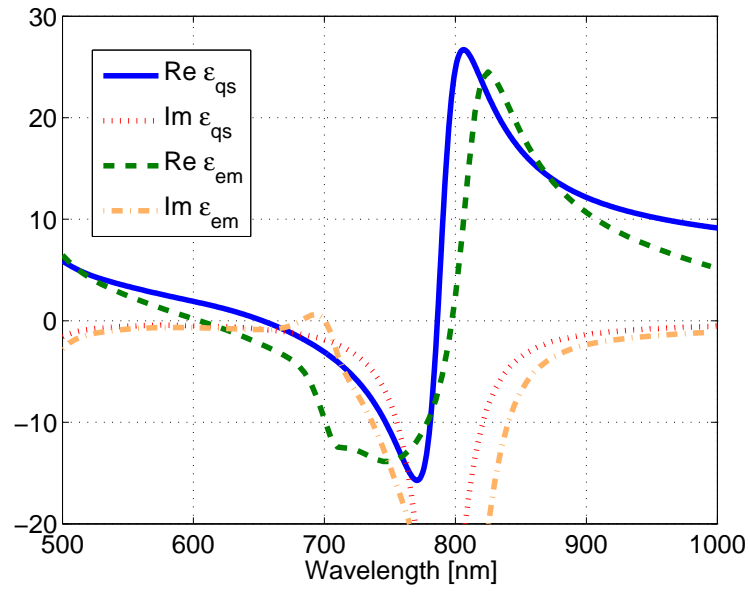
Figure 4.15: Comparison between the quasistatic dielectric permittivity ϵ_{qs} computed using recipes of Section 2.2 and fully electromagnetic ϵ_{eff} extracted using single-layer EMPR.
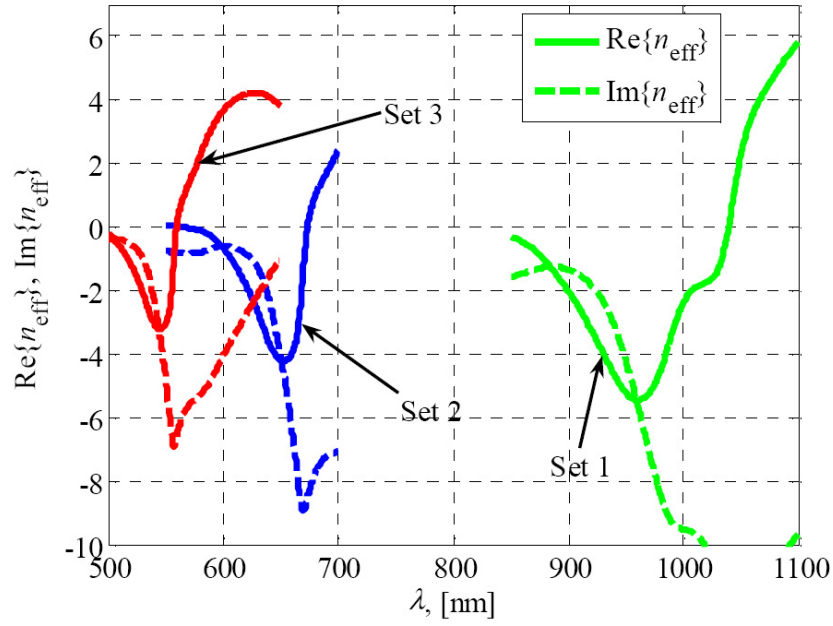
Figure 4.16: Effective index of refraction n_{eff} for different sets of parameters for a single DNM layer. Set 1 (green): $L_x = 150$nm, $L_z = 52$nm, $w = 90$nm, $d_s = 15$nm, $d_f = 8$nm, $h = 11$nm. Set 2 (blue): $L_x = 100$nm, $L_z = 52.5$nm, $w = 50$nm, $d_s = 15$nm, $d_f = 8.5$nm, $h = 11.25$nm. Set 3 (red): $L_x = 100$nm, $L_z = 57$nm, $w = 40$nm, $d_s = 15$nm, $d_f = 10$nm, $h = 13.5$nm. Evidently the double-negative band of SPOF can be tuned to any wavelength in near-IR and the entire visible spectrum, while remaining in deeply sub-wavelength regime.
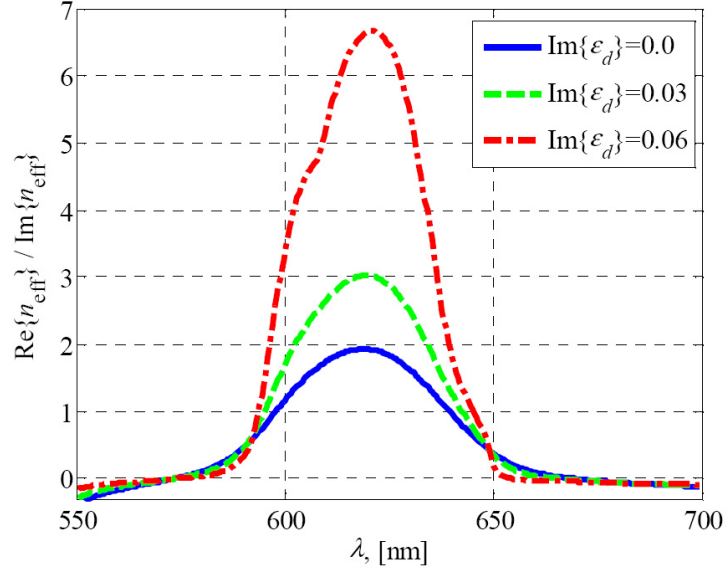
Figure 4.17: The ratio Re n_{eff}/Im n_{eff} characterizing the losses in the system as a function of formally introduced gain (modeled by Im ϵ_d of the wrong sign) in the dielectric layer for a single DNM layer. Structural parameters: $L_x = 100$nm, $L_z = 51.5$nm, $w = 50$nm , $d_s = 15$nm, $d_f = 7.5$nm, $h = 10.75$nm.

a DNM in the entire range from near-IR to visible by depicting Re n_{eff} and Im n_{eff} for three sets of structure parameters, resulting in a double-negative band in three wavelength ranges $\lambda = 820 - 1040$ nm, $550 - 670$ nm, and $500 - 560$ nm respectively for sets labeled 1,2,3.

Losses of the proposed DNMs are illustrated by Fig. 4.17, which shows the ratio Re n_{eff}/Im n_{eff}, also known as the NIM Figure of Merit (FoM). Three DNM structures are considered: one embedded in a passive dielectric and two embedded in a dielectric with gain. Geometrical parameters of the DNMs and selected values of gain are listed in the caption and legend. The considered values of Im $\epsilon_d = 0.03$ (0.06) correspond to gain coefficient of 1500cm^{-1} $(3000$cm$^{-1})$, respectively. Such values of the gain coefficient can be experimentally achieved with semiconductor polymers or laser dyes [Law04, HSDGH97]. These parameters were chosen to demonstrate a possibility to improve the DNM operation by means of active materials. It is seen that the largest FoM is obtained for $\lambda = 620$ nm in
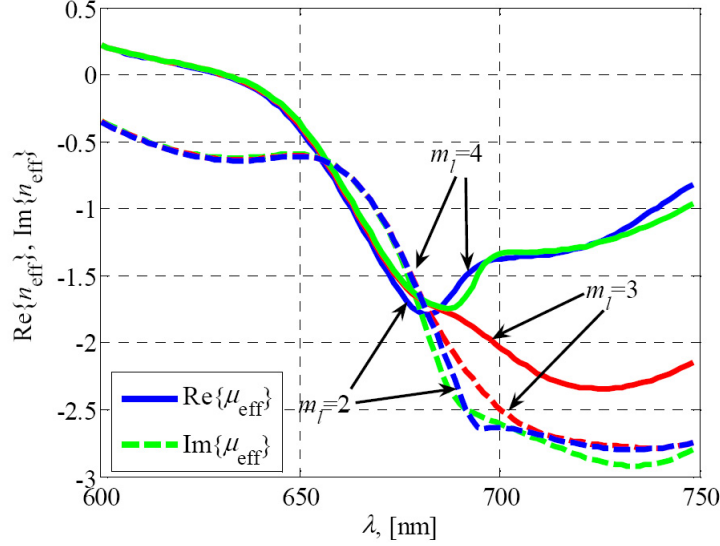
Figure 4.18: Effective index of refraction of SPOF metamaterial computed with EMPR procedure for different number of layers m_l (green: $m_l = 2$, red: $m_l = 3$, blue: $m_l = 4$). Solid lines: Re n_{eff}, dashed lines; Im n_{eff}. Structural parameters are chosen as $L_x = 100$ nm , $L_z = 102.5$ nm, $w = 50$ nm, $d_s = 15$ nm, $d_f = 8.5$ nm, $h = 11.25$ nm. Evidently the negative index band in the range $\lambda = 640 - 680$ nm exists for any number of layers.

all three cases with larger FoM corresponding to larger gains. From these results we learn that even in the passive version of SPOF metamaterial, optical losses are reasonably low, thus allowing practical applications of the suggested DNM. The loss can be further reduced by incorporating active materials with modest gain.

Figure 4.18 depicts the extracted Re n_{eff} for the structure described as set 3 in Fig. 4.16 (with $d_f = 8.5$nm), now with variable numbers of layers $m_l \geq 1$, in order to demonstrate that the structure can operate as a bulk metamaterial. These simulations show that although Re n_{eff} depends weakly upon the number of layers, it is reliably negative in the range $600 < \lambda < 680$ nm for any m_l. Recent studies indicate, however, that in the tight-binding regime where unit cells interact strongly, effective medium parameters determined from EMPR procedure may depend upon m_l a lot stronger [DUS07] than for the SPOF geometry reported here. Weak dependence of the negative-index band upon the number of layers provides evidence that
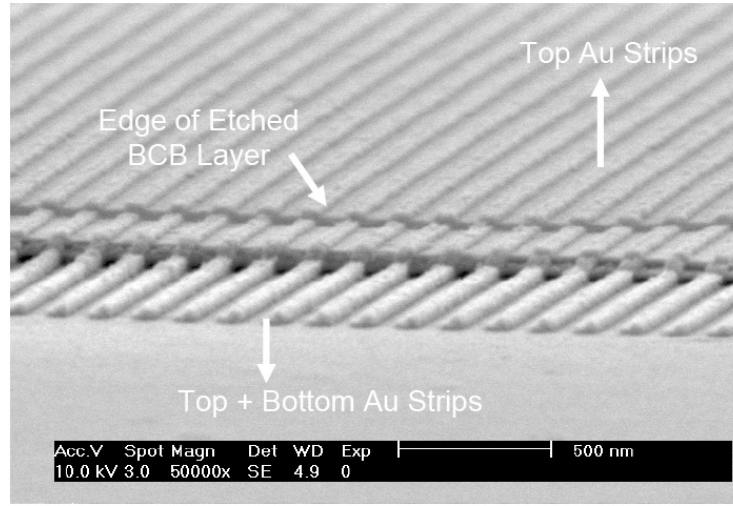
Figure 4.19: Scanning Electron Microscopy image of a single-layer SPOF metamaterial fabricated by Davanço et al. from gold and transparent polymers [DZF+07]. Grating period 150 nm, strip width 80 nm, thickness of strips and film ≈ 20 nm, dielectric spacer between strips and film ≈ 15 nm. Image courtesy Marcelo Davanço, Xuhuai Zhang and Stephen Forrest, Univ. of Michigan.

the properties of SPOF metamaterial are determined predominantly by properties of a single resonator, in agreement with the concept of quasistatic electromagnetic susceptibilities introduced in Section 2.3.

Finally, we note that the value of the scattering frequency Γ in the Drude model in all simulations above is more than 3 times larger as compared to values assumed for simulations in some other recent works (e.g. [ZFP+05, ASE06]). Simulation results in this Section indicate that the SPOF structure performs very well even with these, more realistic values of damping in noble metals. Evidently, reducing the value of Γ by a factor of 3 would significantly enhance the NIM FoM of this metamaterial.

4.3.5 Conclusions

A novel realization of a double-negative metamaterial (DNM) comprising unit cells of deeply subwavelength size was introduced in this Section. The DNM is composed of unit cells each comprising a continuous optically thin metal film

sandwiched between two identical thin metal strips separated by a small distance from the film. The region between the metal strips operates as a nano-scale sub-wavelength cavity; this metamaterial's properties are determined largely by the resonances of such a cavity. It was shown that the SPOF structure supports both magnetic and electric resonances that can be tuned to occur in overlapping frequency bands. It was further shown that the crucial role in the ability to achieve DNM operation is played by the presence of the middle film that enables tuning the electric resonances independently from the magnetic ones. Tunability of this structure is so high that the NIM band can be adjusted to any wavenumber from near-infrared to the blue end of the visible band. Existence of the NIM band in the bulk metamaterial is verified by multiple layer simulations, which confirm that the negative index band is determined mostly by single-resonator properties and remains intact in multi-layered structures. The proposed DNM can be manufactured using standard nanofabrication methods from materials compatible with these methods; gold and optically transparent polymers are typically used for the plasmonic and dielectric components, respectively. First prototypes of the SPOF NIM have been recently fabricated at the University of Michigan by the Optoelectronic Components and Materials group [DZF+07]; Figure 4.19 shows SEM image of a selected sample. Extensions of the presented 2D structure to 3D by using patches instead of strips are straightforward and will allow for constructing DNMs with effective parameters independent on the incident plane and wave polarization.

4.4 Isotropic optical magnetism and negative refraction in plasmonic metafluids

In this Section, we introduce a novel concept of electromagnetic *metafluids* — liquid metamaterials based on Artificial Plasmonic Molecules (APM) [WBNH07, USF$^+$07]. Isotropic APMs in the shape of tetrahedral plasmonic nanoclusters are analyzed using quasistatic plasmon resonance theory and vectorial finite element frequency domain (FEFD) electromagnetic simulations. With the aid of group theory, we identify the resonances that provide the strongest electric and magnetic response, and study them as a function of separation between spherical nanoparticles. It is demonstrated that a colloidal solution of plasmonic tetrahedral nanoclusters can act as an optical medium with very large, small, or even negative effective permittivity, ϵ_{eff}, and substantial effective magnetic susceptibility $\chi_M = (\mu_{\text{eff}} - 1)/(4\pi)$ in the visible or near infrared bands. Ideas are suggested for further improvement of magnetic metafluids, which will hopefully result in development of a negative-index metafluid (NIMF).

4.4.1 Introduction and motivation

The optical properties of metallic multi-nanoparticle structures have been of great theoretical and experimental interest in recent years due to biological and chemical sensing applications, including Surface Enhanced Raman Spectroscopy (SERS) and Localized Surface Plasmon Resonance (LSPR) sensing [Met84, CG02, MTYH02, JH04, WGL$^+$07, AM06, JEES06]. In the former, large electric field enhancements near the surfaces of particles or in the gaps of nanoparticle clusters near the plasmon frequencies lead to an increased Raman cross section. In the latter, a change of refractive index from a nearby molecule causes a red-shift of the plasmon frequencies. Plasmonic nanostructures have also attracted a great deal of attention as an approach to construct electromagnetic metamaterials — media with optical properties previously unavailable in nature.

In this Section, we introduce a novel concept called a *metafluid* — a liquid metamaterial containing Artificial Plasmonic Molecules (APMs) [WBNH07, USF$^+$07]. APMs are geometrically ordered aggregates of plasmonic nanoparticles that typically consist of 2-15 individual "atoms"; structures of this type were recently

fabricated from non-plasmonic materials [MEP03, YMM⁺04, MP04, CYK⁺05].
With the flexibility to engineer APM geometries, the optical properties of APMs
can differ tremendously from those found in natural molecules. The size of an APM
greatly exceeds that of a typical molecule yet may be considerably smaller than
the optical wavelength. Due to the small spatial extent of the APMs compared
to optical wavelengths, the resulting metafluid can still be viewed as an effective
medium and characterized by its effective coefficients such as, for example, dielec-
tric permittivity and magnetic permeability. By changing the size and arrangement
of the constituent plasmonic nanoparticles inside an APM, the APM's optical re-
sponse at the frequency of interest can be controlled in both magnitude (strong or
weak) and character (electric or magnetic, scattering or dissipative). Recent interest
in liquid-liquid optical waveguides [PQY06] further motivates the development of
metafluids.

The term "metafluid" in this Section is composed of two words: metamaterial
and fluid. By "metamaterial" we mean an artificially created composite of regular
materials that exhibits unusual electromagnetic properties, such as, for example,
negative magnetic permeability or negative index of refraction. One can ascribe
effective index of refraction to a composite medium, for example, when the structure
is periodic (regardless of the distances between particles and their sizes). Such
situation is known as the *Bloch-Floquet regime* or the photonic crystal regime.
Assignment of refractive index is also possible in the *effective medium regime*, i.
e. when the size of individual scatterers is much smaller than the wavelength
in immersion medium. These two regimes are not mutually exclusive when the
distance between particles is sub-wavelength; in Section 4.4.5 we take advantage
of periodic boundary conditions to characterize the optical properties of a dense
nanoparticle colloid. Since optical parameters of an effective medium depend mostly
on the average distance between identical particles in the ensemble, and little on
the locations of individual particles, period-independent spectral features of periodic
ensembles must be shared by all random ensembles with the same particle number
density.

In this Section we theoretically investigate an APM composed of four metal-
lic nanospheres situated equidistant from one another at the vertices of a regular
tetrahedron, as the first candidate for optical metafluids. We refer to this structure
as the *tetramer*. This structure has recently attracted attention as a candidate for

a coherently controlled nanorotor [SLBZ06]. For electromagnetic metafluids, APMs with tetrahedral symmetry are attractive because their single-particle polarizabilities are orientation-independent. We have already used this property of tetramers in Sec. 2.3.4 to illustrate quasi-static magnetic response of rotationally-invariant resonators. The effective dielectric tensor, $\hat{\epsilon}$, of most fluids is effectively a scalar because of the rapid rotation and high spatial density ($\sim 10^{23}$ cm^{-3}) of the constituent molecules. However, when gigantic artificial plasmonic molecules described in this paper are part of the metafluid, their rotational frequency and concentration in the solution may not be sufficient to provide isotropization by temporal and spatial averaging. Therefore, the isotropic polarizability of tetrahedral plasmonic molecules becomes crucial for ensuring that the tensors $\hat{\epsilon}$ and $\hat{\mu}$ of a metafluid are spherical. In addition, isotropy helps maintain effective medium regime by suppressing non-coherent elastic scattering (related to transitions between degenerate states with different projections of angular momentum) and suppressing non-scalar coherent scattering (see §60 and especially Eq. 60.11 of Ref. [BLP82]); both types of scattering contribute to optical opacity of suspensions of freely-oriented systems. Dynamic light scattering effects associated with fluctuations of particle orientations and positions [vMMWM98] are out of scope of this Section.

In effective medium regime, appropriate quantities to describe the propagation of a plane wave are dielectric and diamagnetic susceptibilities of the compound medium. In general, for a linear medium there are four such (tensor) quantities, defined by Eq. 2.18 in Sec. 2.3. In this Section we focus only on non-bianisotropic (non-gyrotropic) media, which can be described with an effective permittivity $\hat{\epsilon}_{\text{eff}}$ and permeability $\hat{\mu}_{\text{eff}}$ only. In Section 2.3.5, it was proven that the tetrahedral group T_d of the tetramer has sufficient symmetry to prohibit bianisotropy (i.e., magneto-electric coupling) in the electromagnetic response of sub-wavelength plasmonic particles (see Table 2.2).

Thus, an effective medium composed of tetramers is isotropic, non-chiral, and described by two scalar quantities, ϵ_{eff} and μ_{eff}. It should be mentioned that the tetramer is not the only metamolecule that forms metafluids with such properties. There are seven 3-dimensional point groups which guarantee a second-rank tensor to be spherical: three chiral groups (T, O, I) and 4 non-chiral groups (T_d, O_h, T_h, I_h). These groups are known as the cubic or *isometric* symmetries. We note that, in general, magneto-electric coupling terms $\hat{\xi}$ and $\hat{\zeta}$ do not average to zero when

accounting for the rotation of APMs. This means, for example, that a medium consisting of chiral APMs is also chiral. The remaining 4 groups can be utilized for the design of isotropic, non-gyrotropic optical metamaterials. The minimum number of identical spherical nanoparticles is 4 for T_d symmetry (vertices of a regular tetrahedron), 6 for O_h (octahedron), 12 for I_h (icosahedron) and 20 for T_h (pyritohedron), as summarized in Table 4.1. A tetramer is thus the *minimal* non-chiral, fully isotropic "metamolecule".

Experimental routes exist to assemble colloidal nanoparticles into highly ordered clusters. One experimental route to the assembly of tetramers and larger symmetric structures, including isotropic 6-particle "octamers" and 12-particle "icosamers", is particle clustering in an oil-in-water emulsion process [MEP03]. Particles are first functionalized to be hydrophobic and then transferred to an oil solvent. The oil is then added to water with surfactant and sheared in a homogenizer, which yields surfactant-stabilized oil droplets in water. Next, the oil is evaporated from the emulsion, and particles are forced into clusters due to capillary forces and are held solidly together by van der Waals forces. Tetrahedral clusters are separated from clusters of other particle number by centrifugation in a density gradient. This technique for creating clusters is versatile and applies to all types of particles ranging from silica to PMMA [YMM+04]. In addition, clustering is possible for hydrophilic particles through a water-in-oil emulsion [CYK+05].

The remainder of the Section is organized as follows: in Section 4.4.2, the plasmon modes of a tetramer are found using the new finite-element implementation of the surface charge integral equation (SCIE) formalism [MFZ05]. Using group theory, we classify the plasmon modes by their electric and magnetic properties. Coupling between deeply sub-wavelength nanoparticles and optical fields is discussed in Sec. 4.4.3. Quasistatic predictions are aided by fully electromagnetic simulations. Section 4.4.4 deals with the optical absorption spectra in the tetramer system using finite element frequency domain (FEFD) calculations. In Section 4.4.5, a tetramer colloid is theoretically characterized as an effective medium with isotropic dielectric permittivity and magnetic permeability.

167

4.4.2   Quasistatic analysis of the plasmon modes of the tetramer

The two most frequently used methods to compute the plasmon resonances of a complex nanostructure in the quasistatic (non-retarded) limit are the Plasmon Hybridization (PH) method [PRHN03] and the Electrostatic Eigenvalue (EE) approach [BS80, MFZ05].

In the PH approach, the plasmon modes of a multi-nanoparticle systems are expressed as linear combination of the (primitive) plasmon modes of the individual particles [PN04]. The primitive plasmon modes interact with each other through the Coulomb forces induced by their surface charges. An appealing feature of the PH approach is that its eigenvalue problem is very similar to the eigenvalue problem for molecular orbitals in quantum chemistry. This analogy gives an insight into the relationship between the plasmon modes of a composite structure and the plasmons of its constituent particles, and encourages the use of the group theory for symmetry classification of these modes [WBNH07]. In contrast with the coupled-dipole approximation (CDA) [HS04, US05a], PH method can account for hybridization of primitive eigenmodes with arbitrary multipole order l.

Electrostatic Eigenvalue approach [BS80, MFZ05] is a general method for computing electrostatic eigenfunctions of arbitrarily-shaped particles or their ensembles. EE method does not take advantage of the simplicity of primitive plasmon modes, which makes it applicable also to structures with non-spherical particles [KUI$^+$06, UKI$^+$07, KUI$^+$07]. Our implementation of EE method for plasmonic sphere clusters is briefly described below.

A surge of recent interest in optical properties of plasmonic nanoparticles originates from the unique property of negative-permittivity interfaces to support source-free excitations known as surface plasmons. These excitations exist even for particle sizes much smaller than the wavelength of light at which they occur, which suggests that they are electrostatic in nature. Consequently, they can be found as solutions of the electrostatic Laplace equation with no external field or charge:

$$\nabla \epsilon(\vec{x}) \nabla \phi = 0. \tag{4.39}$$

For homogeneous negative permittivity particles ($\epsilon_p < 0$) in a uniform transparent immersion medium ($\epsilon_s > 0$), this equation can be recast as a linear generalized eigenvalue problem [BS80] in which the electrostatic permittivity of plasmonic particles

plays the role of an eigenvalue:

$$\nabla \theta(\vec{x}) \nabla \phi = s \nabla^2 \phi, \tag{4.40}$$

where $\theta(\vec{x})$ equals 1 inside the particle(s) and zero elsewhere, and $s = 1/(1 - \epsilon_p/\epsilon_s)$.

If the boundary of plasmonic particles is sufficiently smooth, differential equation (4.40) can be reduced to a linear integral equation [MFZ05] for electrostatic surface charges σ:

$$\sigma(\vec{x}) = \frac{\lambda}{2\pi} \oint dS' \sigma(\vec{x}') \vec{n}(\vec{x}) \cdot \nabla_x G(\vec{x}, \vec{x}'), \tag{4.41}$$

where $G(\vec{x}, \vec{x}')$ is the electrostatic Green's function, $\vec{n}(\vec{x})$ is the outward normal to the surface of plasmonic particle, and

$$\lambda = (\epsilon_p - \epsilon_s)/(\epsilon_p + \epsilon_s) \tag{4.42}$$

is the electrostatic eigenvalue [MFZ05].

The two approaches (4.40,4.41) are equivalent and yield essentially the same set of electrostatic eigenvalues, related to the resonant permittivities according to

$$\epsilon_n = \epsilon_s(1 - 1/s_n) = \epsilon_s(1 + \lambda_n)/(1 - \lambda_n). \tag{4.43}$$

The corresponding eigenfunctions $\{\sigma_n\}$ and $\{\phi_n\}$ are related by integration,

$$\phi_n(\vec{x}) = \oint G(\vec{x}, \vec{x}') \sigma_n(\vec{x}') \, dS', \tag{4.44}$$

or differentiation,

$$\sigma_n(\vec{x}) = \frac{\epsilon_n - 1}{4\pi} (\vec{n} \cdot \vec{E}_n) \equiv -\frac{\epsilon_n - 1}{4\pi} \partial \phi_n/\partial n, \tag{4.45}$$

where the outward normal derivative is applied to the potential inside the plasmonic phase.

The only difference between approaches (4.40,4.41) occurs at the values of $s = 0$ and $s = 1$, at which the volumetric equation (4.40) becomes meaningless, while the surface equation (4.41) remains meaningful. As a result, an FEM discretization of volumetric equation (4.40) returns many spurious, unphysical solutions with

169

$s_n \approx 0$ ($\epsilon_n \to -\infty$) and $s_n \approx 1$ ($\epsilon_n \to 0$). It can be shown mathematically and seen numerically using FEM discretization that the surface equation (4.41) does have meaningful solutions corresponding to $\epsilon_n = -\infty$, and therefore, $s_n = 0$ is indeed an electrostatic eigenvalue. For a single connected surface, this eigenvalue is not degenerate, and corresponds to a uniform charge distribution $\sigma_n = \text{const} \neq 0$ on the particle surface. For disconnected surfaces consisting of a finite number N of connected closed surfaces (for the tetramer, $N = 4$), the $\epsilon_n = -\infty$ eigenvalue is N-degenerate; corresponding N linearly independent eigenfunctions are uniform surface charge distributions on one of the N particles with zero surface charge on the remaining $N - 1$ particles (or linear combinations of such functions). Uniformity of surface charges σ_n in these eigenfunctions holds true regardless of the particle shape or symmetry (corresponding potential eigenfunctions ϕ_n would be constant only for spherically or cylindrically symmetric particles). Note that although for a single particle the $\epsilon_n = -\infty$ eigenvalue can be excluded from spectral analysis of optical response (because it corresponds to non-zero total charge $Q = \int \sigma_n dS = \text{const} \int dS \neq 0$), in clusters with $N \geq 2$ particles linear combinations of such eigenfunctions exist that do not violate charge neutrality of the cluster. Electrostatic eigenvalue $\epsilon_n = -\infty$ corresponds to resonances of perfectly electrically conducting (PEC) particles. For strongly sub-wavelength metallic particles with plasma-like dispersion ($\epsilon \approx 1 - \omega_p^2/\omega^2$) the corresponding resonant frequencies are well outside the optical band and thus do not affect our analysis of optical metamaterials in the visible or near-infrared bands.

Numerical discretization of both versions of the Electrostatic Eigenvalue (EE) method is straightforward and was implemented using FEM software package COMSOL Multiphysics. The differential equation (4.40) method may be preferable for periodic systems [KUI+06, UKI+07, KUI+07], where periodicity is easily imposed as boundary conditions for potential ϕ, whereas in the surface integral approach (4.41) periodic boundary conditions must be embedded into the Green's function $G(\vec{x}, \vec{x}')$. On the other hand, the volumetric equation (4.40) has many more degrees of freedom for the same number of mesh elements on the particle surface than the equivalent equation (4.41). In general, this leads to a large number of unphysical solutions, especially near the singularities at $s_n = 0$, $s_n = 1/2$ and $s_n = 0$. The surface integral approach does not suffer from this problem as much as the differential approach (4.40), at least for very smooth surfaces (such as spheres in

this Section).
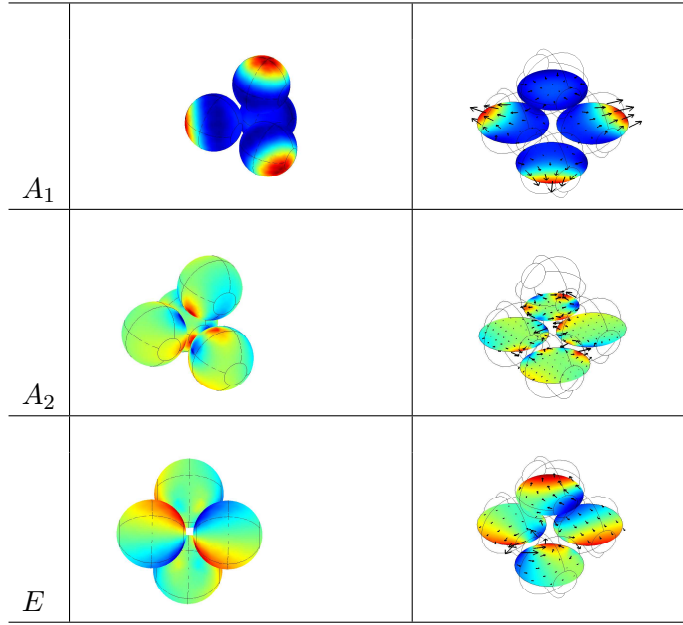
Figure 4.20: Examples of electrostatic resonances of a tetrahedral plasmonic molecule. Left column: potential on the surface. Right: potential (color) and electric field (arrows) in cross-sections. The lowest-lying resonance of each irreducible representation (see Table 2.2) except triplets (T_1, T_2) is presented. Gap-to-diameter ratio in the cluster is 1/10. Triplets are shown separately in Fig. 4.21.

Using the surface charge equation (4.41), we have performed finite element method (FEM) calculations using experimentally relevant parameters. The lowest-lying resonances of each symmetry type are plotted in Fig. 4.20. Since the electrostatic spectrum is scale-invariant, the only dimensionless structural parameter in the problem is the ratio of a sphere diameter D to the gap h between their surfaces. Another dimensionless parameter, the dielectric contrast defined as the ratio of the dielectric constant of the particles ϵ_p and the dielectric constant of the solvent (ϵ_s). The dielectric contrast influences the energies of all electrostatic resonances. The vacuum wavelength λ_{vac} is not a parameter, but rather a label, related unambiguously to the dielectric contrast ϵ_p/ϵ_s.
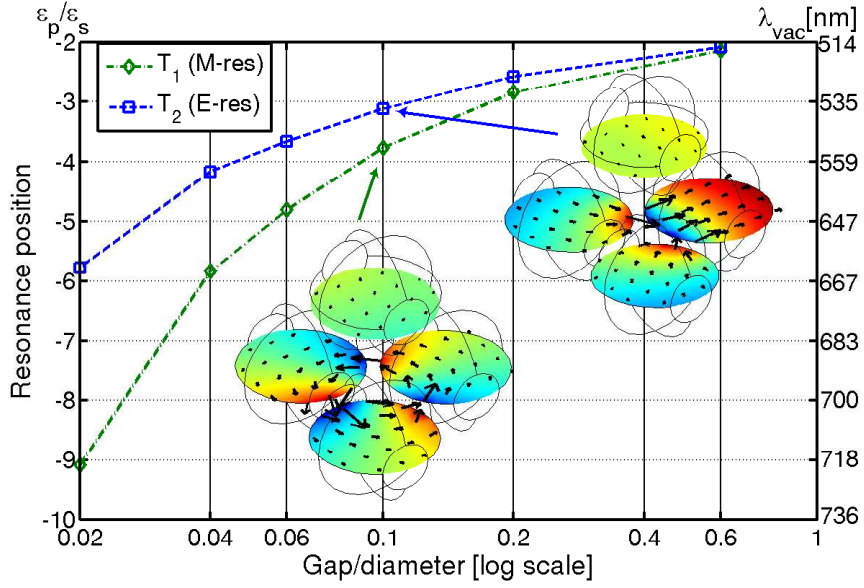
Figure 4.21: Positions of the two lowest-lying electrostatic resonances as a function of the gap-to-diameter ratio. Left vertical axis: resonant permittivity of a plasmonic particle relative to that of solvent (ϵ_p/ϵ_s); the plots are applicable universally to any metal and solvent. Right axis: resonant wavelength for gold silica-coated tetramers in the index-matching solvent with $n_s = 1.4$, assuming dielectric function of gold from [Pal85]. Insets: electrostatic potential and electric field profiles of these T_1 and T_2 modes in clusters with gap/diameter=0.1.

4.4.3 Surface plasmon coupling with long-wavelength radiation

To understand how electrostatic resonances are excited by incident radiation, and how they contribute to optical extinction and absorption spectra, one may start with the quasistatic approximation, described in Chapter 2.

In the quasistatic approximation, the strongest interaction between incident light and particles is the coupling of a nearly uniform electric field with the induced electric dipole moment of the particles. The strength of this interaction is characterized by the normalized dipole moment of an eigenmode (see Sec. 2.3),

$$\vec{p}_n = \frac{\oint \vec{x}(-\partial\phi_n/\partial n)\, dS}{\left(V_p \oint \phi_n \partial\phi_n/\partial n\, dS\right)^{1/2}} = \frac{\int (-\nabla\phi_n)\, \theta\, dV}{\left(V_p \int (\nabla\phi_n)^2\, \theta\, dV\right)^{1/2}}, \tag{4.46}$$

where $\sigma_n(x)$ is the charge eigenfunction of nth resonance, $\phi_n(x)$ is its potential, $\partial/\partial n$ is the normal derivative, and $V_p = \int \theta dV$ is the volume of metal in a cluster.

According to equation (4.46), not all eigenmodes have a non-vanishing electric dipole moment; only those that transform under the same irreducible representation as $\vec{x}$, namely, T_2 modes (Table 2.2), are allowed to have it. We note here that $\sigma_n(x)$ and $\phi_n(x)$ have the same symmetry, and either can be used to characterize the plasmon's irreducible representation. To see that, recall that an integral of any function other than a fully symmetric A_1 function will vanish; the product of two functions – $\sigma_n(x)$ and either Cartesian component of $\vec{x}$ – may contain A_1 coupling only if they both belong to the same representation. Therefore, $\sigma_n(x)$ must belong to the *vector representation* of the symmetry group T_d. Standard character tables of point groups allow one to identify the vector representation of T_d group as T_2 (see Table 2.2).

In addition to the strong excitation of electric dipole resonances, which remains strong even in non-retarded limit, weakly inhomogeneous electric and magnetic fields of an incident electromagnetic wave also induce various electric and magnetic multipoles. Though lots of non-dipolar modes are excited by inhomogeneous fields, only some of them carry magnetic dipole moment. This induced magnetic moment can be calculated in quasistatic approximation from the total current

$$J = J_c + \partial\vec{P}/\partial t \equiv \frac{\epsilon - 1}{4\pi} \partial\vec{E}/\partial t \tag{4.47}$$

Group	Min. polyhedron	ED	MD	LOEM of MD
T_d	tetrahedron (4)	T_2	T_1	octupole ($2^J = 8$)
T_h	pyritohedron (20)	T_u	T_g	quadrupole ($2^J = 4$)
O_h	octahedron (6)	T_{1u}	T_{1g}	hexadecapole ($2^J = 16$)
I_h	icosahedron (12)	T_{1u}	T_{1g}	hexacontatetrapole ($2^J = 64$)

Table 4.1: Non-chiral isometric (cubic) groups, their vector and pseudovector irreducible representations related to electric and magnetic dipole resonances, and the Lowest-Order Electric Multipole (LOEM) of magnetic dipole resonances. All listed minimum-vertex polyhedra except the pyritohedron (T_h) have been observed in colloidal sphere clusters [MEP03].

in plasmonic particles:

$$\vec{\mathcal{M}} = \frac{1}{2c} \int [\vec{x} \times \vec{J}] \, \theta \, dV = \frac{i\omega}{8\pi c} (\epsilon - 1) \int [\vec{x} \times (-\nabla \phi)] \, \theta \, dV. \tag{4.48}$$

After simple transformations, energy-normalized magnetic dipole moment of an eigenmode can be expressed in terms of surface integrals (see Sec. 2.3):

$$\vec{m}_n = \frac{\oint [\vec{n} \times \vec{x}] \, \phi_n \, dS}{\left(V_p \oint \phi_n \frac{\partial \phi_n}{\partial n} \, dS \right)^{1/2}}. \tag{4.49}$$

Expression (4.49) demonstrates that only eigenmodes that transform as a *pseudovector* may have a non-vanishing magnetic dipole moment in the lowest order to retardation parameter η. According to Table 2.2, pseudovectors (such as the rotation operator R_α) transform under the T_1 representation of the group T_d.

The method for calculating electric and magnetic multipole compositions of the plasmon states has been described in Section 2.3.5 and applied to the tetrahedral group T_d in Table 2.2. The most important conclusion following from that analysis is that only T_2 (T_1) modes of tetramers can have non-zero electric (respectively, magnetic) dipole moment. Considering that clusters of other highly symmetric shapes, ranging from octahedral to icosahedral, have already been synthesized from various dielectric materials [MEP03], we have performed such multipolar analysis for all non-chiral isometric (cubic) groups. Results that are relevant to electromagnetic homogenization of colloids are condensed in Table 4.1.

In the remainder of this Section, we pay attention only to the T_2 and T_1 modes of tetramers. Amongst all T_2 (or T_1) modes, the ones with the lowest neg-

ative resonant permittivity eigenvalue (thus, the lowest frequency) should have the strongest electric (respectively, magnetic) response. This is because higher eigenmodes of a particular symmetry type have additional sign changes in their surface charge eigenfunction σ_n, resulting in smaller coupling to the incident electromagnetic field. In addition, the higher-frequency resonances experience stronger damping due to the increase of resistive losses in metal.

Figure 4.21 shows a close-up of the plasmon resonance positions of the lowest two modes of the tetramer, which happen to be T_1 and T_2, plotted against the gap-to-diameter ratio of gold tetramers in a dielectric environment of index $n_s = 1.4$. This index of refraction corresponds to the dielectric medium in which a tetramer may be found after the fabrication process with an appropriate index matching solvent. Gold is assumed as plasmonic material through the remainder of this Section; the dielectric function of gold is modeled using interpolation of optical constants from reference [Pal85]. The graphical insets of Fig. 4.21 show electric fields in cross-sections of these resonances.

4.4.4   Electromagnetic spectra of tetramer colloids

In the previous section we provided some insight into electromagnetic properties of symmetric tetrahedral clusters using quasistatic plasmon theory. In particular, we described plasmonic resonances that may have the right properties to provide enhanced electric and magnetic susceptibilities. However, when finite-sized clusters (not too small compared with the wavelength of light $\lambda \equiv 2\pi c/\omega$), retardation effects become important. Those include: shift in the resonant frequencies (see Sec. 2.5) and excitation of resonant modes that do not possess an electric dipole moment (Sec. 2.3.1). To predict the exact frequencies of these resonances and their strength, we have made finite-element frequency-domain (FEFD) electromagnetic simulations of tetramers using the commercial software package COMSOL.

Extinction and absorption cross-section are measured as functions of frequency in the following fashion. A single tetramer is placed in a rectangular domain, on lateral sides of which either periodic or mirror-symmetry boundary conditions are applied. In effect, a doubly-periodic rectangular array (with periods L_y, L_z) of identical tetramers is simulated. As long as individual tetramers interact only weakly via their near-field, and far-field interactions are not resonantly enhanced [HS04, US05a],

175

spectra of ordered arrays are close to those of randomly distributed and oriented tetrahedral clusters. These conditions are fulfilled by allowing sufficient separation between tetramers, and by using wavelengths sufficiently longer than the largest of the two periods, ruling out Wood's anomalies [US05a]. The array is illuminated by a monochromatic, linearly polarized plane wave of unit intensity, with $\vec{E}||\hat{y}$ and $\vec{H}||\hat{z}$, incident normally ($\vec{k} = k\hat{x}$) on the yz-plane of the array.
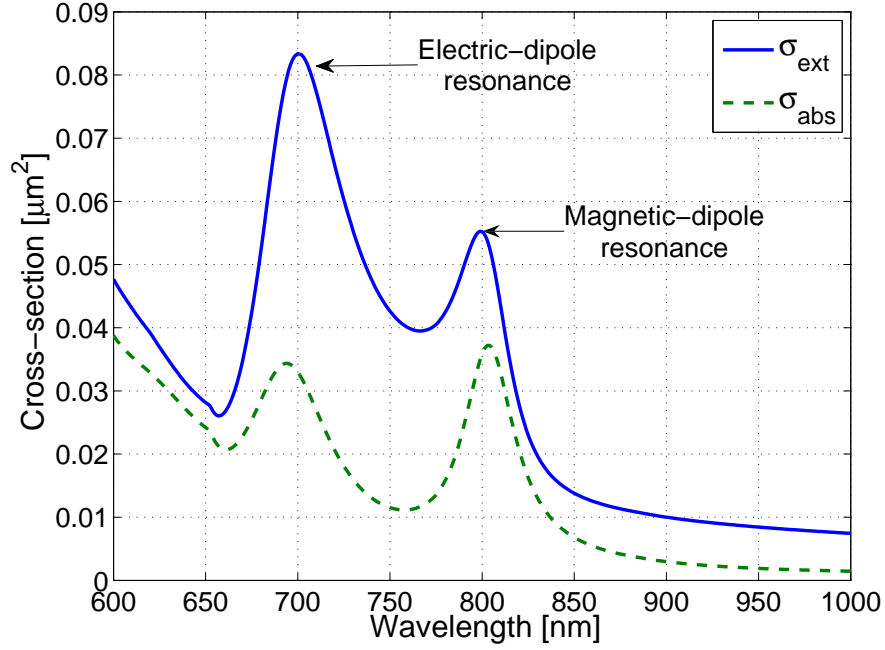
Figure 4.22: Extinction (solid) and absorption (dashed) cross-sections a tetramer consisting of solid gold particles with $D = 90$ nm, gap 2 nm, in solvent with refractive index $n_s = 1.4$.

Complex amplitudes of transmitted (t) and reflected (r) waves are measured in the far field, and interpreted as forward and backward scattering amplitudes, respectively. This allows one to define extinction $\sigma_{ext} = (1 - T)S_0$ and absorption $\sigma_{abs} = (1 - T - R)S_0$ cross-sections, where $S_0 = L_y L_z$ is the cross-sectional area of one unit cell, and $T = |t|^2$ and $R = |r|^2$ are energy transmission and reflection coefficients. In the limit of small extinction, σ_{ext} is related to the decay constant κ (with dimensions of inverse length) through the usual formula $\kappa = \sigma_{ext}n_0$, where

$n_0 = 1/V_0$ is the number density of tetramers, and $V_0 = S_0 L_x \equiv L_x L_y L_z$ is the specific volume per cluster. Indeed, if the distance between consecutive layers of scatterers is L_x, then the wave intensity is damped by factor $T = e^{-\kappa L_x} \approx 1 - \kappa L_x$, which implies $\kappa \approx (1 - T)/L_x \equiv \sigma_{ext}/(S_0 L_x)$.
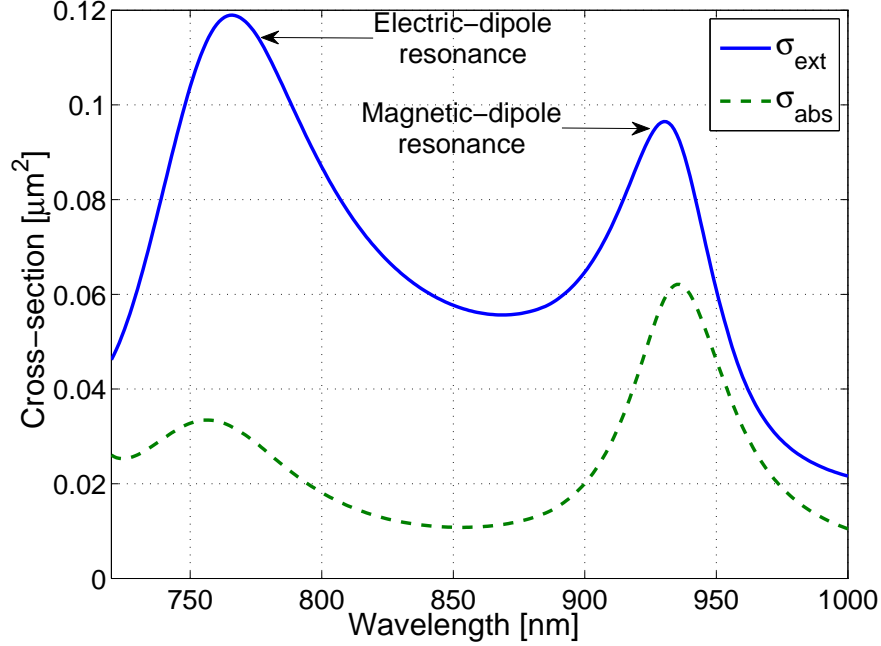
Figure 4.23: Extinction (solid) and absorption (dashed) cross-sections a tetramer consisting of solid gold particles with $D = 120$ nm, gap 2 nm, in solvent with refractive index $n_s = 1.4$.

Optical spectra of tetramers made of 90 nm and 120 nm gold spheres are presented in Fig. 4.22 and 4.23. In both cases, two strong resonances are observed in the extinction and absorption spectra. The positions of these resonances are in rough agreement with electrostatic predictions (see Fig. 4.21) for gap-to-diameter ratios extrapolated to 2/90 and 2/120, although red-shifted notably. This electromagnetic red shift phenomenon is well understood in terms of the surface plasmon dispersion relation [UKI+07]; for sub-wavelength particles it can be quantified as a correction to electrostatic eigenvalues [MFZ05]. Inspection of the field pictures in these resonances (Fig. 4.24) confirms identification of these two lowest-frequency

resonances as electric-dipole and magnetic-dipole. For our choice of tetramer orientation, depicted in Fig. 4.24, the electric dipole resonance is associated mostly with the electric polarization of the two frontal spheres which form a dimer with an axis parallel to the incident electric field $\vec{E}_0 = E_0 \hat{y}$.
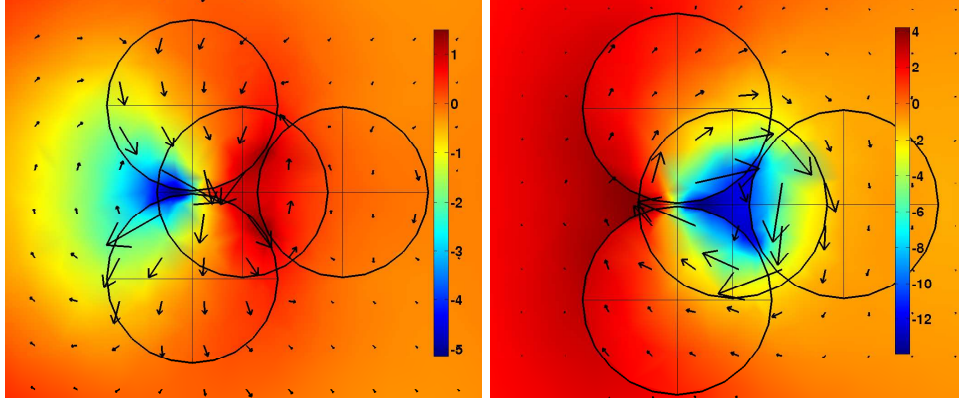
Figure 4.24: Field profiles at the two resonances of a tetramer characterized in Fig. 4.23. Color: out-of-plane magnetic field H_z in the plane containing centers of 3 spheres. Arrows: in-plane electric induction (D_x, D_y) in the same plane. Left: electric-dipole resonance at $\lambda = 756$ nm; right: magnetic-dipole resonance at $\lambda = 935$ nm. Horizontal axis: x, vertical: y.

The magnetic dipole resonance is related predominantly to the *sextupole* (if viewed two-dimensionally) resonance of the three spheres lying in the plane orthogonal to the incident magnetic field $\vec{H}_0 = H_0 \hat{z}$. This corresponds to the A_2 plasmon of the trimer in the plasmon hybridization model [BMN06]. The electric field in this resonance circulates around the center of the trimer, causing a non-vanishing magnetic flux $\Phi = \int B_z \, dx \, dy$ through the $z = $ const plane. Since sextupolar symmetry corresponds to an azimuthal number of $M_J = 3$, it is clear that this resonance is also an electric *octupole* $(J = 3, M_J = 3)$ in three dimensions. The field picture of the electrostatic T_1-symmetric resonance in the inset of Fig. 4.21 supports our conclusion that the lowest-frequency resonance in optical spectra (Fig. 4.22, 4.23) is related to the lowest T_1 resonance.

4.4.5 Effective permittivity and permeability of tetramer colloids

Periodically-arranged cluster arrays are easier to characterize in electromagnetic simulations than random suspensions: a simple procedure for retrieving effective medium parameters was introduced in Section 4.2.4. Yet, in effective medium regime and for sub-wavelength inter-particle distances we expect that spectral features related to single-cluster resonances are common for random and periodic ensembles. To complete our identification of electric and magnetic resonances of a tetramer, we have applied that standard procedure and evaluated ϵ_{eff} and μ_{eff} of a cluster array.

A slightly different orientation of a tetramer has been chosen for these calculations: it was determined that orienting the two opposite, orthogonal edges of a tetrahedron along the major axes of rectangular cluster array minimizes splitting of single-cluster resonances due to the nearest-neighbor interactions between clusters of the lattice. Such judicial choice of orientation makes two of the tetramer symmetry planes compatible with those of rectangular lattice. Since a tetrahedron does not have three mutually orthogonal planes, this array lacks a central symmetry plane; as a result, the simple EMPR procedure described in Sec. 4.2.4 may return different effective medium parameters depending on which side of the slab is illuminated.

Fortunately, homogenization methods for asymmetric structures have been recently developed [SVKS05]. It can be shown rigorously that in reciprocal (time reversal invariant) systems, left-to-right (t_{12}) and right-to-left (t_{21}) transmission coefficients for slabs are equal to each other, but reflection coefficients are generally different ($r_{12} \neq r_{21}$) [Poz98]. It was suggested [SVKS05] that for asymmetric structures, a geometric average $r_{av} = \sqrt{r_{12}r_{21}}$ should be used instead of r_{12} or r_{21} as the input for EMPR procedure of Sec. 4.2.4. It was rigorously proven in Ref. [SVKS05] that such prescription leads to the correct effective medium parameters for layered 1D metamaterials consisting of alternating layers of homogeneous slabs. Assuming that slabs of metamaterials can be approximated as homogeneous slabs with some unknown ϵ_{eff} and μ_{eff}, this paradigm can be applied to periodic sub-wavelength composites consisting of dielectric (or metallic) particles submerged into some uniform dielectric (solid or liquid). With this amendment, EMPR procedure is applied in this Section to colloids of tetramers. It was noted that the difference between r_{12} and r_{21} coefficients was generally comparable to numerical error in FEFD simula-

tions. This observation is in agreement with the postulated rotational invariance of electromagnetic response of a single tetramer, which is disturbed only weakly by interactions between adjacent nanoclusters forming a square lattice.
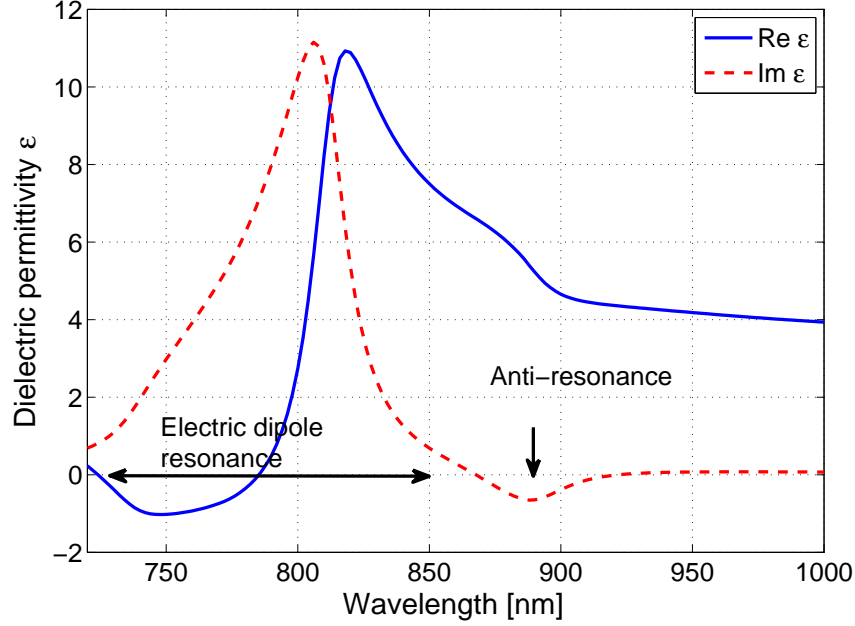
Figure 4.25: Effective permittivity ϵ_{eff} of a solution with uniformly distributed tetramers (solid gold spheres, $D = 90$ nm, gap 1 nm, index of solvent $n_s = 1.4$, volume per cluster $V_0 = 0.0115~\mu m^3$). Electric-dipole resonance ($\lambda = 810$ nm) and magnetic-dipole ($\lambda = 890$ nm) anti-resonance are identified by peaks in Imϵ_{eff}.

Effective medium parameters of slabs of periodic metamaterials, extracted using EMPR, are known to exhibit some unusual (non-Lorentzian) behavior [KMSS03], the origin of which had caused some debate in the past [DLE$^+$04]. This behavior is believed to be associated with spatial dispersion in periodic structures [DLE$^+$04]; examples of non-Lorentzian behavior include bands with negative Im ϵ_{eff} in the vicinity of a magnetic resonance, or negative Im μ_{eff} around an electric resonance. In addition, real parts of ϵ_{eff} (μ_{eff}) show "reversed" Lorentz-shaped kinks in magnetic (electric) resonances. These "anti-resonances" do not violate any laws of physics: for example, the overall medium response remains passive [DLE$^+$04]. Another consequence of dealing with a periodic array is the

fact that the effective permeability determined using the scattering procedure is forced to go to zero near an electric resonance [KMSS03]. Indeed, the refractive index $n_{\text{eff}} = \sqrt{\epsilon_{\text{eff}}}\sqrt{\mu_{\text{eff}}}$ equals $k_{\text{Bloch}}c/\omega$, but k_{Bloch} is limited by the size of the Brillouin zone [KMSS03]. A large rise of ϵ_{eff} (see Fig. 4.25) near electric resonance thus inevitably causes μ_{eff} to go down, as seen in Fig. 4.26. For the purpose of demonstrating optical magnetism in metafluids, we focus on the vicinity of the magnetic resonance frequency and disregard the above-mentioned artifacts.
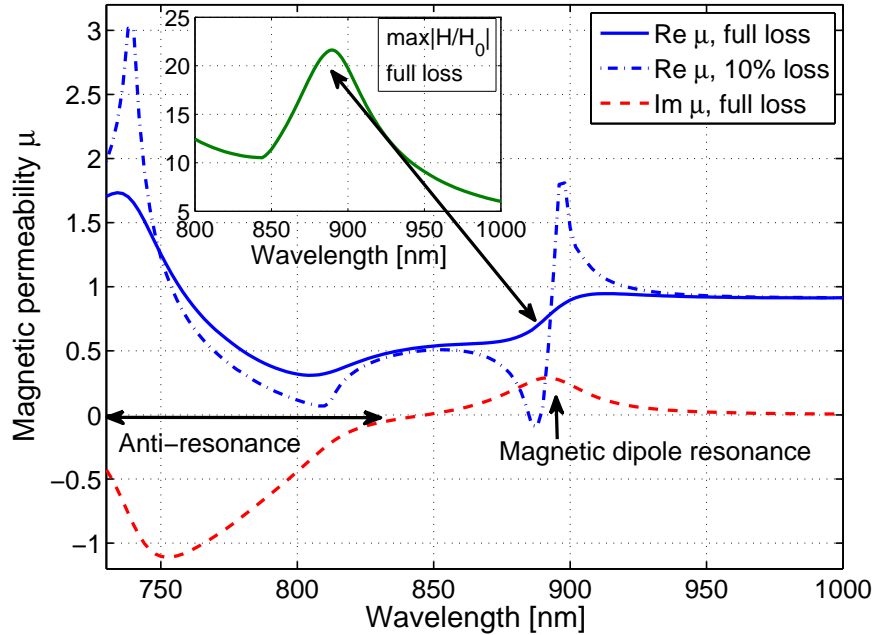
Figure 4.26: Effective magnetic permeability μ_{eff} of the tetramer colloid described in Fig. 4.25. Electric-dipole anti-resonance ($\lambda = 810$ nm) and magnetic-dipole ($\lambda = 890$ nm) resonance are identified by peaks in Im μ_{eff}. Inset: local magnetic field enhancement, max $|H/H_0|$.

For illustration purposes, we have made numerical simulations with an extremely small (1 nm) gap between spheres. Such a small gap serves to maximize the frequency separation of the electric and magnetic resonances and to minimize the effect of the former on the weak magnetic resonance. From Fig. 4.26, it is clear that there is a regular, Lorentz-shaped magnetic resonance at $\lambda = 890$ nm, somewhat distorted by an adjacent anti-resonance band associated with the strong electric
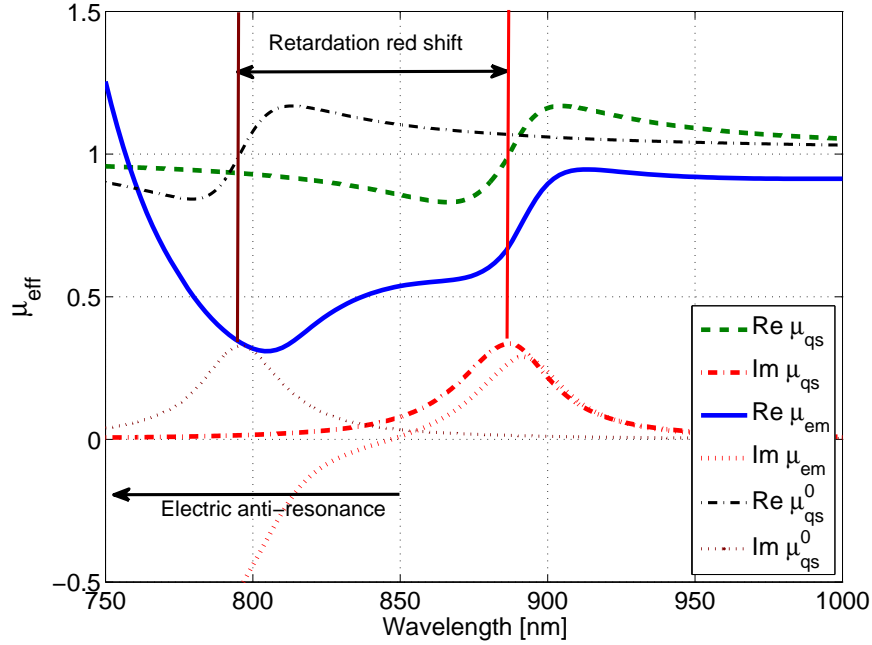
Figure 4.27: Comparison between quasistatic and electromagnetic calculations of μ_{eff} for the tetramer colloid described in Fig. 4.25. Solid and dotted lines (labeled μ_{em}) are calculated from electromagnetic scattering simulations using the standard retrieval method [SVKS05]; dashed and dash-dotted lines (μ_{qs}) — from electrostatic simulations using effective medium estimate (2.21) with the magnetic polarizability (2.48). The position of magnetic plasmon resonance in formula (2.48) is retardation-corrected using the technique described in Section 2.5.

dipole resonance, which begins at 850 nm. To make this magnetic resonance perfectly clear, we have also done these simulations with losses in gold reduced ten-fold with respect to their true values. The dash-dotted curve on Fig. 4.26 demonstrates that with low losses, negative permeability would be possible in a metafluid with the cluster number density of $1/(0.0115 \ \mu m^3)$, in which clusters occupy 13% of the volume.

In addition, quasistatic calculations of μ_{eff} have been made using recipes from Chapter 2, and compared with electromagnetic simulations in Fig. 4.27. Dashed and dash-dotted lines were calculated using just one resonant eigenmode in Eq. 2.48. Frequency of the plasmon resonance was corrected using the method presented in

Sec. 2.5. As a triumph for the quasistatic theory of Chapter 2, there is excellent agreement with EM scattering simulations for $\lambda > 890$ nm; for shorter wavelengths μ_{eff} from EM simulations is clearly affected by the strong electric anti-resonance, which causes μ_{eff} to deviate from μ_{qs} and even leads to change of sign of Im μ_{eff}, as discussed above.

Although suspensions of solid gold particles in water or ethanol aggregate due to strong van der Waals forces at much lower concentrations, typically $0.001 - 0.01\%$ vol., colloids with ~ 100 nm-sized silica particles are stable with volume fractions $\sim 10\%$ and even up to 50% [dKvIVR85, KC02], which is close to the liquid-solid phase transition in a hard-sphere system [PvM86]. We expect that silica-covered gold nanoshells can be concentrated to 1% vol. and above. Experimental studies of such nanoclusters, their formation and stability, are being conducted and will be reported elsewhere. Note that if fluidity of a negative permeability metamaterial is not a requirement, one can simply condense tetrahedral APMs to densities approaching the close-packing density ($\approx 64\%$ for random packing, $\approx 74\%$ for hexagonal or cubic packing) to create a solid metamaterial with isotropic permittivity and permeability. Achieving $\mu_{\text{eff}} < 0$ or $\epsilon_{\text{eff}} < 0$ at such high volume fractions is a much easier task than in liquid form. Thereupon plasmonic metafluids can be used as precursors to isotropic doubly-negative metamaterials operating in effective medium regime; fabrication of photonic crystals and other non-subwavelength metamaterials using colloid condensation has been previously demonstrated [KC02, MP04].

Potentially, the strength of the magnetic resonance, characterized by the normalized magnetic moment, (4.49), can be increased by utilizing nanoparticles with more complicated shapes, including, for instance, non-concentric and non-spherical nanoshells [WBNH07]. In addition, recent progress in fabrication of crystalline SiC nanoparticles [KMJB+02] provides hope that negative-ϵ nanoparticles with losses an order of magnitude smaller than those in gold [KUZS05, KUS06, TKU+06, UKI+07] can be utilized to create metafluids with optical magnetism in the mid-infrared range. We observe from Fig. 4.26 that this 10-fold reduction of losses is sufficient for achieving $\mu_{\text{eff}} < 0$ even without further enhancement of the magnetic response through particle shape engineering or demanding higher cluster density.

Resistive damping and colloid stability are not the only problems that an experimental demonstration of negative permeability in metafluids will face. Additional challenge comes from strong sensitivity of resonant frequencies to the gaps be-

tween particles comprising an APM. The width of plasmon resonances in plasmonic nanostructures is typically on the $\Delta\lambda_E \sim 100$ nm scale for electric and $\Delta\lambda_M \sim 10$ nm scale for magnetic resonances, as seen from Figures 4.25,4.26. From Fig. 4.21 we can now estimate the allowed width of gap distribution in weakly polydisperse colloids. For example, if the gap-to-diameter distribution is centered at 0.06 (which corresponds to a magnetic resonance at $\lambda \sim 650$ nm if retardation red-shift can be ignored), then in order to have magnetic resonances of most particles within the ± 10 nm range around that wavelength, the gap/diameter ratios must be contained in the $0.05 - 0.07$ interval. For 100 nm spheres, this translates into a ± 1 nm requirement for gap distributions. Although such unprecedented uniformity of gaps is almost impossible to achieve with solid gold particles, it may be possible if thin gold nanoshells are grown on silica nanoparticles, which can be created in almost perfectly spherical shapes and with very smooth surfaces [YMM$^+$04]. Numerical simulations indicate that effective medium parameters of metafluids with gold nanoshells differ very little from those with solid spheres, as long as the shell is thicker than the skin depth in metal ($\sim 20 - 25$ nm).

In this Section, we have shown theoretically that colloidal solutions of plasmonic nanoclusters can have both negative dielectric permittivity and negative magnetic permeability. However, the most exciting applications, such as the negative index metafluid (see Fig. 4.28), demand ϵ_{eff} and μ_{eff} simultaneously negative. Achieving $\epsilon_{\text{eff}} < 0$ and $\mu_{\text{eff}} < 0$ at some frequency requires one more design step: the positions of the strongest electric (ED) and magnetic dipole (MD) resonances must be engineered such that $\omega_{MD} > \omega_{ED}$. In that case, MD resonance could be placed within the narrow $\epsilon_{\text{eff}} < 0$ band above ω_{ED}. This could be accomplished by adding to the metafluid plasmonic core-shell particles that have been shown [PRHN03] to exhibit red-shifted ED resonance. Alternatively, re-ordering of ED and MD resonances in a tetramer can be accomplished by letting plasmonic spheres touch each other in the cluster. More sophisticated choices of particle and cluster geometry and topology are possible and may be utilized in negative-index metafluid engineering.

In conclusion, a new concept of metafluids has been introduced in this Section. Metafluids consist of Artificial Plasmonic Molecules (APM) dissolved in a regular fluid. A detailed study of APMs in the shape of tetrahedral plasmonic nanoclusters is presented. The properties of plasmonic tetramers are investigated using electrostatic methods aided by group theory and fully electromagnetic finite-
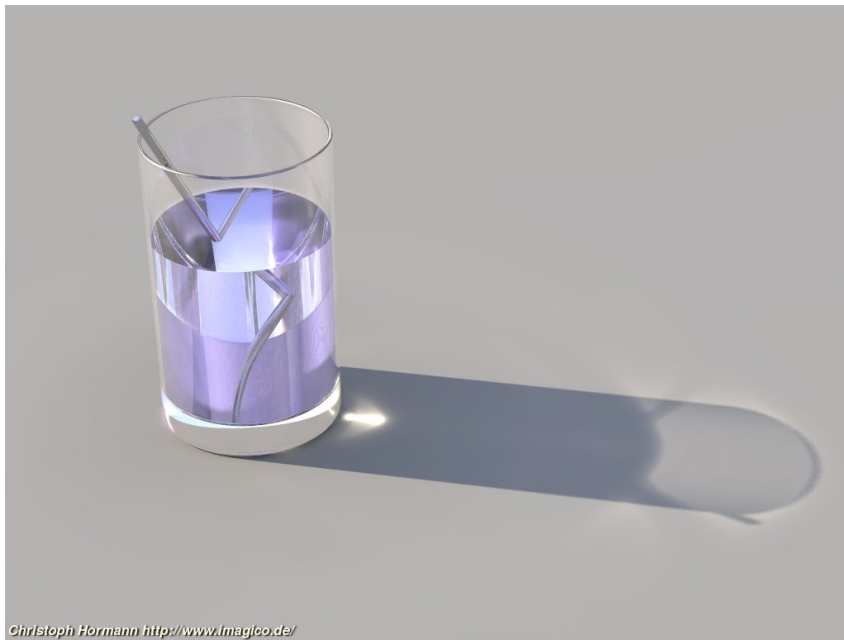
Figure 4.28: A photorealistic ray-tracing simulation of a straw in a glass filled with lossless negative-index metafluid, produced by Christoph Hormann [DWLH06]. Reproduced from C. Hormann's Worldwide Web publication http://www.imagico.de/pov/metamaterials.html.

element simulations. We found that in agreement with the quasistatic theory of Chapter 2, electric response of T_d-symmetric metamolecules is dictated only by T_2-symmetric plasmons and magnetic response only by T_1 plasmon states, which are excited by electric field as electric octupoles due to retardation effects. The latter electric octupoles are shown to be associated predominantly with sextupolar ($J = 3$) resonances of nanoparticle trimers. The electric and magnetic response of the tetramer allows one to construct an effective medium with a completely isotropic electric and magnetic response. Electromagnetic simulations indicate that achieving $\epsilon_{\mathrm{eff}} < 0$ and $\mu_{\mathrm{eff}} < 0$ in colloidal solutions of "artificial molecules" should be possible using either sufficiently high concentrations of gold clusters or materials with low-loss negative permittivity such as SiC in mid-IR.

Chapter 5

Conclusions

5.1   Summary of results

Main scientific results of this dissertation can be summarized as follows.

In Sections 2.2–2.5, we have introduced an effective medium theory of sub-wavelength (unit cell size $a \ll \lambda$) metallic, semiconducting and dielectric nanostructures that encompasses their electric, magnetic and magneto-electric response at optical frequencies. The theory departs from purely electrostatic description of non-magnetic composites and uses surface plasmon eigenstates as the basis for analytic expansions. Magnetism and other retardation phenomena are taken perturbatively into account as corrections to electrostatic equations. The theory has revealed a generalized sum rule for electric dipole oscillators and provided its rigorous proof.

In Section 2.6, we have theoretically predicted and experimentally confirmed the phenomenon of enhanced optical transmission (EOT) in mid-IR through a square array of sub-wavelength round holes pierced through an optically thin polaritonic (SiC) membrane. It is shown and explained that EOT is accompanied by a slightly blue-shifted absorption peak corresponding to enhanced optical absorption (EOA). Both EOT and EOA were shown to be caused by excitation of quasi-electrostatic polaritonic resonances of the film that can be traced to even-parity surface phonon-polaritons of the smooth film.

In Chapter 3, a superlens in mid-infrared spectral range has been numerically modeled and experimentally confirmed. The superlens is a flat sub-micron three-layer structure, $SiO_2/SiC/SiO_2$, in which the polaritonic material SiC has a

negative dielectric permittivity in the reststrahlen band between the frequencies of the transverse and longitudinal optical phonons. Superlensing takes place in a particular band (of width ~ 100 nm) around wavelength $\lambda \approx 11\mu$m and manifests itself in imaging a sub-micron slit cut in a metal screen with spatial resolution exceeding the usual near-field resolution. A novel far-field diagnostic of superlensing that uses a tunable CO_2 laser and an FTIR spectromicroscope has been developed theoretically and supported by experimental results. This diagnostic has confirmed that the fabricated superlens has resolution of at least 1250 nm $\approx \lambda/9$ at $\lambda \approx 11\mu$m. More recent experiments have brought this number down to 500 nm$\approx \lambda/20$.

In Chapter 4, four electromagnetic metamaterials have been suggested and theoretically studied. In Section 4.1, a new class of two-dimensional periodic nanostructured materials, Sub-wavelength Plasmonic Crystals (SPC), is introduced and exemplified using a circular nanorod array. It is found that two types of propagating EM waves are supported by SPCs: (a) scale-invariant modes whose dispersion relation is almost independent of the lattice period, and (b) scale-dependent narrow-band resonances whose dispersion strongly depends on the lattice period. The scale-invariant modes are accurately described using a frequency-dependent QS permittivity $\epsilon_{\mathrm{qs}}(\omega)$ and a vacuum magnetic permittivity $\mu = 1$. The scale-dependent resonances exist inside narrow frequency bands where they can have a modified magnetic permittivity $\mu \neq 1$. Magnetic properties originate from the non-vanishing magnetic moment produced by the currents inside any given plasmonic inclusion due to the close proximity of the adjacent inclusions.

In Section 4.2, conceptually important electromagnetic properties of two-dimensional meta-materials consisting of an array of metallic strips pairs (MSPs) are studied. Simulations of scattering through a single layer of MSPs show that electromagnetic resonances corresponding to electric and magnetic dipole resonances can be excited. Perfectly conducting MSPs are shown to possess electric and magnetic dipole resonances which are very close in frequency. This property of MSPs is used to demonstrate a sub-wavelength negative index meta-material based on MSPs. These resonances are related to the well-known antenna resonances occurring at the wavelength approximately equal to twice the strip height H. A new approach to making a strongly sub-wavelength MSP-based meta-material is demonstrated. This approach involves reducing the size of the unit cell to the point at which plasmonic (electrostatic) resonances of MSPs become dominant. Two types

of electrostatic resonances, dipole and quadrupole, are investigated. The quadrupole resonance is shown to contribute to magnetic moment of the meta-material and, therefore, to result in the optical magnetism.

In Section 4.3, a novel realization (Strip Pair One Film) of a double-negative metamaterial comprising unit cells of deeply subwavelength size was introduced. It was shown that the SPOF structure possesses magnetic and electric resonances that enable negative μ_{eff} and ϵ_{eff} in overlapping frequency bands. Tunability of this structure is so high that the negative-index band can be adjusted to any wavenumber from near-IR to near-UV. It was found that the middle film in the SPOF geometry enables independent tuning of electric and magnetic resonances. The proposed DNM has been manufactured by collaborators using standard nanofabrication methods.

In Section 4.4, a conceptually new field of research — plasmonic metafluids — has been introduced. Artificial plasmonic molecules, tetramers of plasmonic nanospheres, are investigated by means of the quasistatic theory of Chapter 2, group theory and full-wave EM simulations. It is found that magnetic response is dictated only by T_1-symmetric plasmon states, which possess magnetic dipole moment but cannot be excited as electric dipoles or quadrupoles because their ED and EQ moments are prohibited by symmetry-related selection rules. The electric and magnetic response of the tetramer is used to construct an effective medium with completely isotropic electric and magnetic response. It is shown that achieving $\epsilon_{\text{eff}} < 0$ and $\mu_{\text{eff}} < 0$ in colloidal solutions of "artificial molecules" could be possible with sufficiently high concentrations of nanoshells made of plasmonic (gold) or polaritonic (SiC) materials.

5.2 Directions for future research

In accordance with a common law of nature, scientific studies raise more questions than they solve. Below we outline several important issues that emerged as a result of this study and await their solution.

1. A more general (and accurate) homogenization theory of periodic dielectric (i.e., locally non-magnetic) composites with sub-wavelength unit cells that accounts for optical magnetism and other dispersive properties is highly desirable. In all likelihood, such theory must introduce a more general effective permittivity tensor with spatial dispersion, $\epsilon_{\text{eff}}(\omega, \vec{k})$ that incorporates electric-dipole active and

magnetic-dipole active plasmon resonances as well as higher multipole resonances that are not accounted for by $\epsilon_{\text{eff}}(\omega)$ and $\mu_{\text{eff}}(\omega)$ introduced in this work. In addition, such homogenization theory could serve as a unification theory for phenomena related to electromagnetic resonances of very different origin: from scale-invariant electrostatic (plasmon) resonances (described in Chapter 2) to essentially electromagnetic resonances, such as antenna resonances of PEC strips (Sec. 4.2) and MD resonance of a sphere (Sec. 2.3.2).

Such a theory could be an extension of the multi-scale homogenization approach introduced by Felbacq et al. [FB05] for high-ϵ dielectric fibers. Unfortunately, there seems to be no straightforward way to generalize the suggested formalism of Ref. [FB05] to allow negative-ϵ or finite-ϵ dielectric components. A major mathematical difficulty in constructing homogenization theories based on eigenmode expansions in the general electromagnetic case is the lack of appropriate orthonormal basis: the eigenvalue problem that generalizes electrostatic Laplace equation to electromagnetic Helmholtz equation with arbitrary phase shift per cell (ka) is neither self-adjoint nor symmetric. Only for vanishingly small phase shift per cell (when the eigenvalue problem is symmetric [BS80]), or for very small period-to-wavelength ratios (when non-retarded eigenfunctions can be used as a basis, Chapter 2) some theoretic progress has been made.

In our perception, and in agreement with the logic of Chapter 2, a meaningful homogenization theory of electromagnetic metamaterials must consist of two components: (i) a rigorous definition of homogenized linear response tensor, $\epsilon_{\text{eff}}(\omega, \vec{k})$, expressing this quantity through integrals over local electromagnetic fields, and (ii) an appropriate choice of orthonormal basis of eigenfunctions that allows $\epsilon_{\text{eff}}(\omega, \vec{k})$ to be expressed as a sum over poles of the scattering matrix (i.e., all electromagnetic resonances in the system). A solution to subproblem (i) has been suggested by Pendry, Smith et al. [PHRS99, SVKS00, SP06]; however, it is still not clear whether their definition is accurate for large phase shifts per cell [SVKS00], and how it should be applied in periodic systems with no evident choice of a unit cell. Solution to subproblem (ii) implies that an eigenvalue equation can be formulated on a unit cell that allows numerical computation of all the eigenmodes and eigenfrequencies of the periodic structure. The residue at each pole of $\epsilon_{\text{eff}}(\omega, \vec{k})$, i.e. strength of a resonance, shall be expressed through integrals over a unit cell involving the eigenfunction of that resonance.

At this time, it is not known whether this maximum programme can be accomplished. Existing works on electromagnetic homogenization [Ole96, OS92, Wel01, SEK$^+$05] automatically yield $\mu_{\text{eff}}(\omega) \equiv 1$ for any non-magnetic composites (i.e., if the local permeability $\mu(\vec{r}) \equiv 1$). This is clearly not the desired result, and unless the methods of Refs. [Ole96, OS92, Wel01, SEK$^+$05] can be extended to compute spatially-dispersive permittivity $\epsilon_{\text{eff}}(\omega, \vec{k})$ (and not only on the dispersion surface $\omega = \omega(\vec{k})$ of propagating modes, as was done in Ref. [Sjö06]), those approaches cannot be used to explain optical magnetic phenomena or design optical magnetic metamaterials. On the other hand, the results presented in Chapters 2, 4 and especially in Sec. 4.1 indicate that in the limit of small $\omega a/c \propto a/\lambda$ all periodic structures can be described by some sort of homogenized constitutive parameters, even when the phase shift per cell ka is not small. Homogenization formalism of Ref. [FB05] points at the same conclusion; unfortunately, their method does not allow treatment of negative finite ϵ inclusions that support surface plasmon resonances.

2. With regard to Chapter 3, we note that although the ideal superlens is not limited to sub-wavelength distances between the object and image planes, super-resolved (i.e. near-field) imaging on scales comparable with λ has not yet been demonstrated, since it requires a very low loss double-negative material operating at optical frequencies. Considering that the only currently known implementation of DNMs are resonant sub-wavelength plasmonic nanostructures, whose optical losses are limited by resistive damping in metallic components (and further increased by resonances that create negative μ_{eff}), it may be predicted that demonstration of "far-field" superlensing will require design and fabrication of metal-dielectric composites with large laser gain. This subject has attracted a great deal of attention in the past few years (see Section 1.2), and researchers are hopeful that plasmonic (or polaritonic) metamaterials with fine controllable balance between optical damping and gain will be demonstrated in a not-so-distant future.

3. Even though this work does not specifically deal with issues such as resistive damping and its compensation, there is one more thing that can be possibly accomplished using the presented theory. The quality factor of magnetic resonances, which determines the NIM Figure of Merit (FoM), is proportional to the ratio of magnetic resonance strength to its width. While the latter is determined by resistive damping, the former is dependent upon the shape of plasmonic (or polaritonic)

inclusions and can therefore be maximized by a smart choice of this shape. Now, thanks to Eq. 2.40 and Eq. 2.54, a mathematical problem can be formulated: assuming that the smooth surface S is given by equation $\tilde{S}(\vec{r}) = 0$, find the global maximum of the dimensionless functional

$$\mathcal{M}[\tilde{S}] = \max_n F_n^{zz}/d^2, \tag{5.1}$$

where d is the diameter of surface S, F_n^{zz} is the magnetic resonance strength (which scales as d^2) and $\max_n$ runs over all plasmon states of surface S. Currently, researchers use essentially random fingering aided by time-consuming modeling of electromagnetic spectra to determine what shapes of plasmonic inclusions maximize the magnetic response [KCL$^+$07, DWSL07]; the current record of optical NIM figure of merit stands at 3.37 for rectangular double fishnets [DWSL07]. One possible direction for research in this field, which may at least put an absolute upper limit on the magnetic strength, if not solve the maximization problem (5.1), is finding the sum rule for magnetic oscillator strengths. Analogy between expressions (2.28) for electric and (2.39) for magnetic susceptibilities seems suggestive that such a sum rule must exist in analogy with the electric oscillator sum rule (see Eq. 2.15,2.14 and Ref. [Str79]).

4. This work shows that the very idea of introducing optical magnetic permeability $\mu_{\text{eff}}(\omega)$, blasted half a century ago by L. D. Landau as "unwarranted", is in fact (i) physically justified (inasmuch as magnetic dipole resonances are important to coherent scattering, Eq. 1.4), (ii) aesthetically appealing (as it implements the symmetry between electric and magnetic fields) and (iii) insightful (both super-lensing [Ves62] and impedance-matched cloaking [PSS06] were discovered using the notion of magnetic permeability). However, the peculiar properties of introduced $\mu_{\text{eff}}(\omega)$ discovered in Chapter 2 suggest that caution should be exercised when applying conventional wisdom to the optical μ_{eff}. For example, Eq. 2.40 predicts dependence of μ_{eff} upon polarization of electric field in a wave. This means that magnetic and electric phenomena in optical metamaterials are tied in a knot and cannot be considered separately. As another example, note Eq. 2.73, which suggests that the causal linear response function in plasmonic/photonic crystals is, in fact, $1 - 1/\mu_{\text{eff}}(\omega)$ rather than $\mu_{\text{eff}}(\omega)$. This finding is confirmed by studies of spatial dispersion in crystals [AKSV99], which link $1 - 1/\mu_{\text{eff}}$ to components of the derivative

tensor $\partial^2 \epsilon_{\text{eff}}(\omega, \vec{k})/\partial k^2$ (see [LL84, ASNZ04, AG06]), which are causal inasmuch as $\epsilon_{\text{eff}}(\omega, \vec{k})$ is causal at non-zero $\vec{k}$ [Kir76, DKM81, MRS89]. Apparently, conventional Kramers-Kronig relations may not be directly applicable to this $\mu_{\text{eff}}(\omega)$ but may be applicable to its inverse; this issue could be relevant to some of the non-Lorentzian anomalies in magnetic homogenization results [DLE$^+$04]. Further theoretical studies of optical metamaterials may be necessary to decide whether magnetic metamaterials of the described sort behave much like homogeneous substances with some ϵ and μ; this will determine if they can be used in applications that motivated the development of this field.

5. In relation to Sec. 4.4, it would be interesting to extend the studies of plasmonic metafluids to embrace chiral metafluids. Quasistatic theory developed in Sec. 2.3 shows that chirality is a phenomenon of order $\omega d/c$, while magnetic polarizability is of order $(\omega d/c)^2$. Seemingly, chiral susceptibility ζ comparable with unity should be easier to achieve than magnetic susceptibility $|\mu - 1| \sim 1$. It is known that giant chirality is a pathway to backward waves and negative refraction [Pen04, JH05, TSJ05, AGZ06, Yan06, BSP$^+$07], alternative to double-negative metamaterials. Studies of chiral metamolecules are being pursued by the author and will be published elsewhere.

List of Publications

In relation to the work presented in this dissertation, the following journal and conference papers have been published or submitted for review:

1. [US07a] Y. Urzhumov and G. Shvets, "Optical magnetism and negative refraction using plasmonic metamaterials", submitted to Solid State Comm., Special Issue on Metamaterials (2007).

2. [DZF$^+$07] M. Davanço, Xuhuai Zhang, S. R. Forrest, Y. Urzhumov and G. Shvets, "Nanofabrication and Characterization of Subwavelength Metamaterials for Left-handed Propagation at Near-infrared Wavelengths", Proc. IEEE LEOS Annual Conf., Lake Buena Vista, Florida, October 21-25, 2007.

3. [USF$^+$07] Y. A. Urzhumov, G. Shvets, J. A. Fan, F. Capasso, D. Brandl, and P. Nordlander, "Plasmonic nanoclusters: a path towards negative-index metafluids," Opt. Express 15, pp. 14129-14145 (2007).

4. [US07b] Y. Urzhumov and G. Shvets, "Quasistatic effective medium theory of plasmonic nanostructures", Proc. SPIE 6642, p. 66420X-1 (2007).

5. [LFUS07] V. Lomakin, Y. Fainman, Y. Urzhumov, and G. Shvets, "Optical metamaterials based on thin metal films: From negative index of refraction, to enhanced transmission, and to surface wave guidance," Proc. SPIE 6638, p. 663805-1 (2007).

6. [KUI$^+$07] D. Korobkin, Y. Urzhumov, B. Neuner III, C. Zorman, Z. Zhang, I. D. Mayergoyz, and G. Shvets, "Mid-infrared metamaterial based on perforated SiC membrane: Engineering optical response using surface phonon polaritons," Appl. Phys. A: Mat. Sci. Process. 88, p. 605 (2007).

7. [DUS07] M. Davanço, Y. Urzhumov, and G. Shvets, "Complex Bloch Bands of a 2D Plasmonic Crystal Displaying Isotropic Negative Refraction," Opt. Exp. 15(15), pp. 9681-9691 (2007).

8. [UKI$^+$07] Y. Urzhumov, D. Korobkin, B. Neuner III, C. Zorman and G. Shvets, "Optical Properties of Sub-Wavelength Hole Arrays in SiC Membranes," J. Opt. A: Pure Appl. 9, pp. S322-333 (2007); [KUI$^+$06] e-print `physics/0606207` (2006).

9. [LFUS06] V. Lomakin, Y. Fainman, Y. Urzhumov, and G. Shvets, "Doubly negative metamaterials in the near infrared and visible regimes based on thin film nanocomposites," Optics Express 14 (23), p. 11164 (2006).

10. [TKU$^+$06] T. Taubner, D. Korobkin, Y. Urzhumov, G. Shvets, and R. Hillenbrand, "Near-Field Microscopy Through a SiC Superlens," Science 313, p. 1595 (in Brevia) (2006).

11. [KUS06] D. Korobkin, Y. Urzhumov and G. Shvets, "Enhanced near-field resolution in midinfrared using metamaterials," J. Opt. Soc. Am. B 23 (3), p. 468 (2006).

12. [SU06] G. Shvets and Y. Urzhumov, "Negative index meta-materials based on two-dimensional metallic structures," J. Opt. A: Pure Appl. Opt. 8, pp. S122-130 (2006).

13. [US05a] Y. Urzhumov and G. Shvets, "Applications of Nanoparticle Arrays to Coherent Anti-Stokes Raman Spectroscopy of Chiral Molecules," Proc. SPIE Int. Soc. Opt. Eng. 5927, p. 59271D (2005).

14. [KUZS05] D. Korobkin, Y. Urzhumov, C. Zorman and G. Shvets, "Far Field Detection of the superlensing Effect in Mid-Infrared: Theory and Experiment," J. Mod. Opt. 52 (16), p. 2351 (2005).

15. [SU05] G. Shvets and Y. Urzhumov, "Electric and magnetic properties of subwavelength plasmonic crystals," J. Opt. A: Pure Appl. Opt. 7, pp. S23-31 (2005).

16. [US05b] Y. Urzhumov and G. Shvets, "Extreme Anisotropy of Wave Propagation in Two-Dimensional Photonic Crystals," Phys. Rev. E 72, p. 026608 (2005).

17. [SU04a] G. Shvets and Y. Urzhumov, "Engineering the electromagnetic properties of periodic nanostructures using electrostatic resonances," Phys. Rev. Lett. 93, p. 243902 (2004); e-print `cond-mat/0403400` (2004).

18. [SU04b] G. Shvets and Y. Urzhumov, "Polariton-enhanced Near-field Lithography and Imaging with Infrared Light," Mat. Res. Soc. Symp. Proc., Vol. 820 (2004).

19. [US03] Y. A. Urzhumov and G. Shvets, "Extreme anisotropy of two-dimensional photonic crystals due to mode degeneracy and crystal symmetry," Proc. SPIE Int. Soc. Opt. Eng. 5184, p. 47 (2003).

Bibliography

[AE04]   A. Alu and N. Engheta, *Guided modes in a waveguide filled with a pair of single-negative (SNG), double-negative (DNG), and/or double-positive (DPS) layers*, IEEE Trans. Microwave Theory Tech. **52** (2004), 199–210.

[AG66]   V. M. Agranovich and V. L. Ginzburg, *Spatial dispersion in crystal optics and the theory of excitons*, 1st ed., Interscience Publ., a division of John Wiley, London – New York – Sydney, 1966.

[AG06]   V. M. Agranovich and Yu. N. Gartstein, *Spatial dispersion and negative refraction of light*, Physics – Uspekhi **49** (2006), 1029.

[AGZ06]   V. M. Agranovich, Yu. N. Gartstein, and A. A. Zakhidov, *Negative refraction in gyrotropic medium*, Phys. Rev. B **73** (2006), 045114.

[AKSV99]   M. S. Agranovich, B. Z. Katselenbaum, A. N. Sivov, and N. N. Voitovich, *Generalized method of eigenoscillations in diffraction theory*, Wiley-VCH Verlag, Berlin, 1999.

[AM06]   D. J. Anderson and M. Moskovits, J. Phys. Chem. B **110** (2006), 13722.

[ASE06]   A. Alu, A. Salandrino, and N. Engheta, *Negative effective permeability and left-handed materials at optical frequencies*, Opt. Express **14** (2006), 1557.

[ASNZ04]   V. M. Agranovich, Y. R. Shen, R. H. Naughman, and A. A. Zakhidov, *Optical bulk and surface waves with negative refraction*, J. Luminescence **110** (2004), 167–173.

[Asp82]   D. E. Aspnes, *Local field effects and effective medium theory: a microscopic perspective*, Am. J. Phys. **50** (1982), 704.

[AvEW03]   E. Altewischer, M. P. van Exter, and J. P. Woerdman, *Polarization analysis of propagating surface plasmons in a subwavelength hole array*, J. Opt. Soc. Am. B **20** (2003), 1927.

[BD92]   D. Bergman and K.-J. Dunn, Phys. Rev. B **45** (1992), 13262.

[Bet44]   H. A. Bethe, *Theory of diffraction by small holes*, Phys. Rev. **66** (1944), no. 7-8, 163.

[BLP82]   V. B. Berestetskii, E. M. Lifshitz, and L. P. Pitaevskii, *Quantum electrodynamics*, 2nd ed., Pergamon Press, New York, 1982.

[BMD$^+$04] W. L. Barnes, W. A. Murray, J. Dintiger, E. Devaux, and T. W. Ebbesen, Phys. Rev. Lett. **92** (2004), 107401.

[BMN06]   D. W. Brandl, N. A. Mirin, and P. Nordlander, J. Phys. Chem. B **110** (2006), 12302.

[BS80]   D. J. Bergman and D. Stroud, Phys. Rev. B **22** (1980), 3527.

[BS92]   ———, *Properties of macroscopically inhomogeneous media*, Solid State Physics **46** (1992), 147.

[BS98]   M. J. Bloemer and M. Scalora, Appl. Phys. Lett. **72** (1998), 1676.

[BS03]   D. J. Bergman and M. I. Stockman, *Surface plasmon amplification by stimulated emission of radiation: Quantum generation of coherent surface plasmons in nanosystems*, Phys. Rev. Lett. **90** (2003), 027402.

[BSP$^+$07] A. Baev, M. Samoc, P. N. Prasad, M. Krykunov, and J. Autschbach, *A quantum chemical approach to the design of chiral negative index materials*, Opt. Express **15** (2007), 5730.

[BW80]   M. Born and E. Wolf, *Principles of optics*, Pergamon Press, Oxford, Sixth Edition, 1980.

198

[BYBS99]   R. S. Benninnk, Y.-K. Yoon, R. W. Boyd, and J. E. Sipe, *Accessing the optical nonlinearity of metals with metal-dielectric photonic bandgap structures*, Opt. Lett. **24** (1999), 1416.

[CCKS07]   Wenshan Cai, Udai Chettiar, Alexander Kildishev, and Vladimir Shalaev, *Optical cloaking with metamaterials*, Nature Photon. Lett. **1** (2007), 224–227.

[CCY$^+$07]   W. Cai, U. K. Chettiar, H-K. Yuan, V. C. de Silva, , A. V. Kildishev, V. P. Drachev, and V. M. Shalaev, *Metamagnetics with rainbow colors*, Opt. Express **15** (2007), 3333.

[CG02]   J. M. Chalmers and P. R. Griffiths (eds.), *Handbook of vibrational spectroscopy*, John Wiley, Chichester, 2002.

[CGC05]   S.-H. Chang, S. K. Gray, and G. C.Schatz, Opt. Express **13** (2005), 3150.

[CI03]   C. Caloz and T. Itoh, IEEE Microwave Wireless Comp. Lett. **13** (2003), 547.

[CI04]   ———, *Transmission line approach of left-handed (lh) materials and microstrip implementation of an artificial lh transmission line*, IEEE Trans. Antennas Propagation **52** (2004), 1159–1166.

[CKKS06]   U. K. Chettiar, A. V. Kildishev, T. A. Klar, and V. M. Shalaev, *Negative index metamaterial combining magnetic resonators with metal films*, Opt. Express **14** (2006), 7872.

[CL02]   Q. Cao and P. Lalanne, Phys. Rev. Lett **88** (2002), 057403.

[CMK$^+$99]   R. F. Cregan, B. J. Mangan, J. C. Knight, T. A. Birks, P. St. J. Russell, P. J. Roberts, and D. C. Allan, Science **285** (1999), 1537.

[Com03]   Comsol AB, Burlington, MA, *Femlab reference manual, version 2.3*, 2003.

[Com06]   Comsol AB, Burlington, MA, *Comsol multiphysics user's guide, version 3.3*, August 2006.

199

[CPM+02]   F. Capasso, R. Paiella, R. Martini, R. Colombelli, C. Gmachl, T. L. Myers, M. S. Taubman, R. M. Williams, C. G. Bethea, K. Unterrainer, H. Y. Hwang, D. L. Sivco, A. Y. Cho, A. M. Sergent, H. C. Liu, and E. A. Whittaker, *Quantum cascade lasers: Ultrahigh-speed operation, optical wireless communication, narrow linewidth, and far-infrared emission*, IEEE J. Quant. Elect. **38** (2002), 511–532.

[CPS+06]   S. A. Cummer, B.-I. Popa, D. Schurig, D. R. Smith, and J. Pendry, *Full-wave simulations of electromagnetic cloaking structures*, Phys. Rev. E **74** (2006), 036621.

[CWR+06]   J. V. Coe, S. M. Williams, K. R. Rodriguez, S. Teeters-Kennedy, A. Sudnitsyn, and F. Hrovat, *Extraordinary IR transmission with metallic arrays of subwavelength holes*, Anal. Chem. **78** (2006), 1385.

[CYK+05]   Y.-S. Cho, G.-R. Yi, S.-H. Kim, D. J. Pine, and S.-M. Yang, *Colloidal clusters of microspheres from water-in-oil emulsions*, Chem. Mater. **17** (2005), 5006.

[dAGMS05] F. J. García de Abajo, R. Gómez-Medina, and J. J. Sáenz, *Full transmission through perfect-conductor subwavelength hole arrays*, Phys. Rev. E **72** (2005), 016608.

[DEW+05]   G. Dolling, C. Enkrich, M. Wegener, J. F. Zhou, C. M. Soukoulis, and S. Linden, *Cut-wire pairs and plate pairs as magnetic atoms*, Opt. Lett. **30** (2005), 3198.

[DEW+06]   G. Dolling, C. Enkrich, M. Wegener, C. M. Soukoulis, and S. Linden, *Simultaneous negative phase and group velocity of light in a metamaterial*, Science **312** (2006), 892.

[DKM81]   O. V. Dolgov, D. A. Kirzhnits, and E. G. Maksimov, *On an admissible sign of the static dielectric function of matter*, Rev. Mod. Phys. **53** (1981), 81–93.

[dKvIVR85] C. G. de Kruif, E. M. F. van Iersel, A. Vrij, and W. B. Russel, *Hard*

200

sphere colloidal dispersions: Viscosity as a function of shear rate and volume fraction, J. Chem. Phys. **83** (1985), 4717.

[DLE+04]   R. Depine, A. Lakhtakia, A. L. Efros, T. Koschny, P. Markoŝ, D. R. Smith, and C. M. Soukoulis, Phys. Rev. E **70** (2004), 048601–048603.

[DUS07]   M. Davanço, Y. Urzhumov, and G. Shvets, *Complex Bloch bands of a 2D plasmonic crystal displaying isotropic negative refraction*, Opt. Express **15** (2007), 9681–9691.

[DWLH06]   Gunnar Dolling, Martin Wegener, Stefan Linden, and Christoph Hormann, *Photorealistic images of objects in effective negative-index materials*, Opt. Express **14** (2006), 1842–1849.

[DWSL07]   G. Dolling, M. Wegener, C. M. Soukoulis, and S. Linden, *Design-related losses of double-fishnet negative-index photonic metamaterials*, Opt. Express **15** (2007), 11536.

[DZF+07]   M. Davanço, Xuhuai Zhang, S. R. Forrest, Y. Urzhumov, and G. Shvets, *Nanofabrication and characterization of subwavelength metamaterials for left-handed propagation at near-infrared wavelengths*, IEEE LEOS'07 (2007).

[ELG+98]   T.W. Ebbesen, H. J. Lezec, H. F. Ghaemi, T. Thio, and P. A. Wolff, Nature **391** (1998), 667.

[ESA05]   N. Engheta, A. Salandrino, and A. Alu, *Circuit elements at optical frequencies: Nanoinductors, nanocapacitors, and nanoresistors*, Phys. Rev. Lett. **95** (2005), 095504.

[EZ05]   N. Engheta and R. W. Ziolkowski, *A positive future for double-negative metamaterials*, IEEE Trans. Microwave Theory Tech. **53** (2005), 1535–1556.

[FB05]   D. Felbacq and G. Bouchitté, *Theory of mesoscopic magnetism in photonic crystals*, Phys. Rev. Lett. **94** (2005), 183902.

[FLSZ05]   N. Fang, H. Lee, C. Sun, and X. Zhang, *Sub-diffraction-limited optical imaging with a silver superlens*, Science **308** (2005), 534.

201

[FLYZ03]   N. Fang, Z. Liu, T. J. Yen, and X. Zhang, *Regenerating evanescent waves from a silver superlens*, Opt. Exp. **11** (2003), 682.

[FM03]   D. R. Fredkin and I. D. Mayergoyz, Phys. Rev. Lett. **91** (2003), 253902.

[GBM02]   P. Gay-Balmaz and O. J. F. Martin, J. Appl. Phys. **92** (2002), 2929.

[GBSS98]   P. Gadenne, F. Brouers, V. M. Shalaev, and A. K. Sarychev, *Giant Stokes fields on semicontinuous metal films*, J. Opt. Soc. Am. B **15** (1998), 68.

[GE03]   A. Grbic and G. Eleftheriades, *Periodic analysis of a 2-d negative refractive index transmission line structure*, IEEE Trans. Antennas Propagation **51** (2003), 2604–2611.

[GE07]   C. Genet and T. W. Ebbesen, Nature **445** (2007), 39.

[GGG$^+$05] A. N. Grigorenko, A. K. Geim, H. F. Gleeson, Y. Zhang, A. A. Firsov, I. Y. Khrushchev, and J. Petrovic, *Nanofabricated media with negative permeability at visible frequencies*, Nature **438** (2005), 335.

[GKLU07]   Allan Greenleaf, Yaroslav Kurylev, Matti Lassas, and Gunther Uhlmann, *Electromagnetic wormholes and virtual magnetic monopoles from metamaterials*, Phys. Rev. Lett. **99** (2007), 183901.

[GSSW04]   D. A. Genov, A. K. Sarychev, V. M. Shalaev, and A. Wei, Nano Letters **4** (2004), 153.

[GTG$^+$98] H. F. Ghaemi, T. Thio, D. E. Grupp, T. W. Ebbesen, and H. J. Lezec, Phys. Rev. B **58** (1998), 6779.

[GvEW03]   C. Genet, M. P. van Exter, and J. P. Woerdman, Opt. Commun. **225** (2003), 331.

[GVP96]   F. J. Garcia-Vidal and J. B. Pendry, Phys. Rev. Lett. **77** (1996), 1163.

[HBC03]   A. A. Houck, J. B. Brock, and I. L. Chuang, *Experimental observations of a left-handed material that obeys Snell's law*, Phys. Rev. Lett. **90** (2003), 137401.

[HL97]   T. E. Huber and L. Luo, Appl. Phys. Lett. **70** (1997), 2502.

[HS04]   E. Hao and G. C. Schatz, *Electromagnetic fields around silver nanoparticles and dimers*, J. Chem. Phys. **120** (2004), 357.

[HSDGH97]   F. Hide, B. J. Schwartz, M. A. Diaz-Garcia, and A. J. Heeger, *Conjugated polymers as solid state laser materials*, Synth. Met. **91** (1997), 35.

[IHH+04]   T. Ichimura, N. Hayazawa, M. Hashimoto, Y. Inouye, and S. Kawata, *Tip-enhanced coherent anti-Stokes Raman scattering for vibrational nanoimaging*, Phys. Rev. Lett. **92** (2004), 220801.

[JAN06]   Z. Jacob, L. V. Alekseyev, and E. Narimanov, *Optical hyperlens: far-field imaging beyond the diffraction limit*, Opt. Express **14** (2006), 8247–8256.

[JC72]   P. B. Johnson and R. W. Christy, Phys. Rev. B **6** (1972), 4370.

[JEES06]   P. K. Jain, S. Eustis, and M. A. El-Sayed, J. Phys. Chem. B **110** (2006), 18243.

[JH89]   J. R. James and P. S. Hall, *Handbook of microstrip antennas*, P. Peregrinus on behalf of the Institution of Electrical Engineers, London, U.K., 1989.

[JH04]   J. B. Jackson and N. J. Halas, Proc. Nat. Acad. Sci. USA **101** (2004), 17930.

[JH05]   Yi Jin and Sailing He, *Focusing by a slab of chiral medium*, Opt. Express **13** (2005), 4974.

[JKL+06]   Z. Jiangfeng, T. Koschny, Z. Lei, G. Tuttle, and C. M. Soukoulis, *Experimental demonstration of negative index of refraction*, Appl. Phys. Lett. **88** (2006), 221103–221101.

[JMW95]   J. D. Joannopoulos, R. D. Meade, and J. N. Winn, *Photonic crystals: Molding the flow of light*, Princeton University Press, Princeton, NJ, 1995.

[Joh87]   Sajeev John, Phys. Rev. Lett. **58** (1987), 2486.

[JWH+03]   J. B. Jackson, S. L. Westcott, L. R. Hirsch, J. L. West, and N. J. Halas, Appl. Phys. Lett. **82** (2003), 257.

[KC02]   D. Kang and N. A. Clark, *Fast growth of silica colloidal crystals*, J. Kor. Phys. Soc. **41** (2002), 817.

[KCL+07]   Alexander V. Kildishev, Uday K. Chettiar, Zhengtong Liu, Vladimir M. Shalaev, Do-Hoon Kwon, Zikri Bayraktar, and Douglas H. Werner, *Stochastic optimization of low-loss optical negative-index metamaterial*, J. Opt. Soc. Am. B **24** (2007), A34–A39.

[KDWS63]   G. F. Koster, J. O. Dimmock, R. G. Wheeler, and H. Statz, *Properties of the thirty-two point groups*, MIT Press, Cambridge, Mass., 1963.

[Kel64]   Joseph B. Keller, *A theorem on the conductivity of a composite medium*, J. Math. Phys. **5** (1964), 548.

[Kir76]   D. A. Kirzhnits, *Are Kramers-Kronig relations for dielectric permittivity of matter always valid? (in Russian)*, Sov. Physics - Uspekhi **119** (1976), 357–369.

[Kit76]   C. Kittel, *Introduction to solid state physics*, Wiley, New York, 1976.

[KKK+04]   N. Katsarakis, T. Koschny, M. Kafesaki, E. N. Economou, and C. M. Soukoulis, Appl. Phys. Lett. **84** (2004), 2943.

[KMJB+02] A. Kassiba, M. Makowska-Janusik, J. Boucle, J. F. Bardeau, A. Bulou, N. Herlin, M. Mayne, and X. Armand, Diamond and Related Materials **11** (2002), 1243.

[KMSS03]   T. Koschny, P. Markoŝ, D. R. Smith, and C. M. Soukoulis, *Resonant and antiresonant frequency dependence of the effective parameters of metamaterials*, Phys. Rev. E **68** (2003), 065602.

[KS03]   P. Kolinko and D. R. Smith, *Numerical study of electromagnetic waves interacting with negative index materials*, Opt. Express **11** (2003), 640–648.

[KUI⁺06]   D. Korobkin, Y. Urzhumov, B. Neuner III, G. Shvets, Z. Zhang, and I. D. Mayergoyz, *Giant transmission and dissipation in perforated SiC films mediated by surface phonon polaritons*, arXiv:physics/0606207 (2006).

[KUI⁺07]   D. Korobkin, Y. Urzhumov, B. Neuner III, C. Zorman, Z. Zhang, I. D. Mayergoyz, and G. Shvets, *Mid-infrared metamaterial based on perforated SiC membrane: Engineering optical response using surface phonon polaritons*, Appl. Phys. A **88** (2007), 605–609.

[KUS06]   D. Korobkin, Y. Urzhumov, and G. Shvets, *Enhanced near-field resolution in mid-infrared using metamaterials*, J. Opt. Soc. Am. B **23** (2006), 468.

[KUZS05]   D. Korobkin, Y. Urzhumov, C. Zorman, and G. Shvets, *Far field detection of the super-lensing effect in mid-infrared: Theory and experiment*, J. Mod. Opt. **52** (2005), no. 16, 2351.

[Law04]   N. M. Lawandy, *Localized surface plasmon singularities in amplifying media*, Applied Physics Letters **85** (2004), no. 21, 5040–5042.

[Law07]   Nabil M. Lawandy, *Subwavelength lasers*, Applied Physics Letters **90** (2007), no. 14, 143104.

[LDL⁺07]   Zhaowei Liu, Stephane Durant, Hyesog Lee, Yuri Pikus, Nicolas Fang, Yi Xiong, Cheng Sun, and Xiang Zhang, *Far-field optical superlens*, Nano Lett. **7** (2007), 403–408.

[Leo06]   Ulf Leonhardt, *Optical conformal mapping*, Science **312** (2006), 1777.

[Ler05]   Robert Lerner, *The Lamont Cranston effect, Harry Potter's cloak, and other forms of invisibility*, IEEE A&E Systems Mag. **03.2005** (2005), 3–7.

[LEW+04]   S. Linden, C. Enrich, M. Wegener, J. Zhou, T. Koschny, and C. M. Soukoulis, *Magnetic response of metamaterials at 100 terahertz*, Science **306** (2004), 1351.

[LFUS06]   V. Lomakin, Y. Fainman, Y. Urzhumov, and G. Shvets, *Doubly negative metamaterials in the near infrared and visible regimes based on thin film nanocomposites*, Opt. Express **14** (2006), no. 23, 11164.

[LFUS07]   ———, *Optical metamaterials based on thin metal films: From negative index of refraction, to enhanced transmission, and to surface wave guidance*, Proc. SPIE **6638** (2007), 663805–1.

[LHS04]   M. J. Lockyear, A. P. Hibbins, and J. R. Sambles, *Surface-topography induced enhanced transmission and directivity of microwave radiation through a subwavelength circular metal aperture*, Appl. Phys. Lett. **84** (2004), 2040.

[LJJP03]   C. Luo, S. G. Johnson, J. D. Joannopoulos, and J. B. Pendry, *Subwavelength imaging in photonic crystals*, Phys. Rev. B **68** (2003), 045115.

[LL84]   L. D. Landau and E. M. Lifshitz, *Electrodynamics of continuous media*, Pergamon Press, London, 1984.

[LLX+07]   Zhaowei Liu, Hyesog Lee, Yi Xiong, Cheng Sun, and Xiang Zhang, *Far-field optical hyperlens magnifying sub-diffraction-limited objects*, Science **315** (2007), 1686.

[LP06]   Ulf Leonhardt and Thomas Philbin, *General relativity in electrical engineering*, New J. Phys. **8** (2006), 247.

[LP07]   Ulf Leonhardt and Thomas G. Philbin, *Quantum levitation by left-handed metamaterials*, arXiv: quant-ph/0608115v5 (2007).

[LS97]   O. Levy and D. Stroud, *Maxwell Garnett theory for mixtures of anisotropic inclusions: application to conducting polymers*, Phys. Rev. B **56** (1997), 8035.

[LSB04]   K. Li, M. I. Stockman, and D. J. Bergman, Phys. Rev. Lett. **92** (2004), 057402.

[LT04]   H. Lezec and T. Thio, Opt. Exp. **12** (2004), 3629.

[LWM$^+$05] Z. Q. Li, G. M. Wang, K. J. Mikolaitis, D. Moses, A. J. Heeger, and D. N. Basov, Appl. Phys. Lett. **86** (2005), 223506.

[Lyu60]   G. Y. Lyubarskii, *Application of group theory in physics*, Pergamon Press, New York, 1960.

[Mal51]   G. D. Malyuzhinets, *A note on the radiation principle (in Russian)*, Zhurnal Technicheskoi Fiziki **21** (1951), 940–942.

[Man50]   L. I. Mandelshtam, *Lectures on some problems of the theory of oscillations (in Russian)*, Complete Collection of Works, vol. 5, Academy of Sciences USSR, Moscow, 1950, pp. 428–467.

[Mar00]   S. L. Marshall, *A periodic Green function for calculation of Coulomb lattice potentials*, J. Phys.: Condens. Mat. **12** (2000), 4575.

[MBW04]   D. O. S. Melville, R. J. Blaikie, and C. R. Wolf, *Submicron imaging with a planar silver lens*, Appl. Phys. Lett. **84** (2004), 4403.

[MBW06]   Graeme W. Milton, Marc Briane, and John R. Willis, *On cloaking for elasticity and physical equations with a transformation invariant form*, New J. Phys. **8** (2006), 248.

[MEP03]   V. N. Manoharan, M. Elsesser, and D. Pine, *Dense packing and symmetry in small clusters*, Science **301** (2003), 483.

[Mer04]   R. Merlin, *Analytical solution of the almost-perfect-lens problem*, Appl. Phys. Lett. **84** (2004), 1290.

[Met84]   H. Metiu, Prog. Surf. Sci. **17** (1984), 153.

[MFZ05]   I. D. Mayergoyz, D. R. Fredkin, and Z. Zhang, *Electrostatic (plasmon) resonances in nanoparticles*, Phys. Rev. B **72** (2005), 155412.

[Mil02]   G. W. Milton, *The theory of composites*, Cambridge University Press, 2002.

[MJB00]   A. M. Michaels, J. Jiang, and L. Brus, J. Phys. Chem. **104** (2000), 11965.

[MK90]   S. M. Mansfield and G. S. Kino, Appl. Phys. Lett. **57** (1990), 2615.

[MM93]   A. R. McGurn and A. A. Maradudin, Phys. Rev. B **48** (1993), 17576.

[MMGVL⁺01] L. Martin-Moreno, F. J. Garcia-Vidal, H. Lezec, K. M. Pellerin, T. Thio, J. B. Pendry, and T. W. Ebbesen, *Theory of extraordinary optical transmission through subwavelength hole arrays*, Phys. Rev. Lett. **86** (2001), 1114.

[MMREI02]   R. Marques, F. Medina, and R. Rafii-El-Idrissi, Phys. Rev. B **65** (2002), 144440.

[Mor00]   A. Moroz, Europhys. Lett. **50** (2000), 466.

[MP04]   V. N. Manoharan and D. J. Pine, *Building materials by packing spheres*, Mater. Res. Soc. Bull. **29** (2004), 91.

[MRS89]   T. Musienko, V. Rudakov, and L. Solov'ev, *On the application of Kramers-Kronig relations to media with spatial dispersion*, J. Phys.: Condens. Matter **1** (1989), 6745–6753.

[MS03]   P. Markoŝ and C. M. Soukoulis, *Transmission properties and effective electromagnetic parameters of double negative metamaterials*, Optics Express **11** (2003), 649.

[MTYH02]   M. Moskovits, L. Tay, J. Yang, and T. Haslett, Topics Appl. Phys. **82** (2002), 215.

[NPRH03]   P. Nordlander, E. Prodan, C. Radloff, and N. J. Halas, Science **302** (2003), 419.

[NTF04]   M. P. Nezhad, K. Tetz, and Y. Fainman, *Gain assisted propagation of surface plasmon polaritons on planar metallic waveguides*, Opt. Express **12** (2004), 4072–4079.

[NZB⁺06]   M. A. Noginov, G. Zhu, M. Bahoura, J. Adegoke, C. E. Small, B. A. Ritzo, V. P. Drachev, and Vladimir M. Shalaev, *Enhancement of*

surface plasmons in an ag aggregate by optical gain in a dielectric medium, Optics Letters **31** (2006), no. 20, 3022–3024.

[OC82]   D. Olego and M. Cardona, Phys. Rev. B **25** (1982), 3889–3896.

[Ole96]   O. A. Oleinik, *Some asymptotic problems in the theory of partial differential equations*, Cambridge University Press, New York, 1996.

[OP02]   S. O'Brien and J. B. Pendry, Journ. Phys. Cond. Matt. **14** (2002), 4035.

[OS92]   O. A. Oleinik and A. S. Shamaev, *Mathematical problems in elasticity and homogenization*, North-Holland, Amsterdam, 1992.

[Paf59]   V. E. Pafomov, Sov. Phys. – Uspekhi **36** (1959), 1853.

[Pal85]   E. D. Palik, *Handbook of optical constants of solids*, Academic Press, Orlando, 1985.

[Pen00]   J. B. Pendry, *Negative refraction makes a perfect lens*, Phys. Rev. Lett. **85** (2000), no. 18, 3966–3969.

[Pen04]   _____, *A chiral route to negative refraction*, Science **306** (2004), 1353.

[PGL$^+$03] C. G. Parazzoli, R. B. Greegor, K. Li, B. E. C. Koltenbah, and M. Tanielian, *Experimental verification and simulation of negative index of refraction using Snell's law*, Phys. Rev. Lett. **90** (2003), 107401.

[PHRS99]   J. B. Pendry, A. J. Holden, D. J. Robbins, and W. J. Stewart, *Magnetism from conductors and enhanced nonlinear phenomena*, IEEE Trans. Microwave Theory Tech. **47** (1999), 2075–2084.

[PHSY96]   J. B. Pendry, A. J. Holden, W. J. Stewart, and I. Youngs, *Extremely low frequency plasmons in metallic mesostructures*, Phys. Rev. Lett. **76** (1996), 4773–4776.

[PLS$^+$99] O. Painter, R. K. Lee, A. Scherer, A. Yariv, J. D. O'Brien, P. D. Dapcus, and I. Kim, Science **284** (1999), 1819.

[PMMGV04]   J. B. Pendry, L. Martin-Moreno, and F. J. Garcia-Vidal, Science **305** (2004), 847.

[PN04]   E. Prodan and P. Nordlander, J. Chem. Phys. **120** (2004), 5444.

[PN05a]   V. A. Podolskiy and E. E. Narimanov, Opt. Lett. **30** (2005), 75.

[PN05b]   _____ , Phys. Rev. B **71** (2005), 201101.

[PO06]   I. E. Protsenko and E. P. O'Reilly, *Dipole lasing phase transitions in media with singularities in polarizabilities*, Physical Review A (Atomic, Molecular, and Optical Physics) **74** (2006), no. 3, 033815.

[Poz98]   David M. Pozar, *Microwave engineering*, 2nd ed., John Wiley & Sons, New York, 1998.

[PQY06]   D. Psaltis, S. R. Quake, and C. Yang, *Developing optofluidic technology through the fusion of microfluidics and optics*, Nature **442** (2006), 381.

[PRHN03]   E. Prodan, C. Radloff, N. J. Halas, and P. Nordlander, Science **302** (2003), 419.

[PS04]   J. B. Pendry and D. R. Smith, Physics Today **57** (2004), 37.

[PSS03]   V. A. Podolskiy, A. K. Sarychev, and V. M. Shalaev, *Plasmon modes and negative refraction in metal nanowire composites*, Opt. Express **11** (2003), 735.

[PSS06]   J. B. Pendry, D. Schurig, and D. R. Smith, *Controlling electromagnetic fields*, Science **312** (2006), 1780.

[PvM86]   P. N. Pusey and W. van Megen, *Phase behaviour of concentrated suspensions of nearly hard colloidal spheres*, Nature **320** (1986), 340.

[RP03]   S. A. Ramakrishna and J. B. Pendry, *Removal of absorption and increase in resolution in a near-field lens via optical gain*, Phys. Rev. B **67** (2003), 201101.

[RSBK03]   J. Gomez Rivas, C. Schotsch, P. Haring Bolivar, and H. Kurtz, *Enhanced transmission of THz radiation through subwavelength holes*, Phys. Rev. B **68** (2003), 201306(R).

[SBK04]   M. I. Stockman, D. J. Bergman, and T. Kobayashi, *Coherent control of nanoscale localization of ultrafast optical excitation in nanosystems*, Phys. Rev. B **69** (2004), 054202.

[SCC+05]   V. M. Shalaev, W. Cai, U. K. Chettiar, H-K. Yuan, A. K. Sarychev, V. P. Drachev, and A. V. Kildishev, *Negative index of refraction in optical metamaterials*, Opt. Lett. **30** (2005), 3356–3358.

[SD89]   A. N. Sudarkin and P. A. Demkovich, *Excitation of surface electromagnetic waves on the boundary of a metal with an amplifying medium*, Sov. Phys. Tech. Phys. **34** (1989), 764–766.

[SE06]   Alessandro Salandrino and Nader Engheta, *Far-field subdiffraction optical microscopy using metamaterial crystals: Theory and simulations*, Phys. Rev. B **74** (2006), 075103.

[SEK+05]   Daniel Sjöberg, Christian Engström, Gerhard Kristensson, David J. N. Wall, and Niklas Wellander, *A Floquet-Bloch decomposition of Maxwell's equations applied to homogenization*, Multiscale Model Simul. **4** (2005), 149–171.

[SFB01]   M. I. Stockman, S. V. Faleev, and D. J. Bergman, Phys. Rev. Lett. **87** (2001), 167401.

[SGE05]   J. Seidel, S. Grafström, and L. Eng, *Stimulated emission of surface plasmons at the interface between a silver film and an optically pumped dye solution*, Phys. Rev. Lett. **94** (2005), 177401.

[SGZdF01]   L. Salomon, F. Grillot, A. V. Zayats, and F. de Fornel, Phys. Rev. Lett. **86** (2001), 1110.

[Sha00]   V. M. Shalaev, *Nonlinear optics of random media: Fractal composites and metal-dielectric films*, Springer Tracts in Modern Physics, vol. 158, Springer, Berlin/Heidelberg, 2000.

[Sha07]   Vladimir M. Shalaev, *Optical negative-index metamaterials*, Nature
            Photonics **1** (2007), 41–48.

[SHD07]   Igor I. Smolyaninov, Yu-Ju Hung, and Christopher C. Davis, *Magnifying superlens in the visible frequency range*, Science **315** (2007),
            1699 – 1701.

[Shv03a]   G. Shvets, *Applications of surface plasmon and phonon polaritons to
            developing left-handed materials and nano-lithography*, Proc. SPIE,
            Plasmonics: Metallic Nanostructures and Their Optical Properties,
            vol. 5221, 2003, p. 124.

[Shv03b]   _____, *Photonic approach to making a material with a negative
            index of refraction*, Phys. Rev. B **67** (2003), 035109.

[Sil59]   R. A. Silin, *Waveguiding properties of two-dimensional periodical
            slow-wave systems (in Russian)*, Elektronika: Voprosy Radioelektroniki **4** (1959), 11–33.

[Sir98]   C. Sirtori, *Long-wavelength ([lambda] = 8-11.5 [mu]m) semiconductor lasers with waveguides based on surface plasmons*, Opt. Lett. **23**
            (1998), 1366–1368.

[Siv57]   D. V. Sivukhin, *The energy of electromagnetic waves in dispersive
            media (in Russian)*, Opt. Spektrosk. **3** (1957), 308–312.

[Sjö06]   Daniel Sjöberg, *Exact and asymptotic dispersion relations for homogenization of stratified media with two phases*, J. Electromagn.
            Waves and Applications **20** (2006), 781–792.

[SK00]   D. R. Smith and N. Kroll, *Negative refractive index in left-handed
            materials*, Phys. Rev. Lett. **85** (2000), 2933–2936.

[SKRS44]   E. Shamonina, V. A. Kalinin, K. H. Ringhofer, and L. Solymar,
            *Imaging, compression and poynting vector streamlines for negative
            permittivity materials*, Elecronics Lett. **37** (1243-1244), 2001.

[SKS04]   David R. Smith, Pavel Kolinko, and David Schurig, *Negative refraction in indefinite media*, J. Opt. Soc. Am. B **21** (2004), 1032.

[SKW59]   W. G. Spitzer, D. Kleinman, and D. Walsh, Phys. Rev. **113** (1959), 127.

[SL00]   O. N. Singh and A. Lakhtakia (eds.), *Electromagnetic waves in unconventional materials and structures*, John Wiley, New York, 2000.

[SLBZ06]   M. I. Stockman, K. Li, S. Brasselet, and J. Zyss, *Octupolar metal nanoparticles as optically driven coherently controlled nanorotors*, Chem. Phys. Lett. **433** (2006), 130–135.

[SMCH03]   D. R. Solli, C. F. McCornick, R. Y. Chiao, and J. M. Hickmann, Opt. Exp. **11** (2003), 125.

[SMJ+06]   D. Schurig, J. J. Mock, B. J. Justice, S. A. Cummer, J. B. Pendry, A. F. Starr, and D. R. Smith, *Metamaterial electromagnetic cloak at microwave frequencies*, Science **314** (2006), 977.

[SMM+06]   M. E. Stewart, N. H. Mack, V. Malyarchuk, J. A. N. T. Soares, T.-W. Lee, S. K. Gray, R. G. Nuzzo, and J. A. Rogers, *Quantitative multispectral biosensing and 1D imaging using quasi-3D plasmonic crystals*, Proc. Nat. Acad. Sc. **103** (2006), 17143.

[SP02]   J. T. Shen and P. M. Platzman, *Near field imaging with negative dielectric constant lenses*, Appl. Phys. Lett. **80** (2002), 3826.

[SP06]   D. R. Smith and J. B. Pendry, *Homogenization of metamaterials by field averaging*, J. Opt. Soc. Am. B **23** (2006), 391.

[SPV+00]   D. R. Smith, W. J. Padilla, D. C. Vier, S. C. Nemat-Nasser, and S. Schultz, *Composite medium with simultaneously negative permeability and permittivity*, Phys. Rev. Lett. **84** (2000), 4184–4187.

[SS04]   A. K. Sarychev and V. M. Shalaev, Proc. SPIE **5508** (2004), 128.

[SSM+04]   D. R. Smith, D. Schurig, J. J. Mock, P. Kolinko, and P. Rye, *Partial focusing of radiation by a slab of indefinite media*, Appl. Phys. Lett. **84** (2004), 2244–2246.

[SSMS02]   D. R. Smith, S. Schultz, P. Markoŝ, and C. M. Soukoulis, *Determination of effective permittivity and permeability of metamaterials from reflection and transmission coefficients*, Phys. Rev. B **65** (2002), 195104.

[SSR+03]   D. R. Smith, D. Schurig, M. Rosenbluth, S. Schultz, S. Ramakrishna, and J. Pendry, *Limitations on sub-diffraction imaging with a negative refractive index slab*, Appl. Phys. Lett. **82** (2003), no. 10, 1506–1508.

[SSS01]   R. A. Shelby, D. R. Smith, and S. Schultz, *Experimental verification of a negative index of refraction*, Science **292** (2001), 77.

[SSS06]   A. K. Sarychev, G. Shvets, and V. M. Shalaev, *Magnetic plasmon resonance*, Phys. Rev. E **73** (2006), 036609.

[ST07]   Andrey K. Sarychev and Gennady Tartakovsky, *Magnetic plasmonic metamaterials in actively pumped host medium and plasmonic nanolaser*, Physical Review B (Condensed Matter and Materials Physics) **75** (2007), no. 8, 085436.

[Str79]   D. Stroud, Phys. Rev. B **19** (1979), 1783.

[SU04a]   G. Shvets and Y. Urzhumov, *Engineering the electromagnetic properties of periodic nanostructures using electrostatic resonances*, Phys. Rev. Lett. **93** (2004), 243902.

[SU04b]   _____, *Polariton-enhanced near-field lithography and imaging with infrared light*, Mat. Res. Soc. Symp. Proc. **820** (2004), R1.2.1.

[SU05]   _____, *Electric and magnetic properties of sub-wavelength plasmonic crystals*, J. Opt. A: Pure Appl. Opt. **7** (2005), S23–S31.

[SU06]   _____, *Negative index meta-materials based on two-dimensional metallic structures*, J. Opt. A: Pure Appl. Opt. **7** (2006), S1–S9.

[SVKS00]   D. R. Smith, D. C. Vier, N. Kroll, and S. Schultz, Appl. Phys. Lett. **77** (2000), 2246.

[SVKS05]   D. R. Smith, D. C. Vier, Th. Koschny, and C. M. Soukoulis, Phys. Rev. E **71** (2005), 036617.

[SVV03]   M. Sarrazin, J. P. Vigneron, and J.-M. Vigoureux, Phys. Rev. B **67** (2003), 085415.

[SWM+05]   Z. Shuang, F. Wenjun, B. K. Minhas, A. Frauenglass, K. J. Malloy, and S. R. J. Brueck, *Midinfrared resonant magnetic nanostructures exhibiting a negative permeability*, Phys. Rev. Lett. **94** (2005), 037402–037401.

[TIZS91]   X. Tang, K. G. Irvine, D. Zhang, and M. G. Spencer, *Linear electro-optic effect in cubic silicon carbide*, Appl. Phys. Lett. **59** (1991), 1938.

[TKU+06]   T. Taubner, D. Korobkin, Y. Urzhumov, G. Shvets, and R. Hillenbrand, *Near-field microscopy through a SiC superlens*, Science **313** (2006), 1595.

[TPF06]   K. A. Tetz, L. Pang, and Y. Fainman, *High-resolution surface plasmon resonance sensor based on linewidth-optimized nanohole array transmittance*, Opt. Lett. **31** (2006), 1528.

[Tre00]   A. Tredicucci, *Single-mode surface-plasmon laser*, Appl. Phys. Lett. **76** (2000), 2164–2166.

[Tre05]   Sergei A. Tretyakov, *Research on negative refraction and backward-wave media: a historical perspective*, Proc. EPFL Latsis Symposium (2005), 30–35.

[TSJ05]   S. Tretyakov, A. Sihvola, and L. Jylhä, *Backward-wave regime and negative refraction in chiral composites*, Photonics and Nanostructures - Fundamental and Aplications **3** (2005), 107–115.

[UKI+07]   Y. Urzhumov, D. Korobkin, B. Neuner III, C. Zorman, and G. Shvets, *Optical properties of sub-wavelength hole arrays in SiC membranes*, J. Opt. A: Pure Appl. **9** (2007), S1–S12.

[US03]   Y. Urzhumov and G. Shvets, *Extreme anisotropy of two-dimensional photonic crystals due to mode degeneracy and crystal symmetry*, Proc. SPIE **5184** (2003), 47.

[US05a]   ———, *Applications of nanoparticle arrays to coherent anti-Stokes Raman spectroscopy of chiral molecules*, Proc. SPIE **5927** (2005), 59271D.

[US05b]   ———, *Extreme anisotropy of wave propagation in two-dimensional photonic crystals*, Phys. Rev. E **72** (2005), 026608.

[US07a]   ———, *Optical magnetism and negative refraction using plasmonic metamaterials*, Solid State Comm. (2007).

[US07b]   ———, *Quasistatic effective medium theory of plasmonic nanostructures*, Proc. SPIE **6642** (2007), 66420X–1.

[USF⁺07]   Y. Urzhumov, G. Shvets, J. Fan, F. Capasso, D. Brandl, and P. Nordlander, *Plasmonic nanoclusters: a path towards negative-index metafluids*, Opt. Express **15** (2007), 14129.

[VA99]   A. P. Vinogradov and A. V. Aivazyan, Phys. Rev. B **60** (1999), 987.

[Ves62]   V. G. Veselago, *Electrodynamics of substances with simultaneously negative values of ϵ and μ*, Sov. Phys. "Uspekhi" **10** (1962), 509–514.

[Vin02]   A. P. Vinogradov, *On the form of constitutive equations in electrodynamics*, Physics – Uspekhi **45** (2002), 331–338.

[vMMWM98]   W. van Megen, T. C. Mortensen, S. R. Williams, and J. Müller, *Measurement of the self-intermediate scattering function of suspensions of hard spherical particles near the glass transition*, Phys. Rev. E **58** (1998), 6073.

[WAM05]   M. S. Wheeler, J. S. Aitchison, and M. Mojahedi, *Three-dimensional array of dielectric spheres with an isotropic negative permeability at infrared frequencies*, Phys. Rev. B **72** (2005), 193103.

[WBNH07]   H. Wang, D. W. Brandl, P. Nordlander, and N. J. Halas, *Plasmonic nanostructures: Artificial molecules*, Acc. Chem. Res. **40** (2007), 53–62.

[Wel01]   Niklas Wellander, *Homogenization of the Maxwell equations: Case I. linear theory.*, Applications of Math. **46** (2001), 29–51.

[WGL⁺07] D. R. Ward, N. K. Grady, C. S. Levin, N. J. Halas, Y. Wu, P. Nord-lander, and D. Natelson, *Electromigrated nanoscale gaps for surface-enhanced Raman spectroscopy*, Nano Lett. **7** (2007), 1396–1400.

[WIG01] R. W. Waynant, I. K. Ilev, and I. Gannot, *Mid-infrared laser applications in medicine and biology*, Phil. Trans. R. Soc. Lond. A **359** (2001), 635.

[WP07] B. Wood and J. B. Pendry, *Metamaterials at zero frequency*, J. Phys.: Condens. Matter **19** (2007), 076208.

[WPS95] A. J. Ward, J. B. Pendry, and W. J. Stewart, *Photonic dispersion surfaces*, J. Phys.: Condens. Matter **7** (1995), 2217.

[Yab87] E. Yablonovich, Phys. Rev. Lett. **58** (1987), 2059.

[Yab94] ———, J. Mod. Opt. **41** (1994), 173.

[Yan06] V. Yannopapas, *Negative index of refraction in artificial chiral materials*, J. Phys.: Condens. Matter **18** (2006), 6883–6890.

[YCI05] Y. Horii Y, C. Caloz, and T. Itoh, *Super-compact multilayered left-handed transmission line and diplexer application*, IEEE Trans. Microwave Theory Tech. **53** (2005), 1527–1534.

[YMM⁺04] G.-R. Yi, V. N. Manoharan, E. Michel, M. T. Elsesser, S.-M. Yang, and D. J. Pine, *Colloidal clusters of silica or polymer microspheres*, Advanced Materials **16** (2004), 1204.

[YPF⁺04] T. J. Yen, W. J. Padilla, N. Fang, D. C. Vier, D. R. Smith, J. B. Pendry, D. N. Basov, and X. Zhang, Science **203** (2004), 1494.

[ZE06] R. W. Ziolkowski and A. Erentok, *Metamaterial-based efficient electrically small antennas*, IEEE Trans. Antennas Propag. **54** (2006), 2113.

[ZFP⁺05] S. Zhang, W. Fan, N. C. Panoiu, K. J. Malloy, R. M. Osgood, and S. R. J. Brueck, *Experimental demonstration of near-infrared negative-index metamaterials*, Phys. Rev. Lett. **95** (2005), 137404.

[ZH01]   R. W. Ziolkowski and E. Heyman, *Wave propagation in media having negative permittivity and permeability*, Phys. Rev. E **64** (2001), 056625–056621.

[Zhi94]   V. V. Zhikov, *Homogenization of differential operators and integral functionals*, Springer Verlag, New York/Berlin, 1994.

[ZKK$^+$05] J. Zhou, T. Koschny, M. Kafesaki, E. N. Economou, J. B. Pendry, and C. M. Soukoulis, *Saturation of the magnetic response of split-ring resonators at optical frequencies*, Phys. Rev. Lett. **95** (2005), 223902–223901.

[ZWCS05]   L. Zhou, W. Wen, C. T. Chan, and P. Sheng, *Electromagnetic wave tunneling through negative permittivity media with high magnetic fields*, Phys. Rev. Lett. **94** (2005), 243905.

Vita

Yaroslav Aleksandrovich Urzhumov, the son of Tamara Aleksandrovna Urzhumova, was born on July 17, 1979 in the city of Frunze (now Bishkek), the capital of Kyrghyzstan (then Kirghiz Republic of USSR). After completing 11 grades at the Secondary School No.4 of Polyarnye Zori, Murmansk region, Russia, in 1996, he entered Moscow Institute of Physics and Technology (MIPT). During the years 1999–2002 he worked as a research assistant at the Institute for Theoretical and Experimental Physics in Moscow. He received his Bachelor of Science degree from MIPT in June 2000, and his Master of Science degree in June 2002. His Ph.D. research began in July 2002 at the Illinois Institute of Technology (IIT) in Chicago. In 2002–2003 he worked as a teaching and research assistant at IIT. In December of 2003, he transferred to the University of Texas at Austin, where he was employed as a research assistant from 2004 to 2007. In 2005, he joined the Graduate Portfolio Program in Nanoscience and Nanotechnology at UT–Austin.

Permanent Address: 1644K West Sixth Street, Austin, Texas 78703

This dissertation was typeset with LaTeX 2_ε[1] by the author.

---

[1]LaTeX 2_ε is an extension of LaTeX. LaTeX is a collection of macros for TeX. TeX is a trademark of the American Mathematical Society. The macros used in formatting this dissertation were written by Dinesh Das, Department of Computer Sciences, The University of Texas at Austin, and extended by Bert Kay, James A. Bednar, and Ayman El-Khashab.